PACIFIC EARTHQUAKE ENGINEERING RESEARCH CENTER

Assessing Seismic Collapse Safety of Modern Reinforced Concrete Moment-Frame Buildings

Curt B. Haselton

Department of Civil Engineering
California State University, Chico

and

Gregory G. Deierlein

Department of Civil and Environmental Engineering
Stanford University

PEER 2007/08
FEBRUARY 2008

Assessing Seismic Collapse Safety of Modern Reinforced Concrete Moment-Frame Buildings

Curt B. Haselton
Department of Civil Engineering
California State University, Chico

Gregory G. Deierlein
Department of Civil and Environmental Engineering
Stanford University

PEER Report 2007/08
Pacific Earthquake Engineering Research Center
College of Engineering
University of California, Berkeley

February 2008

ABSTRACT

A primary goal of seismic design requirements of building codes is to protect the life safety of building inhabitants during extreme earthquakes, which requires that the likelihood of structural collapse be at an acceptably low level. However, building codes and standards are empirical in nature; this results in the collapse safety of new buildings not yet being well understood.

In this research, we develop the tools and methods to quantitatively assess the collapse risk of reinforced concrete (RC) special moment frame (SMF) buildings. This primarily includes treatment of ground motions, element model calibration, and treatment of structural modeling uncertainties.

We use the above tools and methods to assess the collapse risk of 30 RC SMF buildings designed according to ASCE7-02. The collapse probability conditioned on a 2%-in-50 years ground motion ranges from 0.03 to 0.20, with an average of 0.11. The mean annual frequency of collapse (λ_{col}) ranges from $0.7x10^{-4}$ to $7.0x10^{-4}$, with an average of $3.1x10^{-4}$.

The minimum base shear requirement of ASCE7-02 is an important component of ensuring relatively consistent collapse risk for buildings of varying height. Removing this requirement from ASCE7-05 has made taller buildings significantly more vulnerable to collapse; this should be considered in future revisions of ASCE7.

In the course of developing the tools for this research, we found that for an RC column with ductile detailing and low axial load, the median plastic rotation capacity is typically 0.05–0.08 radians, and σ_{LN} = 0.45 to 0.54. Not accounting for proper spectral shape (ε) of ground motion typically leads to an underestimation of the median collapse capacity by a factor of 1.5 and overestimation of λ_{col} by a factor of more than 20. Structural modeling uncertainty is critical and increases λ_{col} by a factor of nearly 10.

Last, this study finds that aspects of the structural design (height, framing layout, etc.) have less impact on the final performance prediction than the aspects of the collapse assessment methodology (structural modeling uncertainties, and spectral shape). This emphasizes the importance of developing a *systematic codified* assessment method that can be used to demonstrate the performance of a structural system.

ACKNOWLEDGMENTS

This work was supported primarily by the Earthquake Engineering Research Centers Program of the National Science Foundation under award number EEC-9701568 through the Pacific Earthquake Engineering Research (PEER) Center. Any opinions, findings, and conclusions expressed in this document are those of the authors and do not necessarily reflect those of the National Science Foundation.

Additional funding was provided by the Federal Emergency Management Agency (FEMA) through the Applied Technology Council (ATC-63). Contributors Sarah Taylor Lange and Jason Chou were supported by the PEER's Research Center's Research Experience for Undergraduates summer internship program.

The research on which this report is based involved many individuals in addition to the authors.

The PEER benchmark team conducted a multi-year effort, and Chapter 2 is based on a subset of findings from that effort. The primary teams for the seismic hazard analysis, the structural design and analysis, and the damage and loss analysis comprise researchers from the University of California at Los Angeles (J. Stewart, P.I., and C. Goulet), Stanford University (G. Deierlein, P.I., and C. Haselton), and the California Institute of Technology (J. Beck, P.I., J. Mitrani-Reiser, and K. Porter), respectively.

The findings of this research contributed directly to work of the Applied Technology Council (ATC) Project 63. Accordingly, we collaborated closely with the ATC-63 Project Management Committee (PMC). This collaboration helped the direction and scope of the research and greatly enhanced the final value of this work. Specifically, Charlie Kircher provided important insights into ground motion issues and on those concerning how research results are adopted into practice and building code applications. Robert Hanson was diligent in reviewing portions of this work and provided a great deal of feedback that refined and honed these research products. Jon Hooper was helpful in reviewing our structural designs. The following ATC-63 project team members also provided useful feedback: Jon Heintz, Jiro Takagi, André Filiatrault, Michael Constantinou, Jim Harris, and Bill Holmes.

Several Stanford University professors were crucial to the success of this project. Professor Helmut Krawinkler was like a second advisor to this work, and contributed to nearly every aspect. Professor Jack Baker was integrally involved in the ground motion and structural uncertainty modeling aspects of this work. Professor C. Allin Cornell provided a great deal of advice regarding aspects of ground motion and structural uncertainty modeling. Professor Miranda also contributed to many aspects of the project.

Abbie Liel was also a critical contributor to this research, collaborating closely on nearly every aspect. She contributed greatly to the topics of element modeling, structural uncertainties, the archetype assessment methodology used in Chapter 6, and on drawing comparisons between performance of modern and existing reinforced concrete frame buildings.

This work was also supported by several hard-working undergraduate and graduate summer interns. Sarah Taylor Lange completed most of the element model calibrations upon which Chapter 4 is based, Brian Dean completed the structural designs and analyses for Chapter 6, and Jason Chou completed the structural designs and analyses for Chapter 7.

CONTENTS

LIST OF FIGURES

LIST OF TABLES

1 Introduction

1.1 MOTIVATION AND BACKGROUND

The primary goal of the seismic design requirements of building codes is to protect the life safety of building inhabitants during extreme earthquakes. First and foremost, this requires controlling the likelihood of structural collapse so that it remains at an acceptably low level. With the implementation of detailing and capacity design requirements in current codes and standards, the assumption is that building codes will meet this safety goal. However, codes are empirical in nature such that the collapse safety they provide has not been rigorously quantified.

Performance-based earthquake engineering (PBEE) offers a transparent method for assessing building collapse safety. PBEE requires both a global probabilistic framework that integrates the various steps of the assessment method and detailed procedures for each step.

The Pacific Earthquake Engineering Research (PEER) Center has recently developed a comprehensive probabilistic framework[1] for PBEE (Krawinkler and Miranda 2004; Deierlein 2004). PEER's PBEE framework builds on previous methods developed in the SAC Joint Venture Steel Project (FEMA 2000b), the FEMA 273/356 project (FEMA 1997, 2000a), and HAZUS (2003). This framework provides a consistent methodology to integrate each component of the overall collapse risk assessment process. Even with such a framework, for rigorous collapse assessment, each step of the process must be carefully executed. These steps include treatment of ground motions, modeling structural collapse, and treatment of uncertainties.

[1] This study focuses on collapse safety, but PEERs PBEE framework is more general, and also includes assessment of damage and monetary losses.

1.2 OBJECTIVES

The two primary objectives of this research are (1) to contribute to the development of methods and tools required for performing rigorous collapse performance assessment and then (2) to utilize these methods to assess the collapse risk of reinforced concrete (RC) special moment-frame (SMF) buildings designed according to modern building code requirements. This research builds on the previous work of many other researchers. More specifically, the objectives of this study and the contributions of this report are as follows.

1. Develop recommendations for selecting and scaling ground motions when simulating the collapse of modern buildings. This builds on the past work of Baker and Cornell (Baker 2005a).
2. Develop a calibrated element model that is capable of simulating the flexural response of RC beam-columns up to global structural collapse. This builds on the past work of Ibarra, Medina, and Krawinkler (2005), as well as Fardis et al. (2003).
3. Develop procedures for treatment of uncertainties in the collapse performance assessment. These uncertainties include ground motion uncertainties, structural modeling uncertainties, and structural design uncertainties. This builds on the past work of Baker and Cornell (2003) and Ibarra and Krawinkler (Ibarra 2003; and Chapter 6).
4. Assess the collapse risk of a single RC SMF building by utilizing techniques 1–3 above within PEER's PBEE framework.
5. Develop a method to generalize the collapse performance assessment from an individual building to a full class of buildings designed according to current building code provisions. Use this method to assess the collapse risk implied by current building code provisions for RC SMF buildings.
6. Examine the effects of building code design requirements (e.g., strength, strong-column weak-beam, drift limits) on collapse performance. Determine how changes to design requirements would affect collapse performance.

1.3 SCOPE

The collapse performance assessment framework and many of the methods/tools developed in this report are general to any type of building (reinforced concrete or steel, frames or walls) and general to any type of site (far field, near field, any soil type). However, this report focuses on assessing the collapse risk of 65 modern RC SMF buildings designed for the seismic hazard of coastal California. In addition, this study is limited to firm-soil sites that are not subject to near-field effects such as directivity.

To support the above collapse risk assessment, this report looks closely at the selection and scaling of ground motions for collapse simulation, considering the spectral shape of the extreme motions that cause the collapse of modern buildings. We also discuss the calibration of a RC beam-column element model capable of capturing the nonlinear cyclic flexural response to large levels of displacement associated with collapse. Structural modeling uncertainties and their impacts in the collapse assessment are also considered in this report.

1.4 ORGANIZATION AND OUTLINE

This report is based on a compilation of research papers. Many of these papers are coauthored, so the first section of each chapter gives credit to the contributions of each author. Chapter 2 serves as an overview of the collapse assessment process, Chapters 3–5 present detailed examinations of each step of the process, and then Chapters 6–7 present the collapse risk findings for 65 RC SMF buildings.

Chapter 2 serves as an overview and example of how to assess the collapse performance of a single building. This chapter (a) presents the PEER PBEE collapse assessment framework, (b) shows how we developed the tools and methods needed to complete a rigorous collapse assessment, and then (c) applies these to assess the collapse performance of a 4-story RC SMF building. Chapter 2 is based on an early study, so the modeling guidelines in of Chapter 2 are superseded by those presented later in Chapter 4.

Chapter 3 discusses ground motions and issues of accounting for spectral shape in the selection and scaling of ground motions. This chapter shows the impact that spectral shape considerations have on collapse performance assessment and then compares two methods to account for this issue. We then propose a simplified method that can be used to adjust collapse predictions for spectral shape through use of the parameter ε which come from dissagregation of seismic hazard.

Chapter 4 presents a fully calibrated RC element model that is capable of capturing the flexural response of beam-columns out to large displacements associated with the collapse of RC frame buildings. The model employs a nonlinear spring developed by Ibarra et al. (2005), which we calibrated to 255 experimental tests of RC columns. From these calibrations, we propose empirical equations to predict element modeling parameters (including prediction of mean and uncertainty). Chapter 4 presents the resulting equations to predict initial stiffness, post-yield hardening stiffness, plastic rotation capacity, post-capping rotation capacity, and parameters for cyclic deterioration.

Chapter 5 discusses how to account for structural modeling uncertainties in collapse performance assessment. This work looks at past research and calibration of test data in order to quantify uncertainties in structural modeling parameters (uncertainties in plastic rotation capacity, etc.). We then look at how these uncertainties affect the collapse capacity of the 4-story RC SMF building from Chapter 2. These uncertainties are then propagated using first-order second-moment (FOSM) to estimate the total uncertainty in collapse capacity. To incorporate this modeling uncertainty into the collapse assessment process, we compare the mean estimate method to the method of confidence level prediction. We then show how structural modeling uncertainties impact the final predictions of collapse risk.

Chapter 6 proposes a method to extend the assessment method for the collapse risk of individual buildings to a full class of buildings. In essence, this process involves (a) defining the important attributes of building design (i.e., height, bay spacing, etc.) and setting bounds for the building class of interest, (b) carefully choosing a set of buildings that are representative of building designs within the bounds defined in (a), and then (b) assessing the collapse risk of each building using the methods developed in Chapters 2–5. This chapter presents the collapse predictions for the 30 representative RC SMF buildings used in this study. We then look at trends in these predictions to reveal the effects of building properties and design parameters (e.g., height, etc.). To illustrate the full collapse assessment process, this chapter presents a detailed summary of the collapse performance assessment for one of the 30 buildings.

Chapter 7 looks at how building code design requirements (e.g., strength, strong-column weak-beam, drift limits) affect collapse performance. To understand how changes to design requirements would impact collapse performance, we redesigned several buildings with varied strength demands, varied strong-column weak-beam ratios, and varied design drift limits. We then predicted the collapse performance of each building to see how the change in design affects the collapse performance. This chapter presents a total of 35 buildings designed with various design requirements.

Chapter 8 presents the summary and conclusions of this research, as well as the limitations and future research needs.

2 Assessment to Benchmark Seismic Performance of Single Code-Conforming Reinforced Concrete Moment-Frame Building

2.1 PEER PERFORMANCE-BASED EARTHQUAKE ENGINEERING METHODOLOGY OVERVIEW

Performance-based earthquake engineering (PBEE) consists of the evaluation, design, and construction of structures to meet seismic performance objectives (expressed in terms of repair costs, downtime, and casualties) that are specified by stakeholders (owners, society, etc.). Figure 2.1 illustrates the PBEE methodology developed by the Pacific Earthquake Engineering Research (PEER) Center, which is applied in this chapter. This methodology involves conditional probabilities to propagate the uncertainties from one level of analysis to the next, resulting in a probabilistic prediction of performance.

Figure 2.1 and Equation (2.1) illustrate the four primary steps of PBEE: hazard analysis, structural analysis, damage analysis, and loss analysis. The terminology is as follows: $p[X|Y]$ denotes the probability density of X conditioned on Y, $\lambda[X|Y]$ denotes the mean exceedance rate (mean frequency) of X given Y, IM denotes an intensity measure, EDP denotes engineering demand parameters, DM denotes damage measures, and DV denotes decision variables. Equation 2.1 is also conditioned on the facility definition and site, but this is excluded from the equation for clarity.

$$\lambda[DV] = \iiint p[DV \mid DM] \cdot p[DM \mid EDP] \cdot p[EDP \mid IM] \cdot d\lambda[IM] \cdot dIM \cdot dEDP \cdot dDM \qquad (2.1)$$

The first step in PBEE is the hazard analysis, in which $\lambda[IM]$, the mean annual rate of exceedance as a function of a particular ground shaking intensity measure IM (or a vector of IMs), is evaluated for the site, considering nearby earthquake sources and site conditions. We take the spectral acceleration at the fundamental-mode building period [denoted $S_a(T_1)$] as the principal IM in this work. A suite of acceleration histories are selected that are compatible with site hazard, and these records are scaled to match the *IM* determined from seismic hazard analysis for subsequent use in dynamic analysis.

The second step involves performing a suite of nonlinear response history analyses of a structural model of the facility to establish the conditional probabilistic response, $p[EDP|IM]$, for one or more engineering demand parameters, conditioned on *IM*. Some examples of *EDPs* are peak interstory drift, peak floor acceleration, and peak plastic-hinge rotation. Simulation of strength and stiffness degradation in the nonlinear response history analyses enable the collapse limit state (for select failure modes) to be simulated directly.

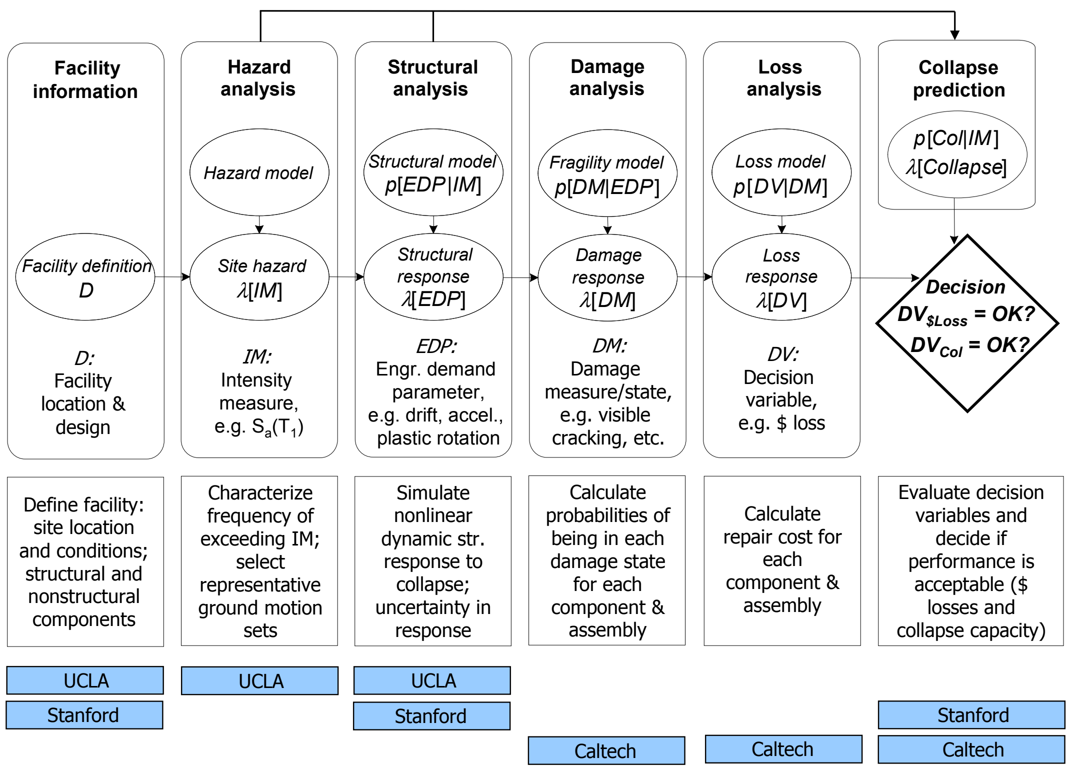

Fig. 2.1 Schematic of PBEE methodology (after Porter 2003).

The third step is damage analysis, in which fragility functions are utilized to express the conditional probability, $p[DM|\ EDP]$, that a component (e.g., beam, column, wall partition, etc.) is in, or exceeds, a particular damage state specified by *DM*. The selected damage states reflect the repair efforts needed to restore the component to an undamaged state. Fragility functions are compiled based on laboratory experiments, analytical investigations, expert opinion, or some combination of these.

The final step of PBEE establishes the conditional probabilistic losses, $p[DV| DM]$, where DV may include repair cost, repair duration, and loss of life. Repair cost is the metric used as the loss DV in this study. By integrating numerically all the conditional probabilities along with the ground motion hazard function, as given by Equation (2.1), the mean annual rate, $\lambda[DV]$, with which various DV levels are exceeded can finally be calculated. The analysis results expressed in this form can be used to inform risk-management decisions.

Figure 2.1 showed how the PEER PBEE methodology can be divided into discrete steps with the boxes at the bottom of the figure showing how we made these divisions among research groups involved in this study. Combining the results from all the steps to obtain the DVs is a highly collaborative process, which requires careful exchange of information among the research groups. Figure 2.2 shows how we structured this flow of information.

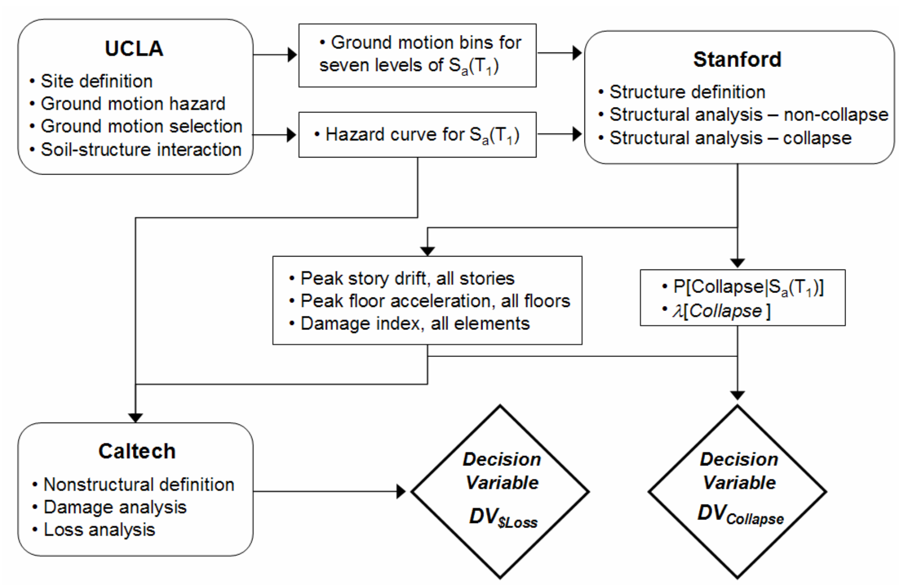

Fig. 2.2 Depiction of information flow among research groups.

In this chapter, the above methodology is applied to eight alternative designs of a 4-story reinforced concrete (RC) special-moment-resisting-frame (SMRF) building, which is designed per current building code requirements. Our objectives are both to illustrate the application of the PBEE methodology and to evaluate the expected performance of similar structures designed and constructed in accordance with modern building code provisions. Uncertainties are included and propagated through each step of the PBEE process. *EDP* distributions evaluated from the structural response simulations reflect record-to-record variability conditioned on a given ground motion intensity. Structural modeling uncertainties are not included in the damage and repair cost analyses for the non-collapse cases, but they are included for the collapse predictions, where they are shown to have a significant effect. This approach is reasonable because previous research has shown that the dispersion (due to modeling uncertainties) of the pre-collapse *EDP* response is less important than uncertainty in the damageable components' capacity and their unit repair costs (Porter et al. 2002).

2.2 GROUND MOTION HAZARD CHARACTERIZATION AND BUILDING SITE

We sought to locate the benchmark building on a site with typical earthquake hazard for urban regions of California where near-fault directivity pulses are not expected. The site used to meet this objective is located on deep sediments south of downtown Los Angeles, and is generally representative of sites throughout the Los Angeles basin. This site is located at 33.996° latitude, -118.162° longitude, and is within 20 km of seven faults, but no single major fault produces near-fault motions that dominate the site hazard. The soil conditions correspond to NEHRP soil category D, with an average shear wave velocity of V_{s-30} = 285 m/s.

2.3 BENCHMARK BUILDING DESIGN

2.3.1 Structural Design

The benchmark building is a 4-story reinforced concrete (RC) frame structure, as illustrated in Figure 2.3, designed according to the 2003 International Building Code (IBC) (ICC 2003). Notice that the building is designed with identical 4-bay frames in each orthogonal direction.

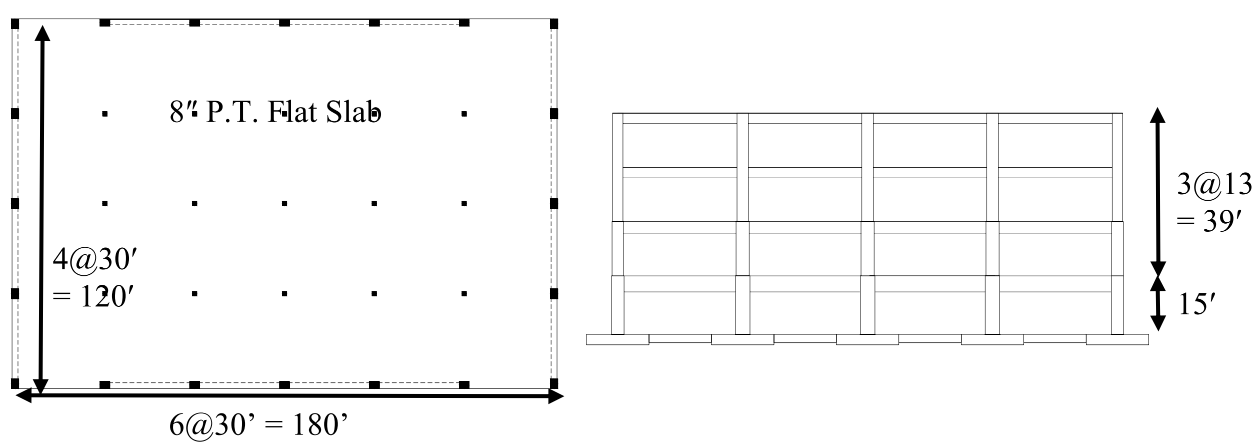

Fig. 2.3 Plan and elevation of 4-story office benchmark building, Design A.

To represent the likely variation in design for a modern building of this size, several alternative designs are considered; these designs are listed in Table 2.1. In the first four design variants, lateral loads are resisted by moment frames at the perimeter of the building (i.e., perimeter frames), with interior columns designed to only carry gravity loads. The last four variants utilize a space-frame design in which each framing line is moment-resisting. Figure 2.3 shows the plan view of the perimeter-frame design; the space-frame designs have a similar layout, but with frames on every grid line. Additional details on the structural design variants are given in Haselton et al. (2006).

Table 2.1 Summary of design variants and related design decisions.

Design	Frame System	Beam Design Strength Factor (ϕMn/Mu)	SCWB Factor (code requirement is 1.2)	Provided ratio of positive to negative beam flexural capacity (ACI 318-05 21.3.2.2)	Beams Designed as T-Beams?	SCWB Provision Applied in Design	Slab Steel
A	Perimeter	1.25	1.3	0.75	No	2003 IBC / ACI 318-02	2 #4 @12" o.c.
B	Perimeter	1.0	1.2	0.5	No	2003 IBC / ACI 318-02	2 #4 @12" o.c.
C	Perimeter	1.25[a]	1.3[a]	0.5	No	2003 IBC / ACI 318-02	2 #4 @12" o.c.
D	Perimeter	1.0	n/a	0.5	No	none[b]	2 #4 @12" o.c.
E	Space	1.0	1.2	0.5	No	2003 IBC / ACI 318-02	2 #4 @12" o.c.
F	Space	1.0	1.2	0.5	Yes	2003 IBC / ACI 318-02	2 #4 @12" o.c.
G	Space	1.0	1.2	0.5	No	1997 UBC	2 #4 @12" o.c.
H	Space	1.0	1.2	0.5	No	1997 UBC	#5, #6 @16" o.c.

a - only the second floor beam and first story columns were proportioned for these ratios; the beams/columns are uniform over the building

b - columns designed for strength demand and not for SCWB; this is not a code-conforming design

Based on the building code limitations on the effective first-mode period ($T_{max} \leq 1.4T_{code}$ = 0.80s), the building has a design seismic coefficient (fraction of the building weight applied as an equivalent static lateral force) of 0.094. Computed fundamental periods of the seven designs range from 0.53–1.25 sec, depending on whether the system is a perimeter or space frame and on the initial stiffness assumptions used for analysis. Columns range in size from 18 in. x 24 in. (46 cm x 61 cm), to 30 in. x 40 in. (76 cm x 102 cm); and the beam dimensions range from 18 in. x 33 in. (46 cm x 84 cm), to 24 in. x 42 in. (61 cm x 107 cm). The designs were controlled primarily by the strength demands to achieve the target seismic design coefficient, the strong-column weak-beam requirement, joint shear capacity provisions, and to a lesser extent, drift limitations (Haselton et al. 2006).

For each structural design realization, a two-dimensional analysis model was created of a typical 4-bay frame in one direction. For the perimeter-frame systems, an equivalent gravity frame was modeled in series with the perimeter frame to account for the additional strength and stiffness provided by the gravity system. For the space-frame systems, the two-dimensional models neglect biaxial bending in the columns. To offset the error introduced by neglecting this biaxial bending in the response, the space frame columns were designed for uniaxial bending (i.e., not for biaxial strength demands).

2.3.2 Nonstructural Design: Building Components Considered in Loss Estimates

The design of the nonstructural components of the building was completed by Mitrani-Reiser et al. and the details can be found in the full report on this study (Haselton et al. 2007e).

2.4 SITE HAZARD AND GROUND MOTIONS

2.4.1 Site Hazard Characterization

Goulet and Stewart conducted the probabilistic seismic hazard analysis (PSHA for the benchmark site (Goulet et al. 2006a; Haselton et al. 2007e). The average fundamental period of the buildings used in this study is 1.0 sec so we use S_a(1 sec) as the intensity measure in this study.

Goulet and Stewart computed and disaggregated the seismic hazard (Bazzurro and Cornell 1999) for seven hazard levels, from the 50%-in-5 years level to the 2%-in-50 years level. They then used this information in the record selection process.

2.4.2 Strong Motion Record Selection Methodology

In Chapter 3, we discuss the problem of ground motion selection in detail, and propose two options for treating ground motions in the context of collapse analysis. For the 4-story building study, we used the option of selecting ground motion sets specific to the site, structural period, and hazard level.

To capture how ground motion properties change over various levels of shaking, Goulet and Stewart (Goulet et al. 2006a; Haselton et al. 2007e) selected seven separate sets of ground motions for hazard levels ranging from 50%-in-5-years to the 2%-in-50-years level. Consistent with the recommendations of Chapter 3, each ground motion set was selected to have the proper spectral shape (epsilon value), as well as other aspects of the ground motion such as event magnitude, distance from source to site, faulting mechanism, etc. These seven sets of motions are used for the structural analysis at the appropriate level of ground motion.

2.5 STRUCTURAL MODELING AND SIMULATION

2.5.1 Overview of Modeling

PBEE requires structural models to be accurate for relatively low-level, frequent ground motions (which can contribute to damage and financial loss) as well as for high-level, rare ground motions (which can contribute to both the collapse risk and financial loss). For low ground motion intensity levels, cracking and tension stiffening phenomena are important to the response of RC structures. For very high ground motion intensity levels, deterioration at large deformations leading to collapse is important.

Structural element models are generally not available to accurately represent the full range of behavior — from initial cracking up through strength and stiffness deterioration behavior that leads to global sidesway collapse. Therefore, we decided to use two models: a fiber model to accurately capture the structural response at low intensity levels (where cracking and initial yielding behavior governs) and a plastic-hinge model to capture the strength and stiffness deterioration and collapse behavior. The fiber model consists of fiber beam-column elements with an additional shear degree-of-freedom at each section, finite joint elements with panel shear and bond-slip springs, and column-base bond-slip springs. The plastic-hinge model lumps the bond-slip and beam-column yielding response into one concentrated hinge.

The OpenSees (2006) analysis platform is used for this study. For all designs, P-delta effects are accounted for using a combination of gravity loads on the lateral resisting frame and gravity loads on a leaning column element. The effects of soil-structure interaction (SSI) were considered in a subset of the simulations, including both inertial effects associated with foundation flexibility and damping as well as kinematic effects on ground motions at the foundation level of the building (Haselton et al. 2006). As expected, the soil-structure interaction effects were found to be insignificant for the rather flexible (long-period) moment frame. Accordingly, SSI effects were not considered in the simulations presented in the remainder of the chapter.

2.5.2 Plastic-Hinge Model for Collapse Simulation

As shown in Figure 2.4a, plastic-hinge models for beam-columns have a trilinear backbone curve described by five parameters (M_y, θ_y, K_s, θ_{cap}, and K_c). Figure 2.4b shows an example calibration of this model to test data, including the observed hysteretic response, the calibrated hysteretic response, and the calibrated monotonic backbone curve. This model was originally developed by Ibarra et al. (2005, 2003) and implemented in OpenSees by Altoontash (2004). The negative branch of the post-peak response simulates strain-softening behavior associated with phenomena such as concrete crushing and rebar buckling and fracture. The accuracy of the onset and slope of this negative branch are among the most critical aspects of collapse modeling (Ibarra et al. 2005, 2003; Haselton et al. 2006).

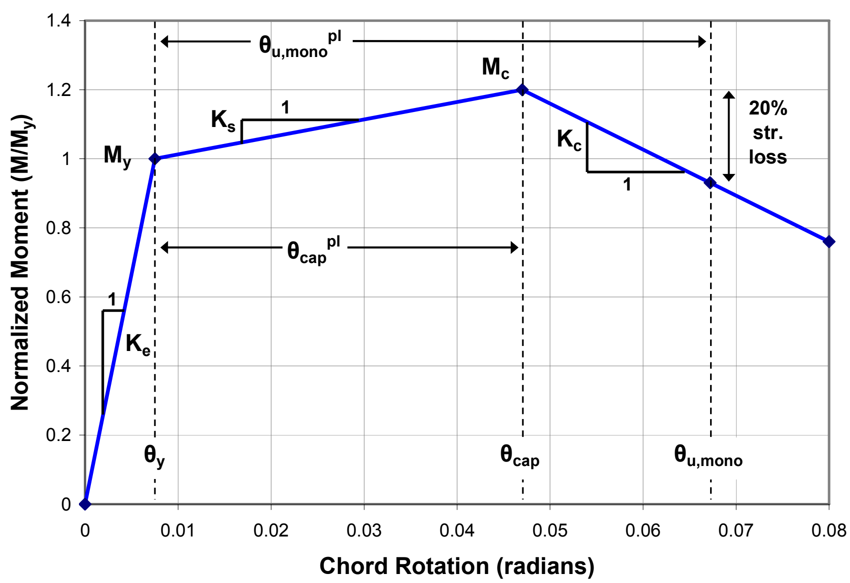

(a)

Fig. 2.4 Illustration of spring model with degradation (a) monotonic backbone curve and (b) observed and calibrated responses for experimental test by Saatcioglu and Grira, specimen BG-6 (1999); solid black line is calibrated monotonic backbone. Calibration completed as part of extensive calibration study (Haselton et al. 2007b, Chapter 4).

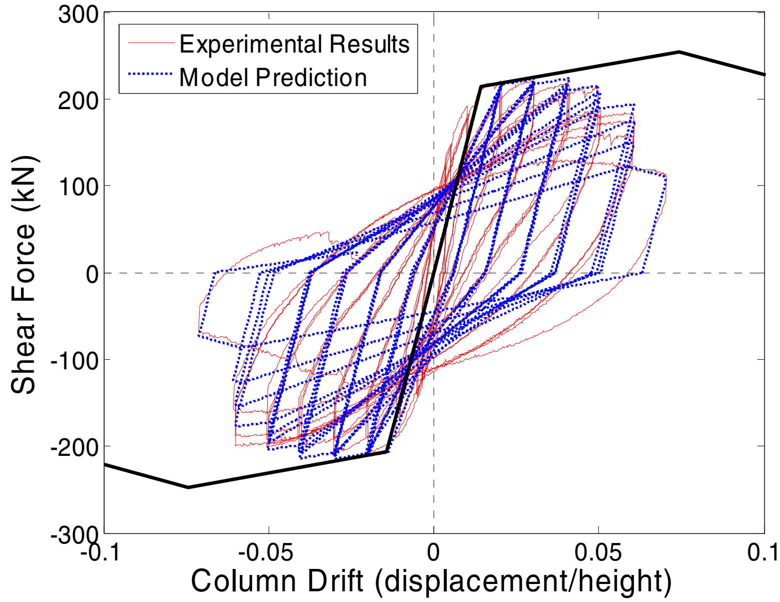

(b)

Fig. 2.4—*Continued.*

The model captures four modes of cyclic degradation: strength deterioration of the inelastic strain-hardening branch, strength deterioration of the post-peak strain-softening branch, accelerated reloading stiffness deterioration, and unloading stiffness deterioration. The cyclic deterioration is based on an energy index that has two parameters that reflect the normalized energy-dissipation capacity and the rate of cyclic deterioration.

Model parameters for RC beam-columns are based on two sources. The first source consists of empirical relationships developed by Fardis et al. (2001, 2003) to predict chord rotation of RC elements at both the yield rotation, θ_y, and at the ultimate rotation, $\theta_{u,mono}{}^{pl}$, where "ultimate" is defined as a reduction in load resistance of at least 20% under monotonic or cyclic loading. Fardis et al. developed these empirical relations using data from over 900 cyclic tests of rectangular columns with conforming details. Typical mean capping rotations are $\theta_{cap}{}^{pl} = 0.05$ radians for columns and $\theta_{cap}{}^{pl} = 0.07$ radians for slender beams. The coefficient of variation (COV) is 0.54 when making predictions of rotation capacity under monotonic loading. These relatively large plastic rotation capacities result from low axial loads, closely spaced stirrups providing shear reinforcement and confinement, and the flexibility introduced by bond-slip deformations.

The second data source consists of an experimental database of RC element behavior (PEER 2005; Berry et al. 2004). As part of the 4-story building study, tests of 30 conforming flexurally dominated columns were assembled from this database to calibrate parameters of the model given in Figure 2.4a. This calibration provided important information on the inelastic hardening and softening slopes, which are found to be $K_s/K_e \approx 4\%$ and $K_c/K_e \approx -7\%$, respectively. The data also provided calibration of cyclic deterioration parameters.

The flexural strength of plastic hinges was computed using fiber moment-curvature analysis in OpenSees (2006). Initial stiffness of plastic hinges (K_θ) is defined using both the secant stiffness through the yield point (i.e., K_e taken as K_{yld}) and the secant stiffness through 40% of the yield moment (i.e., K_e taken as K_{stf}). Stiffness values K_{yld} and K_{stf} are estimated using both empirical estimates from Panagiotakos and Fardis (2001) and the results of our calibration study (Haselton et al. 2007b, Chapter 4). The predictions by Panagiotakos and Fardis (2001) for K_{yld} are $0.2EI_g$ on average; however our calibrations (Haselton et al. 2007b, Chapter 4) showed a stronger trend with axial load than is suggested by the empirical equation by Panagiotakos and Fardis. Our calibrations show that K_{stf} is roughly twice that of $K_{yld.}$

2.5.3 Static Pushover Analysis

Static pushover analyses were performed to investigate the general load-deflection relationship for the benchmark building models and the sensitivity of results to various modeling assumptions (fiber model vs plastic-hinge model; use of K_{yld} versus K_{stf} for initial stiffness of plastic hinge). These analyses were performed using a static lateral force distribution derived from the equivalent lateral force procedures in the seismic design provisions (ASCE 2002). Figure 2.5 shows the results for design variant "A" (see Table 2.1), which is used for illustration in this chapter. Similar results obtained for other designs are given in (Haselton et al. 2007e). The results illustrate a few important differences in model predictions: (a) the plastic-hinge model using K_{stf} agrees well with the fiber model for low levels of drift, (b) the plastic-hinge model using K_{yld} agrees well with the yield drift of the fiber model, (c) the fiber model is less numerically stable as drift increases, and stops converging at 3% roof drift, and (d) the plastic-hinge model is capable of capturing strain-softening behavior that the fiber model can not capture.

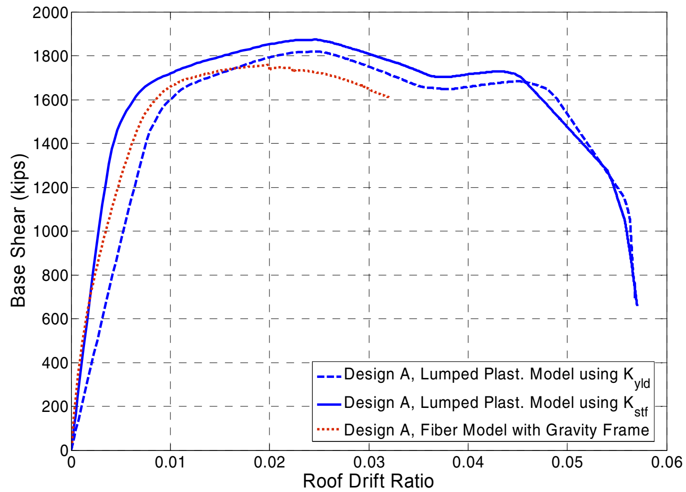

Fig. 2.5 Static pushover curves for both plastic-hinge and fiber models.

2.5.4 Nonlinear Dynamic Analysis: Pre-Collapse Response

We performed nonlinear dynamic analyses for the benchmark building designs using ground motion suites selected by Goulet and Stewart (Goulet et al. 2006a; Haselton et al. 2007e) for seven different ground motion intensity levels, with an additional intensity level of 1.5x the 2%-in-50-years ground motion. Figure 2.6a shows illustrative results for the fiber model, and Figure 2.6b compares the fiber model to the plastic-hinge model with the two estimates of initial stiffness. Also shown for reference are the static pushover results after converting the pushover force to an equivalent spectral acceleration (ATC 1996).

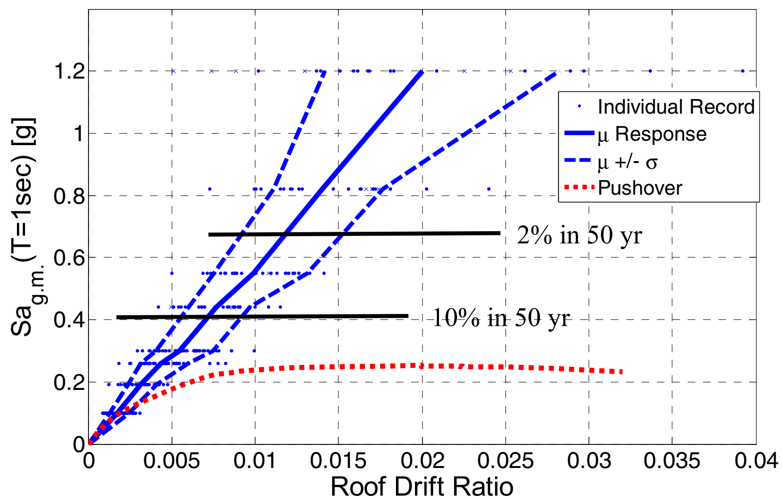

(a)

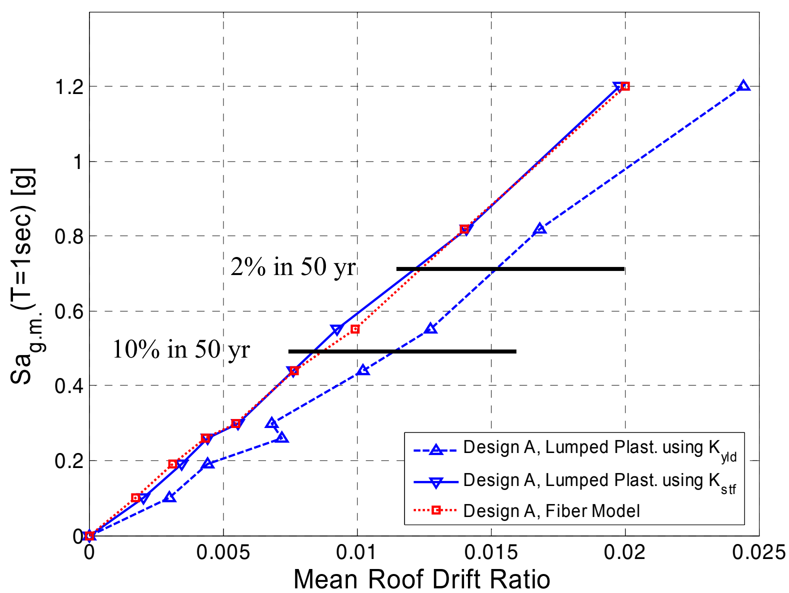

(b)

Fig. 2.6 Nonlinear dynamic analysis results for Design A (a) roof drift ratio using fiber model and (b) comparison of peak roof drift ratios using fiber model and two plastic-hinge models.

The above figures show displacement response using roof drift ratio plotted as a function of geometric mean $S_a(T_1)$ for the input motion suite. The small dots represent the responses from each scaled earthquake ground motion component; and the solid and dashed lines represent the mean and mean +/- one standard deviation (assuming a lognormal distribution) responses across ground motion levels. Figure 2.6a shows that mean roof drift ratios are 1.0% and 1.4% for the 10% and 2%-in-50-years ground motion levels, respectively. This figure also shows that, even though the building yields at a relatively low roof drift ratio, the mean dynamic analysis results obey the equal displacement rule up to the 2% roof drift level demands, corresponding to ground motion intensities about 20% larger than the 2%-in-50-years hazard.

Figure 2.6b compares the mean roof drifts predicted using the fiber model and plastic-hinge models with the two treatments of initial stiffness. The results show that the plastic-hinge model can predict roof drifts consistent with the fiber model only when the larger assumed initial stiffness (K_{stf}) is used. The lower yield level stiffness K_{yld} results in overprediction of roof drifts by 20–25%, which can significantly affect the repair costs and monetary losses, as shown subsequently. These results indicate that the higher initial stiffness (K_{stf}) should be used in the plastic-hinge model for dynamic drift predictions that are consistent with those made using the fiber model.

2.5.5 Nonlinear Dynamic Analysis: Collapse Simulation

To investigate sidesway collapse for the benchmark building, incremental dynamic analyses (IDA) (Vamvatsikos and Cornell 2002) were performed for the benchmark designs. IDA involves amplitude scaling of individual ground motion records to evaluate the variation of *EDP* with the scaled *IM* (in this case $S_a(T_1=1.0\ sec)$). With the goal to evaluate the collapse performance, the IDA was performed with the 34 records in the suite assembled for the 2%-in-50-years motion, which was the highest intensity level for which a ground motion suite was assembled in this study. Indeed, the collapse behavior at ground motion levels stronger than the 2%-in-50-years level can be practically accomplished only by scaling ground motions because of a lack of acceleration records with higher intensities. Such scaling could introduce conservative bias into the collapse capacity estimate, since the ε values of the ground motions should increase when $S_a(T_1=1.0\ sec)$ increases.

For the IDA simulations, sidesway collapse is defined as the point of dynamic instability when story drift increases without bounds for a small increase in the ground motion intensity. Figure 2.7a shows the IDA results from all 68 ground motion components (two components for each of the 34 records in the suite), while Figure 2.7b shows the results obtained using only the horizontal component of each record pair that first causes collapse. The results in these figures are for design variant “A”; for the results of other building designs see (Haselton et al. 2007e). The governing component results of the two-dimensional analyses (Fig. 2.7b) are considered reflective of the building collapse behavior, assuming that the actual (three-dimensional) building will collapse in the more critical of two orthogonal directions when subjected to the three-dimensional earthquake ground motion.[1] Comparison of Figures 2.7a and b shows a 30% lower median spectral acceleration to cause collapse (Sa_{col}), and a 20% lower dispersion ($\sigma_{LN,RTR}$), when only the more critical horizontal ground motion component is used.

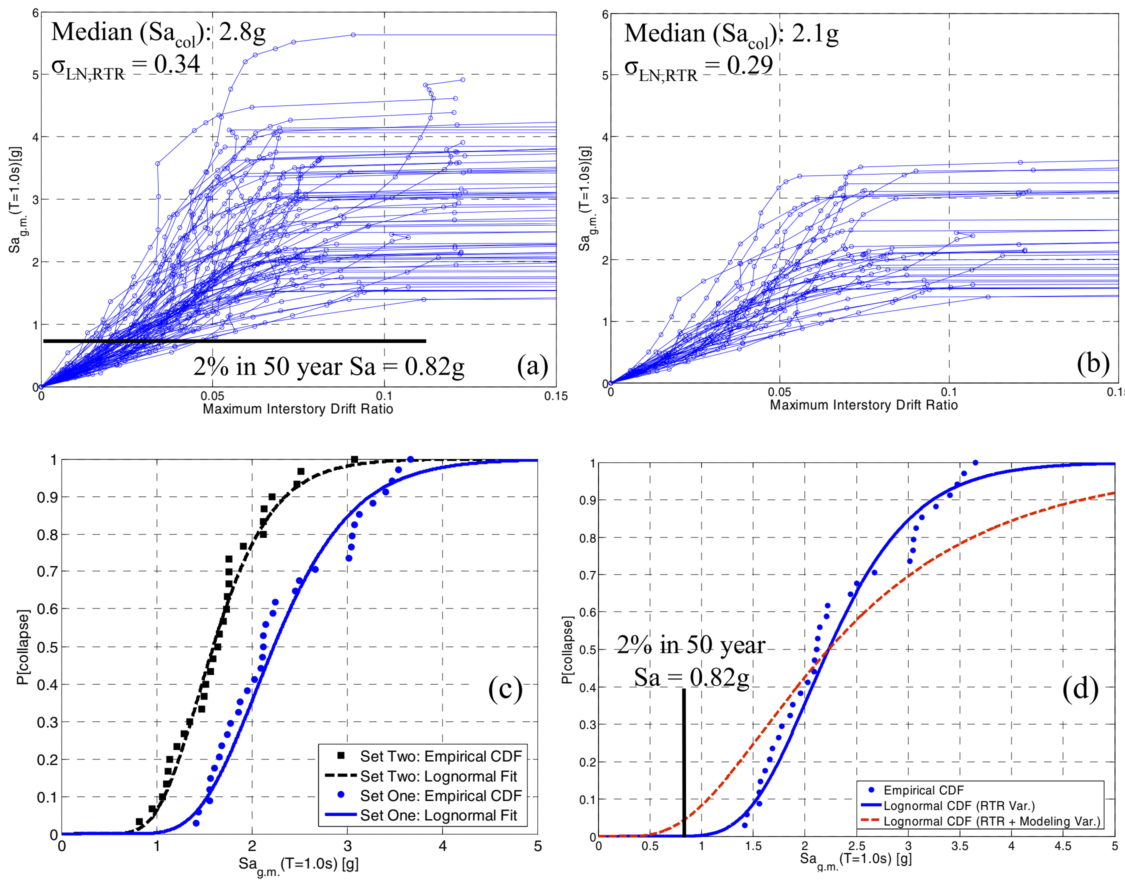

Fig. 2.7 Incremental dynamic analysis for Design A using (a) both horizontal components of ground motion, (b) horizontal component that first causes collapse, (c) effect of epsilon (spectral shape) on collapse capacity, and (d) collapse CDFs including and excluding modeling uncertainty.

The results shown in Figures 2.7a and b are for the ground motion suites developed by Goulet et al., in which ε is accounted for during the selection process; this set was selected for ε = +1.0–2.0, has a mean ε(1s) = 1.4, and is termed "Set One." We also selected an alternative ground motion record set and performed additional analyses to investigate the effect of ε on the

[1] This approximate method considers only the differences between the two horizontal components of ground motion, not 3D structural interactions (3D effects should not be significant for perimeter frames but would be significant for space frame designs).

predicted collapse capacity; this alternative set was selected without regard to ε, has a mean ε(1s) = 0.4, and is termed "Set Two." The collapse Sa(T_1) intensities from the controlling components of Figure 2.7b are plotted as a cumulative distribution function (CDF) in Figure 2.7c (ground motion Set One). Superimposed in this figure are similar collapse points from an IDA using this second set of analyses for ground motions with lower ε values. As shown in Figure 2.7c, a change from Set One to Set Two decreases the expected (median) collapse capacity by 20%. A similar comparison using both horizontal components of ground motion on the benchmark structure instead shows a 40% shift in the median. Chapter 3 discusses the effects of ε in more detail and shows that this 20% value is unusually low; a 50% shift in the median collapse capacity is more typical.

Two recent studies provide a comparison to the results shown here. Zareian (2006) performed collapse simulation using many 3-bay frame models and shear wall models of various heights. He found that a change from ε = 0 to ε = + 2.0 caused an approximate 50–70% increase in the expected collapse capacity. Haselton and Baker (2006) modeled the collapse of single-degree-of-freedom systems using (a) a ground motion set selected without considering ε, (which is the same as Set Two above) and (b) and a set selected to have an average ε = + 1.5. They showed that the median collapse capacities predicted using these two sets varied by 50%. The results from both of the above studies are comparable with the 40% median shift found in this study for the full set of records.

This shift in the collapse capacity CDF data profoundly affects the mean rate of collapse, which depends on the position of the collapse CDF with respect to the hazard curve. For this building where the extreme tail of the hazard curve dominates the collapse results, a 20% increase in the median collapse capacity causes the mean annual frequency of collapse to decrease by a factor of 5–7 (Goulet et al. 2006a). Similarly, a 40% increase in capacity would decrease the mean annual frequency of collapse by a factor of around 10. These results demonstrate the profound importance of ground motion acceleration history selection criteria in accurately predicting building collapse capacity.

The collapse capacity CDF of what is considered as the appropriate ε set is replotted as the solid line in Figure 2.7d, where the data points and fitted CDF are for analyses that only reflect the variability due to record-to-record response in the results. The log standard deviation of this basic (record-to-record) distribution is 0.29 in natural log units. Variability in the collapse capacity arising from uncertain structural properties was also investigated, the results of which are plotted as the dashed CDF in Figure 2.7d. The details of how this "modeling uncertainty" was evaluated are presented next.

Table 2.2 summarizes the structural parameters for which uncertainties were considered in the dynamic response analyses. Many of these parameters were previously defined in Figure 2.4a. As indicated in Table 2.2, the variation in some of the modeling parameters are quite large, e.g., the coefficient of variation in the peak plastic rotation and degradation parameters is on the order of 0.5–0.6. The first-order second-moment (FOSM) method (Baker and Cornell 2003) was used to propagate these structural uncertainties and to estimate the resulting uncertainty in collapse capacity. Correlations between the uncertain structural parameters were considered as described later in Chapter 5. Using reasonable correlation assumptions, the resulting uncertainty in collapse capacity is a standard deviation of 0.5, in natural log units. This rather large value reflects the large variation in some of the underlying modeling parameters that significantly affect the collapse simulation (Table 2.2). To determine the mean estimate of the collapse capacity, in contrast to an estimate at a given level of prediction confidence, we combined both record-to-record and structural variability using the standard square-root-of-sum-of-squares procedure. The combined uncertainties resulted in a total standard deviation of 0.58 in natural log units, which is reflected in the dashed line in Figure 2.7d.

Table 2.2 Summary of random variables considered when estimating uncertainty in collapse capacity resulting from structural uncertainties.

Structural Random Variable	Mean	Coefficient of Variation	Reference(s)
Design Variables:			
Strong-column weak-beam design ratio	1.1*(required)	0.15	Haselton et al. (2007e)
Beam design strength	1.25*(M_u/φ)	0.20	Haselton et al. (2007e)
System Level Variables:			
Dead load and mass	1.05*(computed[a])	0.10	Ellingwood et al. (1980)
Live load (arbitrary point in time load)	12 psf	--	Ellingwood et al. (1980)
Damping ratio	0.065	0.60	Miranda (2005), Porter et al. (2002), Hart et al. (1975)
Beam-Column Element Variables:			
Element strength (M_y)	1.0*(computed[b])	0.12	Ellingwood et al. (1980)
Element initial stiffness (K_e)	1.0*(computed[c])	0.36	Fardis et al. (2003, 2001)
Element hardening stiffness (K_s)	0.5*(computed[b])	0.50	Wang et al. (1978), Haselton et al. (2007e)
Plastic rotation capacity ($\Theta_{cap}{}^{pl}$)	1.0*(computed[d])	0.60	Fardis et al. (2003, 2001)
Hysteretic energy capacity (normalized) (λ)	110	0.50	Ibarra 2003, Haselton et al. (2007e)
Post-capping stiffness (K_c)	-0.08(K_{yld})	0.60	Ibarra 2003, Haselton et al. (2007e)

-- the random variable was treated deterministically
a - computed consistent with common practice
b - computed using fiber analysis with expected values of material parameters
c - computed using [19, 20] and calibrations from [15, 6]
d - computed using empirical equation from [19] (equation is [20] is similar)

Even though the mean estimate method does not result in any shift in the mean collapse point, the increased variation has a significant effect on the collapse probabilities in the lower tail of the distribution. For example, at the 2%-in-50-years ground motion level, the probability of collapse is < 1% when only record-to-record variability is accounted for and 3% when structural modeling uncertainties are included. These results can be used to compute a mean annual frequency of collapse ($\lambda_{collapse}$) by numerically integrating the collapse CDF with the hazard curve (Eq. 7.10 of Ibarra 2003)[2]. The hazard curve information used in this study can be found in Goulet et al. (2006a). Inclusion of the structural modeling uncertainties increases $\lambda_{collapse}$ for design variant A by a factor of 7.5, compared to the $\lambda_{collapse}$ for the analyses that included only record-to-record variability (shown later in Table 2.3). Hence, proper consideration of structural parameter uncertainties is crucial when evaluating collapse probabilities.

This finding that the variability introduced by uncertain structural parameters affects the collapse uncertainty more than record-to-record variability differs from many past studies that concluded that structural uncertainties have only a slight or modest effect on performance

[2] This is the *mean estimate* of the mean annual frequency of collapse.

predictions, e.g., Porter et al. (2002). This apparent contradiction is due to the fact that the present study is focused on modeling the building to collapse, whereas previous studies have generally focused on predicting EDPs for lower levels of deformation. The parameters that control element behavior are different for low versus large levels of deformations, and the parameters that are important for large levels of deformation (for collapse simulation) are both more uncertain and have a greater effect on nonlinear response, as compared to the parameters that influence response at lower deformation levels.

Figure 2.8 shows the various collapse mechanisms predicted by nonlinear dynamic analysis. As shown in the figure, there are six distinct failure modes, which depend on the ground motion record. Note that the static pushover analyses with an inverted triangular loading pattern produces collapse mode (c), which occurs in less than 20% of the dynamic collapses.

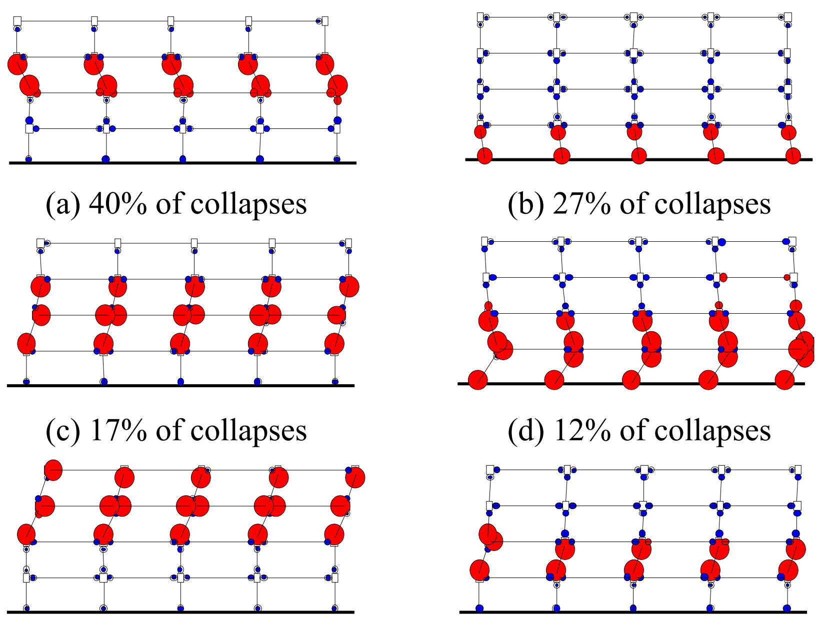

(a) 40% of collapses

(b) 27% of collapses

(c) 17% of collapses

(d) 12% of collapses

(e) 5% of collapses

(f) 2% of collapses

Fig. 2.8 Diagrams showing collapse modes for Design A and percentage of ground motion records causing each collapse mode.

Table 2.3 summarizes the collapse predictions using the approach outlined above for all eight designs and modeling variants. Indicated in the second and third columns for each design are the median collapse capacities and its logarithmic equivalent for the fitted lognormal distributions. Shown in the other columns are the standard deviations of the logarithm of collapse capacities, the estimates of collapse probability conditional on the 2%-in-50-years ground motion level, and the mean annual frequency of collapse ($\lambda_{collapse}$). All results are based on the controlling the horizontal component of ground motion (e.g., Fig. 2.7b rather than Fig. 2.7a for the analysis of Design A). These are distinguished between analyses that do (or do not) consider structural modeling uncertainties. Referring to the results that include modeling uncertainties (the last two columns), the probabilities of collapse are quite low (2–7%) for the 2%-in-50-years ground motion level, and the mean annual frequencies of collapse are similarly low at 40 to 140 x 10-6. Design D represents a non-code-conforming building that is equivalent to Design B except that the strong-column weak-beam code provision (ACI 2005) was not imposed in the design. This building has a 40% conditional probability of collapse given a 2%-in-50-years ground motion intensity (as compared to 2–7% for code-conforming designs) and a mean annual frequency of collapse of 1300 x 10-6 (as compared to 40 to 140 x 10-6 for code-conforming designs).

Table 2.3 Summary of collapse predictions (mean estimates) for all design variants, showing probability of collapse, annual frequency of collapse, and effects of modeling uncertainty.

			With only record-to-record variability			With record-to-record and modeling uncertainty (mean estimate approach)			
Design	Median (Sa,col) [g]	$\mu_{LN(Sa,col)}$	$\sigma_{LN,RTR\,(Sa,col)}$	$\lambda_{collapse}$ (10^-6)	P[Col | $Sa_{2/50}$] [a]	$\sigma_{LN,model\,(Sa,col)}$	$\sigma_{LN,Total\,(Sa,col)}$	$\lambda_{collapse}$ (10^-6)	P[Col | $Sa_{2/50}$] [a]
A	2.19	0.86	0.36	9.2	0.00	0.45	0.58	69	0.03
B	2.08	0.78	0.31	9.0	0.00	0.35	0.47	38	0.02
C	2.35	0.85	0.46	24.8	0.01	0.45	0.64	125	0.05
D[b]	0.95	-0.038	0.39	663	0.34	0.35	0.52	1300	0.38
E	1.95	0.71	0.32	14.5	0.00	0.35	0.47	55	0.03
F	1.86	0.57	0.38	48.1	0.02	0.35	0.52	139	0.07
G	1.88	0.67	0.34	20.6	0.01	0.35	0.49	71	0.04
H	1.92	0.64	0.30	16.2	0.00	0.35	0.46	62	0.03

a - 2% in 50 year ground motion level: Sa(1sec) = 0.82g
b - columns designed for strength demand and not for SCWB; this is not a code-conforming design

2.6 PROBABILISTIC ECONOMIC LOSS ANALYSIS: DIRECT MONETARY LOSS

Mitrani-Reiser, Beck, and Porter estimated the damage and direct monetary losses for the benchmark buildings. The details of their findings can be found in their publications (Goulet et al. 2006a; Haselton et al. 2007e); in addition, we present a brief overview of their findings here.

Mitrani-Reiser et al. developed a MATLAB toolbox to perform the damage and loss analyses. They focused on predicting (a) the probabilities of damage to each damageable component of the building (column, beams, partitions, paint, sprinklers, etc.), (b) the relationship between ground motion level and mean building repair cost (termed a "vulnerability function"), and (c) the expected annual direct monetary loss (EAL) for the building. The major findings of their work are summarized as follows:

- The EAL ranges from \$52,000 to \$95,000 (0.6% to 1.1% of the building replacement cost) for the various building designs.
- Repair costs are dominated by (in order of importance) (1) repairing wallboard partitions, (2) repairing structural members, and (3) repainting the interior.
- EAL values are sensitive to the element initial stiffnesses used in the structural model. For a range of realistic stiffness assumptions, the EAL prediction can change by up to 40%.
- The EAL is 25% lower for space-frame buildings, as compared to perimeter-frames, because of the additional stiffness of the space frame buildings.
- For perimeter-frame buildings, including the gravity system in the structural model causes the EAL prediction to decrease by 15% because of the stiffness added by the gravity frame system.
- For the designs other than Design D, a conservative (high) estimate of the expected annual number of fatalities is 0.001–0.004. This translates to an expected annual monetary loss due to fatalities of \$4,300–\$14,300. For the design that does not enforce the strong-column weak-beam provision (Design D), the expected annual number of fatalities is a much larger value of 0.05 fatalities per year.

2.7 SUMMARY AND CONCLUSIONS

We have implemented a PBEE methodology to predict the seismic performance of a 4-story RC SMRF *benchmark building* that is designed according to the 2003 IBC (ICC 2003). Our work focuses on quantifying the collapse performance in terms of the collapse probability and mean annual rate of collapse. Related work by Mitrani-Reiser et al. (Goulet et al. 2006a; Haselton et al. 2007e) quantified performance in terms of structural and nonstructural damage, repair costs, collapse statistics, and losses due to fatalities. Several design alternatives for the benchmark building are considered along with multiple structural modeling alternatives for a given design.

Accounting for uncertainties in both structural modeling and record-to-record variability, collapse probabilities lie in the range of 2–7% for earthquake ground motions with a 2% probability of exceedance in 50 years. Combining the ground motion hazard with the collapse predictions, we find that the mean annual frequency of collapse is [0.4 to 1.4] x 10^{-4} for the code-conforming benchmark building designs (excluding Design D).

Given these collapse risk predictions, it is difficult to judge whether these buildings meet the intention of current codes and are "safe enough." FEMA 223 (1992b) (Fig. C1.23) suggests that these computed collapse probabilities are high, compared with previous estimates less than 0.5% for a building subjected to 2%-in-50-years ground motion. However, these values in FEMA 223 are from a single study and are not agreed upon by all the stakeholders (policy-makers who represent the public interest, the engineering community, etc.). The topic of acceptable collapse risk is worthy of substantial further study.

In the process of developing the above findings related to collapse, a number of important considerations were revealed that are likely transferable to other buildings:

- For rare ground motions, it is critical to select the ground motion records considering the spectral shape of the recorded motions. Here, this was done through the parameter ε from the PSHA. If ε had been neglected in our simulations, the median predicted collapse capacities would be reduced by 20–40%, which in turn would increase the mean annual rate of collapse by a factor of five to ten.
- Realistic estimates of plastic rotation capacity are essential for accurate collapse predictions. Recent research and new model calibrations conducted as part of this study reveal much larger rotation capacities, on the order of 0.06 radians for a conforming RC element, than are generally assumed in modern practice (see Section 5.2).

- Collapse probability is highly sensitive to structural modeling uncertainties. The introduction of structural modeling uncertainty increased estimated collapse rates by approximately a factor of four to eight. We believe, therefore, that further study of this issue is critical.
- Different collapse mechanisms occur for different ground motions, and the mechanism predicted by nonlinear static pushover analysis was not the predominant collapse mechanism observed in the time series response analyses.
- As expected, the structural design that did not enforce the strong-column weak-beam provision collapsed at significantly lower hazard levels than the code-conforming designs. The collapse probability at the 2%-in-50-years ground motion was 38%, as compared to 2–7% for the seven conforming designs. The mean annual frequency of collapse is 13 $\times 10^{-4}$ and the mean annual number of fatalities is 0.05, as compared to [0.4 to 1.4] $\times 10^{-4}$ and to 0.001–0.004, respectively, for the seven conforming designs.

As part of this same study, findings and conclusions regarding damage and direct monetary losses were developed by Mitrani-Reiser, Beck, and Porter (Goulet et al. 2006a; Haselton et al. 2007e). Some of these findings have been reiterated in Section 2.6.

3 Accounting for Expected Spectral Shape (Epsilon) in Collapse Performance Assessment

3.1 INTRODUCTION AND GOALS OF STUDY

One of the many challenges of using analytical models to predict structural collapse capacity is the choice of ground motions to use in simulation. A key characteristic of ground motions, which is often not as well quantified as it should be, is the *spectral shape*. Baker has shown that for rare ground motions in California, such as motions that have a 2% probability of exceedance (PE) in 50 years, the spectral shape is much different than the shape of the code design spectrum or a uniform hazard spectrum (Baker 2005a, Chapter 6; Baker and Cornell 2006b).

′To illustrate Baker's finding regarding the spectral shape, Figure 3.1 shows the acceleration spectrum of a Loma Prieta ground motion[1] (PEER 2005) that has a rare 2%-in-50-years intensity at a period of 1.0 sec [which is $Sa(T_1 = 1.0 \text{ sec}) = 0.9g$ for this example]. This figure also shows the intensity predicted by the Boore et al. (1997) attenuation prediction, consistent with the event and site associated with this ground motion.

Figure 3.1 shows that this extreme (rare) 2% PE in 50-years motion has an unusual spectral shape with a "peak" from 0.6 to 1.8 sec, much different than the shape of a uniform hazard spectrum. Notice that this peak occurs around the period for which the motion is said to have a 2% PE in 50-years intensity, and at this period the observed Sa(1s) is much higher than the mean expected Sa(1s) (0.9g versus 0.3g). This peaked shape makes intuitive sense because if a ground motion has a much larger than expected spectral acceleration at one period, then it is unlikely that the spectral accelerations at all other periods would be similarly large.

---

[1] This motion is from the Saratoga station and is owned by the California Department of Mines and Geology. To create a consistent illustration, this spectrum was scaled slightly.

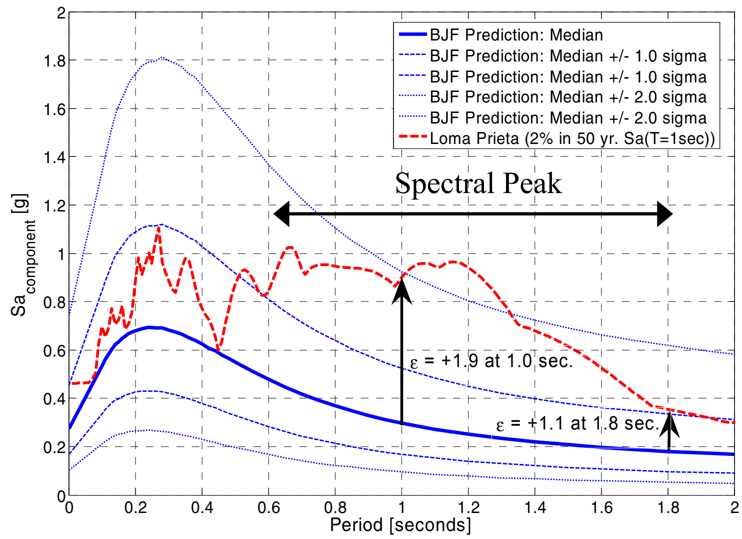

Fig. 3.1 Comparison of observed spectrum with spectra predicted by Boore, Joyner, and Fumal (1997); after Haselton and Baker (2006a).

At the 1.0 sec period, the spectral value is 1.9 standard deviations above the predicted mean spectral value, so this record is said to have "ε = 1.9 at 1.0 sec." ε (epsilon) is defined as the number of logarithmic standard deviations between the observed spectral value and the median prediction from an attenuation function. Similarly, this record has ε = 1.1 at 1.8 sec. So, the ε value is a function of the ground motion record, the attenuation function to which it is compared, and the period at which it is compared.

Observations from Figure 3.1 are general to non-near-field sites in coastal California. In particular, we expect approximately ε = 1 to 2 for the 2% PE in 50-years ground motion level at such sites (Section 3.3.2). These positive ε values come from the fact that the return period of the ground motion (i.e., 2475 years for a 2%-in-50-years motion) is much longer than the return period of the event that causes the ground motion (i.e., typical even return periods are 150–500 years in California). Record selection for analysis at such sites should reflect the expectation of ε = 1 to 2 for 2% PE in 50-years motions.

It should be noted that this expected ε is both hazard level and site dependent. For example, for the 50% PE in 5-years ground motions in coastal California, ε = 0 to -2 are expected (Haselton et al. 2007e). In addition, in the eastern United States, ε = 0.25 to 1.0 are expected for a 2% PE in 50-years motion. The negative ε values for a 50%-in 5-years motion stems from the fact that the return period of the ground motion (i.e., 10 years) is much shorter than the typical return period of the event that causes the ground motion (e.g., 150–500 years).

The low positive ε values in the eastern United States comes from the fact that seismic events are less frequent than California (e.g., 1000-years return period), but the return periods are still typically shorter than the return period of a 2%-in-50-years motion (i.e., 2475 years).

Previous research has shown that this peaked spectral shape significantly increases the collapse capacity of a structure relative to motions without a peaked spectral shape, when the peak of the spectrum is near the fundamental period of the building (T_1) and we use $Sa(T_1)$ as our ground motion intensity measure and scale the motions based on $Sa(T_1)$ (Haselton and Baker 2006a; Baker 2005a, Chapter 6; Goulet et al. 2006a; Zareian 2006). In this report, we define the collapse capacity as the $Sa(T_1)$ value that causes dynamic sidesway collapse.

The above studies have shown that if we improperly used $\varepsilon = 0$ ground motions when $\varepsilon =$ 1.5 to 2.0 ground motions are appropriate, we would underpredict the mean collapse capacity by a factor of 1.3–1.8. For cases where these rare motions (with high positive ε values approaching 2.0) drive the performance assessment, such as with modern buildings, properly accounting for this expected +ε is critical. Such large underpredictions of the mean collapse capacity cause even more drastic overpredictions of the conditional collapse probabilities and the mean annual rate of collapse. These observations are limited to ground motions that are not pulse-like; Baker (2005a, Section 5.5.1) found that use of ε is not appropriate for such records.

The most direct approach to account for spectral shape is to select ground motions that have the appropriate $\varepsilon(T_1)$ expected for the site and hazard level of interest, in addition to having other appropriate aspects such as event magnitude, site-to-source distance, etc. This approach is difficult when assessing the collapse capacities of many buildings with differing T_1 because it requires a unique ground motion set for each building. The purpose of this study is to develop a simplified method where the analyst can use a general ground motion set (selected independent of ε values) for structural simulation and then correct the collapse capacity estimates to account for spectral shape (as quantified by the $\varepsilon(T_1)$ value expected for the site and hazard level of interest, which is computed through disaggregation of the seismic hazard). Developing such a method was motivated by related studies (Haselton et al. 2007c,d, Chapters 6 and 7), which had the goal of assessing the collapse safety of 65 buildings with differing fundamental periods. Selecting a unique ground motion set for each of these buildings was not feasible.

This section starts by discussing how spectral shape and ε are related, then shows how the differences in spectral shape have drastic effects on collapse capacity predictions. We continue by discussing what spectral shapes (ε values) can be expected for various sites and hazard levels.

We then present a regression method to account for spectral shape without needing to select a specific set of records and compare this to the more direct method of selecting a ground motion set considering ε. We apply this regression method to 65 buildings and use these results to develop a simplified/generalized method to account for spectral shape (ε) in collapse assessment. This simplified procedure captures the fact that spectral shape (ε) effects are more important for ductile buildings that have extensive period elongation before collapse, and for higher-mode sensitive buildings where periods smaller than the fundamental period tangibly impact the response.

The expected audiences for this topic are engineers or researchers that are familiar with performance-based earthquake engineering, but may not be well versed in probability and may not be familiar with many of the detailed aspects of seismic hazard analysis disaggregation. Therefore, many of the statistical underpinnings of this work are discussed in concept but not described in extreme technical detail.

3.2 PREVIOUS RESEARCH ON SPECTRAL SHAPE (EPSILON) AND IMPACTS ON COLLAPSE ASSESSMENT

It has been long known that spectral shape has important effects on structural response. This is especially true when higher mode effects are important or when the building is significantly damaged, causing the effective fundamental period to elongate. Even though we understood the importance of spectral shape, we did not previously understand what spectral shape to expect for a given site and ground motion hazard level. Therefore, analysts typically assumed a spectral shape consistent with an equal hazard spectrum or a building code spectrum.

Baker and Cornell found that when ground motions are scaled by $Sa(T_1)$, the shape of the equal hazard spectrum is often inappropriate and can lead to extremely conservative predictions of structural responses. They found this to be especially true for rare ground motions in coastal California, such as a motion with 2% PE in 50 years (Baker 2005a; Baker and Cornell 2006b, 2005b).

This unique spectral shape comes from the fact that we are using $Sa(T_1)$ to define the ground motion hazard. If we instead establish the hazard based on another ground motion intensity measure such as inelastic spectral displacement (Tothong 2007) or an average Sa over a range of periods, this would cause the expected spectral shape to be less peaked for rare ground motions (Baker and Cornell 2006b). Thus, there are alternative ways to address the spectral shape issue, either by adjusting the selection and scaling of ground motions or by modifying the definition of ground motion hazard. The focus of this chapter is on the former method.

3.2.1 How Spectral Shape Relates to Epsilon Values of Ground Motions

Figure 3.1 showed the spectral shape of a single Loma Prieta ground motion record that is consistent with a 2% PE in 50-years hazard level at 1.0 sec and has an ε(1 sec) = 1.9. This figure suggests that a positive ε value tends to be related to a peak in the acceleration spectrum around the period of interest.

Recent studies have verified this relationship between a positive ε value and a peaked spectral shape. To illustrate this, Figure 3.2 compares the mean spectral shape of three ground motion sets[2]: (1) a set selected without regard to ε (basic far-field set; Appendix A gives details for this set), (2) a set selected to have ε(1s) = +2, and (3) a set selected to have ε(2s) = +2. For better comparison, these records are scaled such that the mean Sa(1s) is equal for Sets (1) and (2) and the mean Sa(2s) is equal for Sets (1) and (3). This shows that the spectral shapes are distinctly different when the records are selected with or without regard to ε. When the records are selected to have positive ε values at a specified period, the spectra tend to have a peak at that period. This shape is much different than a standard uniform hazard spectral shape. This makes intuitive sense, because if a ground motion has a much larger than expected spectral acceleration at one period (i.e., high positive ε), then it is unlikely that the spectral accelerations at all other periods are also similarly large.

[2] These ground motion sets contain 80 motions, 20 motions, and 20 motions, respectively.

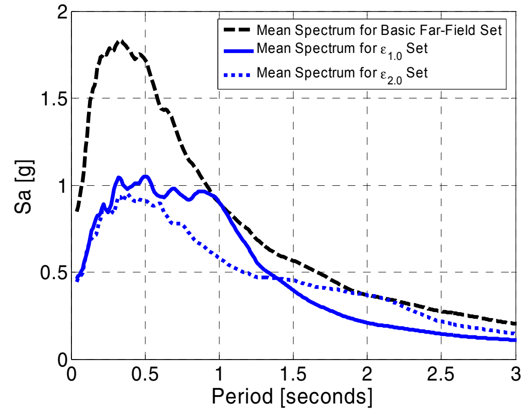

Fig. 3.2 Comparison of spectral shapes of ground motion sets selected with and without considering ε. (After Haselton and Baker 2006a).

3.2.2 How Spectral Shape (Epsilon) Affects Collapse Capacity

Selecting ground motions with proper spectral shape (proper ε) has been shown to significantly increases collapse capacity predictions. The following four studies verify this finding for an array of building types. Conceptually, this difference in collapse capacity can be explained by comparing the spectral shapes of the basic far-field set and the $\varepsilon_{1.0}$ set shown in Figure 3.2. For example, if the building period is 1.0 sec and we scale the ground motion records to a common value of Sa(1s), the spectral values of the $\varepsilon_{1.0}$ set are smaller for Sa(T > 1s) (i.e., the spectral values that are important when the building is damaged and the effective period elongates) and Sa(T < 1s) (i.e., the spectral values that are important for higher mode effects). For an example case where Sa(2s) is the spectral value most important for the collapse of a ductile frame, then we would need to scale Sa(1s) more for the $\varepsilon_{1.0}$ set to produce equivalent Sa(2s) values as the basic far-field set.

Baker and Cornell (2006b) studied the effects of various ground motion properties on the collapse capacity of a 7-story non-ductile reinforced concrete frame building located in Van Nuys, California, and with a fundamental period (T_1) of 0.8 sec. They found that the mean collapse capacity increased by a factor of 1.7 when an ε(0.8s) = 2.0 ground motion set was used in place of a set selected without regard to epsilon (which has mean ε(0.8s) = 0.2).

Goulet et al. (2006a) studied the collapse safety of a modern 4-story reinforced concrete frame building with a period of T_1 = 1.0 sec. They compared the collapse capacities for a ground motion set selected to have a mean $\varepsilon(1.0s) = 1.4$ and a set selected without regard to epsilon (which had a mean $\varepsilon(1.0s) = 0.4$). They found that the set selected considering ε resulted in a 1.3–1.7 times larger mean collapse capacity.

Haselton and Baker (2006a) used a ductile single-degree-of-freedom oscillator, with a period of $T_1 = 1.0$ sec, to demonstrate that a $\varepsilon(1.0s) = 2.0$ ground motion set resulted in a 1.8 times larger mean collapse capacity as compared to using a ground motion set selected without regard to epsilon.

Zareian (2006; Figs. 6.15 and 6.16) used regression analysis to investigate the effects that ε has on the collapse capacities of generic frame and wall structures. For a selected 8-story frame and 8-story wall building, he showed that a change from $\varepsilon(T_1) = 0.0$ to $\varepsilon(T_1) = 1.5$ results in a factor of 1.5–1.6 increase in the mean collapse capacity.

Baker found that use of ε is not appropriate for pulse-type ground motions (Baker 2005a, Section 5.5.1). Therefore, the ε corrections presented later should not be applied when such motions are expected such as at near-field sites.

3.3 WHAT EPSILON VALUES TO EXPECT FOR SPECIFIC SITE AND HAZARD LEVEL

3.3.1 Illustration of Concept Using Characteristic Event

To illustrate the relationship between expected ε, site, and hazard level, we choose a fictitious site where the ground motion hazard is dominated by a single characteristic event:

- Characteristic event return period = 200 years
- Characteristic event magnitude = 7.2
- Nearest distance to fault = 11.0 km
- Site soil conditions – $V_{s\_30} = 360$ m/sec
- Building fundamental period of interest = 1.0 sec

Figure 3.3 shows the predicted spectra for this site, including the mean spectrum and spectra for mean +/- one and two standard deviations. The mean predicted ground motion is Sa(1s) = 0.40g. This figure also includes a superimposed lognormal distribution of Sa(1s).

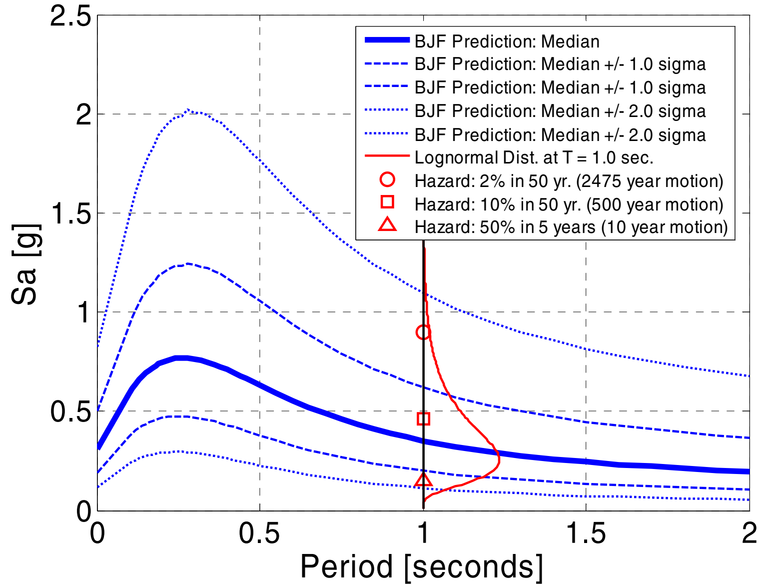

Fig. 3.3 Boore et al. (1997) ground motion predictions for characteristic event, predicted lognormal distribution at T = 1.0 sec, and spectral accelerations for 2%-in-50-years and other hazard levels.

We see that the less frequent (more intense, longer return period) ground motions are associated with the upper tail of the distribution of Sa(1s) for this event. In this simplified case, when a single characteristic event dominates the ground motion hazard, we can compute the mean return period (RP) of the ground motion as follows:

$$\frac{1}{RP_{GroundMotion}} = \left(\frac{1}{RP_{CharacetersticEvent}}\right)\left(P[Sa \geq Sa_0 \mid CharacteristicEvent]\right) \tag{3.1}$$

For example, if we are interested in a 2%-in-50-years motion, we would have (1/2475 years) = (1/200 years)*(0.081). This means that only 8% of motions that come from the characteristic event will be large enough to be considered a 2%-in-50-years or larger motion. For this 2%-in-50-years motion, Figure 3.3 shows that the 8% probability translates to a Sa(1s) = 0.90g, which corresponds to an ε(1s) = 1.43. This reveals an important concept:

When the return period of the characteristic event (e.g., 200 years) is much shorter than the return period of the ground motion of interest (e.g., 2475 years), then we can expect that the ground motion of interest will have positive ε.

For cases where these rare motions drive the performance assessment, such as with collapse assessment of modern buildings, properly accounting for this expected +ε is critical.

As shown above, the expected ε value depends strongly on the return period of the ground motion of interest. Figure 3.3 shows that a 10% PE in 50-years motion (return period of 500 years) is associated with Sa(1s) = 0.46g and ε(1s) = 0.3. For a much more frequent 50% PE in 5-years motion (return period of 10 years), Sa(1s) = 0.15g and ε(1s) = -1.7.

Equation 3.1 also shows that the expected ε value depends on the return period of the characteristic event. In coastal California, a return period of 200 years is common, but in the eastern United States, return periods are much longer. These longer return periods in the eastern United States will cause the expected ε values to be smaller.

3.3.2 Expected Epsilon Values from United States Geological Survey

The previous section explained the concept of expected ε values by using a fictitious site where only a single characteristic event dominates the ground motion hazard. Typically, ground motion hazard comes from multiple faults and a wide range of possible events. For the general case, expected ε values must be computed by disaggregating the results of seismic hazard analysis.

The U.S. Geological Survey (USGS) conducted the seismic hazard analysis for the United States and used disaggregation to determine the mean ε ($\bar{\varepsilon}_0$) values for various periods and hazard levels of interest (Harmsen, Frankel, and Petersen, 2002; Harmsen 2001).

Figure 3.4 shows the $\bar{\varepsilon}_0$(1s) for a 2% PE in 50-years ground motion for the western United States. $\bar{\varepsilon}_0$(1s) = 0.50 to 1.25 are typical in areas other than the seismic regions of California. The values are higher in most of California, with typical value being $\bar{\varepsilon}_0$(1s) = 1.25 to 1.75, but some values ranging up to 3.0.

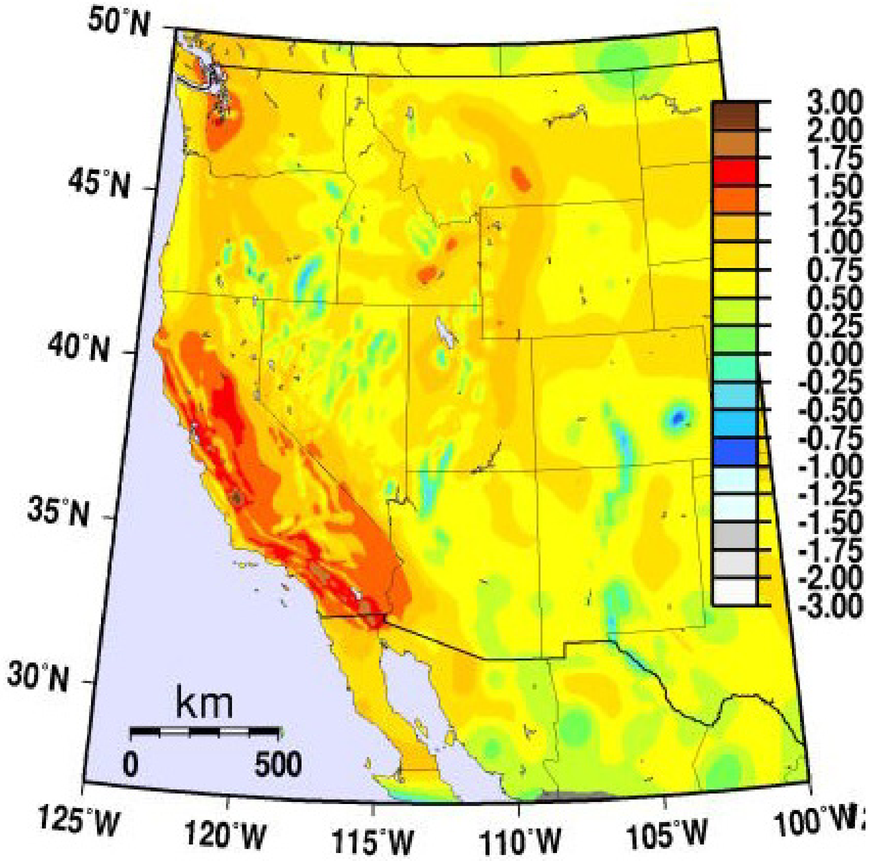

Fig. 3.4 Predicted $\bar{\varepsilon}_0$ values from disaggregation of ground motion hazard for western U.S. Values are for 1.0 sec period and 2% PE in 50-years motion. Figure from U.S. Geological Survey Open-File Report (Harmsen et al. 2002).

Figure 3.5a is the same as Figure 3.4, but is for the eastern United States. This shows typical values of $\bar{\varepsilon}_0$(1s) = 0.75 to 1.0, with some values reaching up to 1.25. Expected $\bar{\varepsilon}_0$(1s) values fall below 0.75 for the New Madrid fault zone, portions of the eastern coast, most of Florida, southern Texas, and areas in the north-west portion of the map.

To see the effects of period, Figure 3.5b shows the $\bar{\varepsilon}_0$(0.2s) instead of $\bar{\varepsilon}_0$(1s). This shows that typical $\bar{\varepsilon}_0$(0.2s) are slightly lower and more variable, having a typical range of 0.25–1.0. This is in contrast to the typical range of 0.75–1.0 for $\bar{\varepsilon}_0$(1s).

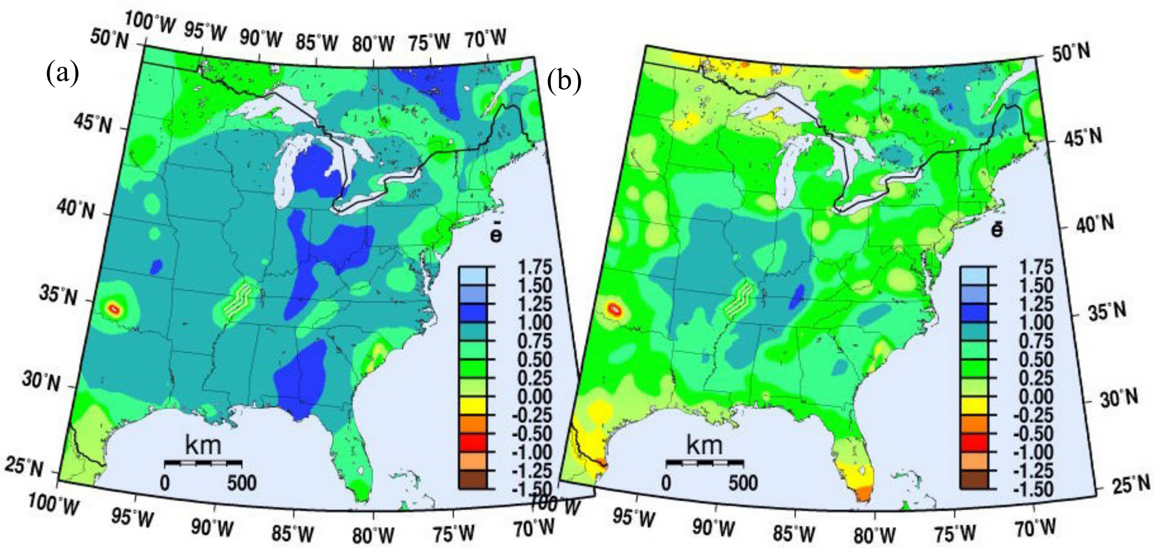

Fig. 3.5 Mean predicted $\bar{\varepsilon}_0$ values from disaggregation of ground motion hazard for eastern U.S. Values are for (a) 1.0 sec and (b) 0.2 sec periods and 2% PE in 50-years motion. Figure from U.S. Geological Survey Open-File Report (Harmsen et al. 2002).

For disaggregation of seismic hazard, two slightly different approaches are typically employed. Bazzuro and Cornell (1999) proposed an approach to disaggregate the hazard conditioned on the Sa *exceeding* the Sa level of interest (i.e., Sa ≥ Sa_0), which is used in probabilistic seismic hazard analysis probabilities of *exceeding* various level of Sa. McGuire (1995) proposed a slightly different approach that is conditioned on the Sa *equaling* the Sa level of interest (i.e., Sa = Sa_0). The USGS maps presented in this section are based on the "Sa = Sa_0" approach proposed by McGuire (Harmsen et al. 2002, 2001). For assessing structural performance, we are typically interested in Sa *equaling* an Sa level of interest (e.g., Sa = $Sa_{2/50}$), so the $\bar{\varepsilon}_0$ values presented in the USGS maps are consistent with this purpose.

3.3.3 Appropriate Target Epsilon Values

The expected $\bar{\varepsilon}_0$ value (also called "proper ε" of "target ε" here) depends on site and hazard level of interest. When computing a target ε, the appropriate target hazard level depends on what collapse index is desired (e.g., conditional collapse probability or mean rate of collapse). When computing P[C|Sa = $Sa_{2/50}$], the appropriate target hazard level is the 2% PE in 50-years level. When computing the mean annual frequency of collapse (λ_{col}), the appropriate target hazard level is more difficult to determine. This target hazard level should be the level that most significantly influences λ_{col}, which will be a function of both the site and the collapse capacity of the structure. We look at this question in Section 5.8.2 and find, for two example 4-story RC frame buildings at a site in Los Angeles, that the ground motion intensity level at 60% of the median collapse capacity is the most dominant contributor to the calculation of λ_{col}.

3.4 APPROACHES TO ACCOUNT FOR SPECTRAL SHAPE (EPSILON) IN COLLAPSE ASSESSMENT

3.4.1 Site and Building Illustration

To illustrate two methods of accounting for ε in collapse assessment, we use an 8-story reinforced concrete (RC) frame model. This model was developed by the authors in a related study (Haselton et al. 2007c, Chapter 6), and consists of a 3-bay special moment-resisting perimeter frame (SMF) with 20′ bay widths, a tributary seismic mass floor area of 7,200 sq ft, and a fundamental period (T_1) of 1.71 sec. Appendix A contains more detail regarding the design of this frame; the collapse simulation method is based on Haselton et al. (2007c, Chapter 6).

The site used for this illustration is the "benchmark site" used in previous studies by the authors and collaborating researchers (Goulet et al. 2006a). This site is in northern Los Angeles and is fairly typical of the non-near-field regions of coastal California. For purposes of this illustration, we assume that the $\bar{\varepsilon}_0(1.71\text{sec}) = 1.7$ for the 2%-in-50-years motion, which is the ground motion level of interest.

3.4.2 Method One: Selecting Ground Motion Set Accounting for Epsilon, Specific to Site and Hazard Level

One method to account for spectral shape (ε) is by selecting ground motions which have ε values consistent with those expected for the site and hazard level of interest (Baker 2006b; Goulet et al. 2006a). Based on the assumed site, we selected ground motion Set Two to include 20 ground motions that have a mean $\varepsilon(T_1) = 1.7$, while imposing a minimum value of 1.25 [3] ($T_1 = 1.71$ sec). In addition to ensuring that the selected motions have the correct $\varepsilon(T_1)$, we imposed additional selection criteria, such as minimum event magnitude, etc. Appendix B lists the motions included in this ground motion set and includes the complete list of selection criteria.

Figure 3.6 shows the resulting collapse distribution predicted by subjecting the 8-story RC SMF to the 20 ground motions of Set Two. The mean[4] collapse capacity is $S_{a,col}(T_1) = 1.15g$, and the variability in capacity is $\sigma_{LN(Sa,col)} = 0.28$. The 2% PE in 50-years ground motion for this site is $Sa(T_1) = 0.57g$, so the probability of collapse for this level of motion is 0.5%.

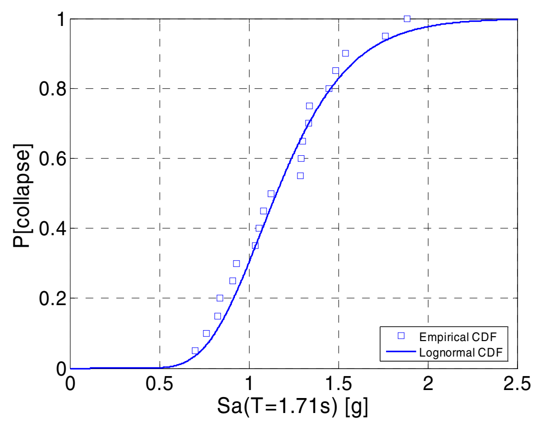

Fig. 3.6 Predicted collapse capacity distribution using ground motion Set Two, selected for proper spectral shape (proper $\varepsilon(T_1)$ value).

3.4.3 Method Two: Using General Ground Motion Set, with Adjustments for Epsilon

3.4.3.1 Motivation and Overview of Method

Selecting a specific ground motion set for a single building (with a specified T_1) at a single site may not be feasible in all situations. For example, related research by the authors (Haselton et al. 2007c, 2007d, Chapters 6 and 7) involved the collapse assessment of 65 buildings, each with differing fundamental periods. In such a study, selecting a specific ground motion set for each building is not feasible.

---

[3] When selecting records, we used the $\varepsilon(T_1)$ values computed using the Abrahamson and Silva attenuation function (1997). For comparison, Appendix B also includes the values computed using the Boore et al. attenuation function (1997), though the Boore et al. values were not used in this study.

[4] Strictly speaking, this is the geometric mean (the exponential of the mean of the logarithms). This is equal to the median of a lognormal distribution, so it is also sometimes referred to as the median. This definition of "mean" is used throughout this report.

The method proposed here allows one to use a general ground motion set selected without regard to ε values, then correct the predicted collapse capacity distribution to account for the $\bar{\varepsilon}_0$ expected for the site and hazard level of interest. This method can be applied to all types of structural responses (interstory drifts, plastic rotations, etc.), but this study focuses on prediction of spectral acceleration at collapse. For illustrating this method, we apply it to assess the collapse capacity of the 8-story RC SMF building. The method is outlined as follows:

1. Select a general far-field ground motion set without regard to the ε values of the motions. This set should have a large number of motions (80 were used in this study), to provide a statistically significant sample and to ensure that the regression analysis in step 3 is precise.
2. Utilize incremental dynamic analysis (Vamvatsikos and Cornell 2002a) to predict the collapse capacity of the structure for the set of selected ground motions.
3. Perform linear regression analysis between $LN[S_{a,col}(T_1)]$ and $\varepsilon(T_1)$, where $S_{a,col}(T_1)$ is the spectral acceleration that causes collapse[5]. This establishes the relationship between the mean $S_{a,col}(T_1)$ and $\varepsilon(T_1)$. Compute the record-to-record variability of $S_{a,col}(T_1)$ after accounting for the trend with $\varepsilon(T_1)$.
4. Adjust the collapse distribution (both the mean and variability) to be consistent with the target $\varepsilon(T_1)$ for the site and hazard level of interest.

3.4.3.2 General Far-Field Ground Motion Set (Set One) and Comparison to Positive ε Set (Set Two)

We selected ground motion Set One to consist of strong motions that may cause structural collapse of modern buildings, without consideration of the ε values of the motions. Appendix B lists these motions and includes the complete list of selection criteria. This ground motion set is also used in Applied Technology Council Project 63 to develop a procedure to validate seismic provisions for structural design.

Based on the previous discussion, we expect the collapse capacities to be smaller for ground motion Set One as compared to Set Two, due to differences in spectral shape. To illustrate this, Figure 3.7 compares the mean spectra of the two sets. This shows that Set Two

---

[5] We perform the regression using $LN[S_{a,col}(T_1)]$ because (a) we expect that this parameter is more linearly related to $\varepsilon(T_1)$ than $S_{a,col}(T_1)$, and (b) this type of regression typically causes the residuals to have constant variance for all levels of Sa.

has the expected peaked spectral shape near a period of 1.71 sec. This comparison is reasonably similar to the comparison shown previously from past research (Fig. 3.2), except that the spectral values of Set Two do not decrease quite as quickly for $T > T_1$.

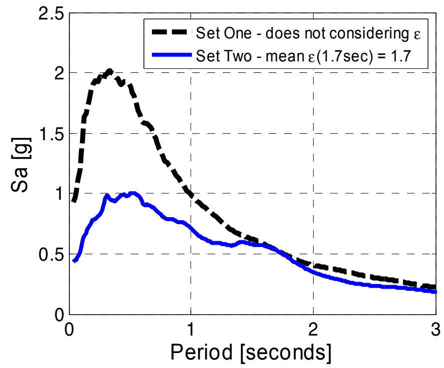

Fig. 3.7 Comparison of mean spectra for ground motion Set One and Set Two.

3.4.3.3 Application of Method Two to Assess Collapse of 8-Story RC SMF Building

Figure 3.8 shows the predicted collapse capacity distribution for the 8-story RC SMF building (T_1 = 1.71s) subjected to ground motion Set One. The mean collapse capacity is $S_{a,col}(T_1)$ = 0.72g, and the variability in capacity is $\sigma_{LN(Sa,col)} = 0.45$. The 2% PE in 50-years ground motion for this site is Sa(1.71s) = 0.57g, so the probability of collapse for this level of motion is 30%. Comparing this figure with Figure 3.6 shows the importance of accounting for ε in collapse assessment. However, since ground motion Set One was selected without regard to ε, the collapse predictions show in Figure 3.8 still need to be adjusted to be consistent with the target $\varepsilon(T_1)$ of 1.7.

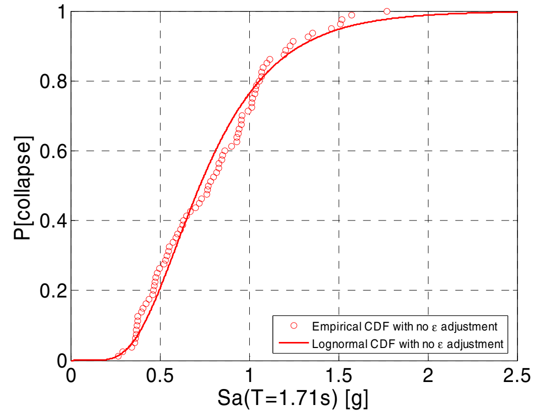

Fig. 3.8 Predicted collapse capacity distribution using ground motion Set One, selected without regard to ε. This collapse capacity distribution results directly from structural analyses not yet adjusted for proper ε(T$_1$).

To find an adjusted mean collapse capacity that accounts for the expected $\bar{\varepsilon}_0$, we perform a standard linear regression (Chatterjee et al. 2000) between LN[$S_{a,col}(T_1)$] and $\varepsilon(T_1)$ for the ground motion record Set One. Figure 3.9 is a plot of $S_{a,col}(T_1)$ versus $\varepsilon(T_1)$ and includes the results of this linear regression. This approach has been used previously by Zareian (2006). The regression is based on all of the data (excluding outliers); in future work, it would be useful to also evaluate the option of fitting to a subset of the data (e.g., fitting to only the positive ε values, since we are typically interested in responses due to positive ε motions). The counted median collapse capacity is shown by the red dot. The relationship between the mean of LN[$S_{a,col}(T_1)$] and $\varepsilon(T_1)$ can be described as:

$$\mu'_{LN[Sa,col(T_1)]} = \beta_0 + \beta_1 \bullet \varepsilon(T_1) \tag{3.2}$$

where β_0 = -0.348 and β_1 = 0.311.

To adjust the mean collapse capacity for the target $\varepsilon(T_1)$ = 1.7, we evaluate Equation 3.2 using this target $\bar{\varepsilon}_0(T_1)$ value.

$$\mu'_{LN[Sa,col(1.71s)]} = \beta_0 + \beta_1 \bullet \left[\bar{\varepsilon}_0\left(T_1\right)\right] = -0.348 + 0.311 \bullet [1.7] = 0.181 \tag{3.3}$$

The corrected mean collapse capacity is now computed by taking the exponential of the result from Equation 3.3; this corrected mean collapse capacity is shown by the black circle in Figure 3.9.

$$Mean'_{Sa,col(T_1)} = \exp\left(\mu'_{LN[Sa,col(T_1)]}\right) = \exp(0.181) = 1.20g \tag{3.4}$$

This correction to the mean collapse capacity can also be expressed as the ratio of corrected to unadjusted mean collapse capacity,

$$Ratio = \frac{\exp\left(\mu'_{LN[Sa,col(T_1)]}\right)}{\exp\left(\mu_{LN[Sa,col(T_1)],records}\right)} = \frac{1.20g}{0.72g} = 1.67 \quad (3.5)$$

where $\mu_{LN[Sa,col(T_1)],records}$ is computed directly from the collapse simulation results using the general ground motion set (Set One) and $\mu'_{LN[Sa,col(T_1)]}$ is based on the regression analysis results and accounts for the proper $\bar{\varepsilon}_0$ (T_1) value.

The variability in the collapse capacity is reduced when we condition on the target $\bar{\varepsilon}_0$ (T_1). This reduced conditional standard deviation can be computed as the following (Benjamin and Cornell, 1970; Eq. 2.4.82),

$$\sigma'_{\mathrm{LN(Sa,col(T_1))}} = \sqrt{\left(\sigma_{\mathrm{LN(Sa,col(T_1)),reg}}\right)^2 + \left(\beta_1\right)^2\left(\sigma_\varepsilon\right)^2} \approx \sigma_{\mathrm{LN(Sa,col(T_1)),reg}} \quad (3.6)$$

where the $\sigma_{\mathrm{LN(Sa,col(T1)),reg}}$ is computed from the residuals of the regression analysis shown in Figure 3.9, and σ_ε is the standard deviation of the $\varepsilon(T_1)$ values from disaggregation for a site and hazard level. Near the example site used in this study, $\sigma_\varepsilon = 0.35$ for the 2% PE in 50-years level of ground motion. Equation 3.7 shows that for this example of a 2%-in-50-years ground motion, the record-to-record variability in the collapse capacity (i.e., $\sigma_{\mathrm{LN(Sa,col(T1)),reg}}$) is more dominant than the effects of variability in the expected ε value (i.e., $\sqrt{\beta_1^2 \sigma_\varepsilon^{\,2}}$). This supports the approximation used in Equation 3.6.

$$\sigma'_{\mathrm{LN(Sa,col(T_1))}} = \sqrt{(0.331)^2 + (0.311)^2(0.35)^2} = 0.348 \approx 0.331 \quad (3.7)$$

This reduced variability is 27% lower than the variability in the collapse capacity that was computed directly from the records, which was $\sigma_{\mathrm{LN(Sa,col(T1)),records}} = 0.45$.

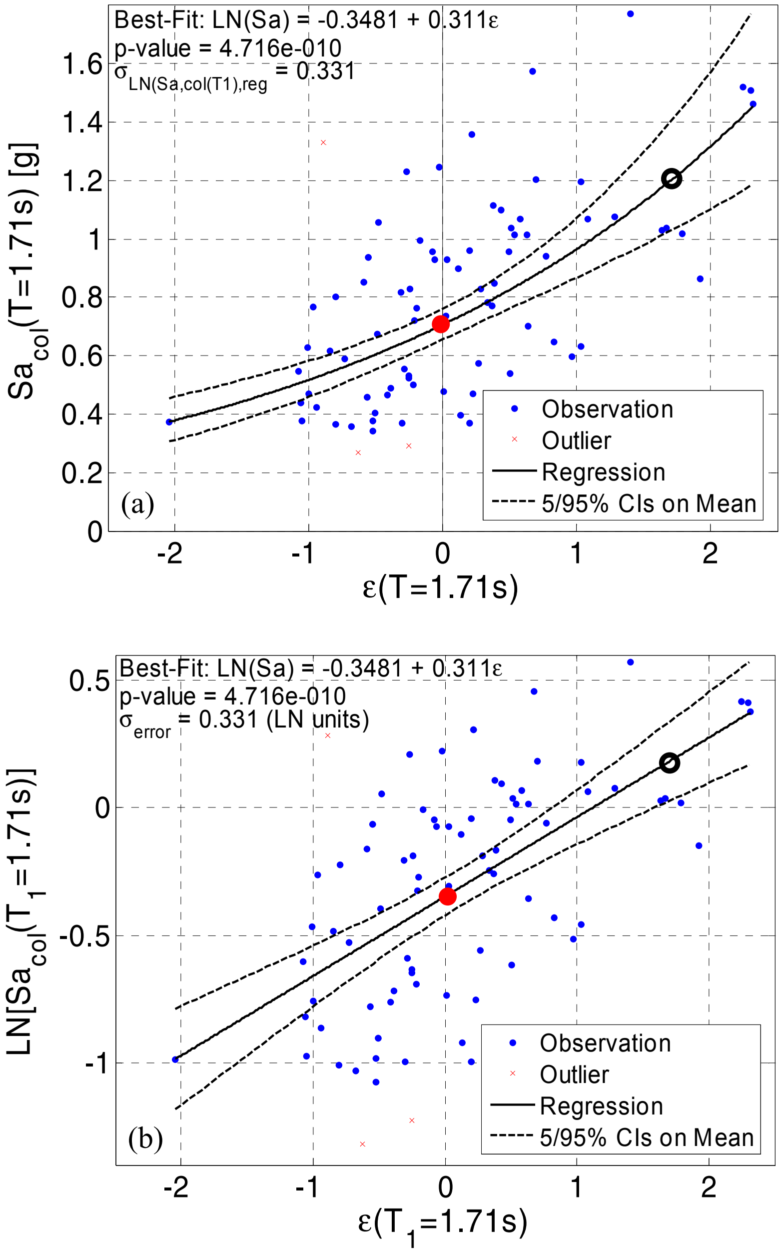

Fig. 3.9 Relationship between spectral acceleration and ε. This includes linear regression relating LN[$S_{a,col}(T_1)$] to $\varepsilon(T_1)$; (a) plots Sa_{col} and (b) plots LN[Sa_{col}].

Figure 3.10 shows both the unadjusted and adjusted collapse capacity distributions. The red dot and black circle show how Figure 3.10 relates to Figure 3.9. The adjustment for ε increases the mean collapse capacity from $Sa(T_1)$ = 0.72g to 1.20g, for a ratio of adjusted/unadjusted of 1.67. This adjustment also decreased the variability from $\sigma_{LN(Sa,col)} = 0.45$

to 0.33, for a ratio of adjusted/unadjusted of 0.73. This increase in the mean collapse capacity has a significant impact on the collapse assessment.

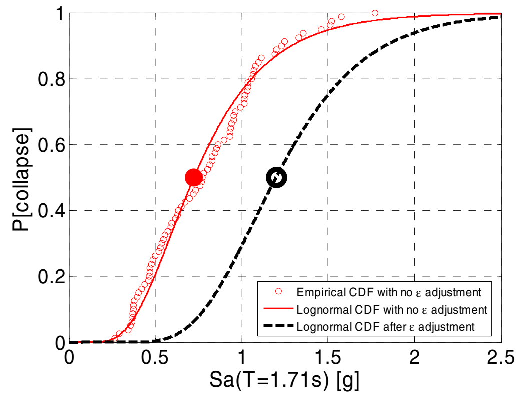

Fig. 3.10 Predicted collapse capacity distributions using ground motion Set One, including unadjusted distribution, and adjusted collapse capacity distribution accounting for $\bar{\varepsilon}_0$ (T_1) expected for site and 2% PE in 50-years hazard level.

3.4.4 Comparison of Two Methods

Figure 3.11a overlays the predicted collapse capacity distributions from Methods One and Two. The plot also includes the collapse predictions of Method Two before the adjustment for ε. The median collapse capacities are shown by the blue square, black circle, and red dot, respectively.

Figure 3.11b is similar to Figure 3.9a, but for comparison also includes the data for ground motion Set Two (which is the positive ε ground motion set). The blue square, black circle, and red dot are also included on this figure to show how this figure relates to Figure 3.11a; note that the colors of these shapes do not relate well to the colors of the other points on this plot.

This figure and Table 3.1 show that the two methods produce nearly the same results, with the predictions of the mean collapse capacity differing by only 4%. The variability in collapse capacity ($\sigma_{LN(Sa,col)}$) differs by 19%, which is reasonable given the large inherent variability in collapse prediction. The probabilities of collapse associated with the 2%-in-50-years motion are similar (0.5% and 1.2%), and the mean annual rates of collapse (λ_{col}) differ only by a factor of 1.24. These differences are negligible when compared to the factor of 23 overprediction of λ_{col} that results from not accounting for the proper ε. In addition, data from Haselton et al. (2007c, Chapter 6) show that even small differences in the structural design (what foundation stiffness is assumed in the design process, etc.) causes the λ_{col} prediction to change by a factor of 1.5–2.2, which is larger than the difference in results resulting from the two methods.

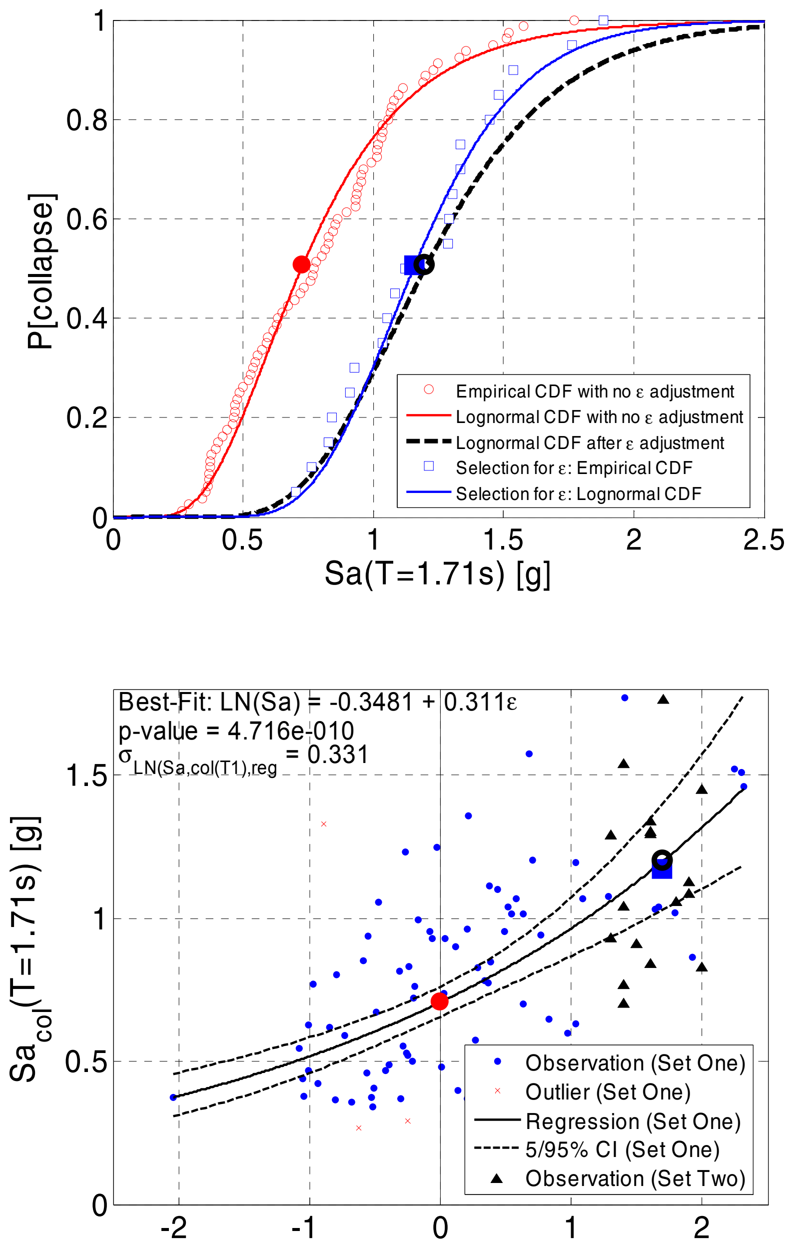

Fig. 3.11 Comparison of collapse capacity distributions predicted using two methods. To illustrate extreme impacts of ε, this also shows collapse capacity distribution obtained using Set One without adjustment for $\overline{\varepsilon}_0$ (T_1) expected for site and 2% PE in 50-years hazard level.

We assume that Method One (the direct selection of appropriate records) is the correct method. Therefore, this comparison between Methods One and Two indicates that Method Two is capable of predicting the collapse capacity distribution with acceptable accuracy. This is an important verification, because we later use Method Two to assess the collapse capacity for many additional buildings, and to develop a simplified method to account for ε in the collapse assessment.

Table 3.1 Comparison of collapse risks predicted using two methods.

Method	Mean[a] Sa,col(1.71s)	σ_{LN}(Sa,col)	P[C|$Sa_{2/50}$][b]	λ_{col} [10^{-4}]
Method One	1.15	0.28	0.005	0.28
Method Two	1.20	0.33	0.012	0.35
Ratio:	1.04	1.19	2.40[c]	1.24

a - Mean when using a lognormal distribution; this value is closer to the median.
b - The 2% in 50 year ground motion for this site is Sa(1.71sec) = 0.57.
c - A factor is not best way to quantify the change in P[C]; the P[C] changes by +0.007.

Table 3.2 shows that there is a large difference between collapse predictions that account for ε and predictions that do not. When accounting for ε, the mean predicted collapse capacity increases by a factor of 1.6, the variability ($\sigma_{LN(Sa,col)}$) decreases by 62%, the probability of collapse decreases from 30–0.5%, and the mean annual rate of collapse (λ_{col}) decreases by a factor of 23.

Table 3.2 Comparison of collapse risks with and without accounting for proper ε.

Method	Mean[a] Sa,col(1.71s)	σ_{LN}(Sa,col)	P[C|$Sa_{2/50}$][b]	λ_{col} [10^{-4}]
Method One	1.15	0.28	0.005	0.28
Predictions with no ε Adj.	0.72	0.45	0.30	6.31
Ratio:	0.63	1.62	59.6[c]	22.6

a - Mean when using a lognormal distribution; this value is closer to the median.
b - The 2% in 50 year ground motion for this site is Sa(1.71sec) = 0.57.
c - A factor is not best way to quantify the change in P[C]; the P[C] changes by +0.29.

3.5 SIMPLIFIED METHOD TO ACCOUNT FOR EFFECTS OF SPECTRAL SHAPE (EPSILON)

3.5.1 Motivation and Overview

The previous section showed that we can obtain roughly the same collapse capacity distribution by either (a) selecting records with appropriate ε values (Method One) or (b) using general ground motions and then applying a correction factors to account for appropriate ε (Method Two, which corrects both mean and variability). Method Two is useful because it allows us to account for proper ε without needing to select a unique ground motion set for each building we want to assess. However, Method Two does still require computation of $\varepsilon(T_1)$ values for each ground motion record and a regression analysis to relate $S_{a,col}(T_1)$ to $\varepsilon(T_1)$, both of which require significant effort.

In this section, we develop a simplified version of Method Two. This simplified version allows the analyst to correct the collapse capacity distribution without computing $\varepsilon(T_1)$ values and without performing a regression analysis. This method involves using ground motion Set One (or the reduced set; see Appendix B), using an empirical equation to predict β_1, determining an approximate value of $[\sigma'_{LN(Sa,col(T1))} / \sigma_{LN(Sa,col(T1)),records}]$, then correcting the collapse capacity distribution accordingly.

To develop this simplified method, we apply Method Two to 65 RC frame buildings and extract general conclusions from the findings. Most of the 65 buildings are ductile RC frames, so this requires further judgment regarding application of the method to less-ductile buildings.

3.5.2 Buildings Used to Develop Simplified Approach, and Results of Epsilon Regression for Each Building

This section presents the results of applying Method Two to 65 RC frame buildings, which come from a related study by the authors (Haselton et al. 2007c, Chapter 6). For the illustrations, we assume that the target $\overline{\varepsilon}_0(T_1) = 1.7$ for all buildings; however, this assumption has no effect on how we develop the simplified method.

3.5.2.1 Code-Conforming Special Reinforced Concrete Frames

Tables 3.3 and 3.4 present the design information and results of the Method Two correction for 30 code-conforming RC SMF buildings. Each building was designed according to current building codes and standards (ICC 2005; ACI 2005; ASCE 2005). The left portion of Table 3.3 presents the structural design information, including building height, bay spacing, framing system, and other design information. The right portion of Table 3.3 shows the fundamental period, the design base shear coefficient, and data from static pushover analysis. The static pushover results include the static overstrength (ratio of ultimate base shear to design base shear) and the ultimate roof drift ratio (i.e., RDR_{ult}) (defined as the drift at 20% loss in lateral strength).

Table 3.3 Design and behavioral information for 30 modern RC SMF buildings.

Design Information							Period and Pushover Analysis Results			
Design Number	Design ID Number	No. of stories	Bay Width [ft]	Framing System	Strength/ Stiffness Distribution Over Height	Foundation Fixity Assumed in Design[a]	First Mode Period (T_1) [sec]	Design Base Shear Coefficient (C_s) [g]	Static Overstr.	Ultimate Roof Drift Ratio (at 20% strength loss) (RDR_{ult})
1	2061	1	20	Space	A	GB	0.42	0.125	4.0	0.077
2	2062					P	0.42	0.125	4.9	0.079
3	2063					F	0.42	0.125	4.0	0.077
4	2069			Perimeter	A	GB	0.71	0.125	1.6	0.077
5	1001	2	20	Space	A	GB	0.63	0.125	3.5	0.085
6	1001a					P	0.56	0.125	4.4	0.085
7	1002					F	0.63	0.125	3.1	0.076
8	2064			Perimeter	A	GB	0.66	0.125	1.8	0.067
9	1003	4	20	Perimeter	A	GB	1.12	0.092	1.6	0.038
10	1004				C	GB	1.11	0.092	1.7	0.043
11	1008			Space	A	GB	0.94	0.092	2.7	0.047
12	1009		30	Perimeter	A	GB	1.16	0.092	1.6	0.050
13	1010			Space	A	GB	0.86	0.092	3.3	0.056
14	1011	8	20	Perimeter	A	GB	1.71	0.050	1.6	0.023
15	1012		20	Space	A	GB	1.80	0.050	2.3	0.028
16	1022				C	GB	1.80	0.050	2.6	0.035
17	2065				B (65%)[b]	GB	1.57	0.050	3.3	0.024
18	2066				B (80%)[b]	GB	1.71	0.050	2.9	0.031
19	1023				B (65%)[c]	GB	1.57	0.050	2.9	0.019
20	1024				B (80%)[c]	GB	1.71	0.050	2.7	0.021
21	1013	12	20	Perimeter	A	GB	2.01	0.044	1.7	0.026
22	1014		20	Space	A	GB	2.14	0.044	2.1	0.022
23	1015				C	GB	2.13	0.044	2.1	0.024
24	2067				B (65%)[b]	GB	1.92	0.044	3.2	0.020
25	2068				B (80%)[b]	GB	2.09	0.044	2.5	0.022
26	1017				B (65%)[c]	GB	1.92	0.044	2.8	0.016
27	1018				B (80%)[c]	GB	2.09	0.044	2.5	0.018
28	1019		30	Space	A	GB	2.00	0.044	2.4	0.023
29	1020	20	20	Perimeter	A	GB	2.63	0.044	1.6	0.018
30	1021		20	Space	A	GB	2.36	0.044	2.0	0.023

a - Fixity assumed only in the design process. Structural model uses expected stiffness.
b - Only first story designed to be weak.
c - First and second stories designed to be weak.
d - This is based on the Sa,component and the Abrahamson and Silva (1997) attenuation model.
A - Expected practitioner design; strength and stiffness stepped as per common design practice.
B (%) - Weak story; sized target weak story(ies) based on code requ. and then strengthened stories above. % is the strength ratio of weak story(ies) to those above.
C - conservative design; neither size nor reinforcement decreased over building height
F - Fixed.
GB - "Grade Beam" - includes rotational stiffness of grade beam and any basement columns.
P - Pinned.

Table 3.4 shows the results of applying Method Two for each of the 30 buildings. The right portion of the table includes the results of regression analysis to relate collapse capacity and $\varepsilon(T_1)$ (i.e., $\mu'_{LN[Sa,col(T1)]} = \beta_0 + \beta_1 \bullet \varepsilon(T_1)$), the ratio between the corrected and uncorrected mean collapse capacities, and the corrected and uncorrected variability. This shows that the β_1 value is 0.29 on average and is exceptionally stable, with a coefficient of variation of only 0.14 for the wide variety of buildings. The ratio between the corrected and uncorrected variability is also exceptionally stable, with a mean of 0.82 and a coefficient of variation of only 0.05.

Table 3.4 Results of regression on ε(T_1) (Method Two) for set of 30 modern RC SMF buildings.

Design Information		Results of Regression on Epsilon[a]					
Design Number	No. of stories	β_0	β_1	$\mu'_{Sa,col(T1)} / \mu_{[Sa,col(T1)],rec}$ for mean $\varepsilon_0(T_1) = 1.7$[b]	σ_{LN} (Sa,col(T1)),rec	σ'_{LN} (Sa,col)	σ'_{LN}/σ_{LN}
1	1	0.771	0.389	1.47	0.48	0.37	0.77
2		0.885	0.365	1.42	0.46	0.35	0.76
3		0.774	0.390	1.47	0.48	0.37	0.77
4		0.286	0.267	1.32	0.42	0.37	0.87
5	2	0.949	0.257	1.27	0.42	0.33	0.78
6		1.018	0.213	1.17	0.42	0.34	0.81
7		0.814	0.238	1.24	0.43	0.35	0.81
8		0.586	0.261	1.29	0.43	0.35	0.81
9	4	0.146	0.274	1.45	0.39	0.33	0.84
10		0.331	0.275	1.47	0.43	0.39	0.90
11		0.479	0.257	1.37	0.38	0.30	0.79
12		0.244	0.318	1.54	0.43	0.36	0.84
13		0.853	0.267	1.40	0.43	0.35	0.81
14	8	-0.348	0.311	1.65	0.40	0.33	0.82
15		-0.171	0.318	1.69	0.38	0.32	0.83
16		-0.091	0.265	1.55	0.36	0.30	0.82
17		0.002	0.299	1.60	0.42	0.31	0.73
18		-0.012	0.329	1.67	0.41	0.32	0.78
19		-0.188	0.287	1.52	0.41	0.32	0.78
20		-0.211	0.280	1.56	0.40	0.33	0.82
21	12	-0.441	0.290	1.65	0.38	0.29	0.76
22		-0.424	0.251	1.53	0.37	0.31	0.83
23		-0.349	0.288	1.63	0.38	0.32	0.84
24		-0.208	0.272	1.58	0.38	0.34	0.88
25		-0.370	0.305	1.69	0.36	0.29	0.80
26		-0.344	0.275	1.61	0.38	0.32	0.86
27		-0.344	0.275	1.74	0.38	0.30	0.79
28		-0.163	0.311	1.71	0.40	0.34	0.85
29	20	-0.611	0.260	1.52	0.36	0.31	0.85
30		-0.345	0.297	1.64	0.39	0.34	0.87
		Mean:	0.289	1.51	0.41	0.33	0.82
		Median:	0.278	1.54	0.40	0.33	0.82
		StDev:	0.040	0.151	0.033	0.026	0.041
		c.o.v.:	0.14	0.10	0.08	0.08	0.05

a - This is based on the Sa,comp and the Abrahamson et al. (1997) atten. model.
b - Only example to show the impacts of adjustment for ε. Not all sites will have a target of 1.7, so this correction factor is not general.

Tables 3.5 and 3.6 have the same format as the previous two tables, but they present the results for 35 RC frame buildings designed for alternative structural design requirements. These building designs come from a related study by the authors (Haselton et al. 2007d, Chapter 7), whose purpose was to determine how changes in structural design provisions (changes to design base shear, etc.) would affect collapse safety.

Table 3.5 Design and behavioral information for 35 RC SMF buildings with varying structural design parameters.

Design Information						Period and Pushover Analysis Results			
Building	Design Num.	Design ID	Design R Value	SCWB Ratio	Drift Limit	First Mode Period (T_1) [sec]	Design Base Shear Coefficient (C_s) [g]	Static Overstr.	Ultimate Roof Drift Ratio (at 20% strength loss) (RDR_{ult})
4-story, 30' bay, space frame	1	2001	4	1.2	0.02	0.74	0.185	2.3	0.047
	2	2020	5.3	1.2	0.02	0.77	0.139	2.6	0.050
	3	1010	8	1.2	0.02	0.86	0.092	2.9	0.056
	4	2022	10	1.2	0.02	0.91	0.074	3.9	0.050
	5	2003	12	1.2	0.02	0.97	0.062	4.1	0.045
	6	2034	8	0.4	0.02	0.87	0.092	2.2	0.018
	7	2025	8	0.6	0.02	0.87	0.092	2.6	0.020
	8	2024	8	0.8	0.02	0.85	0.092	3.0	0.032
	9	2023	8	1.0	0.02	0.85	0.092	3.2	0.043
	10	1010	8	1.2	0.02	0.86	0.092	2.9	0.056
	11	2005	8	1.5	0.02	0.86	0.092	3.6	0.060
	12	2006	8	2.0	0.02	0.85	0.092	3.8	0.067
	13	2007	8	2.5	0.02	0.79	0.092	4.1	0.060
	14	2027	8	3.0	0.02	0.74	0.092	4.3	0.057
4-st., 30' perim.	15	2051	4	1.2	0.02	0.54	0.202	2.0	0.055
	16	1009	8	1.2	0.02	1.16	0.092	1.6	0.050
	17	2052	12	1.2	0.02	1.15	0.062	1.8	0.038
12-story, 20' bay, space frame	18	2008	4	1.2	0.02	1.83	0.070	2.1	0.039
	19	2021	5.3	1.2	0.02	1.97	0.053	2.2	0.028
	20	2009	8	1.2	0.02	1.99	0.044	2.3	0.033
	21	2028	10	1.2	0.02	2.27	0.028	2.7	0.018
	22	2010	12	1.2	0.02	2.40	0.023	3.2	0.020
	23	2015	8	1.2	0.01	1.59	0.044	2.5	0.027
	24	2009	8	1.2	0.02	1.99	0.044	2.3	0.033
	25	2017	8	1.2	0.03	2.20	0.044	2.2	0.022
	26	2018	8	1.2	0.04	2.64	0.044	2.1	0.027
12-story, 20' bay, perimeter frame	27	2053	4	1.2	0.02	1.50	0.079	1.6	0.031
	28	1013	8	1.2	0.02	2.01	0.044	1.7	0.026
	29	2054	12	1.2	0.02	2.84	0.023	1.7	0.009
	30	2060	8	0.9	0.02	2.00	0.044	1.7	0.024
	31	1013	8	1.2	0.02	2.01	0.044	1.7	0.026
	32	2055	8	1.5	0.02	2.01	0.044	1.7	0.029
	33	2056	8	2.0	0.02	2.01	0.044	1.6	0.030
	34	2057	8	2.5	0.02	1.90	0.044	1.7	0.038
	35	2058	8	3.0	0.02	1.84	0.044	1.7	0.045

Table 3.6 Results of regression on ε(T_1) (Method Two) for set of 35 RC SMF buildings with varying structural design parameters.

Design Information						Results of Regression on Epsilon[a]					
Building	Design Num.	Design ID	Design R Value	SCWB Ratio	Drift Limit	β_0	β_1	$\mu'_{Sa,col(T1)}$ / $\mu_{[Sa,col(T1)],rec}$ for mean $\varepsilon_0(T_1) = 1.7$[b]	σ_{LN} $_{(Sa,col(T1)),rec}$	σ'_{LN} $_{(Sa,col(T1))}$	σ'_{LN}/σ_{LN}
4-story, 30' bay, space frame	1	2001	4	1.2	0.02	0.998	0.218	1.28	0.40	0.33	0.83
	2	2020	5.3	1.2	0.02	0.878	0.221	1.29	0.40	0.31	0.79
	3	1010	8	1.2	0.02	0.853	0.267	1.40	0.43	0.35	0.81
	4	2022	10	1.2	0.02	0.708	0.254	1.38	0.40	0.31	0.78
	5	2003	12	1.2	0.02	0.582	0.239	1.34	0.41	0.31	0.76
	6	2034	8	0.4	0.02	0.083	0.175	1.24	0.41	0.34	0.85
	7	2025	8	0.6	0.02	0.225	0.181	1.23	0.42	0.34	0.82
	8	2024	8	0.8	0.02	0.507	0.218	1.28	0.43	0.37	0.86
	9	2023	8	1.0	0.02	0.743	0.258	1.37	0.44	0.35	0.79
	10	1010	8	1.2	0.02	0.853	0.254	1.37	0.43	0.31	0.72
	11	2005	8	1.5	0.02	0.884	0.259	1.38	0.40	0.32	0.80
	12	2006	8	2.0	0.02	0.961	0.236	1.37	0.37	0.29	0.79
	13	2007	8	2.5	0.02	0.976	0.246	1.37	0.36	0.30	0.84
	14	2027	8	3.0	0.02	1.017	0.253	1.35	0.36	0.31	0.85
4-st., 30' perim.	15	2051	4	1.2	0.02	1.085	0.319	1.66	0.40	0.35	0.87
	16	1009	8	1.2	0.02	0.244	0.318	1.54	0.43	0.36	0.84
	17	2052	12	1.2	0.02	0.043	0.308	1.55	0.43	0.36	0.84
12-story, 20' bay, space frame	18	2008	4	1.2	0.02	0.130	0.298	1.64	0.40	0.31	0.78
	19	2021	5.3	1.2	0.02	-0.149	0.280	1.63	0.37	0.32	0.85
	20	2009	8	1.2	0.02	-0.242	0.322	1.73	0.36	0.31	0.85
	21	2028	10	1.2	0.02	-0.667	0.244	1.49	0.36	0.28	0.78
	22	2010	12	1.2	0.02	-0.667	0.250	1.52	0.36	0.30	0.84
	23	2015	8	1.2	0.01	-0.049	0.299	1.62	0.38	0.31	0.80
	24	2009	8	1.2	0.02	-0.242	0.322	1.73	0.36	0.31	0.85
	25	2017	8	1.2	0.03	-0.311	0.277	1.62	0.40	0.32	0.81
	26	2018	8	1.2	0.04	-0.443	0.249	1.54	0.35	0.27	0.77
12-story, 20' bay, perimeter frame	27	2053	4	1.2	0.02	0.211	0.361	1.70	0.46	0.34	0.75
	28	1013	8	1.2	0.02	-0.441	0.290	1.65	0.38	0.29	0.76
	29	2054	12	1.2	0.02	-1.468	0.199	1.39	0.33	0.29	0.87
	30	2060	8	0.9	0.02	-0.534	0.278	1.60	0.39	0.31	0.79
	31	1013	8	1.2	0.02	-0.441	0.290	1.65	0.38	0.29	0.76
	32	2055	8	1.5	0.02	-0.367	0.284	1.62	0.41	0.32	0.79
	33	2056	8	2.0	0.02	-0.280	0.307	1.68	0.40	0.31	0.78
	34	2057	8	2.5	0.02	-0.110	0.304	1.69	0.40	0.30	0.75
	35	2058	8	3.0	0.02	0.041	0.307	1.66	0.38	0.29	0.76
						Mean:	0.268	1.50	0.39	0.32	0.80
						Median:	0.267	1.54	0.40	0.31	0.80
						StDev:	0.043	0.158	0.029	0.025	0.040
						c.o.v.:	0.16	0.11	0.07	0.08	0.05

a - Based on the Sa,comp and the Abrahamson et al. (1997) atten. model.

b - This only serves as an example to show the impacts of adjustement for ε. Not all sites will have a target of 1.7, so this correction factor is not general.

As compared to Table 3.4, Table 3.6 shows virtually identical values for the mean and variability of both β_1 and the ratio between corrected and uncorrected collapse capacity variability.

Looking more closely at Table 3.5, we see that there are several sets of buildings that have varying deformation capacity (as quantified by RDR_{ult}). This is useful and allows us to look more closely at how building deformation capacity may affect β_1. We expect β_1 to be larger for buildings with higher deformation capacity, because ductile buildings soften and the period extends prior to collapse. This makes the spectral shape (specifically spectral values at $T>T_1$) important to the structural response. Figure 3.12a shows how β_1 is affected by RDR_{ult}, for four sets of buildings. These data show a trend for deformation capacities up to 0.04, and suggest that the effects are saturated for $RDR_{ult} > 0.04$.

We also expect β_1 to be larger for taller buildings, because higher mode effects tend to be more important to the dynamic response, thereby making the spectral shape more significant for periods less than T_1. Additionally, if we want to separate the effects of height and deformation capacity, we can look at how height impacts β_1 *for a given* RDR_{ult} *value*. Figure 3.12b compares the β_1 values for six pairs of 4- and 12-story buildings that have identical RDR_{ult} values. This shows a clear and consistent trend between β_1 and building height, for five of the six sets of buildings considered.

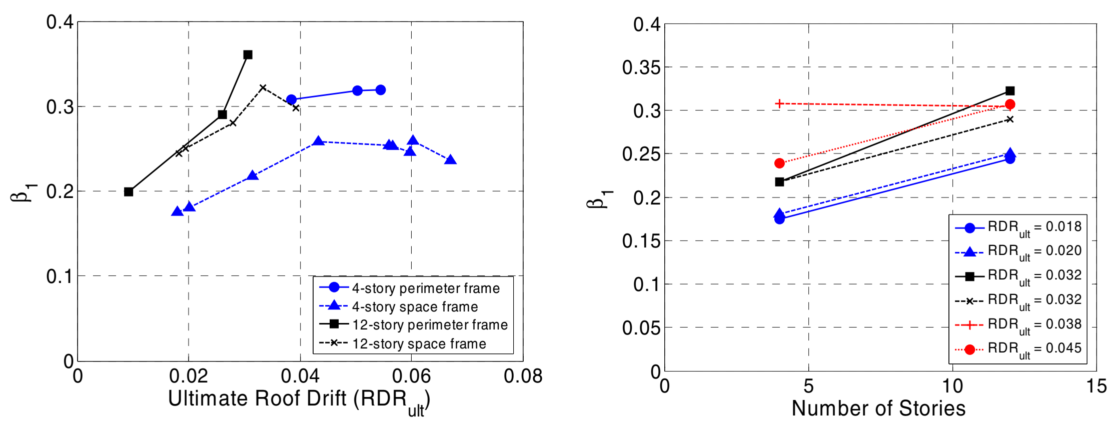

Fig. 3.12 Relationship between (a) β_1 and building deformation capacity (RDR_{ult}) and (b) β_1 and number of stories.

3.5.2.2 Non-Ductile 1967 Reinforced Concrete Frames

To more clearly see trends with building deformation capacity, this study is currently being extended to include results from a set of non-ductile 1967-era RC frame buildings. Due to time constraints, these data are not included in this report, but are expected to be included in the journal paper that will result from this chapter.

3.5.3 Developing Components of Simplified Method

3.5.3.1 Prediction of β_1

Section 3.5.2.1 presented the β_1 values for 65 RC frame buildings and discussed the effects of building height and deformation capacity (Fig. 3.12). To create a predictive equation for β_1, we started by using standard linear regression analysis to predict $\log(\beta_1)$ (Chatterjee et al. 2000) and then applied judgmental corrections to better replicate the trends shown in (Fig. 3.12). These corrections were required because only a small number of the 65 buildings a had low deformation capacity, and standard regression analysis can not accurately capture trends that are revealed by only a few observations in a large data set.

The proposed predictive equation for β_1 is as follows:

$$\hat{\beta}_1 = (0.25)(N+5)^{0.45}\left(RDR^*_{ult}\right)^{0.31} \quad (3.8)$$

$$RDR^*_{ult} = RDR_{ult} \text{ if } RDR_{ult} \le 0.04 \quad (3.9)$$

$$= 0.04 \text{ otherwise}$$

where N is the number of stories and RDR_{ult} is the roof drift ratio at 20% base shear strength loss from static pushover analysis.

The cap of 0.04 shown in Equation 3.9 is based on the previous observations from Figure 3.12a. The form of Equation 3.8 was chosen to fit the data, to make the effects of height fairly linear, and to make the estimated $\beta_1 = 0.0$ when the building has zero deformation capacity.

As previously mentioned, β_1 is fairly consistent for the set of 30 code-conforming RC frame buildings varying from 1 story to 20 stories, showing that the effects of height and deformation capacity (as measured by RDR_{ult}) approximately counteract one another.

Figure 3.13 shows the ratio of observed/predicted β_1 plotted against the building deformation capacity and the number of stories. This shows that Equation 3.8 provides accurate predictions for most of the 65 buildings used in this study. One exception is that β_1 is significantly underpredicted (i.e., conservative) for three of the 1-story buildings, but the prediction is accurate for the fourth 1-story building. Additionally, β_1 is overpredicted by 13% (i.e., unconservative) for the two 20-story buildings. It would be useful to extend this study to include additional tall buildings, as this would help determine if this bias is consistent and warrants revision to Equation 3.8.

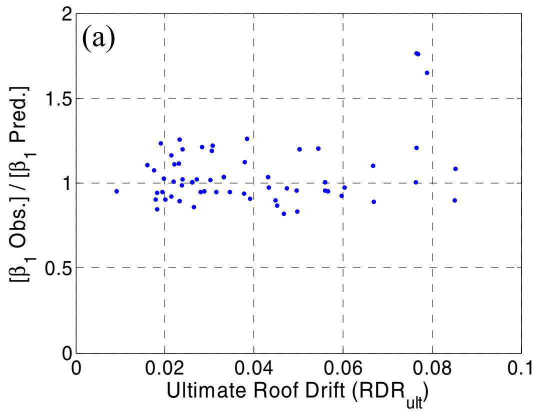

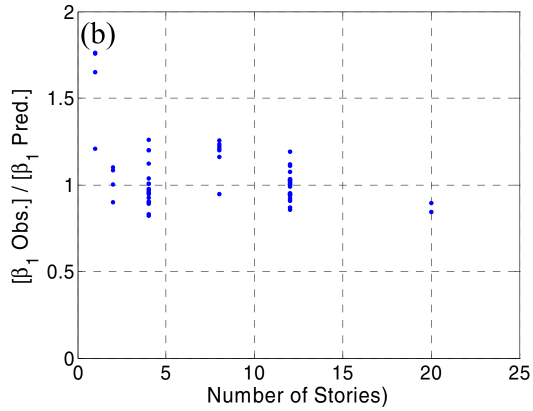

Fig. 3.13 Ratio of observed/predicted β_1 plotted against (a) building deformation capacity (RDR_{ult}) and (b) number of stories.

Figure 3.13 also shows that the predictions are accurate for buildings with low deformation capacity; however, this study includes only a few buildings of this type. We plan to extend this study to include more building with low deformation capacity (see Section 3.5.2.2), so Equation 3.8 can either be verified or improved.

3.5.3.2 Prediction of $\sigma'_{LN(Sa,col(T1))}$

Section 3.5.2.1 showed that the ratio of corrected to uncorrected variability in collapse capacity [$\sigma'_{LN(Sa,col(T1))}$ / $\sigma_{LN(Sa,col(T1))}$] is exceptionally stable, with a mean value of 0.81 and a coefficient of variation of 0.05. This ratio is proposed for reducing the variability.

$$\hat{\sigma}'_{LN(Sa,col(T_1))} = 0.81\left(\sigma_{LN(Sa,col(T_1)),records}\right) \tag{3.10}$$

3.5.4 Proposed Simplified Method

The section summarizes the proposed simplified method for adjusting collapse capacity to reflect appropriate spectral shape, and illustrates the method for a 4-story RC SMF space frame (ID 1008 in Tables 3.3 and 3.4).

Step 1. Build the structural model. Perform an eigenvalue analysis and static pushover analysis using an appropriate lateral load pattern. From the pushover curve, estimate the roof drift ratio at 20% lateral strength loss (RDR_{ult}).

For this example 4-story RC SMF building, T_1 = 0.94 sec. The static pushover analysis was based on the lateral load pattern recommended by ASCE 7-05 (ASCE 2005) and the pushover curve is given in Figure 3.14. From the pushover curve, we estimate RDR_{ult} = 0.047.

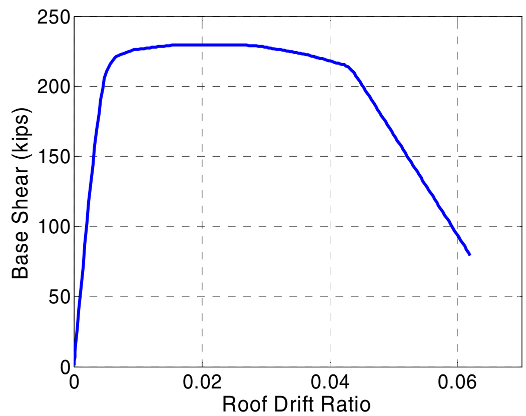

Fig. 3.14 Static pushover curve for example 4-story RC SMF building (ID 1008).

Step 2. Perform nonlinear dynamic analyses to predict collapse capacity using ground motion Set One Reduced[6] (Appendix B). Compute the natural logarithm of the collapse capacity for each record, and then compute the mean and standard deviation of these values (i.e., $\mu_{LN[Sa,col(T1)],records}$ and $\sigma_{LN[Sa,col(T1)],records}$). For the example 4-story RC SMF building, these results of the nonlinear dynamic collapse analyses are shown as follows.

$$\mu_{LN[Sa,col(T1)],records} = \mu_{LN[Sa,col(0.94s)],records} = 0.601 \tag{3.11}$$

$$\sigma_{LN[Sa,col(T1)],records} = \sigma_{LN[Sa,col(0.94s)],records} = 0.38 \tag{3.12}$$

If one is interested in the mean collapse capacity (i.e., not the logarithmic mean), it can be computed as follows.

$$Mean_{[Sa,col(0.94s)],records} = \exp\left(\mu_{LN[Sa,col(0.94s)],records}\right) = 1.82g \tag{3.13}$$

Step 3. Estimate β_1 using Equation 3.8. For the 4-story RC SMF example, this is done as follows:

$$\hat{\beta}_1 = (0.25)(N+5)^{0.45}\left(RDR^*_{ult}\right)^{0.31} \tag{3.14}$$

$$RDR^*_{ult} = 0.04 \tag{3.15}$$

---

[6] Alternatively, one could use the full Set One (39 records instead of 22) but the two sets have the same properties, so the benefit would be minimal. The primary benefit of using the larger set was to better predict the regression line between $LN(S_{a,col}(T_1))$ and $\varepsilon(T_1)$; this additional information is not required in the simplified method.

$$\hat{\beta}_1 = (0.25)(4+5)^{0.45}(0.04)^{0.31} = 0.248 \tag{3.16}$$

Step 4. Determine the target mean ε value ($\varepsilon(\mathrm{T}_1)_{,\mathrm{target}}$) for the site and hazard level of interest (as discussed in Section 3.3.2). For illustration with the 4-story RC SMF, we assume that the target is ($\varepsilon(\mathrm{T}_1)_{,\mathrm{target}}$) = 1.9.

Step 5. We need to adjust for the difference between the appropriate ε value and the ε values of the ground motions used in the collapse simulation. To do so, we must first determine the mean ε value from the record set used in step 2 ($\bar{\varepsilon}(\mathrm{T}_1)_{,\mathrm{records}}$). Figure 3.15 plots the mean ε values for ground motion Set One (for both the full set of 39 records, and the reduced set of 22 records). From this figure one can read $\bar{\varepsilon}(\mathrm{T}_1)_{,\mathrm{records}}$. For the example building, T_1 = 0.94 sec and the collapse simulation is based on the full ground motion set, so $\bar{\varepsilon}(\mathrm{T}_1)_{,\mathrm{records}}$ is 0.17.

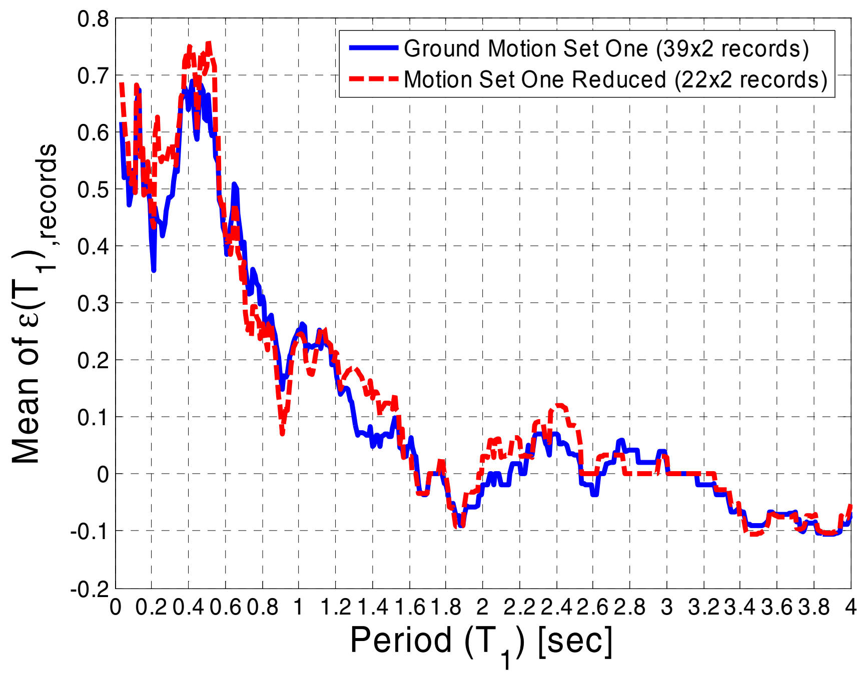

Fig. 3.15 Mean ε values for full and reduced versions of ground motion Set One [$\bar{\varepsilon}(\mathrm{T}_1)_{,\mathrm{records}}$].

Step 6. Compute the adjusted mean collapse capacity. This adjusted capacity accounts for the difference between the mean ε of the record set ($\bar{\varepsilon}(\mathrm{T}_1)_{,\mathrm{records}}$) and the target ε values that comes from disaggregation ($\bar{\varepsilon}_0(\mathrm{T}_1)$). The following equations show this calculation and illustrate this for the example 4-story RC SMF.

$$\mu'_{LN[Sa,col(T1)]} = \mu_{LN[Sa,col(T1)],records} + \hat{\beta}_1\left(\overline{\varepsilon}_0(\mathrm{T}_1) - \overline{\varepsilon}(\mathrm{T}_1)_{,\mathrm{records}}\right) \tag{3.17}$$

$$\mu'_{LN[Sa,col(0.94s)]} = 0.601 + 0.248\left(1.9 - 0.17\right) = 1.030 \tag{3.18}$$

$$Mean'_{Sa,col(0.94s)} = \exp\left(\mu'_{LN[Sa,col(0.94s)]}\right) = \exp\left(1.030\right) = 2.80g \tag{3.19}$$

As additional information, the ratio of the adjusted to unadjusted mean collapse capacity can also be computed using Equations 3.13 and 3.19, as follows:

$$Ratio = \frac{Mean'_{Sa,col(T_1)}}{Mean_{[Sa,col(T_1)],records}} = \frac{Mean'_{Sa,col(0.94s)}}{Mean_{[Sa,col(0.94s)],records}} = \frac{2.80g}{1.82g} = 1.54 \tag{3.20}$$

Step 7. Compute the adjusted variability in the collapse capacity using Equation 3.10. This calculation for the 4-story RC SMF building is as follows.

$$\hat{\sigma}'_{LN(Sa,col(T_1)} = 0.81\left(\sigma_{LN(Sa,col(T_1),records}\right) = 0.81\left(0.38\right) = 0.31 \tag{3.21}$$

3.6 SUMMARY AND CONCLUSIONS

Proper treatment of spectral shape (as quantified using the parameter ε) is critical for accurate collapse assessment. For an example 8-story RC SMF building, we compared the predicted collapse safety using ground motions selected (a) to have proper spectral shape and (b) without regard to spectral shape. When using ground motions with proper spectral shape, the mean collapse capacity increased by a factor of 1.6, the P[C|$Sa_{2/50}$] decreased from 30–0.5%, and the mean annual frequency of collapse decreased by a factor of 23.

The most direct approach to account for proper ε is to select ground motions that have the appropriate $\varepsilon(T_1)$ for the site, hazard level, and structural period of interest. However, this is often not feasible when assessing the collapse performance of a large number of buildings. To address this problem, we propose a simplified method.

To develop and validate this simplified method, we predicted the collapse capacities of 65 RC frame buildings subjected to 78 ground motion records. We then used linear regression analysis to find the relationship between $S_{a,col}(T_1)$ and $\varepsilon(T_1)$ for each building. We found that the results of this regression method agree well with the results obtained by using a ground motion set selected to have the appropriate ε.

After predicting the collapse capacities and performing the regressions for the 65 buildings, we used the set of results to make generalized conclusions and to develop the simplified method. We first found that the relationship between $S_{a,col}(T_1)$ and $\varepsilon(T_1)$ was reasonably stable for the various buildings considered. We also found that this relationship is affected by both building deformation capacity and building height, consistent with expected behavior. The simplified method includes an empirical relationship to account for these trends.

The final proposed simplified method allows the analyst to use a general ground motion set selected without regard to ε, and then correct the predicted collapse capacity distribution (both mean and variability) to account for the $\varepsilon(T_1)$ expected for the site and ground motion hazard level of interest. We also propose a general set of far-field strong ground motions to be used in this simplified procedure.

3.7 LIMITATIONS AND FUTURE WORK

Limitations and future work are listed as follows:

For the period range of 0.5–2.5 sec, the 80 ground motions used in this study typically cover the range of ε = -1.0 to +2.0. The simplified method proposed in this chapter should not be used for ε values outside this range.

- This study primarily included modern RC frame buildings that have large deformation capacity. The authors are currently extending this study to include non-ductile 1967-era frame buildings.
- When computing ε values, we utilized the attenuation function by Abrahamson and Silva (1997) which provides standard deviations for the geometric mean of the spectral accelerations of two horizontal ground motion components. We did not apply a correction factor to account for the increased standard deviation associated with the Sa of a random horizontal component of ground motion. This means that our computed ε values are slightly higher than they would have been with the correction factor applied.
- It would be useful to also examine the results based on other attenuation functions, which would hopefully verify that the findings of this study are robust with respect to the assumed attenuation function.

APPENDIX 3A: DESIGN OF 8-STORY SPECIAL MOMENT FRAME

Figure 3.16 shows the design documentation for the 8-story reinforced concrete special moment-frame building used for illustration in this report. This building is ID 1011 from a related study by the authors (Haselton et al. 2007c, Chapter 6). The building is 120′ x 120′ in plan, uses a 3-bay perimeter frame system with 20′ bay spacing, and has a fundamental period (T_1) of 1.71 sec. The notation used in Figure 3.16 can be found in the notation list.

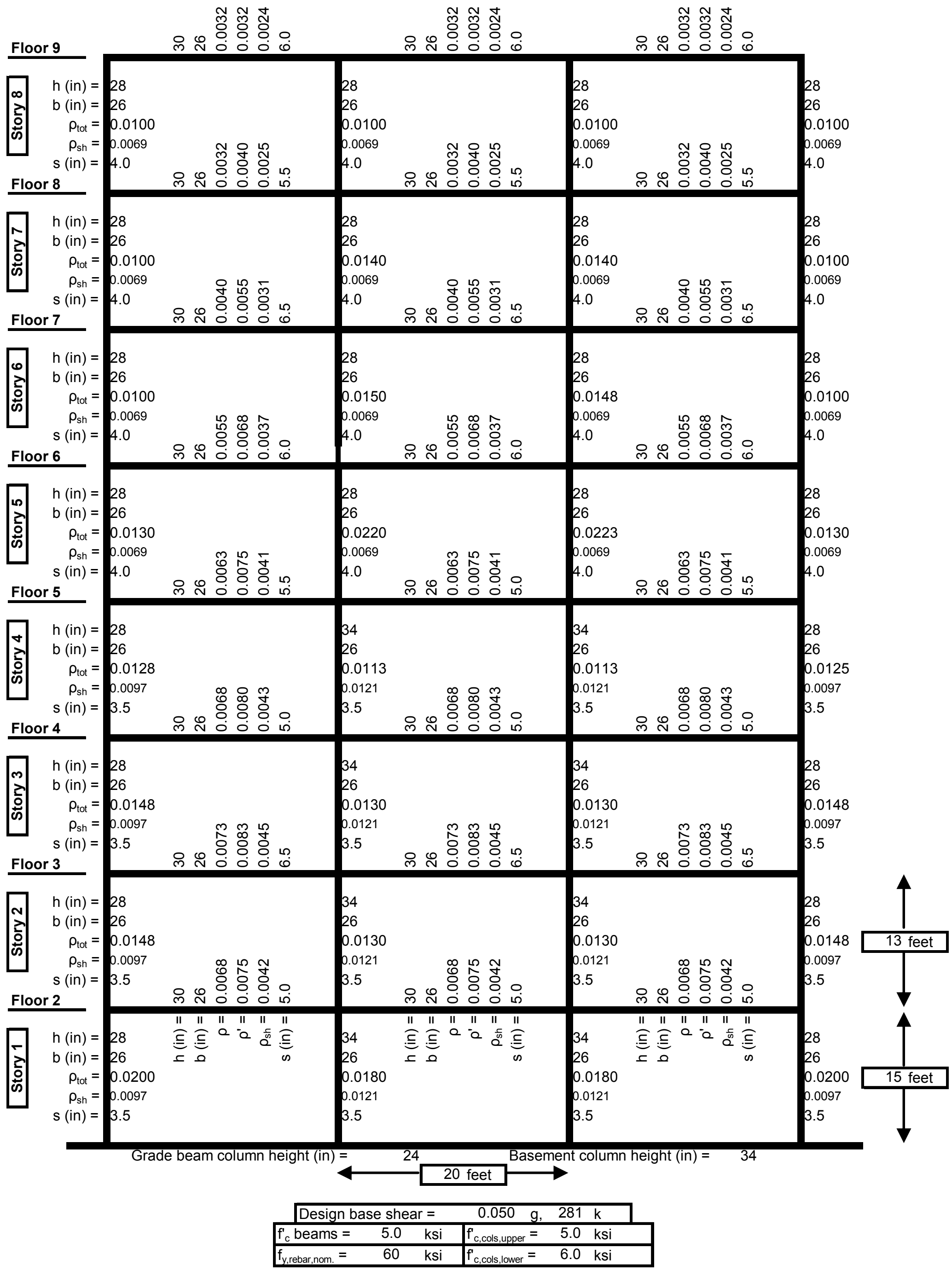

Fig. 3.16 Design documentation for 8-story RC SMF building. Building is from related study (Haselton et al. 2007c, Chapter 6).

APPENDIX 3B: GROUND MOTION SETS

Set One: Basic Far-Field Ground Motion Set Selected without Considering Epsilon

We selected ground motion Set One (also called "basic far-field set" or "set FFext") to consist of strong motions that may cause the structural collapse of modern buildings. This typically occurs at extremely large levels of ground motion, so this ground motion set was selected to represent these extreme motions to the extent possible. To ensure that the records represent strong motion that may cause structural collapse, we imposed minimum limits on event magnitude, as well as peak ground velocity and acceleration. The limits were chosen to balance the selection of large motions, while ensuring that enough motions will meet the selection criteria.

- Magnitude > 6.5
- Distance from source to site > 10 km (average of Joyner-Boore and Campbell distances)
- Peak ground acceleration > 0.2g *and* peak ground velocity > 15 cm/sec
- Soil shear wave velocity, in upper 30m of soil, greater than 180 m/sec (NEHRP soil types A–D; note that all selected records happened to be on C/D sites)
- Limit of six records from a single seismic event; if more than six records pass the initial criteria, then the six records with largest PGV are selected, but in some cases a lower PGV record is used if the PGA is much larger.
- Lowest useable frequency < 0.25 Hz, to ensure that the low-frequency content was not removed by the ground motion filtering process
- Strike-slip and thrust faults (consistent with California)
- No consideration of spectral shape (ε)
- No consideration of station housing, but PEER-NGA records were selected to be "free field"

Table 3.7 lists the ground motions included in Set One. The ε(1.7s) values are not included for each record, but the mean ε(T) values are shown in Figure 3.15. The motions were selected from the PEER-NGA database (PEER 2006b).

For those that desire a smaller ground motion set, we also propose a "Set One Reduced" that includes 22 records rather than 39 records. These records are marked with "*" in Table 3.7 and are based on the same selection criteria above, except that (e) was modified to allow only two records per event. Based on observations by the authors, use of this reduced ground motion set in place of the full set will lead to roughly the same structural simulation results.

This ground motion set was developed for use in both this research and the Applied Technology Council Project 63, which is focused on developing a procedure to validate seismic provisions for structural design.

Table 3.7 Documentation of 78 ground motion recordings (39 records with two horizontal components per record) included in basic far-field ground motion set (Set One).

			Event Information				Site Information				Record Information		
EQ Index	EQ ID	PEER-NGA Rec. Num.	Mag.	Year	Event	Fault Type	Station Name	Vs_30 (m/s)	Campbell Distance (km)	Joyner-Boore Distance (km)	Lowest Useable Freq. (Hz)	Horizontal Acceleration Time History Files	
1*	12011	953	6.7	1994	Northridge	Blind thrust	Beverly Hills - 14145 Mulhol	356	17.2	9.4	0.25	NORTHR/MUL009.at2	NORTHR/MUL279.at2
2*	12012	960	6.7	1994	Northridge	Blind thrust	Canyon Country - W Lost Cany	309	12.4	11.4	0.13	NORTHR/LOS000.at2	NORTHR/LOS270.at2
3	12013	1003	6.7	1994	Northridge	Blind thrust	LA - Saturn St	309	27.0	21.2	0.13	NORTHR/STN020.at2	NORTHR/STN110.at2
4	12014	1077	6.7	1994	Northridge	Blind thrust	Santa Monica City Hall	336	27.0	17.3	0.14	NORTHR/STM090.at2	NORTHR/STM360.at2
5	12015	952	6.7	1994	Northridge	Blind thrust	Beverly Hills - 12520 Mulhol	546	18.4	12.4	0.16	NORTHR/MU2035.at2	NORTHR/MU2125.at2
6*	12041	1602	7.1	1999	Duzce, Turkey	Strike-slip	Bolu	326	12.4	12.0	0.06	DUZCE/BOL000.at2	DUZCE/BOL090.at2
7*	12052	1787	7.1	1999	Hector Mine	Strike-slip	Hector	685	12.0	10.4	0.04	HECTOR/HEC000.at2	HECTOR/HEC090.at2
8*	12061	169	6.5	1979	Imperial Valley	Strike-slip	Delta	275	22.5	22.0	0.06	IMPVALL/H-DLT262.at2	IMPVALL/H-DLT352.at2
9*	12062	174	6.5	1979	Imperial Valley	Strike-slip	El Centro Array #11	196	13.5	12.5	0.25	IMPVALL/H-E11140.at2	IMPVALL/H-E11230.at2
10	12063	162	6.5	1979	Imperial Valley	Strike-slip	Calexico Fire Station	231	11.6	10.5	0.25	IMPVALL/H-CXO225.at2	IMPVALL/H-CXO315.at2
11	12064	189	6.5	1979	Imperial Valley	Strike-slip	SAHOP Casa Flores	339	10.8	9.6	0.25	IMPVALL/H-SHP000.at2	IMPVALL/H-SHP270.at2
12*	12071	1111	6.9	1995	Kobe, Japan	Strike-slip	Nishi-Akashi	609	25.2	7.1	0.13	KOBE/NIS000.at2	KOBE/NIS090.at2
13*	12072	1116	6.9	1995	Kobe, Japan	Strike-slip	Shin-Osaka	256	28.5	19.1	0.13	KOBE/SHI000.at2	KOBE/SHI090.at2
14	12073	1107	6.9	1995	Kobe, Japan	Strike-slip	Kakogawa	312	3.2	22.5	0.13	KOBE/KAK000.at2	KOBE/KAK090.at2
15	12074	1106	6.9	1995	Kobe, Japan	Strike-slip	KJMA	312	95.8	0.9	0.06	KOBE/KJM000.at2	KOBE/KJM090.at2
16*	12081	1158	7.5	1999	Kocaeli, Turkey	Strike-slip	Duzce	276	15.4	13.6	0.24	KOCAELI/DZC180.at2	KOCAELI/DZC270.at2
17*	12082	1148	7.5	1999	Kocaeli, Turkey	Strike-slip	Arcelik	523	13.5	10.6	0.09	KOCAELI/ARC000.at2	KOCAELI/ARC090.at2
18*	12091	900	7.3	1992	Landers	Strike-slip	Yermo Fire Station	354	23.8	23.6	0.07	LANDERS/YER270.at2	LANDERS/YER360.at2
19*	12092	848	7.3	1992	Landers	Strike-slip	Coolwater	271	20.0	19.7	0.13	LANDERS/CLW-LN.at2	LANDERS/CLW-TR.at2
20	12093	864	7.3	1992	Landers	Strike-slip	Joshua Tree	379	11.4	11.0	0.07	LANDERS/JOS000.at2	LANDERS/JOS090.at2
21*	12101	752	6.9	1989	Loma Prieta	Strike-slip	Capitola	289	35.5	8.7	0.13	LOMAP/CAP000.at2	LOMAP/CAP090.at2
22*	12102	767	6.9	1989	Loma Prieta	Strike-slip	Gilroy Array #3	350	12.8	12.2	0.13	LOMAP/G03000.at2	LOMAP/G03090.at2
23	12103	783	6.9	1989	Loma Prieta	Strike-slip	Oakland - Outer Harbor Wharf	249	74.3	74.2	0.13	LOMAP/CH12000.at2	LOMAP/CH10270.at2
24	12104	776	6.9	1989	Loma Prieta	Strike-slip	Hollister - South & Pine	371	27.9	27.7	0.13	LOMAP/HSP000.at2	LOMAP/HSP090.at2
25	12105	777	6.9	1989	Loma Prieta	Strike-slip	Hollister City Hall	199	27.6	27.4	0.13	LOMAP/HCH090.at2	LOMAP/HCH180.at2
26	12106	778	6.9	1989	Loma Prieta	Strike-slip	Hollister Diff. Array	216	24.8	24.5	0.13	LOMAP/HDA165.at2	LOMAP/HDA255.at2
27*	12111	1633	7.4	1990	Manjil, Iran	Strike-slip	Abbar	724	13.0	12.6	0.13	MANJIL/ABBAR--L.at2	MANJIL/ABBAR--T.at2
28*	12121	721	6.5	1987	Superstition Hills	Strike-slip	El Centro Imp. Co. Cent	192	18.5	18.2	0.13	SUPERST/B-ICC000.at2	SUPERST/B-ICC090.at2
29*	12122	725	6.5	1987	Superstition Hills	Strike-slip	Poe Road (temp)	208	11.7	11.2	0.25	SUPERST/B-POE270.at2	SUPERST/B-POE360.at2
30	12123	728	6.5	1987	Superstition Hills	Strike-slip	Westmorland Fire Sta	194	13.5	13.0	0.13	SUPERST/B-WSM090.at2	SUPERST/B-WSM180.at2
31*	12132	829	7.0	1992	Cape Mendocino	Thrust	Rio Dell Overpass - FF	312	14.3	7.9	0.07	CAPEMEND/RIO270.at2	CAPEMEND/RIO360.at2
32*	12141	1244	7.6	1999	Chi-Chi, Taiwan	Thrust	CHY101	259	15.5	10.0	0.05	CHICHI/CHY101-E.at2	CHICHI/CHY101-N.at2
33*	12142	1485	7.6	1999	Chi-Chi, Taiwan	Thrust	TCU045	705	26.8	26.0	0.05	CHICHI/TCU045-E.at2	CHICHI/TCU045-N.at2
34	12143	1524	7.6	1999	Chi-Chi, Taiwan	Thrust	TCU095	447	45.3	45.2	0.05	CHICHI/TCU095-E.at2	CHICHI/TCU095-N.at2
35	12144	1506	7.6	1999	Chi-Chi, Taiwan	Thrust	TCU070	401	24.4	19.0	0.04	CHICHI/TCU070-E.at2	CHICHI/TCU070-N.at2
36	12145	1595	7.6	1999	Chi-Chi, Taiwan	Thrust	WGK	259	15.4	10.0	0.09	CHICHI/WGK-E.at2	CHICHI/WGK-N.at2
37	12146	1182	7.6	1999	Chi-Chi, Taiwan	Thrust	CHY006	438	13.2	9.8	0.04	CHICHI/CHY006-N.at2	CHICHI/CHY006-W.at2
38*	12151	68	6.6	1971	San Fernando	Thrust	LA - Hollywood Stor FF	316	25.9	22.8	0.25	SFERN/PEL090.at2	SFERN/PEL180.at2
39*	12171	125	6.5	1976	Friuli, Italy	Thrust (part blind)	Tolmezzo	425	15.8	15.0	0.13	FRIULI/A-TMZ000.at2	FRIULI/A-TMZ270.at2

* This marks the records that are included a smaller (22 record) far-field set (selected with a maximum of 2 records per event). This smaller set was used in the Applied Technology Council Project 63.

Set Two: Far-Field Ground Motion Set Selected for Positive Epsilon

We selected ground motion Set Two to have a mean $\varepsilon(1.7s) = 1.7$. In addition, we selected motions only from large events and avoided near-field motions and soft-soil sites. The full set of selection criteria are as follows:

- $\varepsilon(1.7s) > 1.25$, with a mean value of 1.7 (computed using Abrahamson and Silva 1997)
- $M > 6.5$
- Closest distance to rupture between 10 and 100 km
- Soil V_{s_30} between 180 and 1500 m/sec
- USGS soil class B, C, or D
- Free-field or ground-level recordings only
- High-pass filter frequency below 0.28 Hz (for both horizontal components)

Table 3.8 lists the ground motions included in Set Two, as well as the $\varepsilon(1.7s)$ values computed using attenuation function from both Abrahamson and Silva (1997) and Boore et al. (1997). These motions were all selected from the PEER-NGA database (PEER 2006b).

Table 3.8 Documentation of 20 ground motion recordings included in ground motion Set Two.

Record Index	PEER-NGA Record Number	Event	Year	Station	Comp.[a]	$\varepsilon_{AS}(1.71s)^c$	$\varepsilon_{BJF}(1.71s)^c$
1	169	Imperial Valley-06	1979	Delta	FP	1.5	2.2
2	292	Irpinia, Italy-01	1980	Sturno	FP	1.4	2.4
3	573	Taiwan SMART1(45)	1986	SMART1 I01	FN	1.7	2.3
4	574	Taiwan SMART1(45)	1986	SMART1 I07	FN	1.6	2.2
5	579	Taiwan SMART1(45)	1986	SMART1 O04	FN	1.3	1.9
6	580	Taiwan SMART1(45)	1986	SMART1 O06	FP	1.6	2.3
7	583	Taiwan SMART1(45)	1986	SMART1 O10	FP	1.4	2.0
8	729	Superstition Hills-02	1987	Wildlife Liquef. Array	FN	1.4	1.7
9	738	Loma Prieta	1989	Alameda Naval Air Stn Hanger	FN	1.8	2.1
10	758	Loma Prieta	1989	Emeryville - 6363 Christie	FP	2.8	3.3
11	771	Loma Prieta	1989	Golden Gate Bridge	FP	1.6	3.4
12	776	Loma Prieta	1989	Hollister - South & Pine	FN	2.0	2.9
13	783	Loma Prieta	1989	Oakland - Outer Harbor Wharf	FN	2.7	3.4
14	789	Loma Prieta	1989	Point Bonita	FN	1.9	3.6
15	953	Northridge-01	1994	Beverly Hills - 14145 Mulhol	FP	2.0	2.9
16	963	Northridge-01	1994	Castaic - Old Ridge Route	FN	1.9	3.1
17	1077	Northridge-01	1994	Santa Monica City Hall	FN	1.3	2.1
18	1087	Northridge-01	1994	Tarzana - Cedar Hill A	FP	1.6	2.1
19	1103	Kobe, Japan	1995	Kakogawa	FP	1.7	2.4
20	1319	Chi-Chi, Taiwan	1999	ILA037	FN	1.4	1.7

a. Records oriented fault-normal (FN) or fault-parallel (FP). Records not near-fault, so orientation judged not significant.
b. ε value computed using the attenuation function developed by Abrahamson et al. (1997).
c. ε value computed using the attenuation function developed by Boore et al. (1997).

4 Beam-Column Element Model Calibrated for Predicting Flexural Response Leading to Global Collapse of RC Frame Buildings

4.1 SUMMARY OF CHAPTER

Performance-based earthquake engineering relies on the structural analysis models that can be used to simulate structural performance, up to the point of collapse. In this chapter, a lumped plasticity element model developed by Ibarra et al. (2005) is used to model the behavior of reinforced concrete beam-columns. The backbone response curve and the associated hysteretic rules of this model provide for versatile simulation of cyclic behavior including the negative stiffness of post-peak response; such modeling of strain-softening behavior is critical for simulating the collapse of RC frame structures.

The Ibarra element model has been calibrated to data from 255 reinforced concrete column tests. For each test, the element model parameters (e.g., plastic rotation capacity, cyclic deterioration parameters, etc.) were systematically calibrated so that the analysis results closely matched the experimental results. Column design parameters (e.g., axial load ratio, spacing of transverse reinforcement, etc.) are then related to the column element model parameters through regression analysis.

The outcome of this work is a set of equations that can be used to predict a column's element model parameters for input into analysis models, given the various design parameters of a reinforced concrete column. Moreover, by demonstrating which column design factors are most important predictors of key aspects of structural collapse behavior, they can provide an important tool for improving design provisions.

4.2 INTRODUCTION AND METHODOLOGY

4.2.1 Purpose and Scope

Emerging performance-based earthquake engineering design approaches seek to enable more accurate and transparent assessment of both life-safety risks and damage, through the use of advanced analysis models and design criteria. The first generation of performance-based assessment provisions, such as FEMA 273 and 356 (FEMA 1997, 2000a) and ATC 40 (ATC 1996), provided an excellent first step toward codifying approaches that embrace nonlinear analysis to simulate system performance and articulate performance metrics for the onset of damage up to structural collapse. As such, these documents marked the first major effort to develop consensus-based provisions that went beyond the traditional emphasis on linear analysis and specification of component strengths, which have long been the mainstay of engineering design practice and building code provisions.

The FEMA 273/356 project (FEMA 1997; ASCE 2000) was an important milestone in codifying degrading nonlinear models and procedures to explicitly evaluate structural collapse. A key component of these procedures is the specification of nonlinear structural component models in the form of monotonic backbone curves that define the characteristic force-deformation behavior of the components as a function of seismic detailing parameters. For example, FEMA 356 specifies backbone curve parameters that define the nonlinear moment-rotation response of reinforced concrete beam-columns as a function of longitudinal and horizontal reinforcement, and axial and shear demands. While these models are limited, in being highly idealized, deterministic, and generally conservative, they are noteworthy in terms of their breadth, and are capable of modeling the full range of behavior for a wide variety of structural components for all major forms of building construction.

Building upon these efforts, the goal of this project is to develop accurate element models that can be used to evaluate the collapse performance of reinforced concrete frame buildings, focusing particularly on reinforced concrete beam-columns. With the availability of an accurate and well-calibrated beam-column element model, nonlinear dynamic simulation may be used to predict building behavior up to the point of collapse. This project is part of a larger research effort coordinated by the Pacific Earthquake Engineering Research (PEER) Center to develop a comprehensive methodology, models, and tools for performance-based earthquake engineering, which builds upon the concepts introduced in FEMA 273/356.

The calibrations of reinforced concrete columns presented here are based on an element model developed by Ibarra, Medina, and Krawinkler (2005, 2003), as implemented in PEER's open-source structural analysis and simulation software tool, OpenSees. The model parameters, hysteretic rules, and implementation are discussed in more detail in the following section. The outcome of the effort is empirical functions relating the seven calibrated model parameters to the physical properties of a beam-column (i.e., axial load, concrete strength, confinement, etc.). These equations predict the mean modeling parameters, and the uncertainty is also quantified[1]. Ideally, the empirical equations developed in this study will help to develop consensus in the engineering community regarding modeling parameters so that equations of this type can be implemented into future performance-based guidelines and standards.

4.2.2 Hysteretic Model

The hysteretic model used in this study was developed by Ibarra, Medina, and Krawinkler (2005). Figure 4.1 shows the trilinear monotonic backbone curve and associated hysteretic rules of the model, which provide for versatile modeling of cyclic behavior. An important aspect of this model is the negative stiffness branch of post-peak response, which enables modeling of strain-softening behavior associated with concrete crushing, rebar buckling and fracture, and bond failure. The model also captures four basic modes of cyclic deterioration: strength deterioration of the inelastic strain-hardening branch, strength deterioration of the post-peak strain-softening branch, accelerated reloading stiffness deterioration, and unloading stiffness deterioration. Additional reloading stiffness deterioration is automatically incorporated through the peak-oriented cyclic response rules. Cyclic deterioration is based on an energy index that has two parameters: normalized energy-dissipation capacity and an exponent term to describe how the rate of cyclic deterioration changes with accumulation of damage. The element model was implemented in OpenSees by Altoontash (2004).

---

[1] Strictly speaking, the equations predict the geometric mean and the prediction errors are quantified in terms of a logarithmic standard deviation. This is consistent with the assumption that the prediction errors are lognormally distributed.

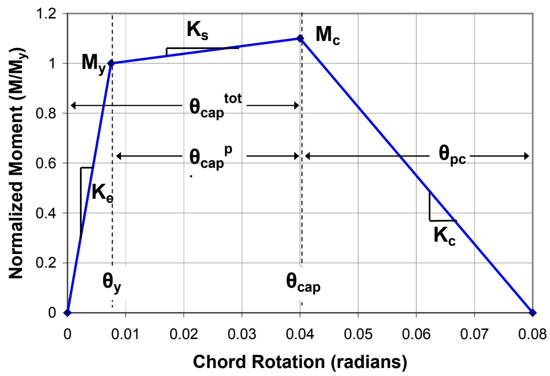

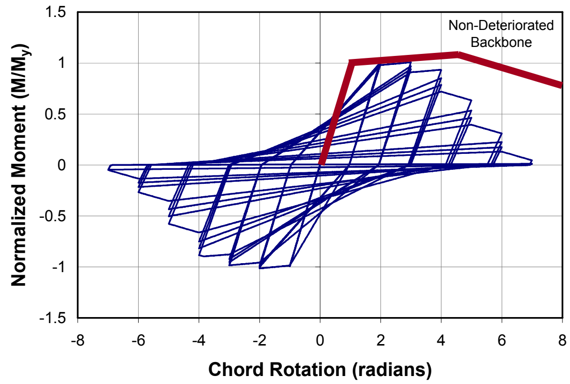

Fig. 4.1 Monotonic and cyclic behavior of component model used in study. Model developed by Ibarra, Medina, and Krawinkler.

This element model requires the specification of seven parameters to control both the monotonic and cyclic behavior of the model: M_y, θ_y, M_c/M_y, $\theta_{cap,pl}$, θ_{pc}, λ, and c (λ and c control the rate of cyclic deterioration). To quantify the post-yield and post-capping stiffnesses, we utilize M_c/M_y and θ_{pc}; K_s and K_c can be computed as $K_s = K_e\left(\theta_y/\theta_{cap,pl}\right)\left(\left(M_c - M_y\right)/M_y\right)$ and $K_c = -K_e\left(\theta_y/\theta_{pc}\right)\left(M_c/M_y\right)$, respectively. The goal of the calibration studies is to empirically determine stiffness, capping (peak) point, post-peak unloading stiffness, and hysteretic stiffness/strength deterioration for reinforced concrete beam-column elements.

The residual strength can be captured using this element model, but was not quantified in this study, due to a lack of experimental data that showed the residual. Some of the non-conforming columns that were tested to large deformations showed little or no residual strength, while most conforming columns did not experience enough strength deterioration to provide a good estimate of a residual strength.

4.2.3 Experimental Database

The database used in this study is the Pacific Earthquake Engineering Research Center's Structural Performance Database that was developed by Berry, Parrish, and Eberhard (PEER 2006a; Berry et al. 2004). This database includes the results of cyclic and monotonic tests of 306 rectangular columns and 177 circular columns. For ease of comparison, Berry et al. systematically processed the data into that of an equivalent cantilever. For each column test, the database reports the force-displacement history, the column geometry and reinforcement information, the failure mode, and often other relevant information.

From this database, we selected rectangular columns failing in a flexural mode (220 tests) or in a combined flexure-shear mode (35 tests), for a total of 255 tests. These tests cover the following ranges of important parameters: $0.0 < P/A_g f'_c < 0.7$, $0.0 < P/P_b < 2.0$, $1.5 < L_s/H < 6.0$, $20 < f'_c$ (MPa) < 120 (with some gaps), $340 < f_y$ (MPa) < 520, $0.015 < \rho < 0.043$, $0.1 < s/d < 0.6$, and $0.002 < \rho_{sh} < 0.02$, where the parameters are defined in the notation list. All test specimens are columns with symmetric longitudinal reinforcement. The extended report on this study lists each experimental test used in this study, with the important design information for each test (Haselton et al. 2007f, Appendix B).

4.3 CALIBRATION PROCEDURE AND RESULTS

4.3.1 Calibration Overview

4.3.1.1 Idealization of Columns

In the OpenSees model, the cantilever columns are idealized using an elastic element and a zero-length plastic hinge at the base of the column. The plastic hinge has a relatively high pre-yield stiffness, and the stiffness of the elastic element is increased accordingly such that the full column assembly has the correct lateral stiffness. The properties of the plastic hinge are the subject of this calibration effort.

4.3.1.2 Calibration Procedure

The calibration of the beam-column element model to each experimental test was conducted in a systematic manner. Standardization of the process reduced possible errors and inconsistencies associated with the judgment present in the calibration.

As noted previously, the hinge model is based on the definition of a monotonic backbone and cyclic deterioration rules. In the calibration, we used cyclic tests with many cycles to calibrate both the monotonic backbone parameters (e.g. capping point, etc.) and the cyclic deterioration rules. As a result, the monotonic backbone and the cyclic deterioration rules are interdependent, and the approximation of the monotonic backbone depends on the cyclic deterioration rules assumed. This approximation of the monotonic backbone from cyclic data is not ideal. Rather, one would ideally like to have both monotonic and cyclic tests to large deformations, but these are not generally available.

Referring to Figure 4.2, each test was calibrated according to the following standardized procedure:

1. The test data are processed to have a consistent treatment of P-delta effects such that the element calibrations are not affected by differences in the experimental setups used by various researchers. Specifically, we transformed all the force-displacement data to be consistent with P-delta case #2 in the column database (Berry et al. 2004).
2. The yield shear force is estimated visually from the experimental results. In order to accurately calibrate the cyclic deterioration in step #6, it was necessary to calibrate the yield force separately for the positive and negative loading directions. Note that where the test data exhibited cyclic hardening, the yield shear force was slightly overestimated because cyclic hardening is not captured by Ibarra's element model.
3. The "yield" displacement is estimated as the point at which the rebar yields or the concrete begins to significantly crush, depending on the level of axial load. In either case, this yield displacement was calibrated to be the point at which there was a significant observed change in the lateral stiffness of the column. Calibration of this point often required some judgment, as the concrete becomes nonlinear well before rebar yielding, and some tests with many pre-yield cycles had significant stiffness changes in the pre-yield region.
4. Displacement at 40% of the yield force is calibrated to capture the near-initial stiffness. 40% of the yield load was chosen because we observed that the stiffness often changes significantly near this level. As in step #3, this was somewhat difficult (and subjective) for those tests that had many cycles before this level of load.
5. The strength increase from the yield point to the capping point is visually calibrated to estimate the post-yield stiffness.
6. The sixth step is to calibrate the normalized cyclic energy-dissipation capacity, λ. The element model allows cyclic deterioration coefficients λ and c (these are defined in the notation list) to be calibrated independently for each cyclic deterioration mode. However, based on a short study of 20 columns, we found that c = 1.0 was acceptable for

columns failing in flexure and flexure-shear modes.[2] We assumed the deterioration rates (λ) to be equal for the basic strength and post-capping strength deterioration modes (Ibarra 2003, Chapter 3). Based on observations of the hysteretic response of the RC columns, we set the accelerated stiffness deterioration mode to have zero deterioration. We also set the unloading stiffness deterioration mode to have zero deterioration.[3] These simplifications reduce the calibration of the cyclic energy-dissipation capacity to one value (λ). When calibrating λ, we aimed to match the average deterioration for the full displacement history, but with a slightly higher emphasis on matching the deterioration rate of the later, more damaging, cycles. Calibration of λ is based only on the cyclic deterioration before capping occurs, so the assumption of an equal post-capping strength deterioration rate has not been verified.

7. The final step of the calibration process involved quantification of the capping point (and associated plastic rotation capacity) and the post-capping deformation capacity. The calibration of the capping point is a critical component of the element model calibration procedure. The capping point and post-capping stiffness are included only when a clear negative post-failure stiffness is seen in the data, causing strength loss to occur *within a single* cycle (often called "in-cycle deterioration"). A negative slope is never used to represent strength deterioration that occurs *between two cycles* (often called "cyclic deterioration").

Often the test specimen did not undergo sufficient deformations for a capping point to be observed (i.e., no negative stiffness post-capping behavior was observed). In such cases, we can not quantify the capping point from the test, but the data do tell us that the capping point is at a displacement larger than those seen in the test. To incorporate this information for these types of tests, we calibrate a "lower-bound value" of the capping point.

In addition, when tests have many cycles and experience a severe drop in lateral load resistance on the second (or later) cycle at the same level of displacement, the tests are treated in the same manner. Again, in this case, we calibrate a lower-bound value for the capping point. This decision is motivated by the observation that earthquakes that can cause the collapse of

---

[2] For the columns failing in flexure, c = 1.2 is the ideal value. For those failing in flexure-shear, c = 1.0 is more appropriate. For simplicity and consistency, we used c = 1.0 for all columns.

[3] We excluded unloading stiffness deterioration when performing these calibrations because there is currently an error in the Opensees implementation of the model; this error causes incorrect cyclic responses when the unloading stiffness deterioration mode is employed. Even so, unloading stiffness deterioration is appropriate and should be used when modeling RC elements. The Drain-2D implementation of the element model does not have this error.

buildings typically do not have many large cycles before failure; instead, a few strong pulses and ratcheting of displacements will likely cause collapse. Therefore, for tests with many cycles, the failure mode observed in the test (e.g., from fatigue, etc.) may not be representative of the failure mode expected for real seismic building behavior. For these cases we chose to use the lower-bound approximation for capping points as shown in Figure 4.3.

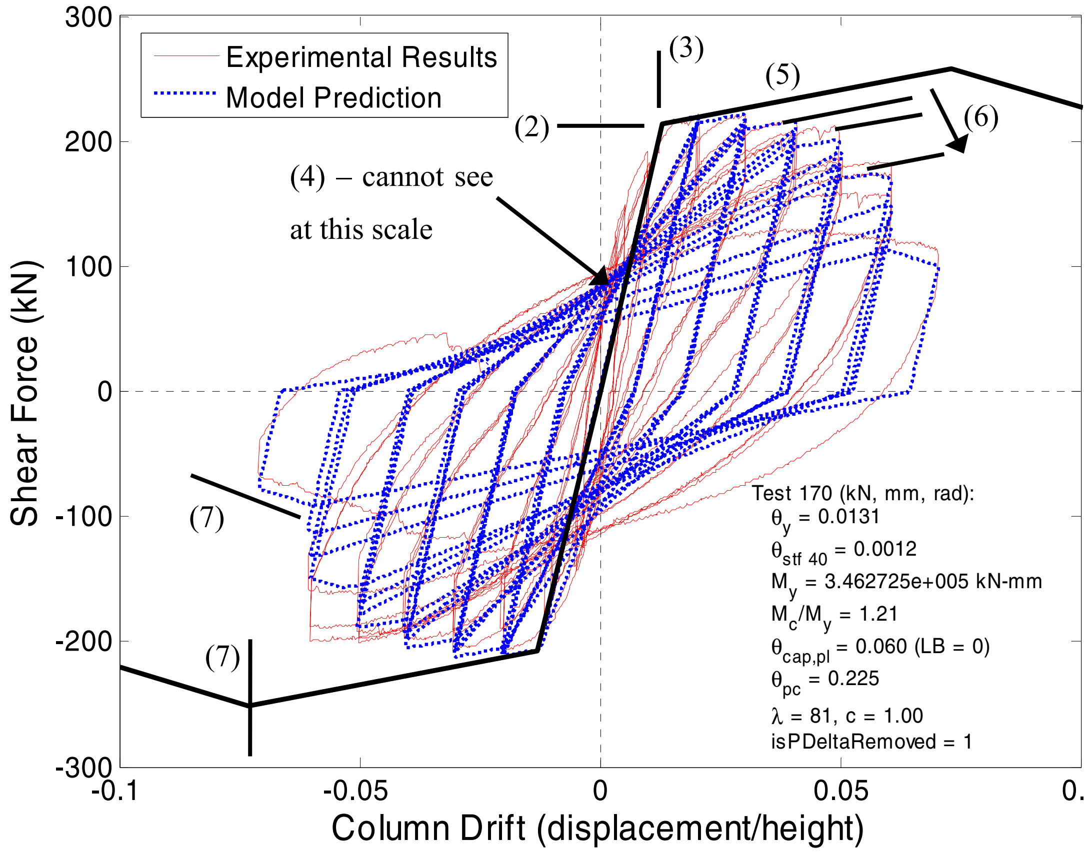

Fig. 4.2 Example of calibration procedure; calibration of RC beam-column model to experimental test by Saatcioglu and Grira (1999), specimen BG-6.

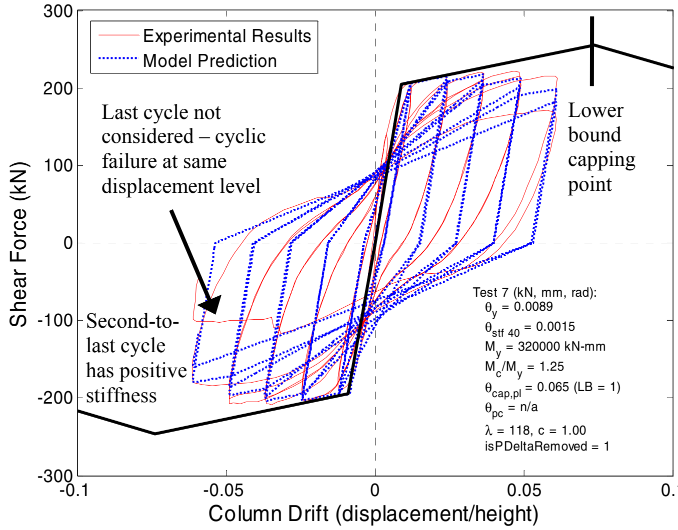

Fig. 4.3 Illustration of lower bound in calibration of capping point. Calibration of RC beam-column model to experimental test by Soesianawati et al. (1986), specimen 1.

A full table of calibrated model parameters for each of the 255 experimental test used in this study can be found in the extended report on this study (Haselton et al. 2007f, Appendix B).

4.3.1.3 Treatment of Pinching

Typically, pinching was not a dominant factor in the 220 tests with flexural failure. In the 35 flexure-shear tests, nine tests exhibited significant pinching behavior. Contrary to common expectation, Medina (2002, Chapter 7) shows that while element pinching behavior does increase the displacements of a building, it has little impact on the collapse behavior. We corroborated Medina's findings with some simple sensitivity studies of our won, and based on this, we chose to not simulate pinching effects in this study. The Ibarra element model does have the capability to represent pinching, so this could be easily incorporated in other calibration efforts where pinching phenomena have more importance.

4.3.1.4 Common Calibration Pitfalls: Incorrect Calibration of Strength Deterioration

Incorrect calibration of strength deterioration can have a significant impact on structural response prediction. To obtain meaningful structural analysis predictions, it is critical to clearly distinguish between in-cycle and cyclic strength deterioration and to correctly account for them in the way the structural model is created and calibrated. The two types of strength deterioration are explained in several references (Ibarra et al. 2005, 2003), but the simplest explanation is given in Chapter 4 of FEMA 440 (2005). The two types of strength deterioration are as follows:

In-cycle strength deterioration: In this mode, strength is lost in a single cycle, which means that the element exhibits a *negative stiffness*. This is the type of strength deterioration that is critical for modeling structural collapse (Ibarra et al. 2005, 2003).

Cyclic strength deterioration: In this mode, strength is lost between two subsequent cycles of deformation, but the *stiffness remains positive*. This type of strength deterioration has less effect on structural collapse (Ibarra et al. 2005, 2003, Chapter 5).

To investigate the significance of how strength deterioration is modeled, we calibrated the model to specimen BG-6 (Saatcioglu and Grira 1999) using both the correct method and two incorrect methods. We then completed collapse predictions for calibrated single-degree-of-freedom systems. A discussion of these three calibration methods is given as follows:

Calibration Method A (correct method): Figure 4.4a shows Saatcioglu and Grira (1999) test specimen BG-6 calibrated with the two modes of strength deterioration properly separated. In this test, we see cyclic strength deterioration in the cycles before 5% drift and in-cycle strength deterioration in the two cycles that exceed 5% drift.

Calibration Method B (incorrect; all in-cycle strength deterioration): Figure 4.4b shows the specimen calibrated incorrectly with all strength loss caused by in-cycle strength deterioration. This is a common calibration error. Often researchers create the "*backbone curve*" by connecting the peak displacements and degraded strengths after each set of cycles at a given level of displacement; this mixes cyclic and in-cycle deterioration. Notice that this method of calibration causes the negative failure slope to be reached at a lower drift level and leads to a steeper post-failure slope than in Figure 4.4a. This is *not* consistent with the *monotonic backbone curve* used in this paper. The backbone used in this paper reflects how the element would respond to a single monotonic push (including only in-cycle deterioration).

Calibration Method C (incorrect; all cyclic strength deterioration): Figure 4.4c shows the same test calibrated incorrectly with all strength loss caused by cyclic strength deterioration. In this case, the element never reaches a capping point and negative stiffness. This is also a common calibration error because many element models do not include a negative post-capping slope. As mentioned previously, this negative post-capping slope is of critical importance for collapse simulation. When an element is calibrated in this way, dynamic instability can occur only with a combination of P-delta and severe cyclic strength loss; however, this is not consistent with how most elements fail.

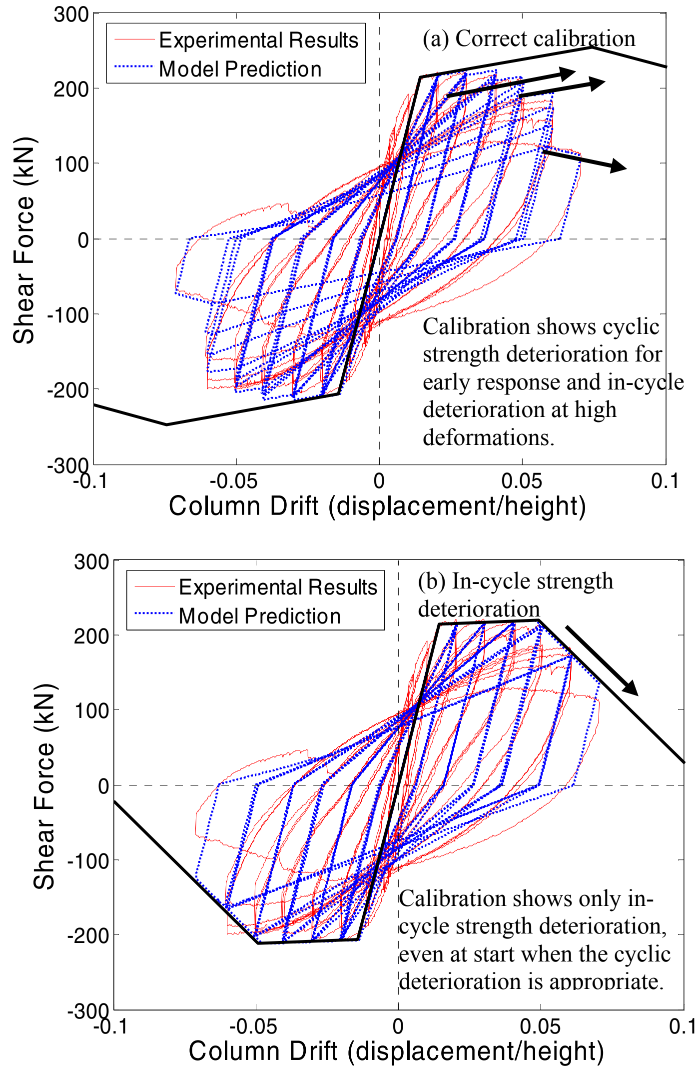

Fig. 4.4 Illustration of (a) correct calibration, (b) incorrect calibration using only in-cycle strength deterioration, and (c) incorrect calibration using only cyclic strength deterioration (Saatciolgu and Grira, specimen BG-6).

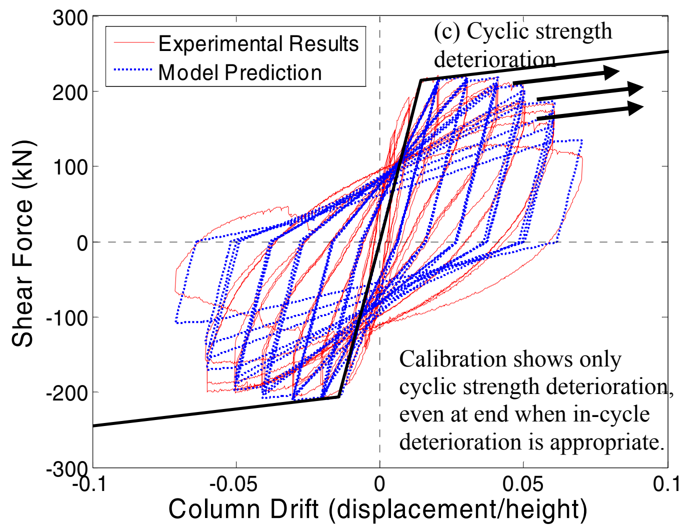

Fig.4.4—*Continued.*

Using the three calibrations from Figure 4.4, we created three single-degree-of-freedom (SDOF) models, each with an initial period of 1.0 sec, a yield spectral acceleration (at 1 sec) of 0.25g, a damping ratio of 5%, and a low axial load (less than 2% of the elastic critical load). We used a set of 20 ground motions developed for a 1.0 sec structure (Haselton and Baker 2006a) and performed incremental dynamic analysis (IDA) (Vamvatsikos and Cornell 2002a) to collapse.

Figure 4.5 shows the collapse capacity predictions for each of the three SDOF models; the collapse capacities are shown for each of the 20 earthquake records, creating an empirical distribution. The median collapse capacity for the correct calibration method (Method A) is 2.9g. If strength deterioration is incorrectly assumed to be all in-cycle (Method B), then the calculated median collapse capacity drops by 65% to 1.6g. If strength deterioration is incorrectly assumed to be all cyclic (Method C) the calculated median collapse capacity increases by 97% to 5.7g.

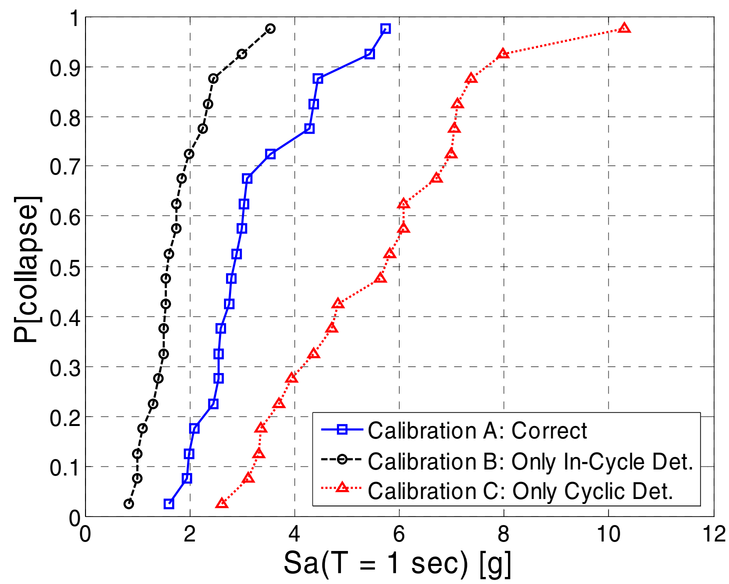

Fig. 4.5 Cumulative distribution of collapse capacity for three SDOF systems calibrated in Fig. 4.4.

This example demonstrates that properly modeling and calibrating the two types of strength deterioration is critical. Nonlinear dynamic analyses based on incorrect modeling/calibration methods will provide inaccurate results.

4.3.2 Interpretation of Calibration Results and Creation of Empirical Equations

The model parameter calibrations to the 255 columns were used to create empirical equations to calculate the element model parameters based on the column design parameters. A variety of analytical and graphical tools were used to interpret the calibration data and to assist in creation of these parametric equations.

The simplest method of visually searching for relationships between the calibrated parameters (e.g., initial stiffness, plastic rotation capacity, etc.) and the column design variables (e.g., axial load ratio, confinement ratio, etc.) is by plotting the parameters versus the design variables and looking for trends. The major limitation of this approach is that these plots, or "scatterplots," may obscure trends when multiple variables are changing between the different tests. As a result, the scatterplots show clear trends only when there are only a few dominant column design variables that affect the modeling parameter of interest. For example, Figure 4.6a demonstrates that a scatterplot between plastic rotation capacity ($\theta_{cap,\,pl}$) and confinement ratio

(ρ_{sh}) does not work well to associate the two variables, even though they are expected to be highly correlated.

To more clearly see how each column design variable affects the model parameters, we separated the data into test series in which only one design variable is changed between the various column tests. We were able to establish 96 distinct series of tests where only one column design parameter was varied[4]; Appendix A of the parent report (Haselton et al. 2007f) presents a complete list of these series.

To illustrate the usefulness of this separation, Figure 4.6b shows a series of tests in which the only parameter varied was the confinement ratio (ρ_{sh}). This figure shows the impact of a change in the value of ρ_{sh} on the plastic rotation capacity of an element, with all other design parameters held constant. Whereas the relationship between plastic rotation capacity and confinement ratio was murky in Figure 4.6a, Figure 4.6b shows a much clearer trend.

(a) (b)

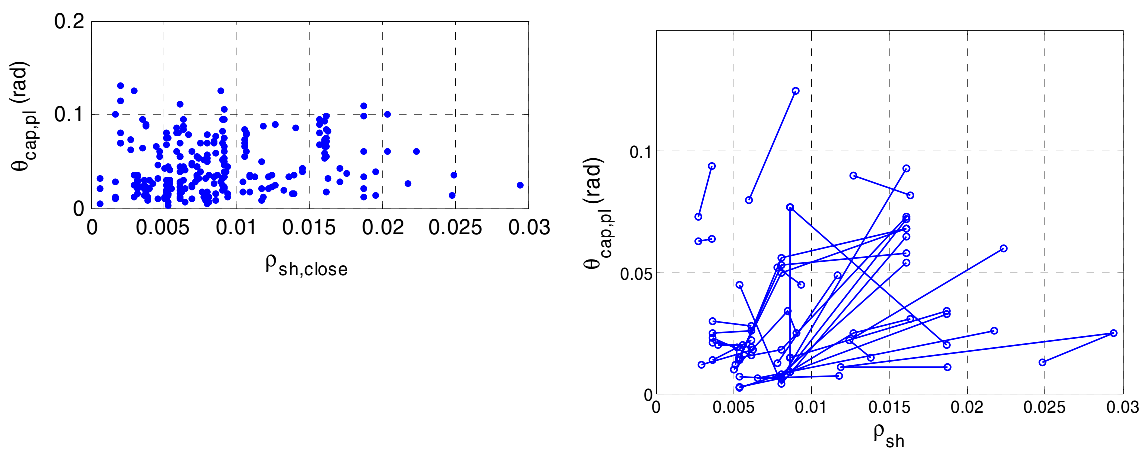

Fig. 4.6 (a) Scatterplot showing trends between $\theta_{cap,\,pl}$ and lateral confinement ratio (ρ_{sh}). Calibrated data shown for each test in data set. (b) Plot showing effects of ρ_{sh} on $\theta_{cap,\,pl}$. Each line connects dots corresponding to single test series in which ρ_{sh} (and stirrup spacing) was only variable changed. This includes only test data that are part of test series that varied ρ_{sh} (31 test series shown in figure).

[4] One exception is that the transverse reinforcement ratio and stirrup spacing are often changed together, so we do not attempt to separate these variables.

More detailed information about the relationship between plastic rotation capacity and confinement ratio can be obtained by looking at the rate of change of $\theta_{cap,pl}$ with ρ_{sh} for each test series, i.e. the slope of each line in Figure 4.6. This information is used to check the results of regression analyses and ensure that the final empirical equations are consistent with a close examination of the data.

The parent report on this study provides more details on how we dissected the data to create empirical regression equations for each parameter (Haselton et al. 2007f).

4.4 PROPOSED PREDICTIVE EQUATIONS

4.4.1 Regression Analysis Approach

4.4.1.1 Functional Form and Transformation of Data

An important challenge in creating the empirical parametric equations is determining a functional form that accurately represents how the individual predictors affect the calibrated parameters and interact with each other. To determine functional form, we incorporated (a) trends in the data and isolated effects of individual variables, as discussed in Section 4.3.2, (b) previous research and existing equations, and (c) judgment based on an understanding of mechanics and expected behavior. The process was often iterative, beginning with a simple equation and then improving the equation form based on the trends between the residuals (prediction errors) and the design parameters (predictors).

After establishing the basic functional form, we transformed the data to fit the functional form (typically using various natural logarithmic transformations) and then used standard linear regression analysis to determine the coefficients in the equation. We assumed that the underlying variability in model parameters (e.g., plastic rotation capacity, etc.) follow a lognormal distribution, so we always performed the regression on the natural log of the model parameter or (or the natural log of some transformed model parameter).[5] The logarithmic standard deviation was used to quantify the error.

We used the stepwise regression approach and included only variables that were statistically significant at the 95% level using a standard F-test. When creating the equations, we

---

[5] Exception: when creating equations for EI_y and EI_{stf40}, we do not use a natural log transformation because the form of the equation does not allow this transformation. Even so, we still report the errors using a lognormal distribution (i.e. we use σ_{LN} to quantify the error).

included all statistically significant variables. (For more details on this regression analysis approach; see Chatterjee et al. 2000.)

After arriving at detailed equations for each parameter, we then simplified many of the equations by removing some of the less influential variables, without sacrificing much prediction accuracy.

4.4.1.2 Treatment of Data without Observed Capping Point

Section 4.3.1.2 discussed how we calibrated the "lower-bound" deformation capacity for experimental tests in which the specimen was not pushed to large enough deformations to exhibit capping behavior (i.e., a negative stiffness). When creating the equations for deformation capacity, this "lower-bound" calibration data can be treated in several ways.

One possible approach is to use the maximum likelihood method to directly account for the fact that some of the data give a lower bound rather than an observed capping point, but still give us information that the true capping point is larger than the calibrated lower-bound value. A second possible approach is to neglect these lower-bound data in the creation of the equation. The third option in creating the equation is to use the lower-bound data in the regression analysis in the same way that we use the more reliable data with an observed capping point.

Due to time constraints, we did not use approach one in this study, but may revisit this in future research. We tried approach two and found that it leads to conservatively biased predictions for ductile elements because the data that exhibit capping are typically the less-ductile elements. Approach two also significantly reduces the amount of data available by eliminating lower-bound data points. We also used approach three and found that it causes the computed prediction uncertainty to be overpredicted due to the inclusion of the lower-bound data (which are more uncertain by nature). Based on these observations, we create the deformation-capacity equations based on all of the data (the third approach, which includes the lower-bound data) and report the prediction uncertainties based on only the data with an observed capping point (approach two). Note that this approach is still conservative for elements with high deformation capacity because the lower-bound data underestimate the actual deformation capacity.

4.4.1.3 Criteria for Removal of Data and Outliers

In the process of creating each predictive equation some data points were removed from the statistical analysis where the experimental data or the calibration results indicated behavior that was at odds with expected response, indicating a likely error in testing, data collection, or data processing. For example, data points were removed from the equation for initial stiffness because of possible errors in the transformation to account for P-Δ effects or when the baseline displacement at the beginning of the test was negative. In addition, some data were removed based on a statistical test to identify which points were outliers, as based on their residuals. To identify the outliers we used a t-test to statistically determine whether each residual had the same variance as the other residuals; outliers were removed when the t-test showed a 5% or lower significance level (Mathworks 2006). In most cases the number of outliers removed was fewer than 10, or approximately 4% of the total number of data points. For each of the equations developed in this study, we report prediction errors computed after removing the outliers.

4.4.2 Equations for Effective Stiffness

4.4.2.1 Literature Review

A great deal of previous research has been completed to determine the effective stiffness of reinforced concrete elements. This section outlines only four of the many studies and guidelines that exist.

The FEMA 356 guidelines (FEMA 2000a, Chapter 6) state that the "component stiffness shall be calculated considering shear, flexure, axial behavior and reinforcement slip deformations," and that generally the "component effective stiffness shall correspond to the secant value to the yield point of the component." Alternatively, for linear procedures, FEMA 356 permits the use of standard simplified values: $0.5E_cI_g$ when $P/(A_g f'_c) < 0.3$, and $0.7E_cI_g$ when $P/(A_g f'_c) > 0.5$. Section 4.4.2.3 will later show that the stiffness associated with the "secant value to the yield point of the component" is typically $0.2E_cI_g$, which is a factor of 2.5 times lower than the simplified recommendation of FEMA 356.

Mehanny (1999) utilized test results from 20 concrete columns and one reinforced concrete beam. From these data and a comprehensive review of previous research and design guidelines, he proposed an equation for the effective flexural stiffness and the effective shear stiffness of a column. The flexural stiffness is given by $EI_{eff} \big/ EI_{g,tr} = \left(0.4 + 2.4\left(P/P_b\right)\right) \leq 0.9$, where $I_{g,tr}$ is the gross transformed stiffness of the concrete section.

More recently, Elwood and Eberhard (2006) proposed an equation for effective stiffness that includes all components of deformation (flexure, shear, and bond-slip), where the effective stiffness is defined as the secant stiffness to the yield point of the component. Their equation proposes $0.2E_cI_g$ when $P/(A_g f'_c) < 0.2$, $0.7E_cI_g$ when $P/(A_g f'_c) > 0.5$, and a linear transition between these two extremes.

Panagiotakos and Fardis (2001) took a slightly different approach and quantified the deformation (chord rotation) at yielding instead of quantifying the stiffness. The Panagiotakos et al. equations are based on a database of more than 1000 experimental tests (mainly cyclic). The empirical equation developed contains three terms: (a) a flexural term based on the yield curvature of the member, (b) a constant shear term, and (c) a bond-slip term that is derived from integrating rebar strains into the support of the column. For low levels of axial load, their equations for yield deformation will typically result in a secant stiffness value of approximately $0.2E_cI_g$.

4.4.2.2 Equation Development

The definition of the stiffness of a reinforced concrete element depends on the load and deformation level one decides is representative of element response. Figure 4.7 shows a monotonic test of a reinforced concrete column (Ingham et al. 2001) with the yield force and displacement labeled. It is clear that the "effective stiffness" depends highly on the force level. In this work, we attempt to bound the possible values of effective stiffness and quantify the effective stiffness in two ways: (a) secant value of effective stiffness to the yield point of the component (i.e., K_y or EI_y) and (b) secant value of effective stiffness to 40% of the yield force of the component (i.e., K_{stf_40} or EI_{stf_40}). In these simplified equations for initial stiffness, we include all modes of deformation (flexure, shear, and bond-slip). For those interested in separating the modes of deformation, we discuss in Section 4.4.2.6 how to separate the flexural from the shear and bond-slip components of deformation.[6] With respect to functional form, we

---

[6] This separation is proposed for use with a fiber element model, where the flexural component of deformation is modeled by the fiber element, but the additional flexibilities from shear and bond-slip need to be accounted for by an additional spring in series.

are attempting to keep the equations for initial stiffness simple, so an additive functional form is used. Using this additive functional form implicitly assumes that the value of one column design variable does not change the impact of another design variable on the effective stiffness, i.e., there are no interactions between the effects of each design variable.

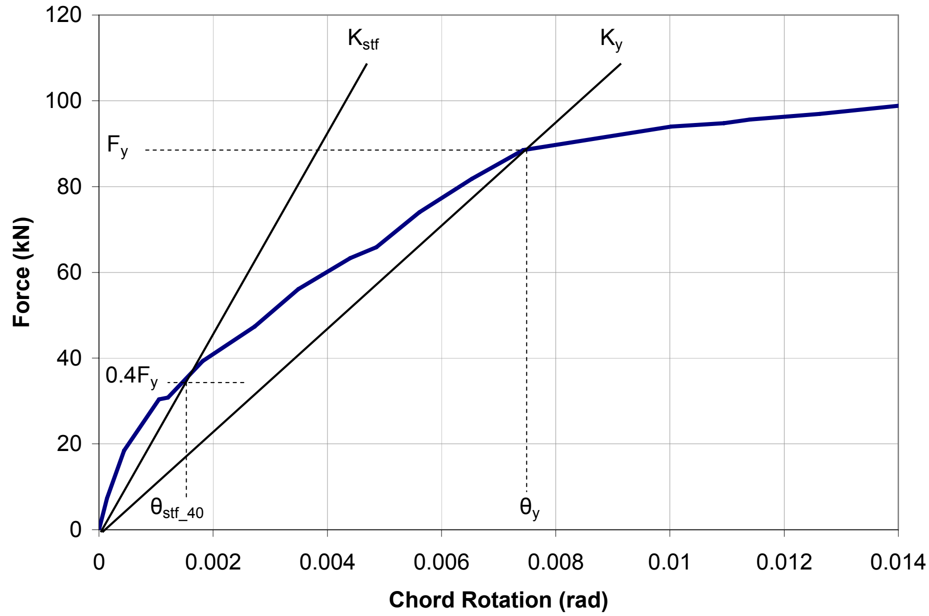

Fig. 4.7 Monotonic test of reinforced concrete element and illustration of definitions of effective stiffness.[7]

4.4.2.3 Equations for Secant Stiffness to Yielding

The full equation for secant stiffness to yield, including axial load ratio and shear span ratio is given as follows:

$$\frac{EI_y}{EI_g} = -0.07 + 0.59\left[\frac{P}{A_g f'_c}\right] + 0.07\left[\frac{L_s}{H}\right] \qquad 0.2 \le \frac{EI_y}{EI_g} \le 0.6 \tag{4.1}$$

This equation represents a mean value, with the prediction uncertainty quantified using a lognormal distribution with σ_{LN} = 0.28 (σ_{LN} is the logarithmic standard deviation). In addition, R^2 = 0.80 for this equation.

This equation shows that the axial load ratio ($P/A_g f'_c$) is important to stiffness prediction. The regression analysis also shows the significance of column aspect ratio (L_s/H) for predicting

[7] Data from Ingham et al 2001

stiffness, with more slender columns having a higher stiffness ratio. This occurs because bond-slip and shear deformations, which are included in the calibration, have proportionally less effect on slender member. We also tried a term involving the ratio of the shear demand at flexural yielding to the shear capacity (using either concrete shear capacity or the full element shear capacity); we found that L_s/H is a better predictor to account for how the level of shear demand affects element stiffness.

We imposed the lower limit on the stiffness because there are limited data for columns with low axial load. The lower limit of 0.2 is based on an (approximate) median stiffness for the tests in the database with $\nu < 0.10$. We imposed an upper limit on the stiffness because for high levels of axial load, the positive trend diminishes and the scatter in the data is large. We chose the upper limit of 0.6 based on a visual inspection of the data.

Table 4.1 illustrates the impact that each variable has on the prediction of initial stiffness. The first row of this table includes the stiffness prediction for a baseline column design, while the following rows show how changes in each design parameter impact the stiffness prediction.

Table 4.1 Effects of column design parameters on predicted values of EI_y/EI_g.

EI_y/EI_g		
parameter	**value**	**EI_y/EI_g**
Baseline	$\nu = 0.10$, $L_s/h = 3.5$	0.23
ν	0	0.20
	0.3	0.35
	0.8	0.60
L_s/h	2	0.20
	6	0.41

Equation 4.1 can be simplified to the following; this equation is useful when simplicity is desired over precision.

$$\frac{EI_y}{EI_g} = 0.065 + 1.05\left[\frac{P}{A_g f'_c}\right], \text{ where } 0.2 \le \frac{EI_y}{EI_g} \le 0.6 \tag{4.2}$$

This simplified equation comes at a cost of larger variability equal to $\sigma_{LN} = 0.36$, versus $\sigma_{LN} = 0.28$ for Equation 4.1. In addition, the $R^2 = 0.60$ instead of $R^2 = 0.80$.

4.4.2.4 Equations for Initial Stiffness

The effective initial stiffness defined by the secant stiffness to 40% of the yield force (see Fig. 4.7) is as follows.

$$\frac{EI_{stf\,40}}{EI_g} = -0.02 + 0.98\left[\frac{P}{A_g f'_c}\right] + 0.09\left[\frac{L_s}{H}\right], \text{ where } 0.35 \le \frac{EI_{stf}}{EI_g} \le 0.8 \tag{4.3}$$

where the prediction uncertainty is $\sigma_{LN} = 0.33$ and $R^2 = 0.59$.

Table 4.2 illustrates the impact that each variable has on the stiffness prediction. For a typical column, Equation 4.3 predicts the initial stiffness (as defined to 40% of yield) will be approximately 1.7 times stiffer than the secant stiffness to yield (Eq. 4.1).

Table 4.2 Effects of column design parameters on predicted values of EI_{stf}/EI_g.

EI_{stf}/EI_g		
parameter	**value**	**EI_{stf}/EI_g**
Baseline	v = 0.10, L_s/h = 3.5	0.39
v	0	0.30
	0.3	0.59
	0.8	0.80
L_s/h	2	0.35
	6	0.62

Equation 4.3 can be simplified to the following form by neglecting the effects of L_s/H:

$$\frac{EI_{stf\,40}}{EI_g} = 0.17 + 1.61\left[\frac{P}{A_g f'_c}\right], \text{ where } 0.35 \le \frac{EI_{stf}}{EI_g} \le 0.8 \tag{4.4}$$

This simplified equation comes at a cost of larger variability equal to $\sigma_{LN} = 0.38$, versus $\sigma_{LN} = 0.33$ for Equation 4.3. In addition, the $R^2 = 0.48$ instead of $R^2 = 0.59$.

4.4.2.5 Comparison of Proposed Equations with Previous Research

The equations proposed for EI_y are similar to one recently proposed by Elwood and Eberhard (2006). Our simplified equation for EI_y (Eq. 4.2) has the same form as the equation by Elwood et al. but gives slightly lower mean stiffness predictions. The variability in our Equation 4.2 of $\sigma_{LN} = 0.36$ is about the same value (coefficient of variation of 0.35) reported by Elwood et al.

Our full equation (Eq. 4.1, which includes L_s/H as an input parameter) has a lower prediction error of $\sigma_{LN} = 0.28$.

The stiffness predictions in FEMA 356 (FEMA 2000) are much higher than our predictions. Elwood and Eberhard (2006) show that most of this difference can be explained if it is assumed that the FEMA 356 values include only flexural deformation and do not account for significant bond-slip deformations

The equation proposed for deformation at yield by Panagiotakos and Fardis (2001) predicts $0.2E_cI_g$ for low levels of axial load, and their equation is less sensitive to axial load than the proposed equations. For high levels of axial load, the effective stiffness predicted by Pangiotakos and Fardis increases to approximately $0.4E_cI_g$ on average. Our equations predict $0.2E_cI_g$ for low levels of axial load transitioning to $0.6E_cI_g$ for high levels of axial load.

4.4.2.6 Fiber Element Modeling: Accounting for Shear and Bond-Slip Deformations

Commonly available fiber element models do not automatically account for bond-slip and shear deformations, so the analyst must determine the best way in account for these additional flexibilities. The purpose of this section is to provide recommendations on how to account for the additional flexibility due to bond-slip and shear when using a fiber element model.

To account for bond-slip and shear deformations when using a fiber-type element model, a common modeling technique is to add a rotational spring at the ends of each fiber element. This section explains how to create these springs, which are bilinear and have a stiffness change at 40% of the yield load.

Deformation at Yielding

At the yield point of the element, the deformation is composed of three components: flexure, bond-slip, and shear:

$$\theta_y = \theta_{y,f} + \theta_{y,b} + \theta_{y,s} \tag{4.5}$$

Using the following equation proposed by Panagiotakos and Fardis (2001), the flexural component can be calculation as:

$$\theta_{y,f(PF2001)} = \phi_{y(PF2001)} \left[\frac{L_s}{3} \right] \tag{4.6}$$

where the terms are defined in the notation list.

Using Equation 4.6, we computed the ratio of the observed yield deformation to the predicted flexural component of deformation, which resulted in the following statistics:

$$\left[\frac{\theta_y}{\theta_{y,f(PF2001)}}\right]\text{: Median = 1.96, Mean = 2.14, } \mu_{LN} = 0.59\text{, } \sigma_{LN} = 0.62 \qquad (4.7)$$

From these results the flexural deformation is approximately half of the total deformation at yield. The balance of the deformation is attributed to bond-slip and shear. Therefore, to determine the appropriate yield deformation for the rotational springs, we start with Equation 4.1 to determine the full flexibility of the element, and then compute the deformation at yielding by assuming the location of the inflection point. We can then use the statistics of Equation 4.7, which show that approximately ½ of the total yield deformation comes from bond-slip and shear.

Deformation at 40% of Yield Force

In addition to capturing the deformation at yielding, which results from bond-slip and shear, one may also want to accurately capture the nonlinearity in stiffness from zero load to the yield load. As mentioned previously, we assume that the stiffness is bilinear to yield, with a stiffness change at 40% of the yield load.

To approximate the relative contributions of flexure, bond-slip, and shear deformation at 40% of the yield load level, we must first make an assumption about how flexural stiffness changes as the load increases. At 40% of the yield load, the flexural stiffness will likely be higher than at yield, due to incomplete cracking and tension stiffening behavior. Even so, to keep these recommendations simple, we assume that the flexural stiffness is constant for all levels of loading. To be consistent with this assumption, when using the recommendations of this subsection for creating a fiber model, one should try to make the flexural stiffness of the fiber element constant over all load levels; this can be approximately done by excluding any additional stiffness from cracking or tension stiffening effects.

Using this assumption, we compute the ratio of total deformation to flexural deformation, at 40% of the yield force, according to the following statistics:

$$\left[\frac{\theta_{stf\_40}}{0.4*\theta_{y,f(PF2001)}}\right]\text{: Median = 0.99, Mean = 1.18, } \mu_{LN} = -0.032\text{, } \sigma_{LN} = 0.71 \qquad (4.8)$$

This shows that the contributions of bond-slip and shear deformations are relatively small at 40% of the yield load, such that assuming pre-cracked concrete accounts for virtually all of the deformation at this load level. This conclusion that bond-slip and shear deformations are small at 40% of yield load is consistent with the common understanding of element behavior and theoretical estimates of bond-slip deformation (Lowes et al. 2004). Therefore, when creating the bilinear spring that accounts for bond-slip and shear deformations, this spring should be almost rigid up to 40% of the yield load.

4.4.3 Chord Rotation at Yield

4.4.4 Flexural Strength

Panagiotakos and Fardis (2001) have published equations to predict flexural strength; therefore, we use their proposed method to determine model parameter M_y. Their method works well, so we made no attempt to improve upon it. When comparing our calibrated values to the flexural strength predictions by Panagiotakos and Fardis (2001), the mean ratio of M_y / $M_{y,Fardis}$ is 1.00, the median ratio is 1.03, and the coefficient of variation is 0.30 (σ_{LN} = 0.31).

Alternatively, a standard Whitney stress block approach, assuming plane sections remain plane and expected material strengths, may also be used to predict the flexural strength (M_y).

4.4.5 Plastic Rotation Capacity

4.4.5.1 Literature Review

Theoretical Approach Based on Curvature and Plastic-Hinge Length

Element rotation capacity is typically predicted based on a theoretical curvature capacity and an empirically derived plastic hinge length. It is also often expressed in terms of a ductility capacity (i.e., normalized by the yield rotation).

A summary of this approach to predict element rotation capacity can be found in many references (Panagiotakos and Fardis 2001; Lehman and Moehle 1998, Chapter 4; Paulay and Priestley 1992; and Park and Paulay 1975). Because the procedure is well documented elsewhere, only a brief summary is provided here.

This approach uses a concrete (or rebar) strain capacity to predict a curvature capacity, and then uses the plastic hinge length to obtain a rotation capacity. The material strain capacity must be estimated, typically associated with a limit state of core concrete crushing, stirrup fracture, rebar buckling, or low cycle fatigue of the rebar. Concrete strain capacity before stirrup fracture can be estimated using a relationship such as that proposed by Mander et al. (1988a,b); such predictions of concrete strain capacity are primarily based on the level of confinement of the concrete core. The material strain capacity is related to a curvature capacity through using a section fiber analysis. The curvature capacity can then be converted to a rotation capacity using an empirical expression for plastic hinge length. Lehman and Moehle (1998, Chapter 2) provide a review of expressions derived for predicting plastic hinge length.

Many researchers have concluded that this approach leads to an inaccurate, and often overly conservative, prediction of deformation capacity (Panagiotakos and Fardis 2001; Paulay and Priestley 1992). Paulay et al. (1992, page 141) explains that the most significant limitation of this method is that the theoretical curvature ends abruptly at the end of the element, while in reality the steel tensile strains (bond-slip) continue to a significant depth into the footing. Provided that the rebar are well anchored and do not pull out, this bond-slip becomes a significant component of the deformation and increases the deformation capacity. Panagiotakos and Fardis (2001) show that bond-slip accounts for over one-third of the plastic rotation capacity of an element.

Based on the preceding observations from past research, we have taken a more phenomenological approach to predicting plastic rotation capacity empirically from the test data.

Empirical Relationships for Rotation Capacity

A small number of researchers have developed empirical equations to predict rotation capacity based on experimental test data. Berry and Eberhard (Berry and Eberhard 2005; Berry and Eberhard 2003) used the PEER Structural Performance Database (Eberhard 2005; PEER 2006a) to create empirical equations that predict plastic rotation at the onset of two distinct damage states: spalling and rebar buckling. The equation for the plastic rotation capacity to the onset of rebar buckling for rectangular columns is as follows (Berry and Eberhard 2005):

$$\theta_{bb,tot} = 3.25\left(1+40\rho_{eff}\frac{d_b}{d}\right)\left(1-\frac{P}{A_g f'_c}\right)\left(1+\frac{L_s}{10d}\right) \tag{4.9}$$

where the variables are defined in the notation list.

For columns controlled by rebar buckling, the rebar buckling damage state should be closely related to the total rotation capacity ($\theta_{cap,tot}$) as defined in this study.

Fardis et al. (Fardis and Biskinis 2003; Panagiotakos and Fardis 2001) developed empirical relationships for ultimate rotation capacity based on a database of 1802 tests of RC elements. Of the 1802 tests, 727 are cyclic tests of rectangular columns with conforming details and which fail in a flexural mode. Fardis et al. developed equations to predict the chord rotation at “ultimate,” where “ultimate” is defined as a reduction in load resistance of at least 20%. Equations are provided for both monotonic and cyclic loading. The Fardis et al. equation for monotonic plastic rotation from yield to point of 20% strength loss (θu,mono,pl) is as follows:

$$\theta_{u,mono}{}^{pl} = \alpha_{st}{}^{pl}(1+0.55a_{sl})(1-0.4a_{wall})(0.2)^{\nu}\left(\frac{\max(0.01,\omega')}{\max(0.01,\omega)}f'_c\right)^{0.225}\left(\frac{L_s}{h}\right)^{0.375}25^{\left(\alpha\rho_{sh}\frac{f_{y,sh}}{f'_c}\right)}1.3^{100\rho_d} \tag{4.10}$$

More recently, Perus, Poljansek, and Fajfar (2006) developed a non-parametric empirical approach for predicting ultimate rotation capacity. Their study utilized test data from both the PEER and Fardis databases.

This past research provides an important point of comparison for the empirical plastic rotation capacity equation proposed in this work. However, their equations do not directly relate to the needs of our study, which is to determine the plastic rotation capacity ($\theta_{cap,pl}$) that can be directly used in the beam-column element model. While Berry et al. quantify the onset of the rebar buckling, their model does not provide a quantitative link to the associated degradation parameters ($\theta_{cap,pl}$ and θ_{pc}) needed in our model. Likewise, Fardis et al. provides explicit equations of the degraded plastic rotations (e.g., $\theta_{u,mono,pl}$), but $\theta_{cap,pl}$ must be inferred based on the ultimate rotation ($\theta_{u,mono,pl}$) and an assumed negative post-capping stiffness. The limitations of the work by Perus et al. (2006) is the same as that of Fardis et al.

Potential Predictors

Previous work (especially by Fardis et al.) in the development of empirical equations and observations from experimental tests were used to identify the most important column design parameters in the prediction of plastic rotation capacity. These parameters are listed below:

- Axial load ratio ($\nu = P/A_g f'_c$), lateral confinement ratio (ρ_{sh}): These are particularly important variables that are incorporated by Fardis et al. and also in the proposed equations. We considered using the ratio of axial load to the balanced axial load (P/P_b) in place of the axial load ratio ($\nu = P/A_g f'_c$). However, we concluded that the prediction improvement associated with using P/P_b did not warrant the additional complexity, so the basic axial load ratio is used.

- Bond-slip indicator variable (a_{sl}): Fardis et al. showed that bond-slip is responsible for approximately one-third of the ultimate deformation; and he uses an indicator variable to distinguish between tests where slip is (a_{sl} = 1) or is not (a_{sl} = 0) possible. We use the same variable in our proposed equation.
- Concrete strength (f'_c): Fardis et al. use a concrete strength term that causes the predicted deformation capacity to increase with increases in concrete strength (Panagiotakos and Fardis 2001). Our regression analysis revealed the opposite trend, so our proposed equation predicts a decrease in deformation capacity with an increase in concrete strength.
- Column aspect ratio (L_s/H): Fardis et al. found this term to be a statistically significant predictor. In our regression analyses, we consistently found this term to be statistically insignificant and chose to exclude it.
- Confinement effectiveness factor: Fardis et al. use a term for confinement effectiveness based on Paultre et al. (2001), $\rho_{sh,eff} = \rho_{sh} f_{y,sh} / f'_c$. In the regression analysis, we found this to be a slightly more statistically significant predictor than the transverse reinforcement ratio, but we decided to use ρ_{sh} for lateral confinement in the interest of simplicity.
- Rebar buckling terms: Dhakal and Maekawa (2002) investigated the post-yield buckling behavior of bare reinforcing bars and developed the rebar buckling coefficient: $s_n \left(s/d_b\right)\sqrt{\left(f_y/100\right)}$ where f_y is in MPa units. We found that this coefficient is a better predictor of element plastic rotation capacity than simple stirrup spacing, and we use it in our proposed equation. In another study, Xiao et al. (1998) found that columns with large diameter rebars have larger deformation capacity because the rebar buckling is delayed. In their test series, they kept the stirrup spacing constant, so their statement could be interpreted to mean that a larger deformation capacity can be obtained by either increasing d_b or decreasing s/d_b. We tried using both s/d_b and s_n, and found that s_n is a slightly better predictor, but s/d_b could have been without a significant change in the prediction accuracy.

4.4.5.2 Equation Development

We created the equation for plastic rotation capacity using standard linear regression analysis by transforming the data with log-transformations. We used a multiplicative form of the equation, which introduces interaction between the effects of the predictors. The resulting equation form is similar to that used by Fardis et al. (Fardis and Biskinis 2003; Panagiotakos and Fardis 2001).

As discussed previously, many of the column tests in the calibration study were not submitted to large enough deformations to observe a capping point. This presents challenges in developing the capping point equation. During the calibration process we labeled tests as lower bound LB = 0 or 1. LB = 0 refers to tests where a cap and negative stiffness was observed. When a cap was not observed in the data, we set LB = 1 and calibrated a lower-bound plastic rotation capacity (see Section 4.3.1.2).

While the lower-bound data only provide a lower-bound estimate of the capping rotation, we found it necessary to use all the data (i.e., LB = 0,1) because the LB = 0 data tended to include mostly columns with small rotation capacities. As a result, LB = 0 excludes most of the ductile column data from the regression and the resulting equation underestimates the rotation capacity for ductile columns. This trend is probably due to limitations of most experimental loading apparatus that could achieve the deformations required to reach the capping point in less ductile specimens but not in more ductile ones. Including all the data (LB = 0 and LB = 1) provides more accurate predictions for conforming elements but is still conservative for columns of high ductility (because of the use of lower-bound data for the most ductile columns).

4.4.5.3 Proposed Equations

The following equation is proposed for predicting plastic rotation capacity, including all variables that are statistically significant:

$$\theta_{cap,pl} = 0.12\left(1+0.55a_{sl}\right)\left(0.16\right)^{\nu}\left(0.02+40\rho_{sh}\right)^{0.43}\left(0.54\right)^{0.01c_{units}f'_c}\left(0.66\right)^{0.1s_n}\left(2.27\right)^{10.0\rho} \tag{4.11}$$

This equation represents a mean value, with the prediction uncertainty quantified using a lognormal distribution with σ_{LN} = 0.54 (σ_{LN} is the logarithmic standard deviation). In addition, R^2 = 0.60 for this equation. We checked the possibility of high correlation between ρ_{sh} and stirrup spacing, but we found that the correlation coefficient between ρ_{sh} and s_n is only -0.36 for the data set, which shows that colinearity is not a problem in this equation.

The impact of each of these input parameters on the predicted plastic rotation capacity predicted by Equation 4.11 is shown in Table 4.3. Within the range of column parameters considered in Table 4.3 the plastic rotation capacity can vary from 0.015 to 0.082. The table shows that the axial load ratio (ν) and confinement ratio (ρ_{sh}) have the largest effect on the predicted value of $\theta_{cap,pl}$. The concrete strength (f'_c), rebar buckling coefficient (s_n), and longitudinal reinforcement ratio (ρ) have less dominant effects, but are still statistically significant.

Table 4.3 Effects of column design parameters on predicted values of $\theta_{cap,pl}$, using proposed full equation.

$\theta_{cap,pl}$		
parameter	**value**	**$\theta_{cap,pl}$**
Baseline	ρ_{sh} = 0.0075, f'_c = 30 MPa, ν = 0.10, α_{sl} = 1, s_n = 12.7, ρ = 0.02	0.055
α_{sl}	0	0.035
ν	0	0.066
	0.3	0.038
	0.8	0.015
ρ_{sh}	0.002	0.033
	0.01	0.062
	0.02	0.082
f'_c *(MPa)*	20	0.058
	40	0.052
	80	0.040
s_n	8	0.067
	16	0.048
	20	0.040
ρ	0.01	0.050
	0.03	0.059

The shear span ratio (L_s/H) is notably absent from the equations developed. The stepwise regression process consistently showed L_s/H to be statistically insignificant. The relative unimportance of this predictor implies that the ductility capacity concept is not well-supported by these data. The flexural component of the yield chord rotation was also consistently shown to be statistically insignificant in prediction of plastic rotation capacity. These findings differ from the results from Panagiotakos and Fardis (2001).

Equation 4.11 can be simplified by excluding some statistically significant variables, with only minimally reducing the prediction accuracy.

$$\theta_{cap,pl} = 0.13\left(1+0.55a_{sl}\right)\left(0.13\right)^{v}\left(0.02+40\rho_{sh}\right)^{0.65}\left(0.57\right)^{0.01c_{units}f'_c} \quad (4.12)$$

This simplified equation comes at a cost of larger variability equal to $\sigma_{LN} = 0.61$, versus $\sigma_{LN} = 0.54$ for Equation 4.11. In addition, the $R^2 = 0.37$ instead of $R^2 = 0.60$.

4.4.5.4 Comparisons to Predictions by Fardis et al.

It is useful as verification to compare the predicted rotation capacity (Eq. 4.11) to the ultimate rotation capacity predicted by Fardis et al. as given by Equation 4.10 (Fardis and Biskinis 2003, Panagiotakos and Fardis 2001). Figure 4.8 compares these predictions and includes only the data that have an observed capping point.

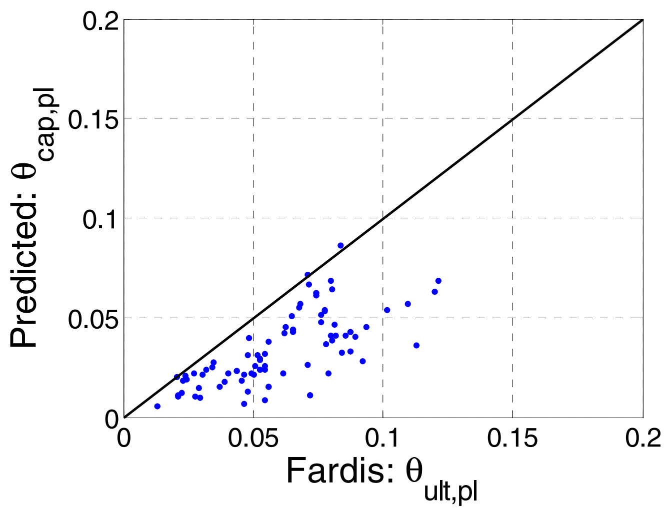

Fig. 4.8 Our prediction for plastic rotation capacity at capping point (Eq. 4.12) compared to Fardis prediction of ultimate rotation capacity (at 20% strength loss) (Eq. 4.10).

The Fardis et al. equation consistently predicts higher values, which is expected, since we are predicting the capping point and Fardis et al. the ultimate point (where the ultimate point is defined as the point of 20% strength loss[8]). The mean ratio of our prediction to the Fardis et al.

[8] For reference see Figure 4.1.

prediction is 0.56, and the median ratio is 0.53. These results are not directly comparable, so the ratio is expected to be less than 1.0.

To make a more consistent comparison between the predictions from Equation 4.12 and the equation from Fardis et al., we used their prediction of the ultimate rotation (at 20% strength loss) and use our calibrated value of post-capping slope (θ_{pc}) to back-calculate a prediction of $\theta_{cap,pl}$ from Equation 4.10. These results are plotted in Figure 4.9, which shows that the two predictions are closer, but the Fardis et al. prediction is still higher, on average, than ours. The mean ratio of our prediction to Fardis et al.'s prediction is 0.94, while the median ratio is 0.69. If the two equations were completely consistent, we would expect these ratios to be near 1.0, but our equation predicts slightly lower deformation capacities on average. There are several differences between these two equations that may cause this difference in prediction, but one primary reason is that our equation in based on data that include calibration of a lower-bound of deformation capacity (Section 4.4.1.2). From this comparison with Fardis' equation, we conclude that our equations are likely to still include some conservatism, even though Table 4.3 showed that the predicted deformation capacities are already much higher than what is typically used (e.g., values in FEMA 273/256 are typically less than ½ of those shown in Table 4.3).

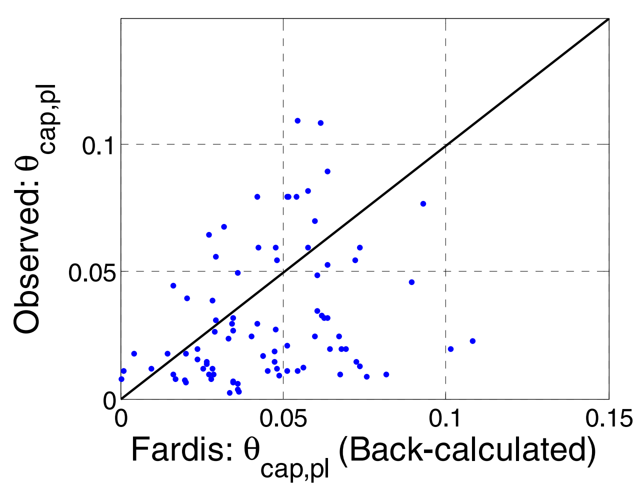

Fig. 4.9 Our prediction for plastic rotation capacity at capping point (Eq. 4.12) compared to back-calculated prediction of capping point using Fardis equation for ultimate rotation capacity (Eq. 4.10) and our calibrated post-capping stiffness (θ_{pc}) (presented in Eq. 4.17).

It is also possible to compare the prediction error obtained from our equation (Eq. 4.12), and the one developed by Fardis et al. (Eq. 4.10). Fardis et al. reports their prediction error in terms of coefficient of variation and the value ranges from 0.29–0.54 for various subsets of the data. The primary difference in the Fardis et al. level of prediction uncertainty is whether the element was subjected to monotonic or cyclic loading. Since our equation predicts a capping plastic rotation for monotonic loading, the fair comparison would be to use Fardis et al.'s reported error for monotonic loading, which is a coefficient of variation of 0.54. Our equation resulted in a prediction uncertainty of σ_{LN} = 0.54 (which is later reduced to σ_{LN} = 0.45 when we use total rotation instead of plastic rotation; see Eq. 4.14). The coefficient of variation and σ_{LN} are fundamentally different quantities, but should be numerically similar; comparison of these two values shows that the prediction uncertainty is surprisingly similar when considering that these equations are based on entirely different data sets.

4.4.5.5 Accounting for Effects of Unbalanced Reinforcement

The experimental data used in this study are limited to tests of columns with symmetrical arrangements of reinforcement. Therefore, Equation 4.12 applies only to columns with symmetric reinforcement. This is a significant limitation, as virtually all beams have asymmetric reinforcement that will affect the plastic rotation capacity. Typically, the rotation capacity is smallest when the element is loaded such that the side with more steel is in tension, which induces large compressive stresses and strains in the concrete and compression steel.

Fardis et al.'s data set did not have this limitation, so they developed a term that accounts for the effects of unbalanced reinforcement (Fardis and Biskinis 2003). To remove the balanced reinforcement limitation from Equation 4.11 or 4.12, we propose multiplying either of these equations by the term proposed by Fardis et al.; this term is given in Equation 4.13. This term accounts for the ratio between the areas of compressive and tensile steel, with normalization by the material strengths.

$$FardisTerm = \left(\frac{\max\left(0.01, \dfrac{\rho' f_y}{f_c'}\right)}{\max\left(0.01, \dfrac{\rho f_y}{f_c'}\right)} \right)^{0.225} \tag{4.13}$$

4.4.6 Total Rotation Capacity

Whereas Equation 4.11 predicts the inelastic portion of hinge rotation capacity, sometimes it is useful to have an equation to predict the total rotation capacity to the capping point, including both elastic and plastic components of deformation. Using similar logic to that used for developing Equation 4.11, the proposed equation for the total rotation capacity is as follows, including all variables that are statistically significant (note that the s_n term is not significant in this equation):

$$\theta_{cap,tot} = 0.12\left(1+0.4a_{sl}\right)\left(0.20\right)^{v}\left(0.02+40\rho_{sh}\right)^{0.52}\left(0.56\right)^{0.01c_{units}f'_c}\left(2.37\right)^{10.0\rho} \quad (4.14)$$

The prediction uncertainty of $\sigma_{LN} = 0.45$ is significantly smaller than the prediction uncertainty of $\sigma_{LN} = 0.54$ for the plastic rotation capacity (Eq. 4.11). This suggests that the total rotation capacity is a more stable parameter than the plastic rotation capacity; this likely comes from the significant uncertainty in the yield chord rotation, which is around $\sigma_{LN} = 0.36$ (Panagiotakos and Fardis 2001). Even so, the change in the R^2 value is counterintuitive and is 0.46 for total rotation and 0.60 for plastic rotation.

The impact of each of these parameters on the predicted total rotation capacity is shown in Table 4.4. Within the range of column parameters considered in Table 4.4, the total rotation capacity can vary from 0.024 to 0.129. The table shows that the axial load ratio (ν) and confinement ratio (ρ_{sh}) have the largest effects on the predicted value of $\theta_{cap,tot}$. The concrete strength (f'_c) and longitudinal reinforcement ratio (ρ) have less dominant effects, but are still statistically significant.

Table 4.4 Effects of column design parameters on predicted values of $\theta_{cap,tot}$.

$\theta_{cap,tot}$		
parameter	**value**	$\theta_{cap,tot}$
Baseline	ρ_{sh} = 0.0075, f'_c = 30 MPa, v = 0.10, α_{sl} = 1, ρ = 0.02	0.079
α_{sl}	0	0.056
v	0	0.093
	0.3	0.057
	0.8	0.026
ρ_{sh}	0.002	0.043
	0.01	0.091
	0.02	0.129
f'_c *(MPa)*	20	0.084
	40	0.075
	80	0.059
ρ	0.01	0.072
	0.03	0.086

Equation 4.15 presents the simplified equation where some statistically significant variables were excluded from this equation to make the equations simpler and easier to use, and removing these variables caused no observable reduction in the prediction accuracy.

$$\theta_{cap,tot} = 0.14\left(1+0.4a_{sl}\right)\left(0.19\right)^{v}\left(0.02+40\rho_{sh}\right)^{0.54}\left(0.62\right)^{0.01c_{units}f'_c} \tag{4.15}$$

This simplified equation comes at a cost of only slightly larger variability equal to σ_{LN} = 0.46, versus σ_{LN} = 0.45 for Equation 4.14. In addition, the R^2 = 0.42 instead of R^2 = 0.46.

4.4.6.1 Accounting for Effects of Unbalanced Reinforcement

Similarly to the adjustment for the plastic rotation capacity, Equation 4.16 presents a correction factor that can be multiplied by Equations 4.14 and 4.15 to approximately capture the effects of unbalanced longitudinal reinforcement. This correction factor is based on work by Fardis et al. (Fardis and Biskinis 2003); note that the exponent in the correction term is different for Equations 4.16 (total rotation) and 4.13 (plastic rotation).

$$FardisTerm = \left(\frac{\max\left(0.01, \frac{\rho' f_y}{f_c'}\right)}{\max\left(0.01, \frac{\rho f_y}{f_c'}\right)} \right)^{0.175} \tag{4.16}$$

4.4.7 Post-Capping Rotation Capacity

Previous research on predicting post-capping rotation capacity has been limited despite its important impact on predicted collapse capacity. The key parameters considered in the development of an equation for post-capping response are those that are known to most affect deformation capacity: axial load ratio (ν), transverse steel ratio (ρ_{sh}), rebar buckling coefficient (s_n), stirrup spacing, and longitudinal steel ratio. The equation is based on only those tests where a post-capping slope was observed, denoted LB = 0.

The proposed equation for post-capping rotation capacity is as follows, where the prediction uncertainty is $\sigma_{LN} = 0.72$ and $R^2 = 0.51$.

$$\theta_{pc} = (0.76)(0.031)^{\nu}(0.02 + 40\rho_{sh})^{1.02} \leq 0.10 \tag{4.17}$$

This equation reflects the fact that stepwise regression analysis identified the axial load ratio and transverse steel ratio as the two statistically significant parameters. Note that we do not propose a simplified equation to predict post-capping rotation capacity.

The upper bound imposed on Equation 4.17 is judgmentally imposed due to lack of reliable data for elements with shallow post-capping slopes. We found that test specimens with calibrated $\theta_{pc} > 0.10$ (i.e., very shallow post-capping slopes) typically were not tested deformation levels high enough to exhibit significant in-cycle degradation. This makes the accuracy of the calibrated value of θ_{pc} suspect because the post-capping slope may become increasingly negative as the column strength degrades toward zero resistance. To determine the appropriate limit, we looked at all data that had well-defined post-capping slopes that ended near zero resistance (approximately 15 tests); the limit of 0.10 is based on an approximate upper bound from these data. Using this approach, this 0.10 limit may be conservative for well-confined, "conforming" elements with low axial load. However, the test data are simply not available to justify using a larger value.

The range of θ_{pc} expected for columns with different parameters is demonstrated in Table 4.5, where both ν and ρ_{sh} are observed to significantly affect the predicted value of θ_{pc}. For the range of axial load and transverse steel ratios considered, θ_{pc} varies between 0.015 and 0.10.

Table 4.5 Effects of column design parameters on predicted values of θ_{pc}.

θ_{pc}		
parameter	**value**	**θ_{pc}**
Baseline	ρ_{sh} = 0.0075, ν = 0.10	0.100
ν	0	0.100
	0.3	0.084
	0.8	0.015
ρ_{sh}	0.002	0.051
	0.01	0.100
	0.02	0.100

4.4.8 Post-Yield Hardening Stiffness

Post-yield hardening stiffness is described by the ratio of the maximum moment capacity and the yield moment capacity (M_c/M_y). There is limited literature on this topic, though Park et al. (1972) found that the hardening ratio depended on the axial load and tensile reinforcement ratios. In developing an equation for post-yield hardening stiffness, we investigated the same key predictors as in the previous equations.

Regression analysis shows that the axial load ratio and concrete strength are the key factors in determining hardening stiffness (M_c/M_y). Using these predictors M_c/M_y may be given by the following.

$$M_c / M_y = (1.25)(0.89)^{\nu}(0.91)^{0.01 c_{units} f'_c} \tag{4.18}$$

where the prediction uncertainty is σ_{LN} = 0.10.

Table 4.6 shows the effect of concrete strength and the axial load ratio on the predicted value of M_c/M_y. For a typical column with a concrete strength of 30 MPa and an axial load ratio of 0.10 M_c/M_y is predicted to be 1.20. For columns within a typical range of f'_c and *ν,* M_c/M_y varies between 1.11 and 1.22.

Table 4.6 Effects of column design parameters on predicted values of M_c/M_y.

M_c/M_y		
parameter	**value**	**M_c / M_y**
Baseline	f'_c = 30 MPa, v = 0.10	1.20
f'_c (MPa)	20 40 80	1.21 1.19 1.15
v	0 0.3 0.8	1.22 1.17 1.11

For applications where simplicity is desired over precision, a constant value of M_c/M_y = 1.13 can be used while still maintaining a prediction uncertainty of σ_{LN} = 0.10.

4.4.9 Cyclic Strength and Stiffness Deterioration

Cyclic energy-dissipation capacity has been a topic of past research, but most of this was primarily focused on the use of damage indices for predicting damage states and accumulation of damage in a post-processing mode. This is similar to, but not the same as, the goal of this study, which is to determine an energy-dissipation capacity that can be used as an index to deteriorate the strength and stiffness of the hinge model during nonlinear analysis. Therefore, past work on damage indices is of limited value to the present discussion and is not reviewed here.

In a state-of-the-art review focused on reinforced concrete frames under earthquake loading and of relevance here, the Comité Euro-International du Béton (1996) noted that cyclic degradation was most closely related to both the axial load level and the degree of confinement of the concrete core. They note that the cyclic energy-dissipation capacity decreases with increasing axial load and decreasing confinement.

As described previously, Ibarra's hysteretic model captures four modes of cyclic deterioration: basic strength deterioration, post-cap strength deterioration, unloading stiffness deterioration, and accelerated reloading stiffness deterioration. Each mode is defined by two parameters, normalized energy-dissipation capacity (λ), and an exponent term (c) to describe the rate of cyclic deterioration changes with accumulation of damage. To reduce complexity, we use simplifying assumptions to consolidate the cyclic deterioration parameters from eight to two (as per Ibarra 2003): λ and c. Calibration of λ is the topic of this section and c, the exponent, is set to 1.0 in all cases.

As before, we used regression analysis to determine which parameters were the best predictors for cyclic energy-dissipation capacity. For quantifying confinement effects, the ratio of stirrup spacing to column depth (s/d) was found to be a better predictor of deterioration than transverse steel ratio (ρ_{sh}). Based on the observed trends in the data, the following equation is proposed for the mean energy-dissipation capacity, including all statistically significant predictors.

$$\lambda = (127.2)(0.19)^{v}(0.24)^{s/d}(0.595)^{V_p/V_n}(4.25)^{\rho_{sh,eff}} \tag{4.19}$$

where the prediction uncertainty is $\sigma_{LN} = 0.49$ and $R^2 = 0.51$.

Table 4.7 shows the range of λ predicted by Equation 4.19 in a typical conforming column. There is a large variation in λ depending on the axial load ratio and tie spacing. As expected, increasing the axial load ratio can significantly decrease the cyclic energy-dissipation capacity. Likewise, increasing tie spacing (decreasing confinement) also decreases the cyclic energy-dissipation capacity.

Table 4.7 Effects of column design parameters on predicted values of λ.

λ		
parameter	**value**	**λ**
Baseline	$v = 0.1$, $s/d = 0.2$, $V_p/V_n = 0.5$, and $\rho_{sh,eff} = 0.1$	72
v	0 0.3 0.8	85 52 23
s/d	0.1 0.4 0.6	83 54 41
V_p/V_n	0.2 0.8 1.5	84 62 43
$\rho_{sh,eff}$	0.01 0.10 0.20	63 72 83

Equation 4.19 can be simplified without greatly reducing the prediction accuracy. This simpler equation follows and has virtually the same prediction accuracy.

$$\lambda = (170.7)(0.27)^{\nu}(0.10)^{s/d} \tag{4.20}$$

This simplified equation has virtually the same prediction uncertainty of $\sigma_{LN} = 0.50$, versus $\sigma_{LN} = 0.49$ for Equation 4.19. In addition, the $R^2 = 0.44$ instead of $R^2 = 0.51$.

4.5 SUMMARY AND FUTURE RESEARCH DIRECTIONS

4.5.1 Summary of Equations Developed

The purpose of this research is to create a comprehensive set of equations which can be used to predict the model parameters of a lumped plasticity element model for a reinforced concrete beam-column, based on the properties of the column. The equations were developed for use with the element model developed by Ibarra et al. (2003, 2005), and can be used to model cyclic and in-cycle strength and stiffness degradation to track element behavior to the point of structural collapse. Even though we use the Ibarra et al. model in this study, the equations presented in this chapter are general (with the exception that cyclic deterioration must be based on an energy index) and can be used with most lumped plasticity models that are used in research.

Empirical predictive equations are presented for element secant stiffness to yield (Eqs. 4.1 and 4.2), initial stiffness (Eqs. 4.3 and 4.4), plastic rotation capacity (Eqs. 4.11–4.13), total rotation capacity (elastic + plastic) (Eqs. 4.14–4.16), post-capping rotation capacity (Eq. 4.17), hardening stiffness ratio (Eq. 4.18) and cyclic deterioration capacity (Eq. 4.19). The predictive equations are based on a variety of parameters representing the important characteristics of the column to be modeled. These include the axial load ratio (ν), shear span ratio (L_s/H), lateral confinement ratio (ρ_{sh}), concrete strength (f'_c), rebar buckling coefficient (s_n), longitudinal reinforcement ratio (ρ), ratio of transverse tie spacing to column depth (s/d), and ratio of shear at flexural yielding to shear strength (V_p/V_n).

The prediction error associated with each equation is also quantified and reported. These provide an indication of the uncertainty in prediction of model parameters, and can be used in sensitivity analyses or propagation of structural modeling uncertainties. Table 4.8 summarizes the prediction error and bias for each full equation. This table presents the median and mean ratios of predicted/observed parameters, as well as the uncertainty in prediction (quantified by the logarithmic standard deviation). These values are based on the full set of data. In addition, the plastic rotation capacity equation is assessed using several subsets of the data to ensure that the predictions are not biased for any of the particularly important cases.

The correlations between the prediction errors are also important when using these predictive equations to quantify the effects of structural modeling uncertainties. We did not look at these correlations in this study but plan to do so in continued research.

Table 4.8 Summary of accuracy of predictive equations proposed in chapter.

Predictive Equation	Median (predicted/ observed)	Mean (predicted/ observed)	σ_{LN}
EI_y/EI_g (Equation 4.1)	1.05	1.23	0.28
EI_{stf40}/EI_g (Equation 4.3)	0.98	1.52	0.33
$M_{y,Fardis}$ (section 4.5.4)	1.03	1.00	0.30
$\theta_{cap,pl}$ (Equation 4.11) (all data)	0.99	1.18	0.54
Conforming confinement (ρ_{sh} > 0.006, n = 30):	1.14	1.23	0.46
Non-conforming confinement (ρ_{sh} < 0.003, n = 9):	0.99	1.16	0.63
High axial load (v > 0.65, n = 11):	0.92	0.97	0.59
$\theta_{cap,tot}$ (Equation 4.14)	0.98	1.07	0.45
θ_{pc} (Equation 4.17)	1.00	1.20	0.72
M_c/M_y (Equation 4.18)	0.97	1.01	0.10
λ (cyclic deterioration) (Equation 4.19)	1.01	1.25	0.49

The regression analyses were completed in such a way that the prediction error is assumed to be lognormally distributed, so the median ratio of predicted/observed should be close to 1.0. Table 4.8 shows that when using all the data, this ratio ranges from 0.97–1.05, showing that the predictive equations do not have much bias.

When we look more closely at the prediction of plastic rotation capacity ($\theta_{cap,pl}$) for subsets of the data, we see that the prediction is unbaised for non-conforming elements (ρ_{sh} < 0.003). The equation overpredicts the plastic rotation capacity by approximatley 14% for conforming elements (ρ_{sh} > 0.006) and underpredicts the plastic rotation capacity by approximatley 8% for elements with extremely high axial load (v > 0.65). Considering the large uncertainty in the prediction of plastic rotation capacity, and the small number of datapoints in some of the subsets, these relatively computed biases seem reasonable.

Table 4.8 also shows that the prediction uncertainty is large for many of the important parameters. For example, the prediction uncertainty for deformation capacity ranges from σ_{LN} =

0.45 for total deformation to σ_{LN} = 0.54 for plastic deformation. Previous research has shown that these large uncertainties in element deformation capacity cause similarly large uncertainties in collapse capacity (Ibarra 2003; Goulet et al. 2006a; Haselton et al. 2007e).

4.5.2 Limitations

The predictive empirical equations developed here provide a critical linkage between column design parameters and element modeling parameters, facilitating the creation of nonlinear analysis models for RC structures needed for performance-based earthquake engineering. The limitations of these equations, in terms of scope and applicability, are discussed in this section.

4.5.2.1 Availability of Experimental Data

The equations developed here are based on a comprehensive database assembled by Berry et al. (Berry et al. 2004; PEER 2006a). Even so, the range of column parameters included in the database is limited, which may likewise limit the applicability of the derived equations. Section 4.2.3 discusses the ranges of column parameters included in this calibration study. The primary limitation of the data set is that it includes only columns with symmetric reinforcement, however, this was overcome by using Equations 4.13 and 4.16.

The equations are also limited more generally by the number of test specimens available that have an observed capping point. Data with clearly observable negative post-capping stiffnesses are severely limited. For model calibration and understanding of element behavior, it is important that future testing continue to deformation levels large enough to clearly show the negative post-capping stiffnesses. With additional data, it may be possible to reduce the prediction uncertainties. Section 4.5.3 also discusses the need for this further test data.

We are further limited by the fact that virtually all of the available test data have a cyclic loading protocol with many cycles and 2–3 cycles per deformation level. This type of loading may not be representative of the type of earthquake loading that may cause structural collapse, which would generally contain only a few large displacement cycles before collapse occurs. This is problematic because we use the cyclic data to calibrate both the monotonic backbone and cyclic deterioration behavior of the element (Section 4.3.1.2). More test series are needed that subject identical columns to multiple types of loading protocols. This will allow independent calibration of the monotonic backbone and cyclic deterioration behavior, and will also help verify that the element model cyclic behavior is appropriate. For example, data from a monotonic push can be used to calibrate the monotonic backbone of the element. Cyclic tests, using multiple loading protocols, can then both (a) illustrate cyclic deterioration behavior and its variation with loading protocol and (b) show how the backbone should migrate as damage progresses.

Ingham et al. (2001) completed a test series as described above. This series provides useful data on the monotonic backbone curve and shows how cyclic behavior varies with loading protocol. The important limitation of the Ingham test series is that the tests were not continued to deformations levels large enough to show negative post-capping stiffness of the element. For future testing with the purpose of calibrating element models, we suggests a test series similar to that used by Ingham, possibly with fewer cycles in the loading protocols to better represent expected seismic loading that may cause structural collapse, but the tests should be continued to deformations large enough to clearly show negative post-capping stiffness.

In addition to the above issue, we should also remember that the empirical equations proposed in this paper are all based on laboratory test data where the test specimen was constructed in a controlled environment and thus have a high quality of construction. Actual buildings are constructed in a less controlled environment, so we expect the elements of actual buildings to have a lower level of performance than that predicted using the equations of this paper. This paper does not attempt to quantify this difference in performance coming from construction quality, but this may be a useful topic to consider in future work.

4.5.3 Future Research

4.5.3.1 Suggestions for Future Experimental Tests

From our experiences calibrating the element model to 255 column tests, our wish list for future experimental tests includes both more tests and different types of tests. The following general suggestions can be made:

Monotonic tests are needed in addition to cyclic tests, both for identical test specimens when possible. In this study we used cyclic tests with many cycles to calibrate both the monotonic backbone and the cyclic deterioration rules. As a result, the monotonic backbone and the cyclic deterioration rules are interdependent, and the approximation of the monotonic backbone depends on cyclic deterioration rules assumed. Ideally, we would have enough test data to separate these effects.

Tests should be conducted with a variety of cyclic loading histories. This will lead to a better understanding of how load history affects cyclic behavior, and provide a basis for better development/calibration of the element model cyclic rules. Section 4.5.2.1 discusses this point in more detail. Ideally, for the purpose of calibrating element models to simulate structural collapse, loading histories should be more representative of the type of earthquake loading that causes structural collapse. Tests with loading protocols including too many cycles can cause failure modes that are unlikely to occur in a seismic event. Even so, these loading protocols may still be appropriate for studies focused on structural damage and losses because response at lower levels of shaking (which will have more cycles of motion) is important.

For predicting collapse, tests should be conducted at large enough deformations for capping and post-capping behavior to be clearly observed. Most current test data do not continue to large enough deformations; this is a serious limitation in the available data and makes it difficult to accurately predict the capping point. Due to this limitation in test data, we were forced to make conservative assumptions when predicting the capping point in this work; better data would allow this conservatism to be removed from our predictions. In addition, there is virtually no data that show post-peak cyclic deterioration behavior.

The proposal of a loading protocol suitable for calibrating element material model for collapse is outside the scope of this research. Interested readers should investigate the loading protocols developed for testing of steel components (e.g., ATC 1992).

4.5.3.2 Consensus and Codification[9]

The outcome of this study, empirical equations to predict element model parameters for RC beam-columns based on column design parameters, is an important contribution to wider research efforts aiming to provide systematic collapse assessment of structures. Research by the PEER Center and others is progressing close to the goal of directly modeling the sidesway structural collapse of some types of structural systems through use of nonlinear dynamic simulation. However, the collapse assessment process sometimes requires considerable

[9] Readers are referred to Haselton and Deierlein, 2006, *Toward the Codification of Modeling Provisions for Simulating Structural Collapse*, which provides the basis for the remarks in this section.

interpretation and engineering judgment. As a result, it is critical for the required models and methods to be put through a consensus and codification process — as has long been the tradition in building code development. This consensus process will allow a larger group of researchers and engineering professionals to review the research development, assumptions, and judgment that provide the basis for the newly proposed collapse assessment methods.

We propose that such a consensus and codification process be started to develop consensus guidelines that explain proper procedures for directly simulating sidesway collapse. These procedures would include guidance on all important aspects of the collapse assessment process, including treatment of failure modes, element-level modeling, system-level modeling, numerical issues for nonlinear dynamic analyses, treatment of structural modeling uncertainties, etc.

These codified models and guidelines for collapse assessment will give engineers the basis for directly predicting structural collapse based on realistic element models. In addition, the existence of such models will provide a foundation for advancing simplified performance-based design provisions (e.g., a codified equation predicting plastic rotation capacity from element properties could be used to make detailing requirements more flexible, allowing the engineer to design the element based on a target plastic rotation capacity).

5 Effects of Structural Design and Modeling Uncertainties on Uncertainty in Collapse Capacity

5.1 INTRODUCTION AND PURPOSE OF CHAPTER

The characterization and propagation of uncertainty is at the heart of robust performance-based earthquake engineering assessment and design. Seismic performance assessment should quantify the building performance probabilistically, accurately quantifying the mean and variability of building response parameters such as peak interstory drift ratio, peak floor acceleration, element plastic rotation, and global or local collapse. This probabilistic description of response is needed in order to estimate probabilities of "failure" (i.e., reaching or exceeding some predefined limit state). In addition, once we have a distribution of response, we can combine the response information with the site hazard to obtain yearly rates of exceedance of performance metrics and limit states of interest. We apply this probabilistic approach in this chapter to assess the collapse performance of the 4-story RC SMF building considered previously in Chapter 2 of this report (specifically, Design A from Chapter 2). In completing this probabilistic collapse performance assessment, this chapter illustrates the important impacts that structural modeling uncertainties have in the collapse assessment.

This probabilistic approach is starkly different than approaches currently used in engineering practice, even when advanced nonlinear dynamic time history analyses are employed. For example, the most advanced nonlinear dynamic procedure (FEMA 2000a) requires the use of only three to seven earthquake ground motions scaled to a single design hazard level, and considers only the mean response (or maximum response when less than seven motions are used). This approach neglects the variability in response due to record-to-record variations, the variability in the structural modeling, and the variability in the limit state criteria (FEMA 2000a). The method used in this study is quite different, as it uses between 10–30 earthquake ground motions, scales the ground motions to seven different hazard levels, and estimates both the mean and the variability in response due to the variability between different earthquake ground motions. In addition to accounting for effects of record-to-record variability, uncertainty in the structural model is recognized and accounted for to achieve a probabilistic estimate of structural response that is as complete as practically possible. The method to account for the effects of the uncertainty in the structural design and structural modeling is the subject of this chapter.

It should be noted that there is good reason that current engineering practice uses a more simplified method; the more complete probabilistic method is extremely time consuming and computationally expensive. In creating a mathematical structural model and trying to quantify all of the uncertainty that is inherent in the model, it quickly becomes apparent that there are numerous uncertainties that must be included in order to obtain a full probabilistic description of the structural responses and collapse behavior. The number of random variables can quickly become unreasonable, even from a research perspective. While we discuss the many random variables that may exist, we limit our detailed analyses to and select a subset of these variables that we judge to be most important.

5.2 UNCERTAINTIES CONSIDERED IN STUDY

The uncertainty and variability considered in this work is broken into three categories: record-to-record variability, design uncertainty, and modeling uncertainty. The record-to-record variability comes from variations between the properties of different ground motions; this variability is quantified directly by using nonlinear dynamic time history analysis with a sufficiently large number of ground motions. Design uncertainty accounts for the variability in the engineer's design choices, given the prescriptive code requirements that govern the design (each possible design is termed a design realization). Design uncertainty is essentially the variation in how an engineer applies the code criteria in building design. Modeling uncertainty accounts for the variability of the physical properties and behavior of a structure for a *given design realization*. An example of an important design variable is the amount of additional strength that the engineer provides in a beam (above the code required strength), and an example of an important modeling variable is the plastic rotation capacity (capping point) of the structural components.

5.2.1 Important Uncertainty Not Considered in Study: Human Error

There are other important uncertainties that this study does not address. Some of the most important ones may be associated with construction and human error (Melchers 1999, Chapter 2). Melchers shows that the majority of failures are caused by human error and not by mere randomness in loading and structural response.

Melchers reviewed the causes of over 100 documented structural failures before 1980 and summarized the primary causes of each failure[1]. Table 5.1 presents the results of the work by Melchers. This table shows that the majority of structural failures involve human error.

Even though human error is a primary contributor to many structural failures, this study does not consider the effects of human error. The reason for this exclusion is that the understanding of human error is limited and most information regarding human error is qualitative and difficult to incorporate (Melchers 1999). In addition, to the authors' knowledge, the failures caused by human error are not typically associated with seismic events, so it is unclear how human error affects the failure probabilities of a building subjected to ground motion. The effects of human error could be incorporated using a judgmental increase in the final estimate of uncertainty; this was not done in this study but may be included in future work.

Table 5.1 Primary cause of structural failures (after Melchers 1999).

Primary Cause of Failure	%
Inadequate appreciation of loading conditions or structural behavior	43
Inadequate execution of erection procedures	13
Random variation in loading, structure, materials, workmanship, etc.	10
Violation of requirements in contract documents or instructions	9
Mistakes in drawings or calculations	7
Unforeseeable misuse, abuse/sabotage, catastrophe, deterioration	7
Inadequate information in contract documents or instructions	4
Other	7

[1] Note that these failures were of many types and are not limited to seismically induced failures.

5.2.2 Design Variables

When an engineer applies building code criteria in structural design, conservatism and architectural and constructability constraints typically lead to a structural design that is above the code minimum level. For example, higher than average floor loading in one span of a floor system can easily cause the engineer to increase the beam strength for the full floor, thus adding additional strength to the design. Overdesign for the convenience and economy of construction is a prevalent contributor to overstrength.

When benchmarking the performance of new construction, this conservatism and uncertainty in design is important to quantify, as this conservatism can create significant additional strength and stiffness above the code minimum requirements. This design conservatism may be one of the important reasons that we seldom observe catastrophic failures of new buildings that are correctly designed.

Table 5.2 gives a partial list of the code provisions that are used by practitioners in the design of new buildings; each of these will have uncertainty in how they are applied in the building design.

Table 5.2 Partial list of design variables.

Uncertain Structural Design Parameters	
1	Strong-column weak-beam ratio (code limit of 1.2)
2	Member strength
3	Structural system: Exterior vs. interior frame
4	Beams: Designed as T-beams, or excluding slab effects
5	Maximum story drifts allowed in design
6	Member stiffness assumed in design
7	Column footing rotational stiffness assumed in design
8	Element shear force demands allowed in design
9	Joint shear force demands allowed in design
10	Slab column joints: Stress levels allowed in design
11	Column axial load ratio
12	Detailing: Confinement ratio and stirrup spacing
13	Column spacing for lateral system
14	Bay spacing for gravity system

As can be seen from Table 5.2, there can be much variability in alternate building designs, even though the designs are based on the exact same code design provisions. The uncertain application of these design provisions can cause significant variability in the resulting performance of the building. The complete quantification of all the design variables in Table 5.2 would involve reviewing a great number of practitioner-designed buildings, which is beyond the scope of this study. We focus on the first four items of Table 5.2 in this study.

In order to quantify the first two items of Table 5.2, we reviewed two practitioner-designed buildings (details in Haselton et al. 2007e). Table 5.3 shows some of the quantitative information from these reviews. Note that the mean and c.o.v. estimates are highly judgmental due to the limited number of designs reviewed.

Table 5.3 Design variables used in study.

Uncertain Structural Design Parameters	Mean	Coefficient of Variation
Strong-column weak-beam ratio	1.3 (code limit of 1.2)	0.15
Member strength	25% above code required minimum	0.2

As evident when comparing Tables 5.2 and 5.3, much additional work is required to better quantify variability in design. As we only reviewed designs from two practitioners, the values shown in Table 5.3 are tempered by our judgments, such as discounting some overstrength that arose from architectural considerations in the designs. Therefore, the values in Table 5.3 represent a *conservative estimate* of the design overstrengths.

Even though the amount of statistically robust quantitative information that we could extract from the review of the practitioner designs was minimal, reviewing these designs provided a great deal of qualitative information regarding how the practitioner designed each of the buildings. Both the qualitative and quantitative information was used in the design of the benchmark buildings, to make the benchmark buildings "representative of current practice."

In addition to the design variables in Table 5.3, we investigated the third item in Table 5.2 by designing several perimeter and space frame buildings. We addressed item four in Table 5.2 by designing a space frame building both including and excluding the slab steel effects in the beam design strength (Design F and Design E, respectively). All of these designs are described in Section 2.4.1.

5.2.3 Modeling Variables

In contrast to design variables, much previous research has focused on quantifying modeling variables. Table 5.4 presents the mean and coefficient of variation (c.o.v.) of each of the basic design and modeling variables. In addition, the table shows the references used to quantify each of the uncertainties, and the level of accuracy of the c.o.v. estimates. Note that some of the variables in Table 5.4 are not used in the uncertainty analysis to follow in Sections 5.4 and 5.5; even so, they are documented here for completeness.

Table 5.4 Summary of modeling and design random variables.

Random Variable	Mean	Coefficient of Variation, or σ_{LN}	Level of Accuracy of RV Value	Reference(s)
Design Variables:				
Strong-column weak-beam design ratio	1.3	0.15	2	This study
Beam design strength	1.25	0.20	2	This study
System Level Variables:				
Dead load and mass	1.05(computed)	0.10	1	Ellingwood (1980)
Live load (arbitrary point in time load)	12 psf	--	1	Ellingwood (1980)
Damping ratio	0.065	0.60	1	Miranda (2005), Porter et al. (2002), Hart et al. (1975)
Beam-Column Element Variables:				
Element strength	1.0(computed)	0.12	1	Ellingwood (1980)
Element initial stiffness	1.0(computed)	0.36	1	Panagiotakos (2001), Fardis (2003)
Element hardening stiffness	0.5(computed)*	0.50	2	Wang (1978), Melchers (1999), Fardis (2003)
Plastic rotation capacity	1.0(computed)	0.60	1	Panagiotakos (2001), Fardis (2003)
Hysteretic energy capacity (normalized)	110-120	0.50	2	This study, Ibarra (2003)
Post-capping stiffness	0.08($-K_{elastic}$)	0.60	2	This study, Ibarra (2003)
Concrete tension softening slope	1.0(computed)	0.25	2	Kaklauskas et al. (2001), Torres et al. (2004)
Beam-Column Material Variables (note that these only contribute to element-level variables):				
Rebar yield strength	66.8 ksi	0.04--0.07	1	Melchers (1999)
Rebar strain hardening	$0.018E_s$	--	1	Wang (1978)
Rebar stiffness (E_s)	29,000 ksi	0.033	1	Melchers (1999)
Concrete strength	4030 ksi	0.21	1	Ellingwood (1980)
Gravity System Variables:				
Slab strength (effective width)	1.0(computed)	0.2	1	Ellingwood (1980), Enomoto (2001)
Drift at slab-beam capping	4.5% drift	0.6	1	Haselton et al. 2007e, Appendix 7a
Other Variables:				
Column footing rotational stiffness	1.0(computed)	0.3	2	This study
Joint shear strength	1.40**	0.1	2	Altoontash (2004), Meinheit (1981)

Level of Accuracy of Random Variable Quantification:
1: Coefficient of variation computed from a relatively large amount of data and/or from a computed value stated in the literature
2: Coefficient of variation computed from a relatively small amount of data or estimated from a figure in a reference
Notes:
-- the RV was treated deterministically or another model variable accounts for the same uncertainty
* value is a fraction of the value computed using fiber analysis with expected values of material parameters
** value is a fraction of the value computed from ACI 318-02 provisions

The detailed explanation of how we quantified each of the important random variables in Table 5.4 is given an Appendix of Haselton et al. (2007e).

After the sensitivity study and the propagation of uncertainty were completed, further research yielded improved estimates for some random variable values. Further calibrations to experimental data (Haselton et al. 2007b, Chapter 4) verified that the coefficient of variation of the plastic rotation capacity should be 0.48–0.54. The same study verified that the coefficient of variation of energy-dissipation capacity should be 0.49 and showed that the coefficient of variation of post-capping stiffness should be increased to 0.72. Recent work by Miranda (2005) shows that a mean damping ratio of 6–7% and a coefficient of variation of 0.60 are more appropriate than what was used in this study. This new information was discovered after the current sensitivity study was completed, so these improvements were not used in this study but should be used for future uncertainty studies.

5.3 CORRELATIONS BETWEEN VARIABLES

The correlations between each of the modeling and design variables are difficult to quantify but prove to be one of the most important aspects in quantifying the uncertainty in structural response. To our knowledge, these correlations have not been significantly investigated in previous research. However, Section 5.8 will show that the assumptions regarding these correlations *significantly affect* our final predictions of structural response. This is particularly true for predictions of low probabilities of collapse and for the predictions of the mean annual frequency of collapse.

We completed sensitivity analyses for both fiber and lumped plasticity models, but for brevity, only the results for the collapse analyses using the lumped plasticity model are presented in this chapter. Table 5.5 presents the ten random variables used in the sensitivity study and uncertainty propagation with the lumped plasticity model. These variables were selected based on preliminary analyses to determine which variables could be excluded.

Table 5.5 Ten random variables used for uncertainty propagation.

Random Variable Number	RV Name
RV1	Plastic rotation capacity
RV2	Hysteretic energy capacity (normalized)
RV3	Post-capping stiffness
RV4	Element strength
RV5	Strong-Column Weak-Beam design ratio
RV6	Element initial stiffness
RV7	Element hardening stiffness
RV8	Damping ratio
RV9	Dead load and mass
RV10	Beam design strength

In order to use each of these random variables and propagate the combined effects of their uncertainties, we need to quantify the correlations between the variables. These correlations are of two basic types, each described in the next two sections:

(a) Correlations between parameters of a given structural component

(b) Correlations between parameters of different components

5.3.1 Correlations for Single Element (Type-A Correlation)

An example of the correlations between random variables for a single element is the correlation between the strength of a column and the stiffness of that same column. This correlation comes from the fact that the strength and stiffness of an element are affected by some of the same things such as member dimensions, rebar placement, and quality of construction.

In this study, we calibrated the modeling parameters to only 30 column tests, which we thought was too small of a sample to compute correlations from the test data. Therefore, we simply used judgment to decide which random variables we expect to be correlated, and then assumed full correlation between these variables. Table 5.6 shows the resulting correlation matrix for the ten random variables of a single element. This matrix reflects several sets of correlation assumptions, one of which is full correlation between plastic rotation capacity, post-capping stiffness, and energy-dissipation capacity.

Later, for estimates of uncertainty in collapse capacity, Section 5.5.2 will present uncertainty estimates assuming no type-correlation, full Type-A correlation, and expected Type-A correlation (expected correlations are reflected in Table 5.6).

Table 5.6 Correlation matrix used for correlations for single element.

	RV1	RV2	RV3	RV4	RV5	RV6	RV7	RV8	RV9	RV10
RV1	1									
RV2	1	1								
RV3	-1	-1	1				(Symmetric)			
RV4	0	0	0	1						
RV5	0	0	0	0	1					
RV6	0	0	0	1	0	1				
RV7	0	0	0	0	0	1	1			
RV8	0	0	0	0	0	0	0	1		
RV9	0	0	0	1	0	1	0	0	1	
RV10	0	0	0	0	1	0	0	0	0	1

5.3.2 Correlations for Random Variables of Different Elements (Type B)

Examples of the correlations between random variables for different elements is the correlation between the strength of two columns at different locations in the building or strengths of beams and columns in the building. Such correlations are difficult to quantify and are affected by many factors. For example, the contractor may fabricate a large number of stirrups at the same time and systematically make the stirrups larger than what is called for in the plans. In this case, when the longitudinal rebars are placed into the elements with larger stirrups, the effective depth of the rebars will tend to be systematically larger than expected. This will cause a high positive correlation between the strengths of all of the affected elements.

To rigorously solve this problem, we would need to accurately quantify all of these correlations between elements, and then analyze the structure using unique RVs for each element, while maintaining the proper correlation structure for all of the elements of the frame. This is a prohibitive task when using nonlinear dynamic time history analysis for performance assessment. If we do not assume full correlation between elements, then we will need to have a separate random variable for each element; for the single two-dimensional 4-story 4-bay frame of interest, this results in a total of 360 random variables for the 36 elements of a single frame. If we assume full Type-B correlation, we can reduce the total number of random variables to 10 (i.e., one variable for each item in Table 5.5). Therefore, when running the sensitivity analysis, we assumed full Type-B correlation, as shown in the correlation matrix in Table 5.7.

Note that this full Type-B correlation assumption may not be a conservative assumption. The possible impacts of this assumption are mentioned at the end of this section.

Table 5.7 Correlation matrix used for correlations for multiple elements.

		Element$_i$										Element$_j$									
		RV1	RV2	RV3	RV4	RV5	RV6	RV7	RV8	RV9	RV10	RV1	RV2	RV3	RV4	RV5	RV6	RV7	RV8	RV9	RV10
Element$_i$	RV1	1																			
	RV2	1	1																		
	RV3	-1	-1	1																	
	RV4	0	0	0	1																
	RV5	0	0	0	0	1										(Symmetric)					
	RV6	0	0	0	1	0	1														
	RV7	0	0	0	0	0	1	1													
	RV8	0	0	0	0	0	0	0	1												
	RV9	0	0	0	1	0	1	0	0	1											
	RV10	0	0	0	0	1	0	0	0	0	1										
Element$_j$	RV1	1	1	-1	0	0	0	0	0	0	0	1									
	RV2	1	1	-1	0	0	0	0	0	0	0	1	1								
	RV3	-1	-1	1	0	0	0	0	0	0	0	-1	-1	1							
	RV4	0	0	0	1	0	1	0	0	1	0	0	0	0	1						
	RV5	0	0	0	0	1	0	0	0	0	1	0	0	0	0	1					
	RV6	0	0	0	1	0	1	1	0	1	0	0	0	0	1	0	1				
	RV7	0	0	0	0	0	1	1	0	0	0	0	0	0	0	0	1	1			
	RV8	0	0	0	0	0	0	0	1	0	0	0	0	0	0	0	0	0	1		
	RV9	0	0	0	1	0	1	0	0	1	0	0	0	0	1	0	1	0	0	1	
	RV10	0	0	0	0	1	0	0	0	0	1	0	0	0	0	1	0	0	0	0	1

To investigate the effects of this correlation assumption, we developed a simple approximate method for quantifying the effect of partial correlation between parameters of different elements. This approximate method is appropriate only for elements in parallel (e.g., two columns of the same story) and for responses that are global in nature (e.g., drift and floor acceleration); this will not work for engineering demands parameters (EDPs) like plastic rotation in a single element. An appendix of Haselton et al. (2007e) explains this approximate method and shows the effects that the correlation assumptions have on the estimated uncertainty in collapse capacity. Depending on Type-B correlation assumptions, the final uncertainty in collapse capacity can change by a *factor of 2.0* (Section 5.5.2).

One *extremely important point* that was not considered in this study is the possibility of partial correlation between elements at different story levels. In this work, we assume that the variables (like strength, ductility, etc.) are *perfectly correlated* from story to story. This was done to reduce the number of random variables, and thus the computational expense, since the sensitivity study presented in this chapter took several weeks of continuous computer run-time using five 2004-era desktop computers. However, this simplifying assumption does not allow the sensitivity analysis to account for the fact that partial correlation may cause one story to be weaker or less ductile than adjacent stories, thus causing the damage to concentrate in that story.

Future research needs to look more closely at these uncertainty issues, to better understand the impacts of simplifying assumptions, such as those made in this study.

5.4 SENSITIVITY STUDY: COLLAPSE CAPACITY

To learn how the previously discussed uncertainties affect the uncertainty in collapse capacity, we vary the value of each random variable (RV) individually, rerun the collapse analysis, and then observe how the RV affects the collapse capacity. This section discusses this sensitivity of collapse capacity to each RV. As previously mentioned, when varying each RV value, we assume full Type-B correlation to reduce the computational burden and to make the problem tractable.

To find the total uncertainty in collapse capacity that results from the uncertainty in all of the RVs, we use the first-order second-moment (FOSM) method to combine the effects of each RV with correlation information. Section 5.5 presents these calculations and the final estimated uncertainty in collapse capacity.

5.4.1 Sensitivity of Collapse Capacity to Each Random Variable

To determine the sensitivity of the collapse capacity to each of the ten RVs listed in Table 5.5, we took each RV individually, set the RV value to μ_{RV} +/- $\sqrt{3}\,\sigma_{RV}$, and then ran the collapse analysis for ten ground motions. We used Design A for the sensitivity analysis and used the records from Bin 4A[2] (one random component from each record pair) because these are the records selected for the highest ground motion intensity level closest to what may cause structural collapse. We used μ_{RV} +/- $\sqrt{3}\,\sigma_{RV}$ because these values are needed for the moment-matching method that we were considering for uncertainty propagation; however over the course of this project, we decided to instead use the FOSM approximation (Section 5.5.1). When moment matching is not used, μ_{RV} +/- σ_{RV} is more appropriate (Baker 2003).

---

[2] The structural designs are defined in Section 2.4.1. The ground motions are described in Goulet et al. (2006a) and Haselton et al. (2007e); Bin 4A (and 4C used later) were selected for the 2%-in-50-years ground motion level.

Figure 5.1a shows the collapse cumulative density functions (CDFs) for the plastic rotation capacity (RV1) set to μ_{RV1} +/- $\sqrt{3}\,\sigma_{RV1}$[3]. Similar graphs for the other random variables are given in Figure 5.1b–h. Note that these sensitivity analysis results use a slightly different structural model and set of ground motions than for other collapse results presented elsewhere in this report, so the collapse capacities will not precisely match other presented values. Even so, the differences in the structural models are relatively minor, so we believe that the sensitivity of the collapse capacity predictions is similar for the different models used.

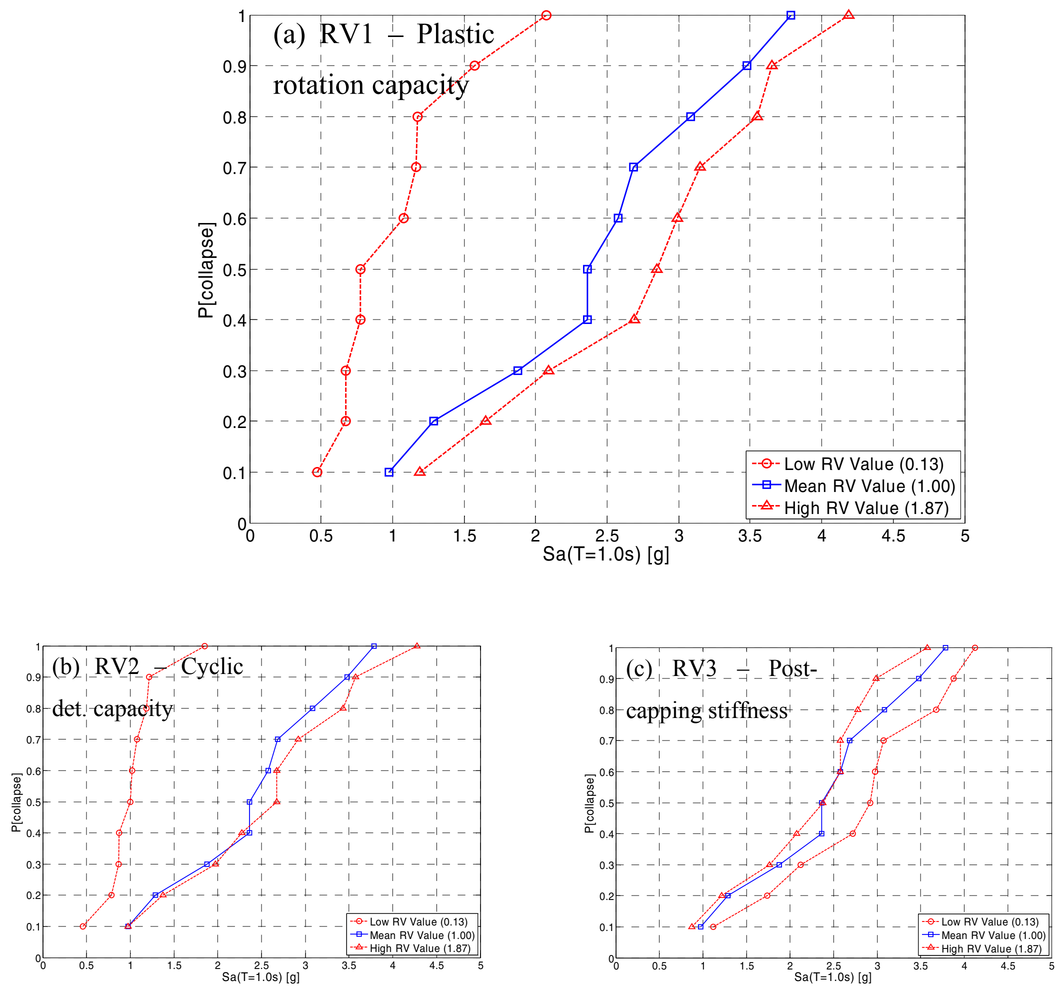

Fig. 5.1 Variation in collapse cumulative distribution function (CDF) with individual RV values varied to μ_{RV} +/- $\sqrt{3}\,\sigma_{RV}$. Note that Table A5c.5 defines RV indices. Spectral acceleration shown is spectral acceleration of ground motion component.

[3] When we computed the altered random variable values used in the sensitivity study, we inadvertently used a normal standard deviation; a lognormal standard deviation should be used in future sensitivity analyses of this type (Ibarra 2003; Chapter 6).

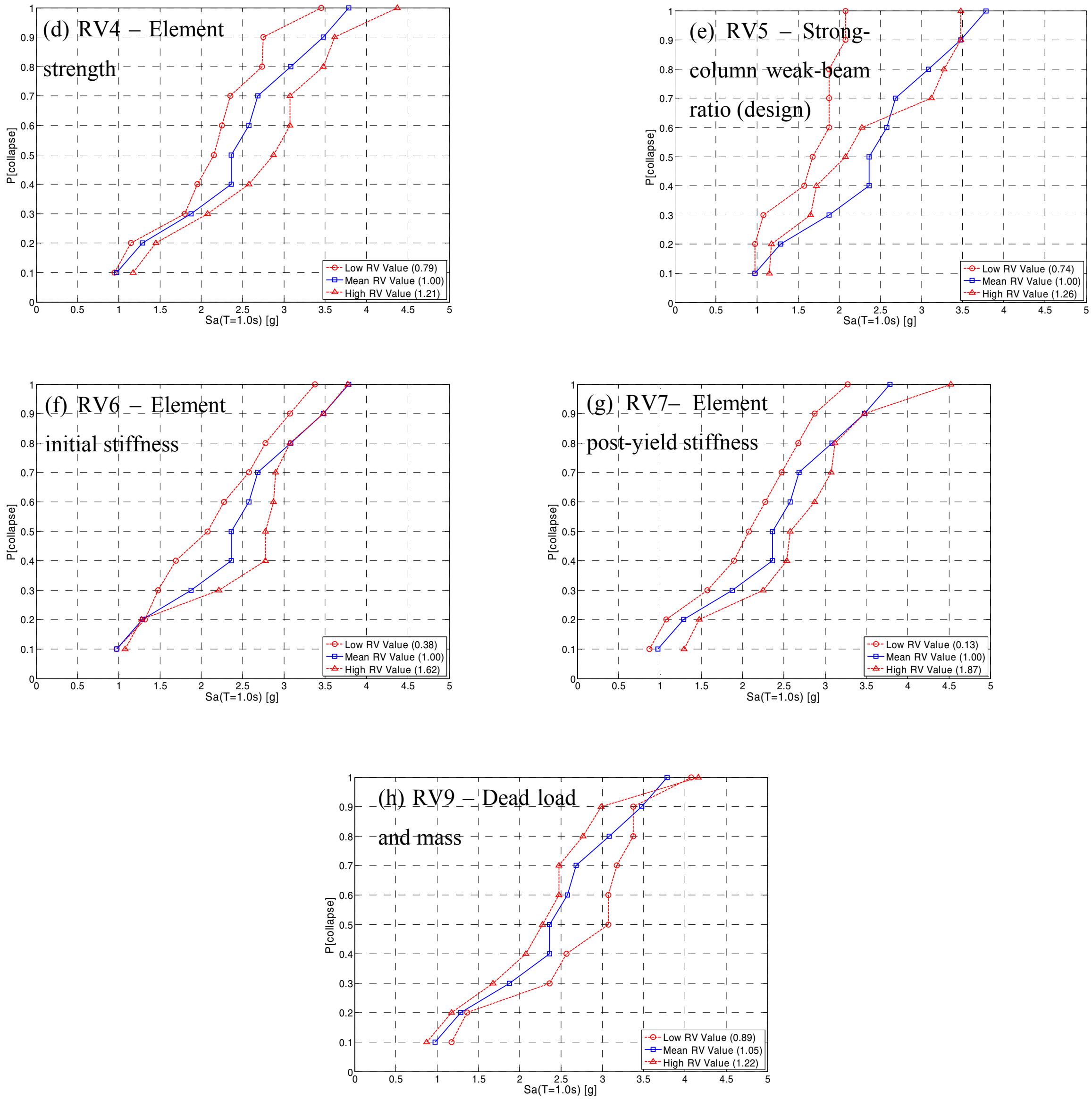

Fig. 5.1—*Continued*

Figure 5.1 shows how the RVs affect the full collapse cumulative distribution function (CDF). A tornado diagram may also be used to show only the change in the mean collapse capacity (Porter 2003). Figure 5.2 shows a tornado diagram derived from the information in Figure 5.1. This tornado diagram shows only the *mean* collapse capacities from each of the above figures, and the variables are ordered by relative importance (note that the tornado diagram uses the mean of a fitted lognormal distribution).

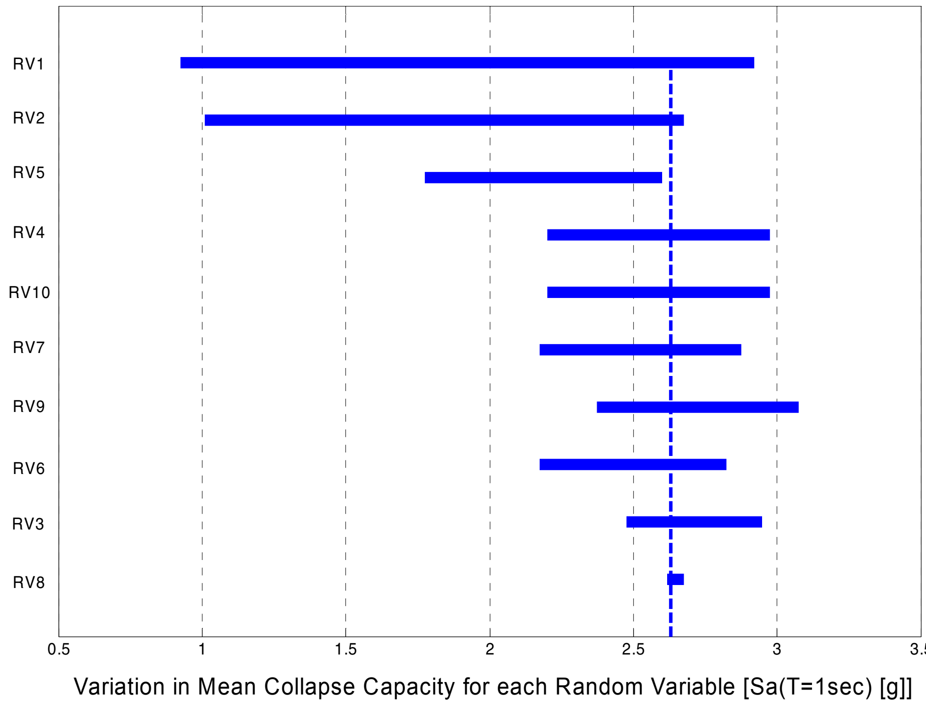

Fig. 5.2 Tornado diagram showing sensitivity of mean collapse capacity to each RV. RVs varied to μ_{RV} +/- $\sqrt{3}\,\sigma_{RV}$, and values displayed are means of fitted lognormal distribution. Note that Table 5.5 defines RV indices.

Figures 5.1 and 5.2 show the relative importance of each random variable, showing how changes to the random variable values affect the median collapse capacity and collapse capacity distribution. Observations from these figures are as follows:

- Element plastic rotation capacity (RV1) most influences the collapse capacity. This agrees with findings by Ibarra (2003). Note that the apparent insignificance of increasing the plastic rotation capacity comes from the fact that for large increases in plastic rotation capacity, the element hardens enough to cause the joints to fail in shear. Figure 5.3 shows this in more detail.
- Cyclic deterioration capacity (RV2; λ) is shown to be the second most influential variable, but this is not consistent with findings from Ibarra (2003). Ibarra found that the effects of cyclic deterioration are not important for conforming elements with slow deterioration rates. The apparent importance of the cyclic deterioration in Figure 5.1b is related to the fact that we used μ_{RV} +/- $\sqrt{3}\,\sigma_{RV}$ for the sensitivity study, and $\lambda = \mu_{\lambda} - \sqrt{3}\,\sigma_{\lambda}$ with a normal distribution is an unreasonably low value to use for assessing sensitivity.

The following section looks into this issue more closely and shows that for more reasonable values, λ is not as significant as suggested by Figure 5.1b. The following section shows that the final findings regarding cyclic deterioration agree well with the findings of Ibarra.

- Reducing the strong-column weak-beam ratio (RV5) causes the collapse capacity to decrease (Fig. 5.1e). Increasing the strong-column weak-beam ratio causes no systematic change to the collapse capacity, and with the ground motion randomness the mean collapse capacity actually decreases slightly.
- The post-capping stiffness ratio (RV3; α_c) is shown to be almost insignificant. Ibarra has previously shown for single-degree-of-freedom systems that the post-capping stiffness is of critical importance when α_c is changed from -10% to -30%, but almost insignificant when α_c is changed from -30% to -50% (Ibarra 2003, Fig. 4.13). The mean *element-level* α_c is -8% (Table 5.4), but Figure 2.5 shows that the *system-level* post-capping stiffness to be nearly -30% of the initial stiffness, because the damage localizes in only two of the four stories of the building. With the effective building-level α_c being -30%, our findings about the unimportance of post-capping slope agree with findings of Ibarra (2003).
- The sensitivity to damping ratio (RV8: ξ) is not shown here because the damping values used in the sensitivity study differ from those used in other analyses presented in this report. Not reporting these values is warranted because the damping value does not have large impacts on the collapse capacity. However, continued studies have indicated that the damping *formulation* may be an important factor in collapse simulation; this is a topic of continued study (Ibarra 2003).

This section showed the sensitivity of the collapse capacity for each RV individually. This information, combined with the correlations between random variables, can be used with the FOSM approximation to determine the total uncertainty in collapse capacity. However, before computing the final uncertainty in collapse capacity, the next section takes a closer look at the two RVs that this section showed to be most critical to the prediction of collapse capacity.

5.4.1.1 Closer Look at Sensitivity to Important Random Variables

Figures 5.1 and 5.2 showed that the plastic rotation capacity and the cyclic energy-dissipation capacity are the two variables that most influence the collapse capacity estimate. Part of the reason that these variables appear so significant is the fact that the sensitivity study was completed using μ_{RV} +/- $\sqrt{3}\,\sigma_{RV}$. These points represent extremely large changes to the RV values, which may not be appropriate when combined with the FOSM assumption that each variable linearly affects the collapse capacity. Ibarra found that using such extreme changes to random variable values can skew the uncertainty predictions when using the FOSM approximation (Ibarra 2003).

In order to check the linearity assumption of the FOSM method, Figures 5.3 and 5.4 show how the two most important random variables (plastic rotation capacity and hysteretic energy-dissipation capacity) affect the collapse capacity for earthquake number 941082 (Loma Prieta E-W motion from the 58235 Saratoga station). To come to more reliable trends, it would be good to do this comparison for ten or more records and use average results for the multiple ground motions, but the records used were primarily for illustration.

Figure 5.3 shows that the relationship between plastic rotation capacity and collapse capacity is linear for reductions in plastic rotation capacity. Since reducing the plastic rotation capacity will lead to earlier collapse, we used the leftward gradient for the FOSM calculations. Since the leftward gradient is linear, the gradient estimate is not sensitive to the amount of change to the random variable, so we did not adjust the gradient estimate based on the results shown in Figure 5.3.

For increases in plastic rotation capacity, the elements undergo significant strain hardening, and the predicted failure mode of the building is changed to joint shear failure; therefore the predicted collapse capacity does not increase with increases in the plastic rotation capacity. This alteration of the failure mode for larger plastic rotation capacities is likely only an artifact of the model, as the strain-hardening stiffness will likely reduce at large levels of plastic rotation. The current element model does decrease the strain hardening based on cyclic deterioration, but this reduction is typically too low in comparison to experimental results (see calibration plots from Haselton et al. 2007f).

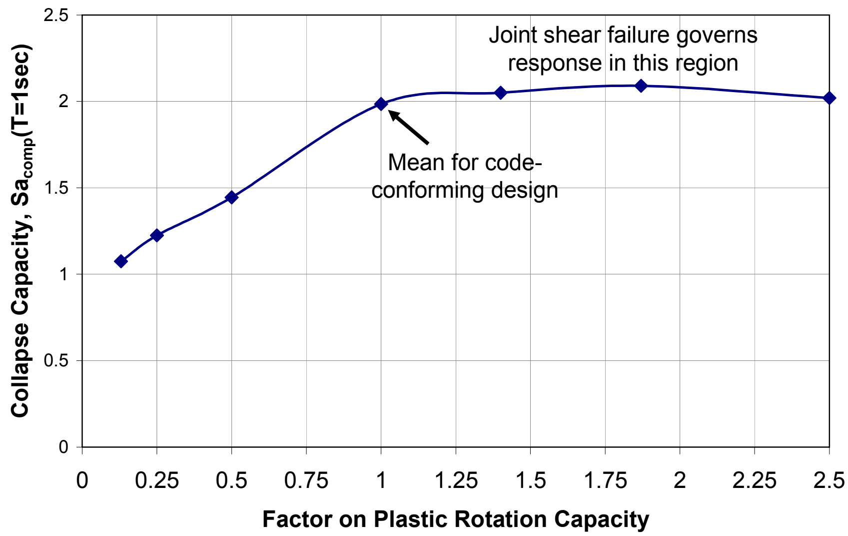

Fig. 5.3 Effect of plastic rotation capacity on collapse capacity for earthquake number 941082.

Figure 5.4 shows that for reductions in hysteretic energy-dissipation capacity, the effect on the collapse capacity is highly nonlinear. The original gradient estimate (previously in Figs. 5.1 and 5.2) was based on a large reduction in the random variable value. Figure 5.4 shows that this gradient reduces by a factor of 2.5 if a random variable alteration of μ_{RV} - σ_{RV} is used rather than μ_{RV} - $\sqrt{3}\,\sigma_{RV}$.

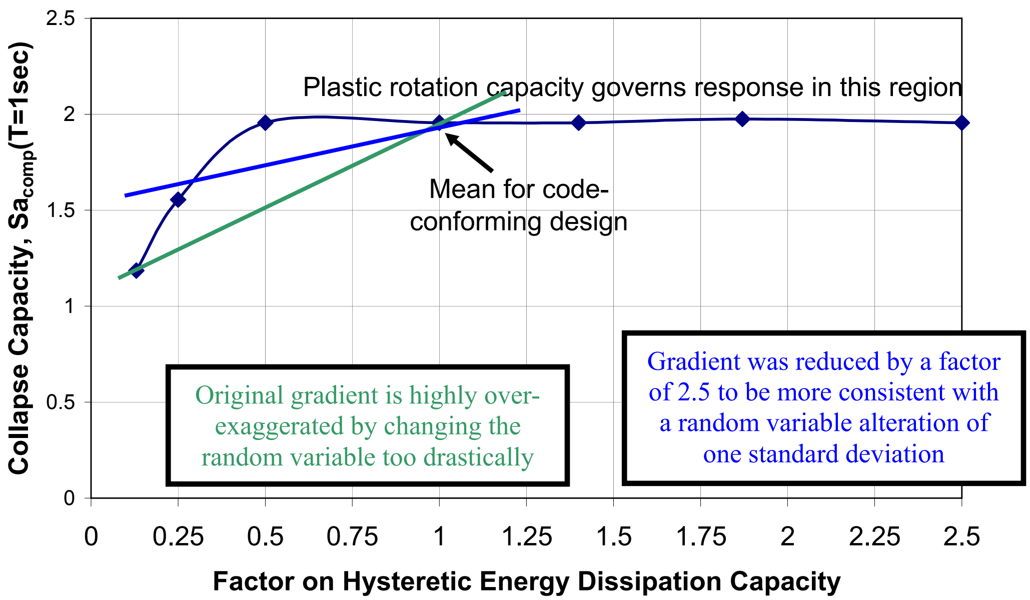

Fig. 5.4 Effect of hysteretic energy-dissipation capacity on collapse capacity for earthquake number 941082.

5.5 PROPAGATION OF UNCERTAINTY: COLLAPSE CAPACITY

The previous two sections discussed the correlations between RVs and the sensitivities of the collapse capacity to these random variables. This section takes this information and uses the first-order second-moment (FOSM) approximation to estimate the total uncertainty in collapse capacity that is caused by the uncertainty in the random variables. This method is proposed for use in performance-based earthquake-engineering studies by Baker and Cornell (2003). This method has been utilized previously by Ibarra and Krawinkler (Ibarra and Krawinkler 2005a; Ibarra 2003, Chapter 6) to estimate the variance of the collapse capacity for single-degree-of-freedom systems, and to look at the many important details of how this method should be applied. This same method can be used for pre-collapse responses (e.g., drift, floor acceleration, etc.) but was not done in this study.

5.5.1 First-Order Second-Moment Method

This section explains the FOSM method (Baker and Cornell 2003; Cornell and Baker 2002). To further clarify application of this method, Haselton et al. (2007e) presents a sample FOSM calculation. The FOSM method assumes that each random variable linearly affects the collapse capacity. This allows us to predict how the standard deviation of collapse capacity is increased by the structural modeling uncertainties. However, the FOSM method is incapable of predicting how the mean (or median) collapse capacity may be affected by structural modeling uncertainties. In cases where a random variable nonlinearly affects the collapse capacity, structural modeling uncertainties will affect the mean collapse capacity in addition to the standard deviation of collapse capacity; the FOSM method can not capture this and may be a considerable approximation in these cases.

To begin the FOSM method, we assume that a function, *g*, relates the random variables to the response of interest, which here is the collapse capacity[4]. The g-function simply represents the structural analysis, which relates the structural random variables to the collapse capacity; this is shown in Equation 5.1.

---

[4] The notation used in this section is written for propagating uncertainty in collapse capacity, but the same equations can be applied to other values of interest, such as drift ratio, by simply replacing $Sa_{collapse}$ by whichever term for which one wishes to estimate the uncertainty.

$$Sa_{collapse} = g\left(X_1, X_2, ..., X_n\right) + X_{RTR} \tag{5.1}$$

where $X_1,..., X_n$ are random variables (e.g., plastic rotation capacity, etc.) and X_{RTR} is a zero-mean random residual representing the record-to-record variability of $Sa_{collapse}$.

To determine the mean and the record-to-record variability of the collapse capacity, we simply set all random variables to their respective mean values and perform the collapse analysis with a sufficiently large number of records (10–30 used in this study); this is shown in Equation 5.2.

$$\mu_{Sa_{collapse}} \cong g\left(M_X\right) \tag{5.2}$$

where M_x is the vector of mean values of the random variables.

Equation 5.3 is then used to determine the total variance in collapse capacity. The correlation coefficients and standard deviations of each random variable were discussed in Section 5.3 and 5.2, respectively. The gradients are obtained from the sensitivity analyses presented in Section 5.4.

$$\sigma^2\left[Sa_{collapse}\right] \cong \left[\sum_{i=1}^{n}\sum_{j=1}^{n}\left[\frac{\partial g\left(X\right)}{\partial x_i}\cdot\frac{\partial g\left(X\right)}{\partial x_j}\right]_{X=M_X}\rho_{ij}\sigma_i\sigma_j\right] + \sigma^2\left[X_{RTR}\right] \tag{5.3}$$

where $\dfrac{\partial g\left(X\right)}{\partial\left(x_i\right)}$ is the gradient of the $Sa_{collapse}$ with respect to random variable i,

ρ_{ij} is the correlation coefficient between RV_i and RV_j, and

σ_i is the standard deviation of RV_i.

Figure 5.5 shows a schematic of how the FOSM method approximates the effect of each RV on $Sa_{collapse}$.

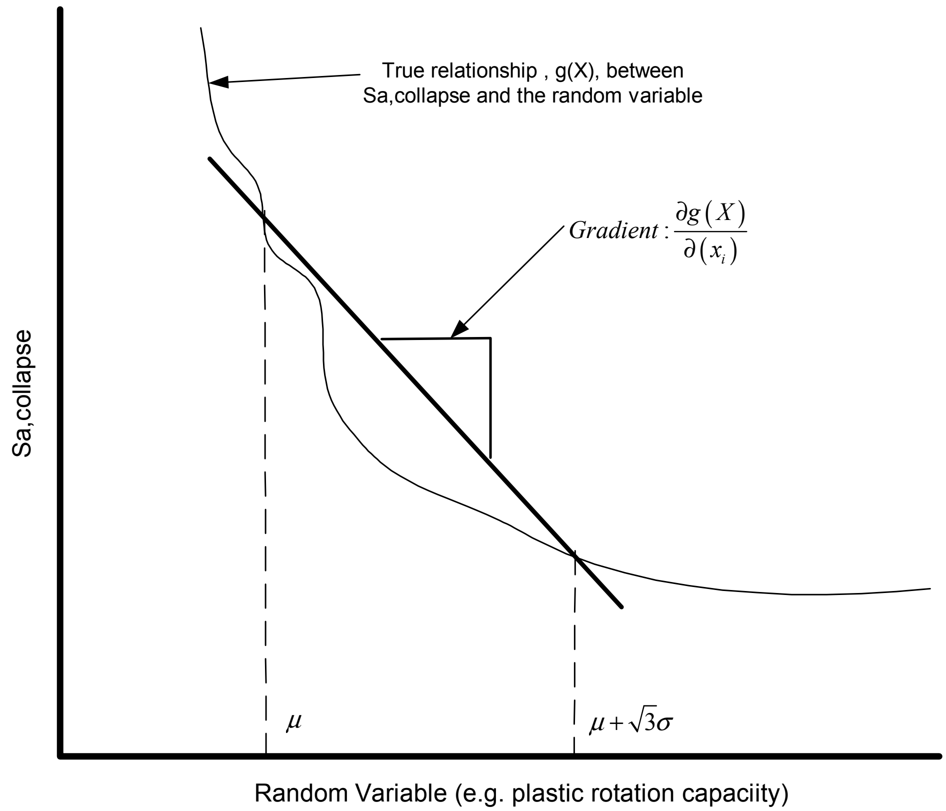

Fig. 5.5 Schematic diagram of true nonlinear relationship, g(x), and FOSM linear approximation.

5.5.2 Estimated Variability of Collapse Capacity

We used the FOSM method to estimate the total variability in the collapse capacity estimate. We performed all FOSM calculations in the log-domain of the data based on recommendations from previous research (Ibarra 2003, Chapter 6). Because correlation assumptions have a large effect on the estimated collapse capacity variability, we completed the FOSM calculations for three levels of Type-A and Type-B correlations (correlations discussed in Section 5.3). Ibarra (2003, Chapter 6) also looked at the Type-A correlations using single-degree-of-freedom systems and illustrated the importance of these assumptions.

Table 5.8 presents the estimated variability in collapse capacity when considering all ten variables shown earlier in Table 5.5 (i.e., both modeling uncertainties and design uncertainties). These values represent the standard deviation of a lognormally distributed random variable (numerically similar to the coefficient of variation). Also, note that the values of Table 5.8 do not include the contribution of record-to-record variability (i.e., they include only the first term in Eq. 5.3); the record-to-record variability is incorporated later in Section 5.7 individually for each structural design. Table 5.8 shows that the estimates depend heavily on the correlation assumption, with Type-A correlations changing predictions by a factor of two to three, and Type-B correlations changing predictions by a factor of two. In later calculations for Design A, to account for both design and modeling uncertainties, 0.45 is used as the "best estimate" of the log-standard deviation of $Sa_{collapse}$ (note that this value does not include record-to-record variability).

The results shown in Table 5.8 are from the FOSM approximation being completed using the data transformed by using the natural logarithm (because the relationships between the random variables and the collapse capacity are typically more linear after the data are transformed using the natural logarithm) (Cornell and Baker 2002). For comparison, the FOSM approximations were also completed without transforming the data by the natural logarithm for a select few sets of correlation assumptions; this resulted in values of 0.67 and 0.52 in place of 0.54 and 0.38, respectively, in Table 5.8. Differences of similar magnitude have been documented by Ibarra (2003, Chapter 6).

Table 5.8 Estimated variability in collapse capacity. Both modeling variability (RVs 1-4 and 6-9) and design variability (RVs 5 and 10) are included, and computations completed for three levels of Types A and B correlations.

$\sigma_{LN,modeling\&design}$ with various correlations		Type B Correlations - Between Parameters of $Element_i$ and $Element_j$		
		Full Correlation	Partial (ρ_{ij} = 0.5) - approx. method	No Correlation
Type A Correlations - Between Different Parameters of the Same Element	Full Correlation	1.00	0.79	0.56
	Full Correlation between Variables Expected to be Correlated	0.54	**0.43**	0.28
	No Correlation	0.38	0.30	0.21

Table 5.8 showed the estimates that include both modeling and design uncertainties. This is appropriate for assessing *future construction,* when there is still uncertainty in how the building may be designed. For a situation in which the design is fully specified, only the

modeling uncertainties should be included. To facilitate this, Table 5.9 presents similar predictions that include only the contributions of the modeling variables (i.e., only variables 1–4 and 6–9). In situations where design uncertainties should not be included, 0.35 is used as the "best estimate" of the log-standard deviation of $Sa_{collapse}$ (note that this value does not include record-to-record variability). Table 5.10 is similar, but shows predictions when only design variables are included (i.e., only variables 5 and 10).

Table 5.9 Estimated variability in collapse capacity. Only modeling variability (RVs 1–4 and 6–9) is included (design variability not accounted for), and computations completed for three levels of Types A and B correlations.

$\sigma_{LN,modeling}$ (no design uncert.) with various correlations		Type B Correlations - Between Parameters of Element$_i$ and Element$_j$		
		Full Correlation	Partial (ρ_{ij} = 0.5) - approx. method	No Correlation
Type A Correlations - Between Different Parameters of the Same Element	Full Correlation	0.68	0.54	0.40
	Full Correlation between Variables Expected to be Correlated	0.43	**0.34**	0.23
	No Correlation	0.30	0.24	0.18

Table 5.10 Estimated variability in collapse capacity. Only design variability (RVs 5 and 10) is included (modeling variability not accounted for), and computations completed for three levels of Types A and B correlations.

$\sigma_{LN,design}$ (no modeling uncert.) with various correlations		Type B Correlations - Between Parameters of Element$_i$ and Element$_j$		
		Full Correlation	Partial (ρ_{ij} = 0.5) - approx. method	No Correlation
Type A Correlations - Between Different Parameters of the Same Element	Full Correlation	0.33	0.26	0.16
	Full Correlation between Variables Expected to be Correlated	0.33	**0.26**	0.16
	No Correlation	0.24	0.19	0.12

5.6 METHODS TO ACCOUNT FOR UNCERTAINTIES

5.6.1 Introduction and Types of Uncertainties

There are two primary ways to consider the impacts that uncertainties have on structural response. We can either separate uncertainties into two abstract categories (aleatory and epistemic, which are defined below), or we can make no distinction between different types of uncertainty. The recent SAC effort (Cornell 2002) separated uncertainties into categories, while our work makes no distinction between types of uncertainties. The recent PEER Van Nuys testbed study also investigated how structural modeling uncertainties affect the collapse risk (Krawinkler 2005).

Uncertainty is often categorized into two conceptual types. The first type of uncertainty is "randomness." This is uncertainty that comes from something that is inherently random, in which case we will never be able to reduce this uncertainty by researching the phenomenon in more detail; this is often called *aleatory* uncertainty. The other type of uncertainty comes from lack of knowledge (ignorance) or modeling error; this is often called *epistemic* uncertainty. Epistemic uncertainty can always be reduced by further research that leads to better understanding and better modeling of the phenomenon.

The remainder of this section discusses the two methods (separating uncertainties or putting them all together) and explains why we chose to not separate uncertainties by type in this study. The example used in this section is for Design A without considering the gravity frame contribution, and subjected to the ground motions from Bins 4A and 4C.

5.6.2 Estimates at Given Level of Prediction Confidence: Separating Uncertainties by Conceptual Type

The motivation to separate uncertainties is to be able to make statements regarding prediction confidence, (e.g., "At 90% prediction confidence, the probability of collapse is only 25%"). In order to make such statements, we need to separate the uncertainties and categorize them into "randomness" (aleatory) or "lack of knowledge" (epistemic). There is much debate about how to separate variability, so in this illustration, we will say that ground motion variability is *aleatory* and that all the modeling and design uncertainties (as computed in Section 5.5) are *epistemic*.

Figure 5.6 shows the distribution of the building collapse capacity and illustrates how these uncertainties are utilized after they are separated.

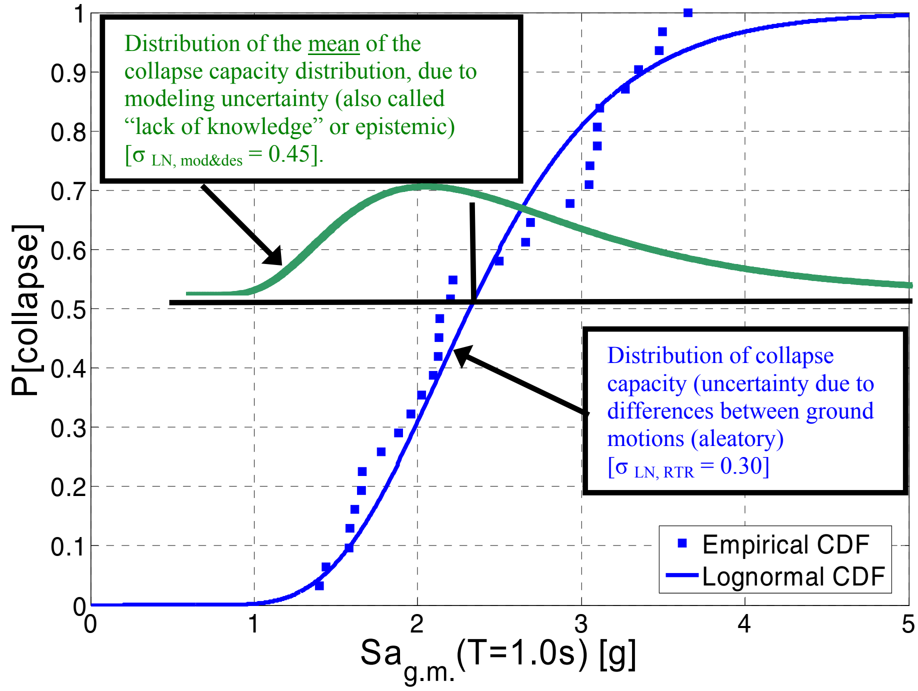

Fig. 5.6 Collapse capacity distributions showing variability coming from ground motion randomness and uncertainty coming from modeling uncertainty.

Figure 5.6 shows how the two types of uncertainty are assumed to interact. We commonly say that the "randomness" causes an inherent uncertainty on the collapse capacity, which is shown as the record-to-record (RTR) CDF (blue CDF). We then continue by saying that the "lack of knowledge" causes an additional *uncertainty on the mean* of the RTR CDF; the uncertainty is shown by the probability density function (PDF) (green PDF). This figure shows the RTR CDF at this position of 50% prediction confidence, since the mean of the RTR collapse CDF is at the 50th percentile of the modeling PDF.

To make predictions at a given prediction confidence level, the RTR collapse CDF must be shifted to the appropriate percentile of the modeling PDF. Figure 5.7 shows an example for 90% prediction confidence. The left-shifted RTR CDF (red dotted line) is the same as the original CDF (blue solid CDF) on the right but the mean has been shifted to the 10th percentile of the PDF (green solid PDF). This figure shows that at a 90% prediction confidence level the probability of collapse for the 2%-in-50-years motion (Sa(T=1s) = 0.82g) is 18%.

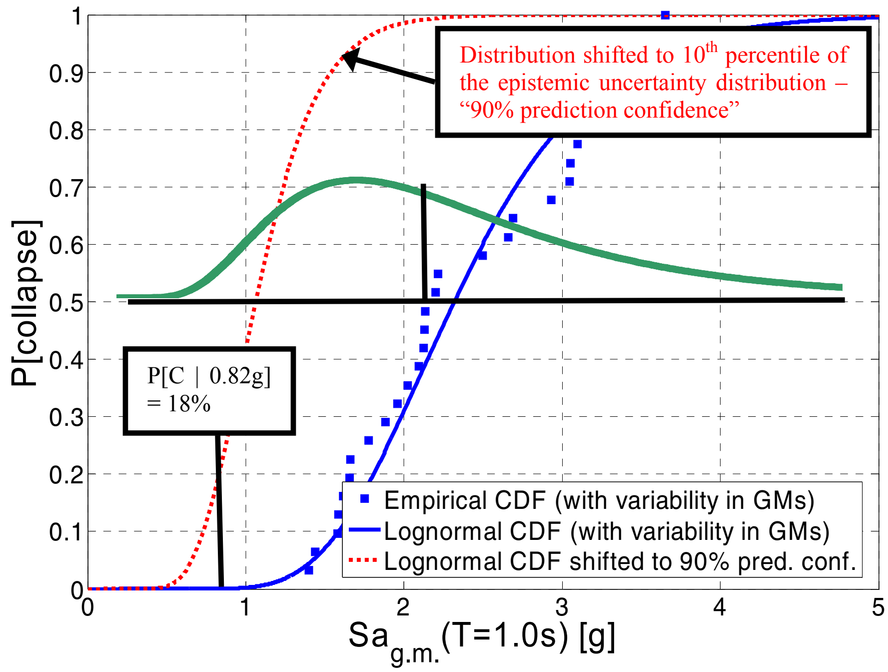

Fig. 5.7 Collapse capacity distributions showing collapse capacity CDF shifted to 90% prediction confidence.

Figure 5.8 follows by showing the P[C | $Sa_{2/50}$] for a range of prediction confidence levels. Notice that the probability is 18% at a 90% prediction confidence, in agreement with Figure 5.7. Figure 5.8 shows that the probability estimates at high levels of prediction confidence are unstable; at a 80% prediction confidence P[C | $Sa_{2/50}$] = 4%, while at 95% prediction confidence P[C | $Sa_{2/50}$] = 45%.

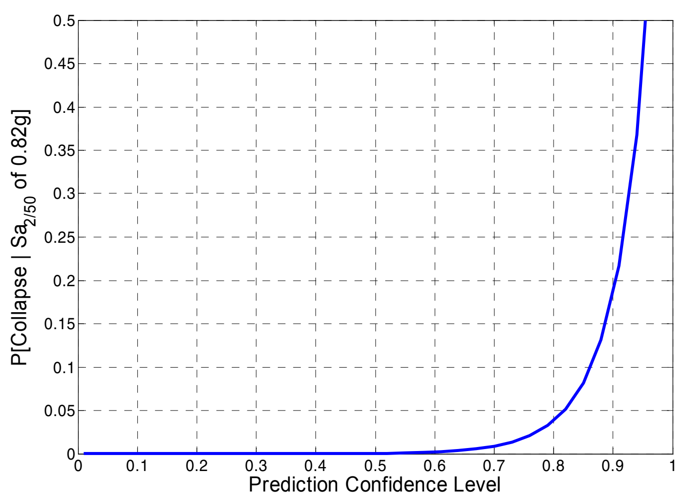

Fig. 5.8 Effect of prediction confidence level on estimate of probability of collapse for 2%-in-50-years event.

Making performance predictions at high levels of confidence is attractive because it produces conclusions based on high levels of statistical confidence. Even so, this approach has two primary drawbacks:

(a) The estimates of $P[C \mid Sa_{2/50}]$ (and similarly $\lambda_{collapse}$) are highly unstable for high levels of prediction confidence. This causes slight variations in the prediction confidence level to have extreme impacts on performance predictions. This is undesirable because the choice of prediction confidence level is somewhat arbitrary, yet the choice will result in large changes in the performance predictions.

(b) Making predictions with a level of prediction confidence requires separation of uncertainty into "randomness" and "lack of knowledge." This separation is quite difficult and quickly becomes a philosophical debate (Cornell 2005).

Based on these two drawbacks of the prediction confidence approach, we use the "mean estimate" approach in this research; this method is discussed in this next section.

5.6.3 Mean Estimates: Not Separating Uncertainties by Conceptual Type

The mean estimate approach is based on the assumption that both the record-to-record variability and the structural modeling uncertainties can be described by a lognormal distribution. Based on these assumptions, one can easily compute the expected (or mean) collapse capacity CDF, accounting for both sources of uncertainty, by simply taking the square-root-of-the-sum-of-squares of the individual uncertainties (i.e., the σ_{LN} values).

This approach makes the final solution not depend on how we separate uncertainties, so it avoids the question of "randomness" versus. "lack of knowledge." This avoids the philosophical debate required to separate the uncertainties, and also makes the performance prediction more stable and not dependent on an arbitrary decision regarding the appropriate level of prediction confidence.

Figure 5.6 showed the distribution of the collapse capacity due to ground motion variability and also the variability in the mean collapse capacity due to modeling variability. By assuming that these two distributions are independent and assume that both are well described by lognormal distributions, we can obtain the mean estimate by simply combining all uncertainties using the square-root-of-sum-of-squares (SRSS) and doing all computations using a new distribution with this combined variance.

Figure 5.9 illustrates the mean estimate approach. The solid red line is the lognormal distribution fitted to the predicted collapse capacities ($\sigma_{LN,RTR(Sa,col)} = 0.36$). The dashed blue line shows the collapse capacity CDF that includes the contributions of both RTR variability and modeling/design uncertainty ($\sigma_{LN,Total(Sa,col)} = [(0.45)^2 + (0.36)^2]^{0.5} = 0.58$). Using this approach, the mean estimate of the P[C | $Sa_{2/50}$] is 3%.

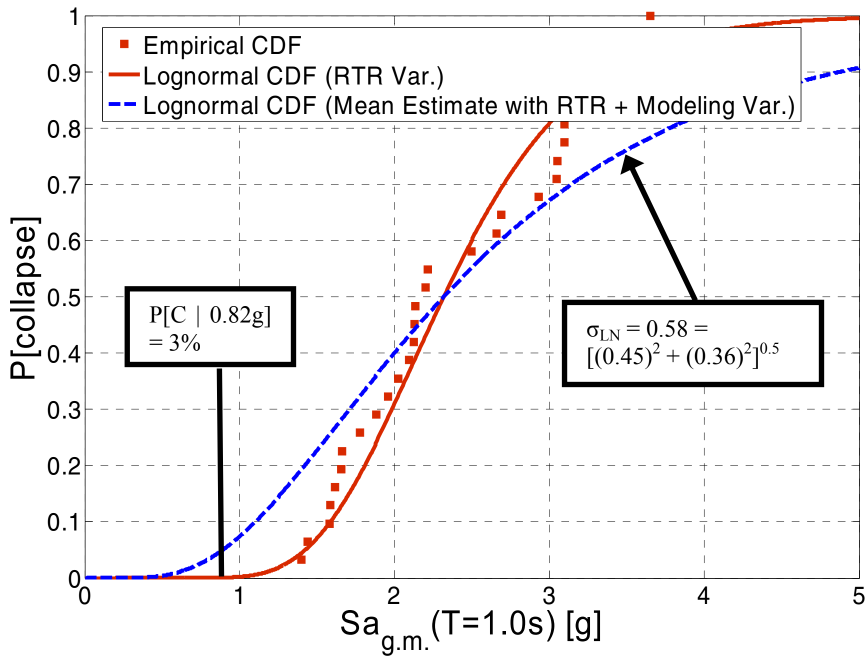

Fig. 5.9 Collapse distributions showing distribution only considering variability between ground motion records (solid red) and distribution with variance expanded to include effects of modeling uncertainty (dashed blue).

5.6.4 Summary

This work uses the mean estimate approach when making performance predictions, as opposed to making predictions at a given level of prediction confidence. Using the mean estimate approach avoids philosophical debates regarding whether uncertainty should be considered as "randomness" (aleatory) or "lack of knowledge" (epistemic). The mean estimate approach also results in predictions that are more stable, because predictions at a given level of prediction confidence are highly dependent on the arbitrary choice of prediction confidence level.

In addition, we decided to use the mean estimate approach because it is simpler. This will be a great benefit when working to get this methodology adopted into engineering practice (Cornell 2005).

5.7 RESULTS FOR PROBABILISTIC PREDICTION OF COLLAPSE PROBABILITY AND RATE

This chapter was the basis for the uncertainty results presents previously in Section 2.6.5. This section combines all of the collapse simulation results presented in Section 2.6.5 with the collapse uncertainty analyses presented in this chapter in order to compute the collapse probabilities and the yearly collapse rates for each design variant considered in this study. The collapse uncertainty was computed by the FOSM method for Design A only; we assume that this level of modeling uncertainty is generally representative of moment-frame buildings examined in this report.

5.7.1 Mean Estimates of Probability and Annual Frequency of Collapse

This study primarily uses the *mean estimates* (Section 5.6.3) of the mean annual frequency of collapse ($\lambda_{collapse}$) and the probability of collapse given the 2%-in-50-years event (P[Col | $Sa_{2/50}$]). The *mean estimate* is used in contrast to computing values at a certain prediction confidence level, as has been done in some recent studies (Cornell et al. 2002; Yun et al. 2002; Jalayer 2003).

Figure 5.10 shows the collapse CDF (from Fig. 5.9) and the ground motion hazard curve for the site at a period of 1.0 sec. This section discusses how these two figures are used to compute the mean estimate of the mean annual frequency of collapse ($\lambda_{collapse}$). The estimates of $\lambda_{collapse}$ and P[Col | $Sa_{2/50}$] are then presented at the end of this section for all the building design variants of Chapter 2.

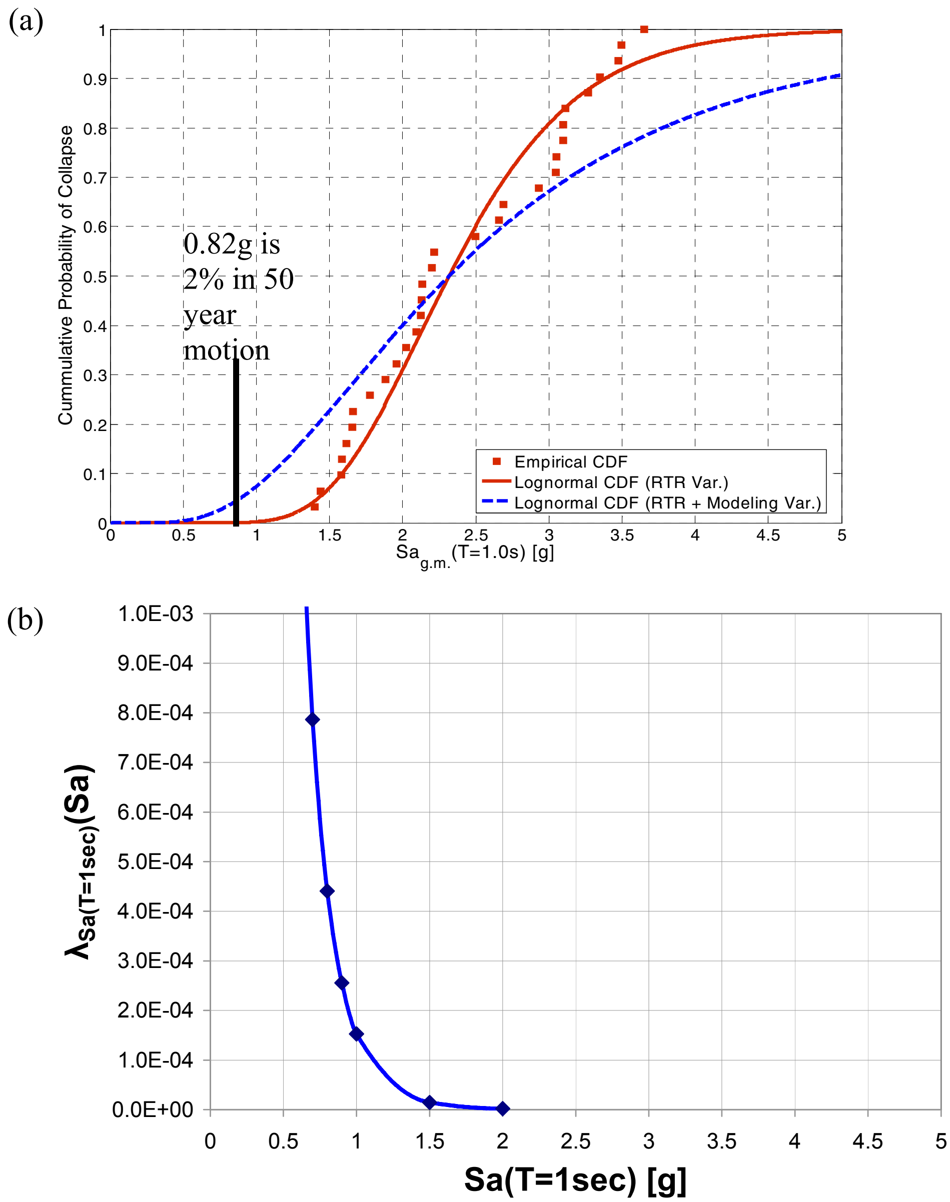

Fig. 5.10 **(a) Collapse predictions for Design A, ground motion Bins 4A and 4C, showing collapse capacity CDF with only RTR variability and with modeling/design variability included; (b) ground motion hazard curve used to compute $\lambda_{collapse}$.**

The mean annual frequency of collapse ($\lambda_{collapse}$) is computed using Equation 5.4 (Ibarra 2003, Eq. 7.10).

$$\lambda_{collapse} = \int P\left[Sa_{collapse} \leq x\right] \cdot \left|d\lambda_{IM}(x)\right| \tag{5.4}$$

where $\lambda_{collapse}$ is the mean annual frequency of collapse,

$P\left[Sa_{collapse} \leq x\right]$ is the probability that x exceeds the collapse capacity (i.e., the probability that the building is collapsed when the ground motion intensity is x), and $\lambda_{IM}(x)$ is the mean annual frequency of the ground motion intensity exceeding x (i.e., a point on the ground motion hazard curve).

There are many ways to approximate Equation 5.4. Baker provides a closed-form solution that involves fitting the hazard function (Baker 2003, Eq. 3.66). To avoid error induced by fitting an exponential function to the hazard curve, we use the 15 discrete hazard points computed by Goulet and Stewart (Goulet et al. 2006a) and use the PCHIP (Piecewise Cubic Hermite Interpolating Polynomial) procedure to interpolate between these points (Matlab 2005). We then use this interpolated curve when completing the numerical integration required to evaluate Equation 5.4.

Table 5.11 presents the estimated $\lambda_{collapse}$ and P[Col | $Sa_{2/50}$] for all design variants considered in this study (from Chapter 2). This table also shows the median collapse capacity, $\sigma_{LN,RTR(Sa,col)}$, the collapse capacity margin, and the parameters for the fitted lognormal distributions.

Table 5.11 Summary of collapse predictions (mean estimates) for all design variants, including probability of collapse, annual frequency of collapse, and effects of modeling uncertainty.

					With only record-to-record variability			With record-to-record and modeling uncertainty (mean estimate approach)			
Design	Ground Motion Set	Median (Sa,col) [g]	Collapse Margin (median / $Sa_{2/50}$) [c]	$\mu_{LN(Sa,col)}$	$\sigma_{LN,RTR\,(Sa,col)}$	$\lambda_{collapse}$ (10^-6)	P[Col | $Sa_{2/50}$] [a]	$\sigma_{LN,model\,(Sa,col)}$	$\sigma_{LN,Total\,(Sa,col)}$	$\lambda_{collapse}$ (10^-6)	P[Col | $Sa_{2/50}$] [a]
A	4A	2.19	2.7	0.86	0.36	9.2	0.00	0.45	0.58	69	0.03
B	4A	2.08	2.5	0.78	0.31	9.0	0.00	0.35	0.47	38	0.02
C	4A**	2.35	2.9	0.85	0.46	24.8	0.01	0.45	0.64	125	0.05
D[b]	4A	0.95	1.2	-0.038	0.39	663	0.34	0.35	0.52	1300	0.38
E	4A	1.95	2.4	0.71	0.32	14.5	0.00	0.35	0.47	55	0.03
F	4A	1.86	2.3	0.57	0.38	48.1	0.02	0.35	0.52	139	0.07
G	4A	1.88	2.3	0.67	0.34	20.6	0.01	0.35	0.49	71	0.04
H	4A	1.92	2.3	0.64	0.30	16.2	0.00	0.35	0.46	62	0.03

a - 2% in 50 year ground motion level: Sa(1sec) = 0.82g
b - columns designed for strength demand and not for SCWB; this is not a code-conforming design
c - collape margin is ratio of median collapse capacity to $Sa_{2/50}$

Table 5.11 shows that the probability of collapse for the 2%-in-50-years ground motion, even including additional uncertainties for structural modeling, is only 2–7% for the various code-conforming buildings. For these same buildings, the mean annual frequency of collapse ($\lambda_{collapse}$) ranges from 40–140 x 10^{-6}.

5.7.2 Disaggregation of Mean Annual Frequency of Collapse

To better understand the spectral acceleration levels contributing most to the $\lambda_{collapse}$, Figure 5.11 shows a disaggregation of $\lambda_{collapse}$ (Baker 2005). This disaggregation diagram is simply created by keeping track of each term of Equation 5.4 during the process of numerical integration. Each term is then normalized by $\lambda_{collapse}$, so the area under the disaggregation plot is equal to is one (unity). This figure shows the results for Designs A and D, based on the hazard curve in Figure 5.10. These figures show that for Design A (expected perimeter code-conforming design), ground motions with $Sa_{g.m.}$(T=1sec) from 0.8g–2.0g (peak at 1.35g) dominate the collapse hazard, while 0.3g–1.5g (peak at 0.60g) dominate the collapse hazard for Design D (perimeter non-code-conforming design that does not comply with the strong-column weak-beam design requirements). These figures also show the median collapse capacities for each structure. This reveals that, even though these two buildings have a large difference in the median collapse capacity, the ground motion intensity level that most dominates the collapse hazard is consistently at 60% of the median structural collapse capacity.

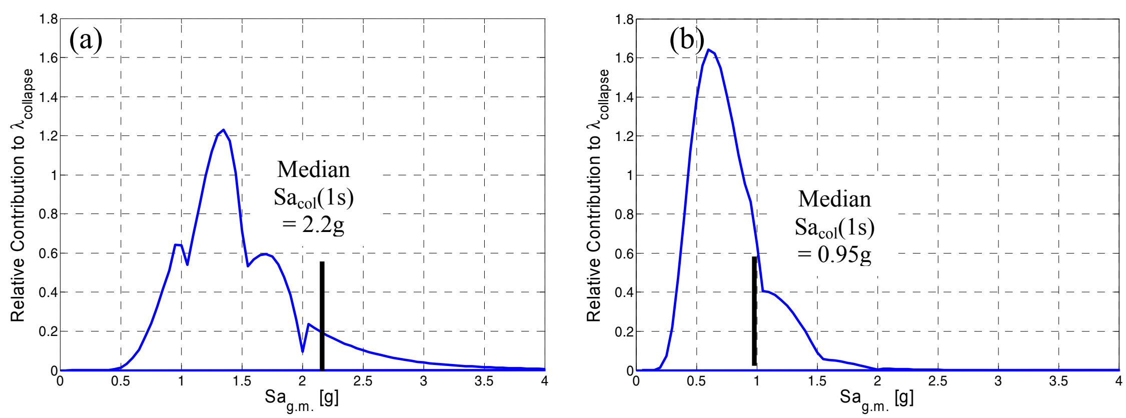

Fig. 5.11 Annual frequency of collapse disaggregation. $\lambda_{collapse}$ computed with fitted lognormal distribution considering only record-to-record variability and using ground motion Bin 4A; (a) for Design A and (b) for Design D.

5.7.3 Estimates of Probability and Annual Frequency of Collapse at Given Level of Prediction Confidence

Section 5.6.2 discussed the approach where the collapse probability and the mean rate of collapse computed at a given level of prediction confidence. Table 5.12 is similar to Table 5.11 but presents predictions at the 10% and 90% levels of prediction confidence instead of using the mean estimate approach. Here the uncertainty is divided between aleatory and epistemic as discussed in the illustrative example of Figure 5.6, where the record-to-record variability is considered aleatory and all of the structural modeling uncertainties are considered epistemic.

Table 5.12 Summary of collapse predictions for all design variants at 10% and 90% levels of prediction confidence, including probability of collapse, annual frequency of collapse, and effects of modeling uncertainty.

						10% Confidence Level			No Modeling Uncert.			90% Confidence Level		
Design	Ground Motion Set	Counted Median (Sa,col) [g]	$\mu_{LN(Sa,col)}$	$\sigma_{LN,RTR (Sa,col)}$	$\sigma_{LN,model (Sa,col)}$	Shifted Median[a] (Sa,col) [g]	$\lambda_{collapse}$ (10^-6)	P[Col | $Sa_{2/50}$][b]	Shifted Median[a] (Sa,col) [g]	$\lambda_{collapse}$ (10^-6)	P[Col | $Sa_{2/50}$][b]	Shifted Median[a] (Sa,col) [g]	$\lambda_{collapse}$ (10^-6)	P[Col | $Sa_{2/50}$][b]
A	4A	2.19	0.86	0.36	0.45	4.2	4.3	0.00	2.36	9.2	0.00	1.1	370	0.23
B	4A	2.08	0.78	0.31	0.35	3.3	3.3	0.00	2.18	9.0	0.00	1.2	190	0.12
C	4A[c]	2.35	0.85	0.46	0.45	4.0	2.6	0.00	2.34	24.8	0.01	1.0	800	0.33
D[d]	4A	0.95	-0.04	0.39	0.35	1.4	155	0.09	0.96	663	0.34	0.4	9400	0.95
E	4A	1.95	0.71	0.32	0.35	3.1	1.3	0.00	2.03	14.5	0.00	1.1	280	0.19
F	4A	1.86	0.57	0.38	0.35	2.6	6.2	0.00	1.77	48.1	0.02	0.9	830	0.41
G	4A	1.88	0.67	0.34	0.35	3.0	2.1	0.00	1.95	20.6	0.01	1.0	390	0.25
H	4A	1.92	0.64	0.30	0.35	3.0	1.4	0.00	1.90	16.2	0.00	1.0	310	0.22

a - Actually the exponential of the shifted μ_{LN}(Sa,col)
b - 2% in 50 year ground motion level: Sa(1sec) = 0.82g
c - Records 94103 and 94107 removed due to numerical problems
d - columns designed for strength demand and not for SCWB; this is not a code-conforming design

5.8 EFFECTS OF FOSM APPROXIMATIONS AND CORRELATION ASSUMPTIONS

Section 5.5.2 discusses how the correlation assumptions and FOSM approximation can *significantly alter* the estimated uncertainty in the collapse capacity coming from uncertainty in the structural modeling ($\sigma_{LN,modeling(Sa,col)}$). Table 5.9 showed that when considering modeling and design uncertainties, the $\sigma_{LN,modeling\&design(Sa,col)}$ can range from 0.21 for the uncorrelated case to 0.54 for the case of full correlation between variables where high correlation is reasonable. In addition, the value can range between 0.54 and 0.67 depending on if the FOSM approximation is done with the original data or the natural logarithm of the data. This shows that a precise estimate of modeling uncertainty is difficult.

This section discusses how the large variability in the value of $\sigma_{LN,modeling\&design(Sa,col)}$ carries over to a large variability in the estimates of the P[Col | $Sa_{2/50}$] and $\lambda_{collapse}$. Figure 5.12 shows the relationship between modeling (and/or design) uncertainty and the mean estimate of $\lambda_{collapse}$ for Design A using ground motion Set 4A. This shows that for the range of 0.21–0.67 for modeling (and/or design) uncertainty, the mean estimate of the $\lambda_{collapse}$ ranges from $9.2x10^{-6}$ to $300x10^{-6}$, *a change of more than an order of magnitude*. Figure 5.13 similarly shows the effect on the estimate of P[Col | $Sa_{2/50}$]. For the same range of modeling (and/or design) uncertainty, 0.21–0.67, the P[Col | $Sa_{2/50}$] varies by an *order of magnitude*, from 0.6% to 8.0%.

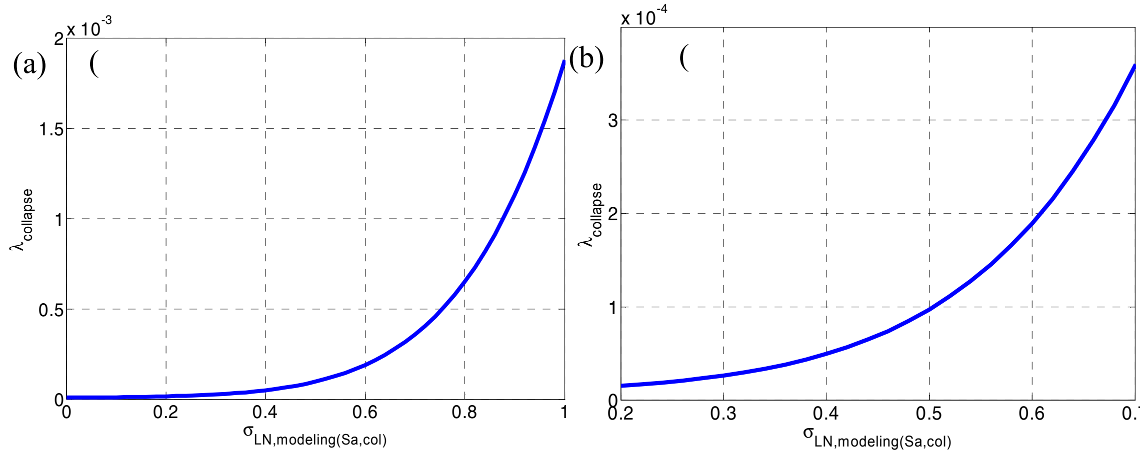

Fig. 5.12 Effect of modeling (and/or design) uncertainty on mean estimate of $\lambda_{collapse}$, for Design A using ground motion Bin 4A; (a) full view of graph and (b) zoomed-in for important values of uncertainty.

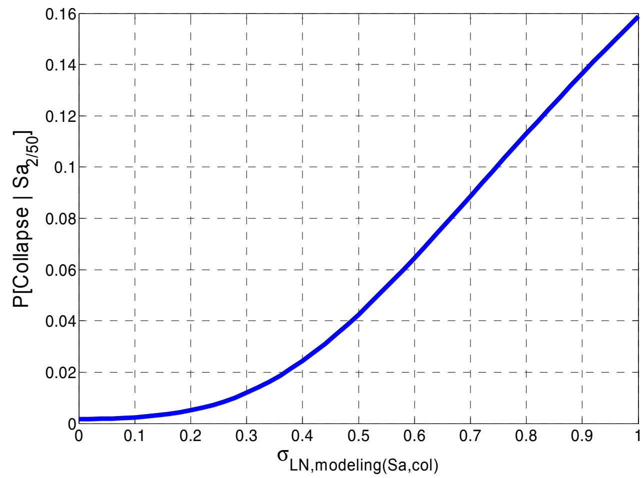

Fig. 5.13 Effect of modeling (and/or design) uncertainty on mean estimate of P[Col | $Sa_{2/50}$] for Design A using ground motion Bin 4A.

5.9 SUMMARY AND CONCLUSIONS

This chapter looked at the question of uncertainties in structural modeling, focusing specifically on the resulting uncertainty in the predicted collapse capacity. This study accounted for uncertainties in structural design, uncertainties in structural behavior and modeling, and ground motion variability. We did not address the question of other important uncertainties such as human error in design and construction.

In the effort to predict the final uncertainty in collapse capacity resulting from uncertainty in design and modeling, we (a) quantified the uncertainties using the results from previous research and additional calibrations to test data, (b) used judgment to establish reasonable correlations between variables, then (c) used the first-order second-moment (FOSM) approximation to propagate the uncertainties. In this process, we found that element plastic rotation capacity is the variable that most significantly impacts the collapse capacity for this building (note that Ibarra shows that the strain-softening slope is also important, but we did not find this to be the case for the 4-story Design A building). In addition, we found that the correlation between variables is the single most important factor when estimating the effects of uncertainties. Correlation assumptions can change the estimated uncertainty in collapse capacity by up to a factor of three-five; this leads to a change in the mean annual frequency of collapse estimates by an *order of magnitude*.

For this single 4-story RC SMF building, we found that the best-estimate of collapse capacity uncertainty is $\sigma_{LN(Sa,col)}$ = 0.35 when considering only modeling uncertainty, and $\sigma_{LN(Sa,col)}$ = 0.45 when considering uncertainties in both modeling and design. The above values reflect uncertainty only from structural modeling and/or design, and do not include effects of record-to-record variability.

We use the mean estimate approach when computing P[C | $Sa_{2/50}$] and $\lambda_{collapse.}$ This approach is in contrast to the approach where predictions are made at a level of prediction confidence. Using the mean estimate approach, we conclude that for the seven code-conforming building designs evaluated, the P[C | $Sa_{2/50}$] = 0.02–0.07 and $\lambda_{collapse}$ = $40x10^{-6}$ – $140x10^{-6}$; these estimates include design uncertainty (as appropriate), modeling uncertainty, and the effects of ground motion variability.

For comparisons, if we instead had made predictions at a 90% prediction confidence level, the following would obtain: P[C | $Sa_{2/50}$] = 0.12–0.41 and $\lambda_{collapse}$ = $190x10^{-6}$ - $830x10^{-6}$. We see that use of a 90% prediction confidence level causes the P[C | $Sa_{2/50}$] to be +22% larger (or a factor of 5.6x larger) and the $\lambda_{collapse}$ to be a factor of 5.7x larger.

6 Archetypes: Generalized Collapse Performance Predictions for Class of Reinforced Concrete Special Moment-Frame Buildings

6.1 INTRODUCTION, MOTIVATION, AND PURPOSE

In previous research, the authors have developed a performance-based earthquake engineering (PBEE) approach to simulate the collapse safety of buildings in large earthquakes. The authors have previously applied this methodology to assess the collapse performance of a single 4-story reinforced concrete (RC) special moment-frame (SMF) building (Goulet et al. 2006a; Haselton et al. 2007e, Chapter 2). This study extends the previous research with the goals of:

- developing a strategy for extending the assessment of a *single* building to a *class* of buildings.
- utilizing this methodology to examine the collapse safety of the class of RC SMF buildings designed by current building codes.

This paper starts by presenting the methodology proposed to assess the collapse performance of a generalized class of a seismic resisting structural system. This process starts with articulating the possible failure/collapse modes of the structural system, and then developing a structural model or alternative strategies to assess the modes important to collapse behavior. The process then involves defining the range of building designs (height, layout, etc.) that describe the building class of interest, and designing a set of buildings that investigates this range. The collapse capacity of each structural design is then evaluated. To the extent that the set of designs represent the range of all possible designs within the specified structural system class, this provides a collapse safety evaluation for that class.

This method is applied to assess the collapse safety of RC SMF buildings designed by current building codes. These predictions shed light on the expected collapse performance implied by building codes and standards, including some insights on how the collapse performance might be improved.

6.2 ARCHETYPE FRAMEWORK AND METHODOLOGY

6.2.1 Overview

The concept of archetypical buildings is proposed as part of a strategy for characterizing building systems to systematically evaluate their performance and quantify the appropriate parameters that should be used in their seismic design. The archetype framework bridges the gap between performance predictions for a single specific building (as described in previous work; Goulet et al. 2006a; Haselton et al. 2007e) and the generalized predictions needed to quantify the performance of a full class of structures. While the focus here is on life-safety risks associated with building collapse, the concepts can be broadly applied to other aspects of building performance.

The key elements of the framework are as follows:

Archetype defined: "The original pattern or model of which all things of the same type are representations or copies" (Merriam-Webster Dictionary).

Archetype design space: Defines ranges of key structural design parameters that prescribe the bounds of the structural system category for which one has established seismic design criteria. A *representative structural archetype design* is a specific structural design included within the defined archetype design space.

Archetype analysis model: A mathematical model used to simulate the general response of buildings that belong to a specific archetype.

The archetypical framework provides an organized approach to evaluating seismic performance for a certain class of structures that are designed based on a specified set of design requirements; these requirements may be ones either existing in the building code, or developed for a newly proposed system. In this study, we apply this framework to reinforced concrete moment-frame buildings that conform to design requirements for special moment frames (RC-SMF), as defined in ASCE 7-02 (ASCE 2002). The following sections summarize the procedure and further details on establishing the scope of the archetype assessment.

6.2.2 Archetype Assessment Procedure

The following steps outline the archetype procedure to assess the performance of a class of buildings.

1. Establish the *archetype design space*.
    a. Explore the relationship between design variables and key characteristics affecting seismic performance and identify critical design variables. For example, in columns of RC SMFs, the column axial load ratio is a parameter that significantly affects the column plastic rotation capacity. Therefore, design parameters that affect the axial load ratio in a column (e.g., bay sizes, building height, effects of joint shear provisions, and lateral load intensity) should be considered in defining the archetype design space.
    b. Establish bounds for the key design variables that define the extent of the archetype design space. This could include, for example, the range of building heights (number of stories), framing span lengths, etc., which are permitted within the archetype design space, as allowed by the governing design provisions and commonly expected in structural design practice.
2. Develop an *archetype analysis model*.
    a. Assess the failure modes that can occur for the structural archetype designs. It is anticipated that all significant failure modes will be assessed by either (i) ruling out those failure modes that are unlikely based on system design and detailing requirements, (ii) explicitly simulating the failure mode through inelastic analyses, or (iii) accounting for the mode in post-analysis checks by using appropriate fragility functions with structural responses that are estimated from inelastic dynamic analyses.
    b. Devise an archetype analysis model that captures failure modes identified in (2a). This model may not need to represent the entire structure, provided that the archetype analysis model sufficiently represents expected behavior and failure modes. The model should be general enough to permit evaluation of the range of characteristics incorporated in the archetype design space. The validity of a simplified model may be assessed through comparison with a more detailed analysis model of a specific building.

3. Develop multiple realizations of *representative structural archetype designs* to explore the range of the archetype design space.
4. Create an *archetype analysis model* for each structural design from (3) and do incremental dynamic analysis (IDA) to predict collapse.
5. Account for non-simulated collapse modes using post-analysis checks that combine structural responses with appropriate fragility functions (see 2a-iii). Combine these findings with the IDA results from (4) to develop the prediction of collapse performance.
6. Synthesize the results of the archetype building assessment studies (from 3 to 5) to develop general conclusions regarding the performance of the class of buildings represented by the archetype.

6.2.3 Expected Outcomes of Archetype Building Assessment

Collapse simulations are performed for each of the archetype analysis models developed, resulting in prediction of collapse capacity and probability for each of archetype designs. With the assumption that the set of representative archetype designs cover the range of possible building designs[1], these results from each design can be used to make general conclusions regarding the collapse safety performance of the full class of structures that the archetype represents.

6.3 ARCHETYPE METHODOLOGY APPLIED TO REINFORCED CONCRETE SPECIAL MOMENT-FRAME BUILDINGS

This section provides as example of how the archetype framework can be applied to the class of reinforced concrete special moment-frame buildings designed according to current building code provisions (ICC 2003; ASCE 2002; ACI 2002).

[1] Due to the large variability in what future designs may be created, it is virtually impossible to capture all possible future designs. Nevertheless, the set of representative archetype designs should cover the range of designs that could occur within the archetype design space, to the extent possible.

6.3.1 Establishing the Archetype Design Space

To establish the archetype design space, design parameters that significantly affect seismic performance are first identified, then bounds on each design parameter are established according to what is allowed by the building code and commonly done in engineering practice. Table 6.1 presents a list of parameters that are important to the seismic performance of an RC frame building. This table relates each of these parameters to physical properties of the structure and then to specific design parameters/decisions, such as building height, bay spacing, etc. This organizational approach is useful for deciding which of the many design parameters should be the focus of close investigation.

This table focuses on what affects the three fundamental aspects of seismic performance: deformation capacity, strength, and stiffness. For example, element deformation capacity is affected by many things such as the axial load ratio and element detailing, while the system deformation capacity is affected by the element deformation capacity and other aspects of system behavior. In this assessment, we do not include the benefit of the strength and stiffness of the gravity system. We also assume that the controlling mode of failure is sidesway collapse, assuming that the gravity system is able to displace without causing a local collapse prior to the onset of global sideway collapse (discussed in Section 6.4.5.1).

Table 6.1 Parameters important to seismic performance of RC SMF and their dependence on design decisions.

Parameters Important to Seismic Performance	Related Physical Properties of Structure	Related Design Decisions and Design Parameters
Column and beam plastic rotation capacity	Axial load ratio (ν)	Building height, bay width, ratio of tributary areas for gravity and lateral loads
	Column aspect ratio (L_s/H)	Building height, bay width, story heights, allowable reinforcement ratio
	Confinement ratio (ρ_s)	Confinement ratio used in design
	Stirrup spacing (s)	Stirrup spacing used in design
	Longitudinal bar diam. (d_b)	Longitudinal bar diam. used in design
	Reinforcement ratios (ρ, ρ')	Reinforcement ratio allowed in design
	Concrete strength (f'_c)	Concrete strength used in design
Element strengths	All element strengths	Conservatism of engineer, dead and live loads used in design
	All element strengths	Dominance of gravity loads in design. This is affected by tributary width and the decision of space versus perimeter framing system.
	Beam strengths	Slab width (steel) assumed effective with beam
	Column strengths	Ratio of factored to expected axial loads, level of conservatism in applying strong-column weak-beam provision
System deformation capacity, including number of stories in collapse mechanism	Strength/stiffness irreg.	How column sizes are stepped down over height of building, strength/stiffness irregularity, ratio of first to upper story heights
	Element def. capacity	(described above)
	Dominance of P-Delta	Building height, gravity loading
Lateral stiffness of frame	Member sizes in frame	Member/joint/footing stiffnesses used in design, effective slab width, ratio of tributary areas for gravity and lateral loads
	Member sizes in frame	Conservatism of engineer, dead and live loads used in design
Gravity system strength/stiffness	Gravity system	Not considered in this assessment

The design parameters that are likely to tangibly affect the seismic performance from the third column of Table 6.1 are re-organized and repeated in the first column of Table 6.2. The second column of Table 6.2 summarizes the range of values these design parameters may typically take on for common engineering practice. One important design variable of Table 6.2 is the ratio of tributary areas for gravity and lateral loads, which is primarily affected by whether the building is designed as a space or perimeter frame system. Table 6.1 shows that we consider a range of 0.1–1.0 for this design variable, and Figure 6.1 illustrates how this range was selected.

These parameters and ranges from Table 6.2 provide the basis for defining a finite number of design realizations for study using archetype analysis models.

Table 6.2 Ranges of design parameters included in definition of archetype design space of RC SMF building.

Design Parameters to Include in Archetype Design Space	Range Considered in Archetype Design Space
Structural System:	
Reinforced Concrete Special Moment Frame (as per 2003 IBC, ACI 318-05)	All designs meet code requirements
Seismic design level	IBC transition region, Design Category D
Seismic framing system	Both perimeter and space frames used
Configuration:	
Building height	Stories: 1, 2, 4, 8, 12, 20
Bay width	20-30 feet
First story and upper story heights	15/13 feet
Element Design:	
Confinement ratio (ρ_s) and stirrup spacing (s)	Conforming to ACI 318-05.
Concrete compressive strength	5-7 ksi
Longitudinal rebar diameters (d_b)	#8 and #9 commonly used
Loading:	
Ratio of frame tributary areas for gravity and lateral loads (A_{grav}/A_{lat})	0.1 (perimeter frame) - 1.0 (space frame)
Design floor dead load (153-slab and str. members, 10-partitions, 12-MEP/Ceil./Finishes)	175 psf
Lower/upper bounds on design floor dead load (for checking sensitivity)	150 - 200 psf
Design floor live load	Constant 50 psf
Irregularities and stepping of strength and stiffness:	See matrix of designs
Other important design conservatisms and assumptions:	See table of design assumptions

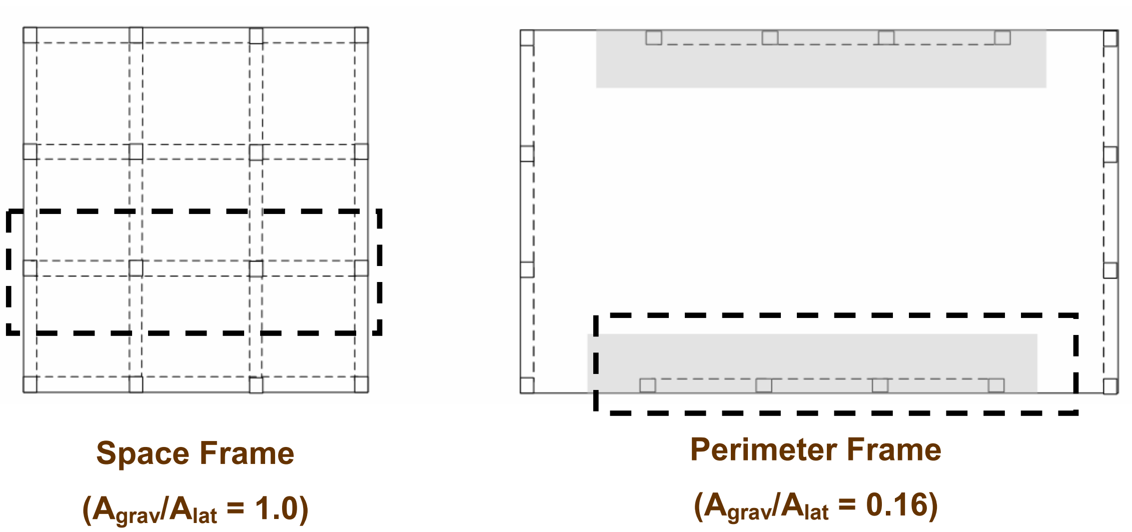

Fig. 6.1 Illustration of gravity/lateral tributary areas for space frame and perimeter frame building.

6.3.2 Representative Archetypical Designs

Based on information summarized in Tables 6.1 and 6.2, we developed a matrix of 30 archetypical designs, as summarized in Table 6.3. The designs are for six building heights from 1–20 stories, 2-bay widths (20′ and 30′), perimeter and space frames, and they cover a range of strength and stiffness variations over the building height that are permissible within the ASCE7-02 (ASCE 2002) seismic design provisions.

Table 6.3 Matrix of archetypical designs for SMFs.

Design Information					
Design Number	**No. of stories**	**Bay Width [ft]**	**Tributary Areas: Gravity/ Lateral**	**Strength/ Stiffness Distribution Over Height**	**Foundation Fixity Assumed in Design [a]**
1	1	20	Space (1.0)	A	GB
2					P
3					F
4			Perimeter (0.11)	A	GB
5	2	20	Space (1.0)	A	GB
6					P
7					F
8			Perimeter (0.11)	A	GB
9	4	20	Perimeter (0.11)	A	GB
10				C	GB
11			Space (1.0)	A	GB
12		30	Perimeter (0.17)	A	GB
13			Space (1.0)	A	GB
14	8	20	Perimeter (0.17)	A	GB
15		20	Space (1.0)	A	GB
16				C	GB
17				B (65%)[b]	GB
18				B (80%)[b]	GB
19				B (65%)[c]	GB
20				B (80%)[c]	GB
21	12	20	Perimeter (0.17)	A	GB
22		20	Space (1.0)	A	GB
23				C	GB
24				B (65%)[b]	GB
25				B (80%)[b]	GB
26				B (65%)[c]	GB
27				B (80%)[c]	GB
28		30	Space (1.0)	A	GB
29	20	20	Perimeter (0.17)	A	GB
30		20	Space (1.0)	A	GB

a - Assumed only in the design process. OpenSees models use grade beam, basement column, and soil stiffnesses.
b - Only first story designed to be weak.
c - First and second stories designed to be weak.
A - Expected practitioner design; strength and stiffness stepped over height as done in common design practice.
B (%) - Weak story; done by sizing the target weak story(ies) based on code requirements and then strengthening stories above. % is the percentage of strength in the weak story(ies) as compared to the stories above.
C - conservative design; neither size nor reinforcement of beams/columns are decreased over building height
F - Fixed.
GB - "Grade Beam" - this considers the rotational stiffness of the grade beam and any basement columns.
P - Pinned.

Each of the buildings shown in Table 6.3 is fully designed by the governing provisions of the 2003 IBC (ICC 2003), ASCE7-02 (ASCE 2002), and the ACI 318-02 (ACI 2002). As such, they are distinct from generic structures that are often used in research to investigate design parameters. These buildings are designed based on all governing code requirements such as strength, stiffness, capacity design, detailing, etc. Thus, the design reflects how certain design rules interact to result in structural parameters, such as overstrength, that may be different than one might expect. In looking at the results of this study, we have found that seemingly subtle design requirements have important effects on the design and resulting structural performance.

The frames are designed to the minimum requirements of the building code, with some slight conservatisms to account for discrete design decisions; these decisions are outlined below in Table 6.4.

6.3.2.1 Differences in Updated ASCE7-05 Provisions

The buildings used in this study were designed according to the ASCE7-02 provisions (ASCE 2002). It is important to recognize that the updated ASCE7-05 provisions (ASCE 2005) have a lower design base shear strength for taller structures, due to removal of a provision for minimum base shear that affects these buildings. The effects of this change to the 2005 provisions are discussed later in Section 6.5.3.

6.3.2.2 Design Assumptions

Table 6.4 lists the important designs assumptions that are used in the design process and in the related elastic structural model. The modeling assumptions employed in the OpenSees assessment model differ and are discussed in Section 6.3.4.1.

Table 6.4 Assumptions used in design of archetype buildings.

Design Parameter	Design Assumption
Assumed Stiffnesses:	
Member stiffness assumed in design: Beams	$0.5EI_g$ (FEMA 356)
Member stiffness assumed in design: Columns	$0.7EI_g$ for all axial load levels (practitioner rec.)
Slab consideration	Slab not included in stiffness/strength design
Footing rotational stiffness assumed in design* - 2-4 story	Effective stiffness of grade beam
Footing rotational stiffness assumed in design* - 8-20 story	Basement assumed; ext. cols. fixed at basement wall, int. cols. consider stiffness of first floor beam and basement column
Joint stiffness assumed in design	Elastic joint stiffness
Expected Design Conservatisms:	
Conservatism applied in element flexural and shear (capacity) strength design	1.15 of required strength
Conservatism applied in joint strength design	1.0 of required strength
Conservatism applied in strong-column weak-beam design	Use expected ratio of 1.3 instead of 1.2
* These are the footing rotational stiffnesses assumed in the structural design.	

In addition to the above design assumptions, we recommend the following guidelines in design:

- Use an approximate 6″ step size when reducing the sizes of beams and columns over the height of the building; keep element sizes constant until the 6″ step is possible.
- Use a beam concrete strength of f′c = 5ksi.
- Start the design using f′c = 5ksi strength concrete. Increase column concrete strength as needed, up to f′c = 7ksi to help satisfy joint shear design requirements. The maximum of f′c = 7ksi is chosen to avoid concrete placement coordination problems with lower strength slab and beam concrete at joints.

6.3.2.3 Review of Designs by Practitioner

To ensure that each of the archetype designs is representative of current design practice, we worked closely with a practicing engineer (Hooper 2006). Before the designs were started, the engineer reviewed all relevant design assumptions (Section 6.3.2.1) to ensure consistency with common design practice; the next section discusses these design assumptions. In addition, the engineer provided a detailed review and feedback for 22 of the 30 archetype designs[2] to ensure consistency with common design practice.

6.3.2.4 Treatment of Overturning Effects

The 3-bay archetype analysis model is generally considered to represent significant design and behavioral features of a real building, which would likely have more framed bays, especially for taller buildings. For the taller buildings, if we simply designed a 3-bay frame, neglecting the fact that the real buildings will have more bays, the overturning effects may make the column design and behavior unrealistic.

To address this issue in a tractable manner, we first assumed typical building footprint sizes for the various buildings, as shown in Table 6.5. To approximately correct the column axial force demands, we used these assumed building sizes, and reduced the lateral loads by a factor of [(base width of real building) / (base width of archetype design frame)]. This correction

---

[2] All designs were reviewed except the 1-story designs (ID 2061-2063, 2069) and four of the weak-story designs (ID 2065-2068).

was applied only to column axial forces due to overturning effects; all other force demands are based on the standard building code design lateral loads.

Table 6.5 Representative building geometries for each building height.

Building Height	Story Heights (first, upper)	Plan Dimensions
1-4 Story	15', 13'	120' x 180'
8-20 Story	15', 13'	120' x 120'

6.3.3 Building Site

We design the archetype models (from Table 6.3) for a general high seismic site in California (soil class S_d, S_{ms} = 1.5g, and S_{m1} = 0.9g). While this characterization of the site hazard is sufficient for a generic performance assessment, such as what is required by the Applied Technology Council Project 63 assessment method, it does not provide sufficient hazard information for a full performance assessment. To quantify the collapse performance in specific terms, it is necessary to consider specific locations where the archetype designs could hypothetically be located. For example, considering a specific site allows calculation of the collapse probability for the 2%-in-50-years ground motion ($P[C|Sa_{2/50}]$) and the mean annual frequency of collapse ($\lambda_{collapse}$).

To evaluate performance more explicitly, we chose a site in northern Los Angeles that has been the topic of recent study and has a soil type and seismic demands that are consistent with those used in design of the archetype buildings. The probabilistic seismic hazard analysis for this site was completed by Goulet and Stewart (Goulet et al. 2006a; Haselton et al. 2007e). Goulet completed the hazard analyses for periods of 0.0–2.0 sec and spectral accelerations up to 2.0g. For lack of more complete information, we extrapolate the spectral demands assuming a 1/T spectral shape, for buildings with a period higher than 2.0 sec, which tends to be a conservative assumption. However, since the building periods considered in this study generally do not exceed 3 sec, the error should be minimal. To approximate the hazard values for spectral accelerations greater than 2.0g, we fit an exponential curve ($\lambda = k_o Sa^k$) to the data between 0.8 to 2.0g and use the functional fit for extrapolation; since these high spectral accelerations have a long return period, we expect them to have minimal impact on the computed collapse rates.

Figure 6.2 compares the 2%-in-50-years hazard to the maximum considered earthquake motion (MCE) used in building code design (ICC 2003). The values are relatively close, with the exception of 0.3–1.2 sec periods, where the 2%-in-50-years demands are lower than the code demands. For comparison, the United States Geological Survey (USGS) predicted 2% PE in 50-years demands are 1.74g and 0.92g for 0.2 sec and 1.0 sec, respectively, which include factors for soil class Sd (USGS 2006).

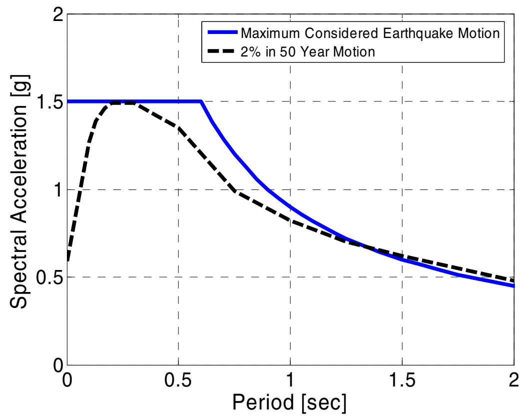

Fig. 6.2 MCE ground motion spectrum compared to equal hazard spectrum for 2%-in-50-years motion at Los Angeles site.

The hazard information will permit assessment of the $P[C|Sa_{2/50}]$ and the mean annual frequency of collapse ($\lambda_{collapse}$) for this single site in Los Angeles. While this site is considered to be generally representative of far-field seismic conditions of coastal California, future research to further generalize these collapse predictions could include selecting many additional sites and assessing the $P[C|Sa_{2/50}]$ and $\lambda_{collapse}$ for these same buildings at the various sites. This would provide useful information to show how the collapse performance varies with the site hazard.

6.3.4 Archetype Analysis Model and Collapse Assessment Methodology

To capture the deterioration and collapse modes of RC SMF buildings, we follow the careful assessment process presented in Deierlein et al. (2005a). We use the element model developed by Ibarra et al. (2005, 2003) and implemented into OpenSees by Altoontash (2004), which captures the modes of monotonic and cyclic deterioration that precipitate sidesway collapse. Figure 6.3 shows the definition of the monotonic backbone for this model, as well as an illustration of the cyclic behavior.

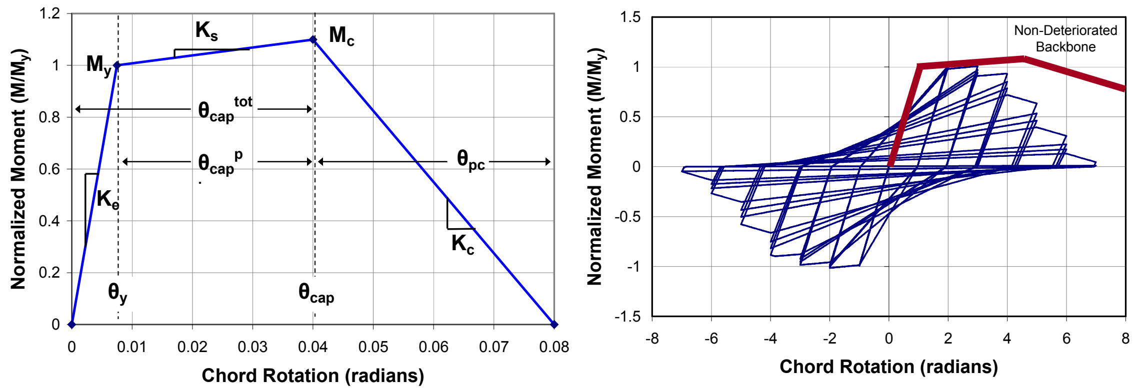

Fig. 6.3 Monotonic and cyclic behavior of component model used in study. Model developed by Ibarra, Medina, and Krawinkler (2005) (after Haselton et al. 2007b, Chapter 4; Haselton et al. 2007f).

We calibrated this element model to 255 tests of reinforced concrete columns from the PEER Structural Performance Database (Berry and Eberhard et al. 2004; PEER 2006a). This calibration effort resulted in a set of empirical regression equations to predict the monotonic and cyclic modeling parameters as a function of physical column properties. The results of this study can be found in Haselton et al. (2007b, Chapter 4).

To assess the collapse performance of each archetype building, we use the methodology laid out in Deierlein et al. (2005a). This method utilizes the incremental dynamic analysis (IDA) approach (Vamvatsikos 2002), and considers other important aspects of collapse assessment such as contribution of modeling uncertainty and consideration of three-dimensional effects. An example of a collapse assessment, for one of the 4-story archetype buildings, is provided later in this paper; this provides more detail on the collapse assessment method used in this work.

Beyond element-level modeling, we must ensure that the archetype analysis model captures the important system behavior. For generalized studies, “fishbone” (Luco et al. 2003) or single-bay (Ibarra 2003) models are often used to capture frame behavior. In this study, we choose a 3-bay frame to more realistically capture frame design and behavior, as shown in Figure 6.4. The 3-bay variable story-height configuration is envisioned as the simplest model to represent important design features that may impact the structural response and collapse performance, thus allowing us to conduct a broad study that will interrogate the full RC SMF design space. A 3-bay model was chosen because it contains both interior and exterior columns, as well as interior and exterior joints. The interior and exterior columns are important for capturing effects of strong-column weak-beam design provisions. Interior joint design often controls column size and beam depth, so this must be reflected in the representative archetype designs and the archetype analysis model. Additionally, the 3-bay frame can capture the additional axial loads due to overturning, which influences both the column design and behavior (although nonlinear axial-flexural interaction is not considered in the plastic-hinge models used in our analyses).

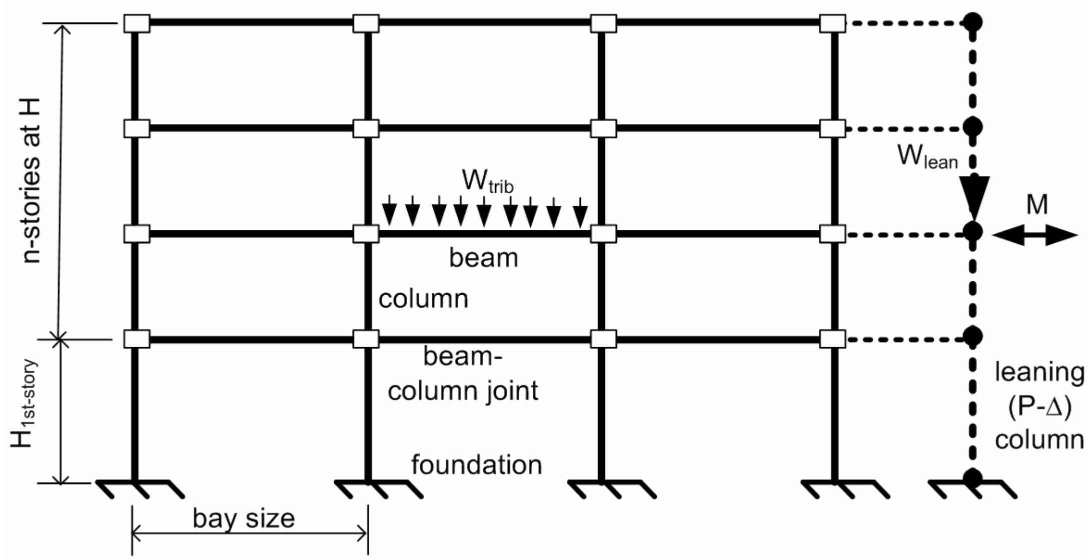

Fig. 6.4 Archetype analysis model for moment-frame buildings.

6.3.4.1 Differences between Collapse Assessment Method and Design Assumptions

The analysis modeling assumptions used in the design and the assessment are different. For design, we made assumptions consistent with what the building code specifies and what is done in current design practice (e.g., using nominal material strengths, not including slab contribution to beam strength/stiffness, using rough values of effective stiffness, etc.). When creating the structural model for collapse assessment (using the OpenSees software), we attempt to model the expected behavior of the building (e.g., expected material strengths, including strength and stiffness of slab, etc.).

Table 6.6 shows some of the important aspects of the collapse assessment modeling, which are different from the assumptions made for design (Table 6.4 presented the design assumptions earlier). Important highlights from Table 6.5 are that the assessment model is based on expected material and component strengths, as opposed to specified nominal strengths.

Specifically, we use expected material properties, calibrated element stiffnesses, slab contributions to beam strength and stiffness, and expected gravity loads in the assessment analysis.

Table 6.6 focuses only on the differences between the structural model used in design and the model used in the collapse assessment. Section 6.3.4 contains more details regarding the model used in the collapse assessment.

Table 6.6 Modeling guidelines used when creating structural models for collapse assessment.

Modeling Parameter	Modeling Guideline
Material Strength:	
Expected rebar yield strength	67 ksi (Melchers 1999)
Stiffness:	
Element stiffness: Beams	$0.35EI_g$ (Haselton et al. 2007)
Element stiffness: Columns	$0.35EI_g$ - $0.8EI_g$ (Haselton et al. 2007)
Footing rotational stiffness: 1-4 story	Effective stiffness of grade beam, stiffness of soil under footing
Footing rotational stiffness: 8-20 story	Basement assumed; ext. cols. fixed at basement wall, int. cols. consider stiffness of first floor beam and basement column
Joint stiffness	Effective stiffness to 60% of yield (Unemura et al, 1969)
Slab Contribution:	
Effective width for strength	Based on ACI 318-05 section 8.10
Effective width for stiffness	1/3 bay width (Robertson 2002)
Gravity Loading:	
Expected dead loads	1.05 of nominal (Ellingwood 1980)
Expected live loads	12 psf (Ellingwood 1980)

6.3.5 Ground Motion Considerations

6.3.5.1 Ground Motion Selection and Consideration of Spectral Shape

Ground motion selection is a critical aspect of collapse assessment. Baker (2006b, 2005a) has shown that rare ground motions have unique spectral shapes that are much different than the shape of a typical building code spectrum. Accounting for this unique spectral shape can remove a great deal of the conservatism that is commonly included in seismic performance assessments.

The common way to account for this unique spectral shape is to select a ground motion set that has a proper spectral shape, which is necessarily specific to one site and also one building fundamental period. This is not possible for this study because we have 30 buildings that are not placed at a specific site and that range in period from 0.4 to 2.6 sec. To get around this problem, Haselton and Baker et al. (2007a, Chapter 3) propose a method using a general ground motion set and then modifying the collapse predictions to account for proper spectral shape. We use this method in this paper, along with far-field ground motion set[3] developed in the Applied Technology Council (ATC) Project 63 (Haselton et al. 2007a, Chapter 3).

The scope of this study does not include consideration of near-field ground motions, though work is ongoing with the ATC Project 63 to consider how the effects of near-field motions would impact the assessment.

6.3.5.2 Ground Motion Scaling

This study is a joint project between the Pacific Earthquake Engineering Research Center (PEER) and the Applied Technology Council Project 63 (ATC-63), and the ground motion scaling method is different in each of the two related studies. This paper presents the collapse results based on the PEER scaling method.[4] Appendix B compares the collapse predictions using both scaling methods and shows that, surprisingly, the predictions from both methods are virtually identical. Note, however, that the similarities in the results are based on the fact that we are looking at collapse capacities; if we instead considered near-linear structural responses, the ATC-63 scaling method would result in higher dispersion.

6.4 SAMPLE COLLAPSE PERFORMANCE ASSESSMENT FOR ONE ARCHETYPE DESIGN

This section presents details of the archetype design and collapse performance assessment for one 4-story space frame building with 30′ bay spacing. For comparison, this section also gives comparisons to the design and performance of a 20-story space frame building with 20′ bay spacing. The design identification numbers for each design will be shown later in Figure 6.9, and these buildings are number 1010 and 1021, respectively.

---

[3] This study uses the extended far-field set, which includes 40 ground motions (each with two horizontal components).

[4] When scaling the pair of ground motions, the geometric mean spectral acceleration of each ground motion recording is scaled to the target. The geometric mean is defined as $Sa_{g.m.}(T_1) = (Sa_{comp1}(T_1) * Sa_{comp2}(T_1))^{0.5}$.

The same type of design and collapse performance assessment was completed for the other 29 archetype buildings used in this study. The detailed design and performance information for the other 29 archetypes are too lengthy to include here but soon will be posted on Haselton's webpage at California State University, Chico.

6.4.1 Archetype Structural Design

The 4-story space frame building was designed for a based shear coefficient of C_s = 0.092g. The details of the design were governed by several other aspects of the code provisions. The column cross-sectional dimension and beam heights were governed by joint shear strength requirements. Beam strengths were controlled by gravity and lateral force demands, and column strengths were governed by the strong-column weak-beam provision. Beam transverse reinforcement was controlled by shear capacity design, and column stirrups were controlled by both shear capacity design and confinement requirements. For this 4-story building design, interstory drift limitations did not control. The other 29 archetype designs were controlled by similar code provisions, with the exception that the taller buildings (8 stories and above) were controlled by drift limits.

Figure 6.5a–b documents the frame design, including element sizes, longitudinal and transverse reinforcement, element overstrength ratios, design drifts, etc. The notation used in this figure can be found in the notation list. Column sizes are all 30″x30″ with longitudinal reinforcement ratios of 0.011–0.016. The beams are 24″x30″ to 30″x30″ and have positive and negative reinforcement ratios of 0.005–0.007 and 0.011–0.013, respectively. Column stirrups are closely spaced at 4″ on center, with a total area ratio of 0.0065. Beam stirrups are spaced at 5.0 to 5.5″, with a total area ratio of 0.0023–0.0034. The computed fundamental period of this frame is T_1 = 0.86 sec.

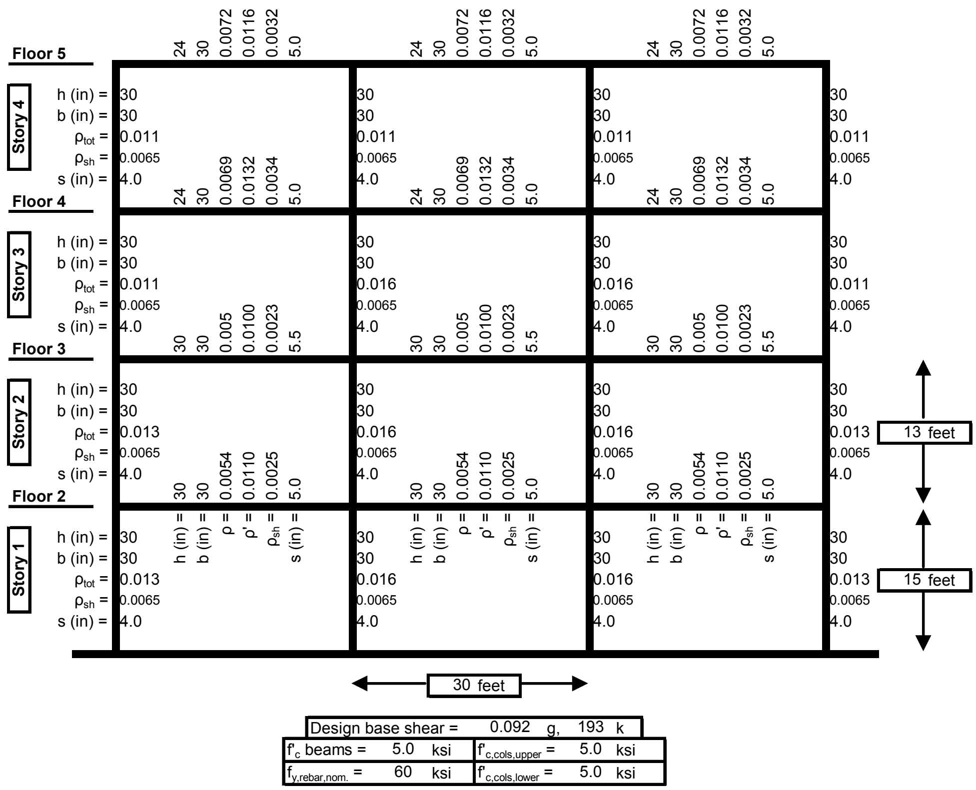

(a)

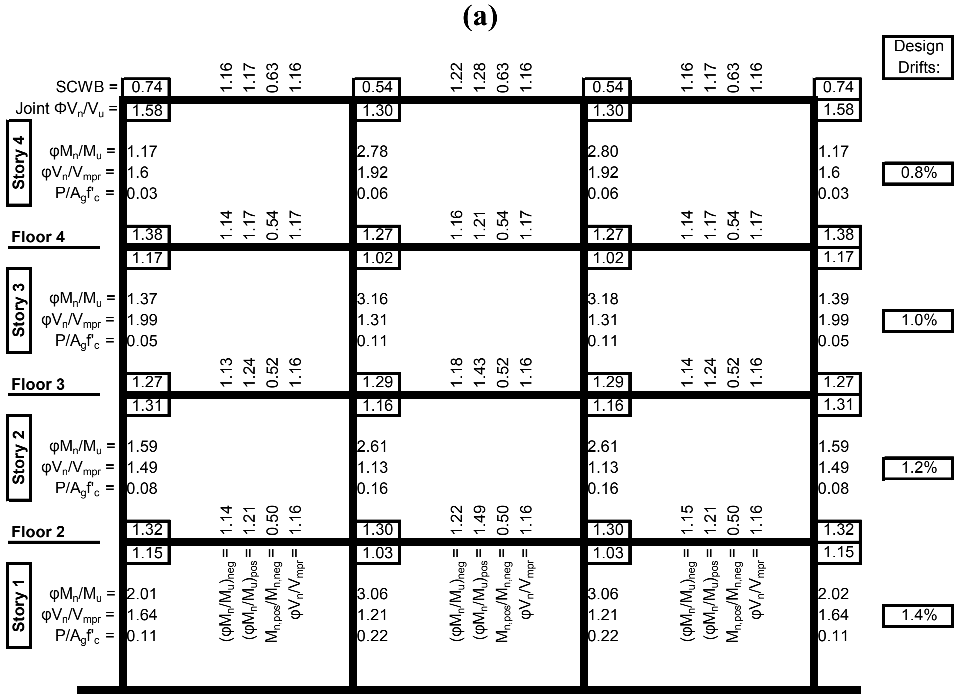

(b)

Fig. 6.5 Design documentation for 4-story space frame archetype with 30′ bay spacing (building ID 1010).

6.4.2 Archetype Structural Model

Figure 6.6 shows the modeling parameters used for each element of the 4-story building. Included are parameters such as strength, stiffness, plastic rotation capacity, hardening and softening stiffnesses, and the cyclic deterioration parameter. The element model and model parameters were defined earlier in Figure 6.3. The element modeling is based on the calibration study that we published in Haselton et al. (2007b, Chapter 4).

Due to the large member sizes and low axial load ratios in columns, all of the member stiffnesses are $0.35EI_g$. For beam stiffness, we include the slab contribution within an effective width of 1/3 of the bay spacing (Robertson 2002). The plastic rotation capacity of columns ranges from 0.056 to 0.069. The plastic rotation capacities of beams are different for positive and negative bending; they range from 0.035 to 0.045 for positive bending, and 0.054 to 0.068 for negative bending. The post-capping slopes, rotation from peak strength to zero strength (termed “post-capping rotation capacity”), are all at the upper limit of 0.10.

For comparison, the interior bottom floor columns of the 20-story space frame building (ID 1021) have a plastic rotation capacity of 0.038 (versus 0.055 for the 4-story), a post-capping rotation capacity of 0.063 (versus 0.10 for the 4-story), and a flexural stiffness of $0.55EI_g$ (versus $0.35EI_g$ for the 4-story). The beams of the 20-story building are similar to the 4-story building.

The large element deformation capacities shown for this building are typical of the low-rise reinforced concrete special moment-frame buildings used in this study. These large deformation capacities come from (a) low column axial load ratios (caused by column sizes being increased to meet joint shear requirements) and closely spaced stirrups combined with a relatively large number of ties at each stirrup location. Note that these deformation capacities include the contribution of bond-slip, which accounts for 35% of the deformation. At the ultimate rotation, approximately 65% of the reported rotation is occurring in the hinge region and 35% is concentrated in bond-slip at the end of the element.

The structural model reflects expected material properties and element properties. Uncertainties in structural properties are accounted for later in the assessment process by increasing the uncertainty in the collapse capacity distribution.

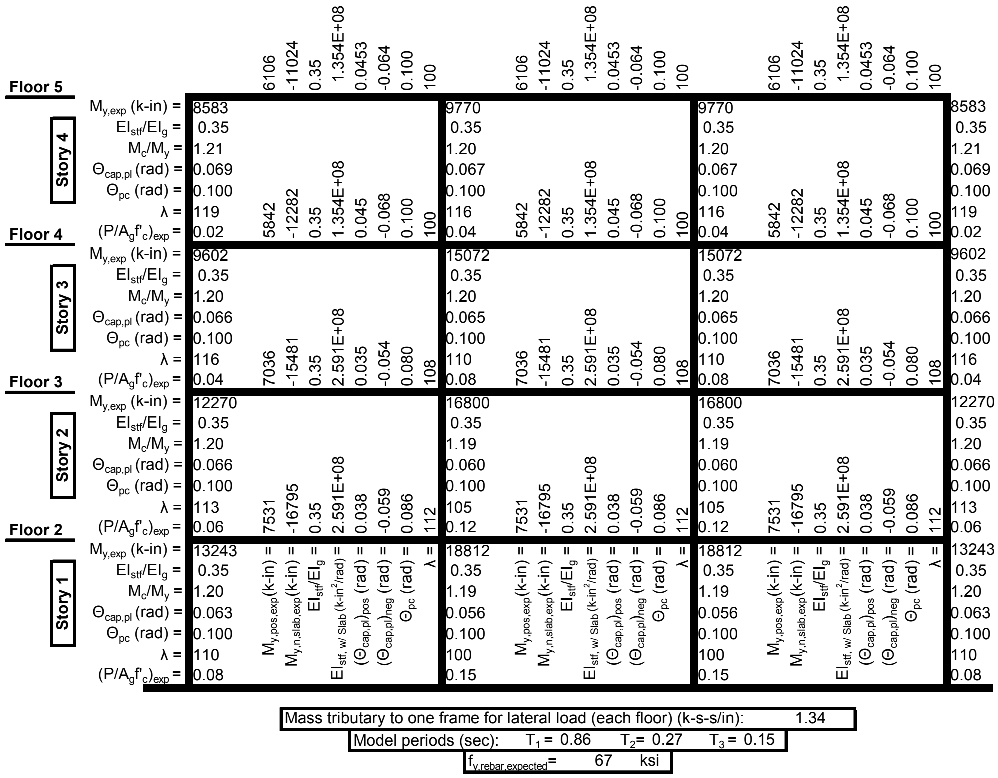

Fig. 6.6 Structural modeling documentation for 4-story space frame archetype with 30′ bay spacing (building ID 1010).

6.4.3 Static Pushover Analyses

Figure 6.7a shows the static pushover curve and Figure 6.7b the peak interstory drifts at the three points indicated on the pushover. This shows yielding at about 0.4% roof drift (0.5% story drift) and the onset of strain softening at 3.5% roof drift (4.0% story drift). For comparison, these values are 0.4% and 1.7%, respectively, for a 20-story building (ID 1021).

The large building deformation capacity shown by this building is typical of the low-rise buildings used in this study. This large deformation capacity comes from large element plastic rotation capacities, the strong-column weak-beam provision being successful in distributing the damage over much of the building, and relatively low P-delta effects.

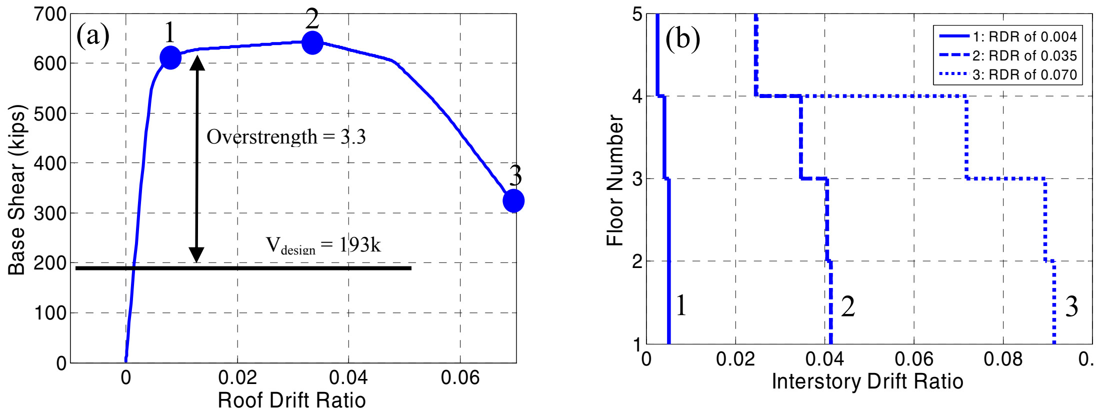

Fig. 6.7 (a) Monotonic static pushover and (b) peak interstory drift ratios at three deformation levels during pushover. Pushover based on building-code-specified lateral load distribution (ASCE 2002).

6.4.4 Structural Responses before Collapse

While the primary focus of this study is collapse, we track a variety of structural response parameters (a) to later use in damage and loss predictions for this set of archetype structures (such as those done recently done in the PEER Center: Goulet et al. 2006a; Haselton et al. 2007e; and Aslani 2005) and (b) to help verify our structural model and have confidence in its' predictions.

Figure 6.8 shows a few highlights of the behavior of this building before collapse. Each point on the plot indicates the results of one earthquake record. At spectral acceleration levels greater than 1.0g where the first collapse was observed, the number of data points are reduced, since the data from simulations that caused collapse are not plotted. The ratio of records causing collapse at each level of spectral acceleration is: 1.0g–0.00, 1.2g–0.04, 1.4g–0.06, 1.6g–0.16, 1.8g–0.20, 2.0g–0.28, 2.4g–0.41, and 2.8g–0.58.

The solid and dashed lines indicate the mean, and mean +/- one standard deviation (not including the simulations that caused collapse), responses using a fitted lognormal distribution. These data are shown in this manner because the structural response conditioned on non-collapse are often used for damage and loss analyses (Goulet et al. 2006a). Note that at the 2%-in-50-years level of motion, none of the 80 records caused collapse (this is shown later in Fig. 6.9).

This figure shows that at the 2%-in-50-years ground motion level of Sa(0.86s) = 0.93g, the median roof drift is 0.014, which corresponds with a maximum interstory drift of 0.020 (not shown in this figure). The median peak roof acceleration is 0.80g. The median peak plastic rotation of the most damaged beam and column in the frame is 0.018 and 0.012, respectively.

For comparison, the 20-story building (ID 1021) performs as follows for the 2%-in-50-years ground motion level: median roof drift of 0.007, maximum interstory drift of 0.023, median peak roof acceleration of 0.75g, and a median peak plastic rotation for all beams and columns in the frame of 0.023 and 0.004, respectively. This comparison shows surprisingly similar performance between the 4-story and 20-story buildings under the 2%-in-50-years ground motion. The primary difference is that column plastic rotation demands are lower in the 20-story building.

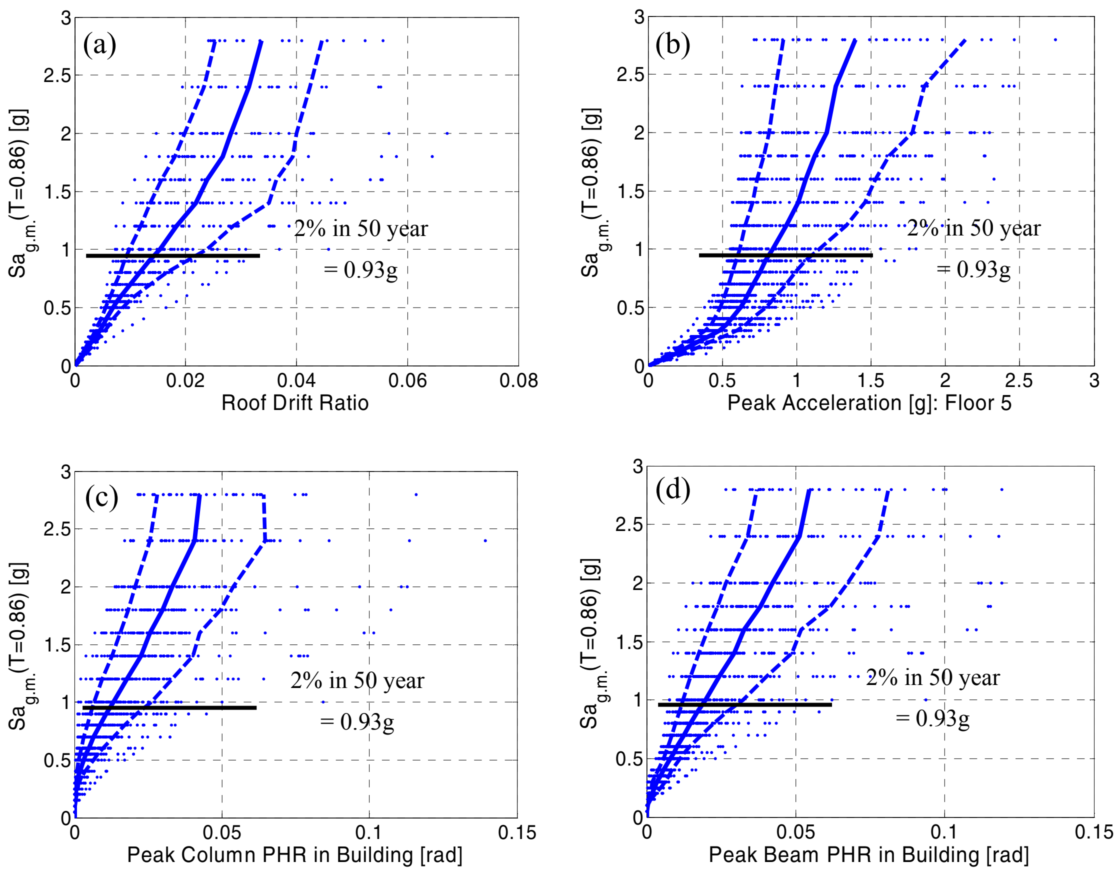

Fig. 6.8 Incremental dynamic analyses (plotted as stripes of response at each intensity level) showing pre-collapse responses for (a) roof drift ratio, (b) peak roof acceleration, (c) peak column plastic-hinge rotation for all columns in building, and (d) peak beam plastic-hinge rotation for all beams in building.

6.4.5 Collapse Performance Prediction

Figure 6.9 shows the collapse IDA results. Each line on the figure corresponds to a single earthquake scaled to increasing intensity levels until sidesway collapse (dynamic instability) occurs. Figure 6.9a displays the results for both horizontal components of ground motion. To approximately account for performance of the three-dimensional building, we assume that the building will collapse when either of the two horizontal ground motion components cause collapse of the two-dimensional frame; therefore, Figure 6.9b shows only those components that first cause collapse (termed the "controlling component"). This approach is based on the simplifying assumption that the building is symmetric and that the same structural model can be used to simulate response in either direction.

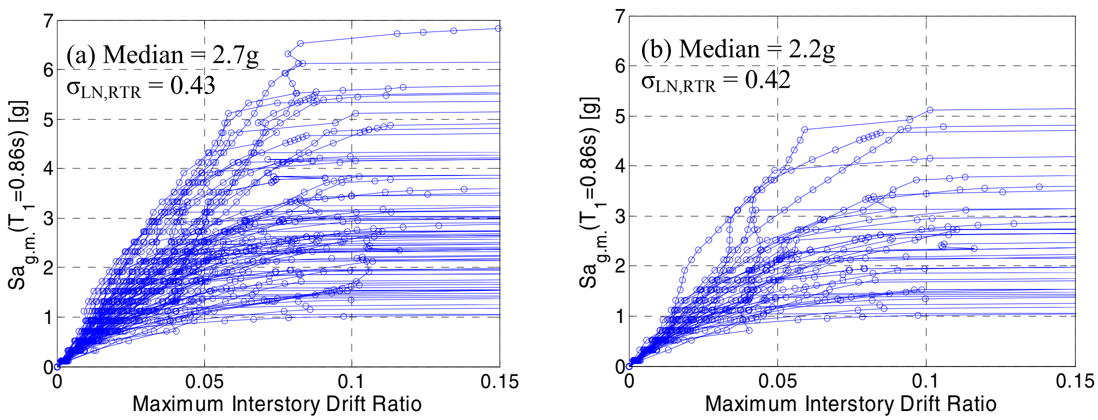

Fig. 6.9 Incremental dynamic analysis to collapse, showing (a) both horizontal components of ground motion and (b) horizontal component that first causes collapse (termed "controlling component").

Figure 6.9 shows that the median collapse capacity is Sa(0.86s) = 2.2g if we use the controlling component of ground motion.

Figure 6.10 shows the collapse capacities from Figure 6.9b plotted as a cumulative distribution function. This shows the collapse capacities from each of the 40 ground motion records, as well as the lognormal fit to these results. This figure also shows the collapse CDF with an expanded standard deviation to account for the effects of structural modeling uncertainties. The additional modeling uncertainty is based on a detailed assessment of a similar 4-story code-conforming RC frame building (Chapter 5, Haselton et al. 2007e; Goulet et al. 2006a), where we calculated the variability to $\sigma_{LN,Modeling}$ = 0.45 (this also includes some variability in the design of the building). For lack of more specific information on modeling uncertainty, we use a slightly larger value of 0.50 for all 30 buildings used in this study, recognizing that there will be variations between buildings.

To incorporate the effects of modeling uncertainties, we use the mean estimate approach (Haselton et al. 2007e, Chapter 5). This approach results in an increase in the uncertainty in the collapse capacity, where the total uncertainty in the collapse capacity is $\sigma_{LN,Total} = (\sigma_{LN,RTR}^2 + \sigma_{LN,Modeling}^2)^{0.5}$, and there is no shift in the median capacity. Continued research by the authors is focused on improving this method to be more generally applicable.

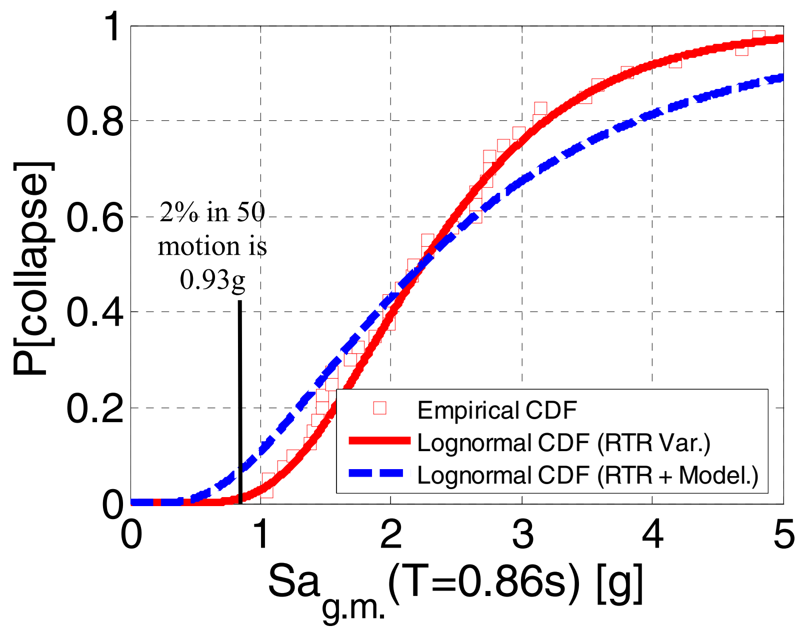

Fig. 6.10 Collapse cumulative density function (CDF) plot showing each controlling ground motion component collapse capacity (squares), lognormal fit (solid line), and change in collapse CDF when including effects of structural modeling uncertainties (dashed line).

The next step of the collapse assessment process is to adjust the collapse capacity distribution to account for proper spectral shape (as quantified through the parameter ε). This adjustment process is explained in detail in Haselton et al. (2007a, Chapter 3). For this example, we assume that ε = 1.5 is appropriate for the 2%-in-50-years ground motion at the Los Angeles site. We apply a correction to the mean collapse capacity, but do not correct the dispersion because we are already adding modeling uncertainty in this process and an additional correction would have little effect.

Figure 6.11 follows the previous figure, but includes the collapse CDF corrected for proper spectral shape (ε=1.5), using the procedure described in Haselton (2007a, Chapter 3). For this specific example, the spectral shape adjustment caused the mean collapse capacity to increase from 2.2g to 3.2g (by a factor of 1.45); this magnitude of increase is typical.

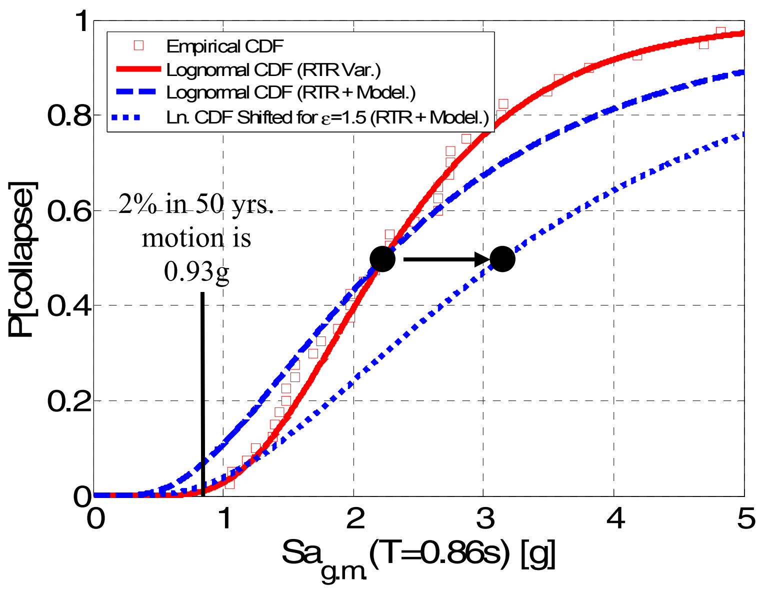

Fig. 6.11 Collapse cumulative density function (CDF) plot that includes adjusted collapse CDF accounting for effects of spectral shape (ε=1.5).

For the site used in this study, the 2%-in-50-years motion is $Sa_{2/50}(0.86s) = 0.93g$, so the margin[5] against collapse is 3.4 for the 2%-in-50-years motion; this margin is uncommonly high, a value near 2.3 is more typical for the RC SMF archetypes (see Fig. 6.14).

Figure 6.11 shows that the probability of collapse given the 2%-in-50-years ground motion is 3%. To estimate the mean annual frequency of collapse ($\lambda_{collapse}$), we can integrate the collapse capacity CDF with the hazard curve (Ibarra 2003, Chapter 7). This results in $\lambda_{collapse}$ = 0.7×10^{-4} collapses/year when including all uncertainty and the spectral shape adjustment; this corresponds to a collapse return period of 14,000 years. These collapse risks are uncommonly low as compared to the results from the other archetype buildings; more typical values would be 11% collapse probability and $\lambda_{collapse} = 3.1 \times 10^{-4}$ collapses/year (as will be shown later in Fig. 6.14).

[5]Margin is a simplistic indicator of collapse risk and is defined as the ratio of median collapse capacity to the ground motion intensity of interest (usually the MCE of the 2%-in-50-years motion).

This paper will later show that the structural modeling uncertainties and spectral shape impact the collapse risk prediction more than any of the design aspects investigated in this study. The large impact of these two issues shows that their proper consideration is critical to a meaningful collapse performance assessment. This is especially true for ductile buildings that collapse under extremely rare ground motions. In these cases, the tail of the collapse capacity distribution dominates the predictions of collapse probability and rate; this causes the predictions to be more sensitive to increases to the uncertainty in the collapse capacity. Additionally, the period of a ductile building elongates significantly prior to collapse, which causes the spectral shape to have extreme impacts on the predicted collapse capacity.

6.4.5.1 Non-Simulated Collapse Modes

In general, the collapse modes that the structural model is not able to capture (such as vertical collapse of the gravity system, etc.) need to be considered in the collapse assessment. For RC SMF buildings designed to meet current building codes, we assume that the capacity design and ductility provisions will prevent local and non-ductile failure prior to sidesway collapse (Haselton et al. 2007e). It may be beneficial to revisit this assumption in future research, taking a closer look at issues such as the displacement capacity of the gravity system before the onset of a local collapse (vertical collapse of slab-column connection or vertical crushing of gravity column). If non-simulated collapse modes were likely, we would need to adjust the collapse capacity distribution using the method outlined in many recent publications (Deierlein et al. 2005a; Krawinkler 2005, Chapter 4; Aslani 2005a).

6.4.6 Collapse Mechanisms

Figure 6.12 shows that this building collapses in two predominant mechanisms. The 2-story mechanism occurs for 80% of ground motions and a first-story mechanism (with hinging the second-floor beams and first-story columns) occurs for the other 20%. It is important to note that the static pushover analysis predicts a 3-story mechanism and *this is never observed in dynamic collapses*. For comparison, the 20-story building (ID 1021) collapses predominantly in a 5-story mechanism.

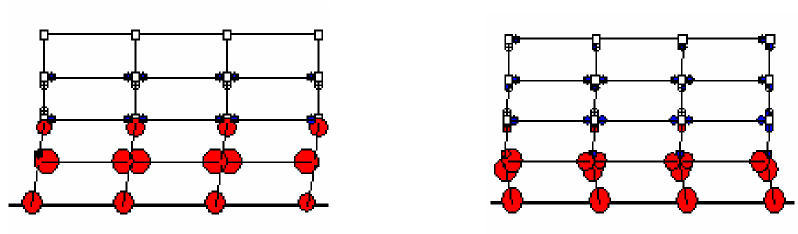

(a) 80% of collapses (b) 20% of collapses

Fig. 6.12 Diagrams showing relative occurrence of collapse modes for 80 ground motions used for collapse performance assessment.

6.4.7 Drifts at Collapse

The elements of this building have large plastic rotation capacities (on the order of 0.04–0.07 radians), which cause the drift capacity to be similarly large. Figure 6.13 shows the collapse drifts for each of the 80 ground motions used in this study; this shows both the peak roof drift and peak interstory drift of the most damaged story. These drifts come from the nonlinear dynamic analyses at the largest ground motion intensity just below the collapse point. Since the increment in ground motion scaling is small, these can be considered as the drifts at collapse.

This figure shows that the building collapses at interstory drifts of 0.04–0.12, with a median value of 0.085. The roof drifts at collapse range from 0.03 to 0.08, with a median of 0.054. While these values are larger than typically envisioned for RC frames, keep in mind that these results are for a code-conforming low-rise RC SMF building at the point of incipient collapse. The large collapse drifts follow almost directly from the large predicted plastic rotation capacities of the elements in the frame. For comparison, the 20-story building (ID 1021) collapses at a median interstory drift of 0.060 and median roof drift of 0.016.

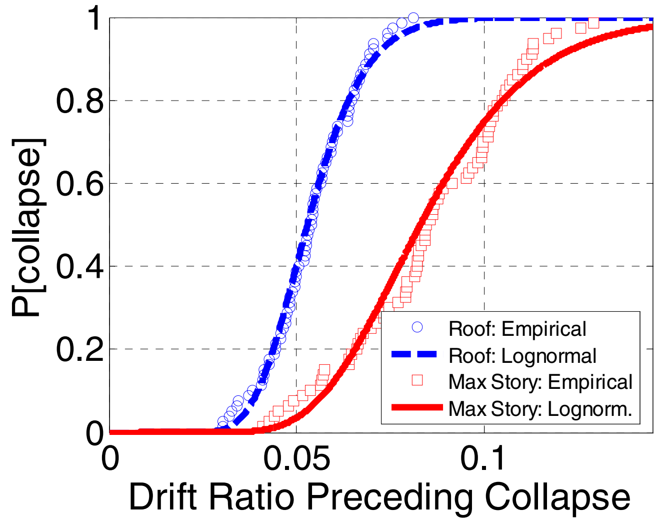

Fig. 6.13 Collapse cumulative density functions of peak drifts from highest earthquake intensity that did not result in collapse of structure.

6.4.8 Summary of Collapse Performance

Table 6.7 summarizes the collapse performance of the 4-story building. The collapse data include the effects of structural modeling uncertainties, expected spectral shape (ε), and the three-dimensional collapse capacity, as discussed previously.

The mean collapse capacity of building 1010 is Sa(0.86s) = 3.2g, and the record-to-record variability is $\sigma_{LN,RTR} = 0.42$. This results in a margin against the MCE of 3.0 and a margin of 3.4 against the 2%-in-50-years motion. These differences in margins come simply from differences in spectral intensities, as shown earlier in Figure 6.2. The probability of collapse is 3% when conditioning on the 2%-in-50-years ground motion. The mean annual frequency of collapse is $0.7\text{x}10^{-4}$, which translates to a collapse return period of 14,000 years.

Table 6.7 Summary of collapse performance for 4-story and 20-story space frame building, using proposed assessment approach. Predictions include effects of structural modeling uncertainties, adjustment for expected spectral shape, and use of controlling horizontal component of ground motion (to approximate 3D collapse capacity).

Building	First Mode Period (T_1) [sec]	Adjusted Mean $Sa_{g.m.}$,col (T_1) [g]	$\sigma_{LN,RTR}$ (Sa,col)	$\sigma_{LN,Total}$ (Sa,col)	Margin Against MCE	Margin Against 2% in 50 Motion	P[C| $Sa_{2/50}$]	$\lambda_{collapse}$ [10^{-4}]
4-story space frame (ID 1010)	0.86	3.17	0.42	0.65	3.0	3.4	0.03	0.7
20-story space frame (ID 1021)	2.36	0.99	0.40	0.64	2.6	2.5	0.08	0.3

6.4.9 Sensitivity of Predicted Collapse Performance to Selected Aspects of Collapse Assessment

This section examines the effects that the following issues have in the collapse assessment: (a) structural modeling uncertainties, (b) the ε adjustment to account for spectral shape, and (c) using the controlling horizontal component of ground motion to approximate the three-dimensional collapse capacity. Table 6.8 summarizes the collapse predictions that consider all of these effects; these results were presented previously. To show the impacts of the various aspects of the collapse assessment methodology, the remaining rows of the table present the collapse predictions that do not include a certain aspect of the collapse methodology.

The second row of the table shows the collapse predictions if structural modeling uncertainties are not considered. Based on the method we use to incorporate the effects of structural modeling uncertainties (the mean estimate method discussed in Chapter 5), the uncertainty in the collapse capacity is significantly increased but the median collapse capacity is not affected. Excluding modeling uncertainty decreases the conditional collapse probability (P[C|$Sa_{2/50}$]) from 3% to 0% and decreases $\lambda_{collapse}$ by a factor of ten. This magnitude of impact is generally consistent with findings from another recent study (Goulet et al. 2006a; Haselton et al. 2007e). This quantitatively shows that proper treatment of structural modeling uncertainties is critical for a collapse performance assessment.

The third row of Table 6.8 shows the collapse predictions if proper spectral shape is not accounted for in the collapse assessment. Excluding this spectral shape adjustment causes the margin to decrease from 3.4 to 2.4, causes the conditional collapse probability to increase from 3% to 9%, and causes the $\lambda_{collapse}$ to increase by a factor of four. This shows that this adjustment for spectral shape is also important.

The fourth row of the table shows the collapse predictions if all components of ground motion are used instead of only the controlling component. This causes the margin to increase from 3.4 to 4.0, causes the collapse probability to decrease from 3% to 2%, and causes the $\lambda_{collapse}$ to decrease by a factor of two.

Table 6.8 Summary of collapse performance for building ID 1010, using various assessment approaches.

Inclusion/Exclusion of Various Aspects of the Collapse Performance Assessment	Median $Sa_{g.m.,col}$ (0.86s) [g]	$\sigma_{LN,RTR}$ (Sa,col)	$\sigma_{LN,Total}$ (Sa,col)	Margin Against 2% in 50 Motion	P[C| $Sa_{2/50}$]	$\lambda_{collapse}$ [10^{-4}]
Proposed Approach: Includes modeling uncert., spectral shape adj., controlling g.m. comp.	3.2	0.42	0.65	3.4	0.03	0.71
Without inclusion of modeling uncertainty	3.2	0.42	0.42	3.4	0.00	0.07
Without spectral shape adjustment	2.2	0.42	0.65	2.4	0.09	2.51
Without using the controling g.m. comp.	3.7	0.43	0.66	4.0	0.02	0.41

If we judge the relative importance of each item by how much it impacts the prediction of mean annual rate of collapse ($\lambda_{collapse}$), then we find that the inclusion of structural modeling uncertainties is the most important item considered here. The spectral shape adjustment follows in level of importance, and the use of the controlling ground motion component has the smallest impact on the predicted collapse risk.

6.5 COLLAPSE PERFORMANCE PREDICTIONS FOR FULL SET OF ARCHETYPE DESIGNS

6.5.1 Collapse Performance Predictions for All Buildings

We predicted the collapse performance for each of the 30 archetype designs in the same way that we assessed the 4-story building discussed in the last section; this is based on the approach reflected by the first row of Table 6.8. Table 6.9 presents information for each archetype design, such as fundamental period, design and yield base shear, static overstrength, and ultimate roof drift ratio. The fundamental periods range from 0.4 sec for 1-story buildings to around 2.5 sec for 20-story buildings. These periods are higher than some may expect, especially for low-rise buildings. This partially comes from the element stiffness model (Haselton et al. 2007b, Chapter 4), which includes effects of cracking, bond-slip, and shear deformations; this model is calibrated to represent the secant stiffness of an element at 40% of yielding. These longer periods also partially come from the fact that the stiffness of nonstructural components are neglected. The static overstrength ratios range from 1.6 to 4.4, where the larger values are observed for the shorter buildings and space frames. The roof drift ratio at "ultimate" (20% strength loss in the pushover analysis) ranges from 0.085 for a low-rise building, to about 0.02 for a 20-story building.

Table 6.9 Fundamental period and static pushover information for each of 30 archetype designs.

Design Information							Period and Pushover Analysis Results					
Design Number	Design ID Number	No. of stories	Bay Width [ft]	Tributary Areas: Gravity/ Lateral	Strength/ Stiffness Distribution Over Height	Foundation Fixity Assumed in Design [a]	First Mode Period (T_1) [sec]	Design Base Shear Coefficient (C_s) [g]	Yield Base Shear Coefficient, from Pushover [g]	Static Overstrength (based on ultimate strength)	Effective R-Factor[d]	Ultimate Roof Drift Ratio (at 20% strength loss) (RDR_{ult})
1	2061					GB	0.42	0.125	0.47	4.0	2.1	0.077
2	2062	1	20	Space (1.0)	A	P	0.42	0.125	0.57	4.9	1.8	0.079
3	2063					F	0.42	0.125	0.47	4.0	2.1	0.077
4	2069			Perimeter (0.11)	A	GB	0.71	0.125	0.20	1.6	4.2	0.077
5	1001					GB	0.63	0.125	0.392	3.5	2.5	0.085
6	1001a	2	20	Space (1.0)	A	P	0.56	0.125	0.509	4.4	2.0	0.085
7	1002					F	0.63	0.125	0.366	3.1	2.6	0.076
8	2064			Perimeter (0.11)	A	GB	0.66	0.125	0.223	1.8	4.1	0.067
9	1003			Perimeter (0.11)	A	GB	1.12	0.092	0.143	1.6	3.8	0.038
10	1004		20		C	GB	1.11	0.092	0.151	1.7	3.6	0.043
11	1008	4		Space (1.0)	A	GB	0.94	0.092	0.237	2.7	2.7	0.047
12	1009		30	Perimeter (0.17)	A	GB	1.16	0.092	0.141	1.6	3.7	0.050
13	1010			Space (1.0)	A	GB	0.86	0.092	0.268	3.3	2.6	0.056
14	1011		20	Perimeter (0.17)	A	GB	1.71	0.050	0.077	1.6	4.6	0.023
15	1012				A	GB	1.80	0.050	0.106	2.3	3.2	0.028
16	1022				C	GB	1.80	0.050	0.114	2.6	2.9	0.035
17	2065	8	20	Space (1.0)	B (65%)[b]	GB	1.57	0.050	0.152	3.3	2.5	0.024
18	2066				B (80%)[b]	GB	1.71	0.050	0.145	2.9	2.4	0.031
19	1023				B (65%)[c]	GB	1.57	0.050	0.136	2.9	2.8	0.019
20	1024				B (80%)[c]	GB	1.71	0.050	0.131	2.7	2.7	0.021
21	1013		20	Perimeter (0.17)	A	GB	2.01	0.044	0.075	1.7	4.0	0.026
22	1014				A	GB	2.14	0.044	0.090	2.1	3.1	0.022
23	1015				C	GB	2.13	0.044	0.088	2.1	3.2	0.024
24	2067	12	20	Space (1.0)	B (65%)[b]	GB	1.92	0.044	0.139	3.2	2.3	0.020
25	2068				B (80%)[b]	GB	2.09	0.044	0.104	2.5	2.8	0.022
26	1017				B (65%)[c]	GB	1.92	0.044	0.106	2.8	3.0	0.016
27	1018				B (80%)[c]	GB	2.09	0.044	0.100	2.5	2.9	0.018
28	1019		30	Space (1.0)	A	GB	2.00	0.044	0.093	2.4	3.2	0.023
29	1020	20	20	Perimeter (0.17)	A	GB	2.63	0.044	0.070	1.6	3.3	0.018
30	1021		20	Space (1.0)	A	GB	2.36	0.044	0.086	2.0	3.0	0.023

a - Fixity assumed only in the design process. OpenSees models use expected grade beam, basement column, and soil stiffnesses.
b - Only first story designed to be weak.
c - First and second stories designed to be weak.
d - This is defined as the ratio of the design base shear strength [(2/3)Sa_{MCE}(T1)] to the yield base shear strength.
A - Expected practitioner design; strength and stiffness stepped over height as would be done in common design practice.
B (%) - Weak story; done by sizing the target weak story(ies) based on code requirements and then strengthening stories above. % is the percentage of strength in the weak story(ies) as compared to the stories above.
C - conservative design; neither size nor reinforcement of beams/columns are decreased over building height
F - Fixed.
GB - "Grade Beam" - this considers the rotational stiffness of the grade beam and any basement columns.

Figure 6.14 presents the collapse predictions for all 30 archetype buildings. These predictions include the correction for spectral shape associated with rare 2%-in-50-years ground motions in California (see Appendix A) and include the effects of structural modeling uncertainties. The margins against collapse range from 1.4 to 3.4 for all buildings, with an average value of 2.3. The collapse probabilities conditioned on the 2%-in-50-years ground motion range from 0.03 to 0.20, with an average of 0.11. The mean annual frequency of collapse ($\lambda_{collapse}$) ranges from 0.7×10^{-4} to 7.0×10^{-4} collapses/year, with an average rate of 3.1×10^{-4}. This collapse rate corresponds to an average collapse return period of 3,200 years, with a range of 1,400 to 14,000 years. Appendix A includes more detailed collapse performance information for each of the 30 buildings considered in this study.

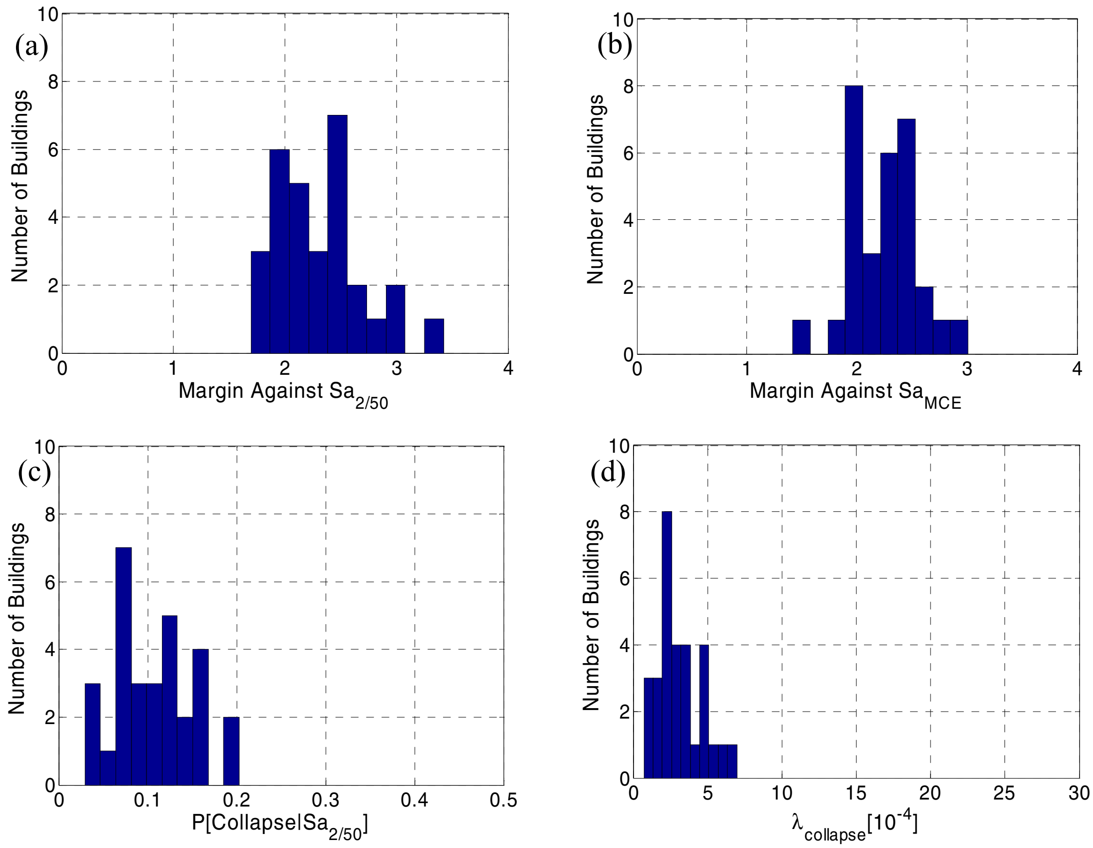

Fig. 6.14 Collapse performance predictions for 30 archetype buildings, including correction for proper spectral shape (ε = 1.5).

For comparative purposes, Figure 6.15 presents similar collapse predictions that do not include the correction for expected spectral shape (expected ε). We do not consider these results to be correct for far-field sites in California, but they are useful to illustrate the significant impact that spectral shape has on collapse assessment. The margin against collapse ranges from 1.1 to 2.4 for all buildings, with an average value of 1.6. The collapse probability conditioned on the 2%-in-50-years ground motion level ranges from 0.09 to 0.44, with an average of 0.26. The mean annual frequency of collapse ($\lambda_{collapse}$) ranges from 2.2x10^{-4} to 25.6x10^{-4} collapses/year, with an average rate of 11.0x10^{-4}. This corresponds to an average collapse return period of 900 years, with a range of 390 to 4,500 years.

Comparison of Figures 6.14 and 6.15 shows that considering spectral shape increases the average collapse margin from 1.6 to 2.3, decreases the average collapse probability from 0.26 to 0.11, and decreases the mean annual frequency of collapse from 11.0×10^{-4} collapses/year to 3.1×10^{-4}.

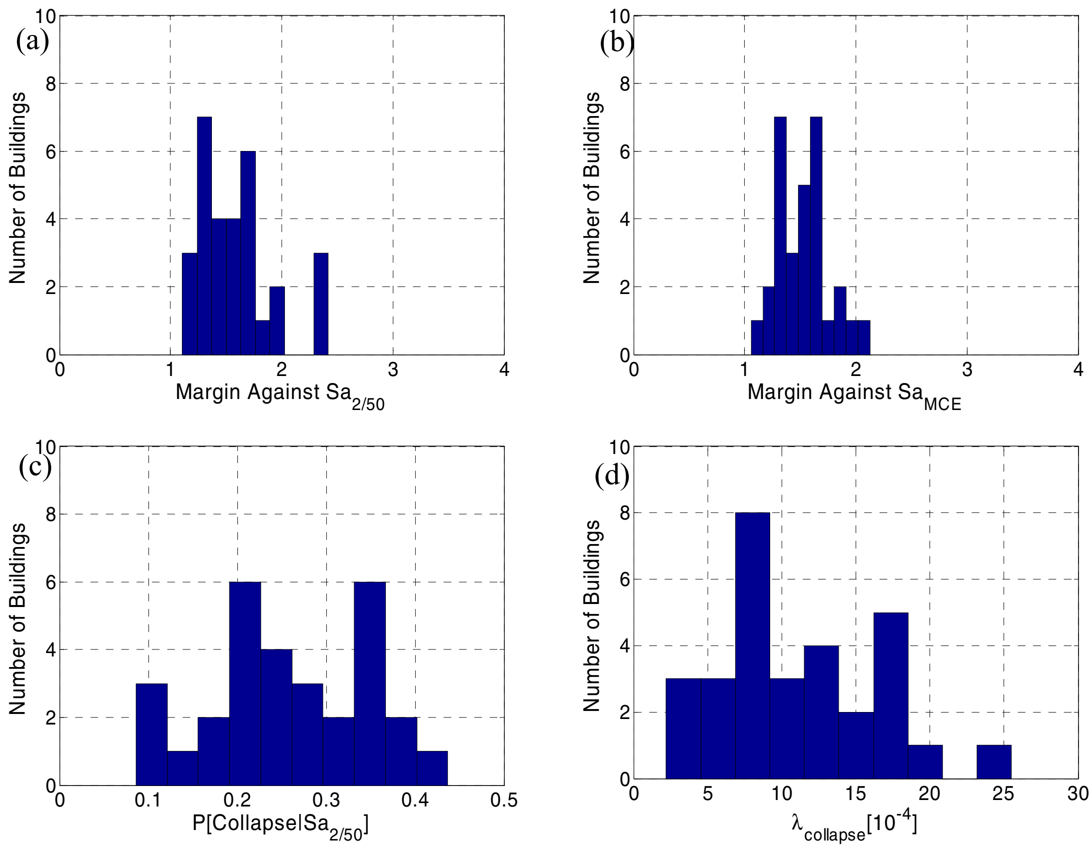

Fig. 6.15 Collapse performance predictions for 30 archetype buildings, excluding needed correction for proper spectral shape.

Table 6.10 follows from Figure 6.15 and presents more detailed collapse capacity information. These results do not include the adjustments for proper spectral shape, so these results should be used only for relative comparisons (e.g., used to compare the performance of buildings with various heights, etc.). This table presents a comprehensive summary of information, while the following sections will investigate these data to illustrate trends and draw conclusions regarding how the collapse performance is affected by parameters such as building height. The collapse performance results shown in Appendix A (which include the adjustment for proper spectral shape) should be used for all purposes other than relative comparisons.

Table 6.10 Collapse predictions for each of 30 archetype buildings (no adjustment for proper spectral shape (ε)).

Design Information							Collapse Predictions with no Adjustment for Spectral Shape, Controlling Horizontal Component of Ground Motion, Including Effects of Structural Modeling Uncertainties						Collapse Drifts	
Design Number	Design ID Number	No. of stories	Bay Width [ft]	Tributary Areas: Gravity/ Lateral	Strength/ Stiffness Distribution Over Height	Foundation Fixity Assumed in Design [a]	Mean[d] $Sa_{g.m.,col}(T_1)$ [g]	$\sigma_{LN}(Sa,col)$	Margin Against MCE	Margin Against 2% in 50 Year Motion	$P[C\|Sa_{2/50}]$	λ_{col} $[10^{-4}]$	Median IDR at collapse	Median RDR at collapse
1	2061	1	20	Space (1.0)	A	GB	2.46	0.46	1.64	1.76	0.20	7.3	0.071	0.071
2	2062					P	2.74	0.44	1.82	1.95	0.16	4.7	0.075	0.075
3	2063					F	2.46	0.46	1.64	1.76	0.20	7.3	0.069	0.069
4	2069			Perimeter (0.11)	A	GB	1.34	0.39	1.06	1.26	0.36	17.3	0.078	0.078
5	1001	2	20	Space (1.0)	A	GB	2.71	0.42	1.88	2.34	0.10	2.6	0.097	0.075
6	1001a					P	2.92	0.40	1.95	2.40	0.09	2.2	0.080	0.061
7	1002					F	2.29	0.43	1.59	1.98	0.15	4.8	0.083	0.059
8	2064			Perimeter (0.11)	A	GB	1.86	0.43	1.36	1.65	0.23	8.7	0.075	0.061
9	1003	4	20	Perimeter (0.11)	A	GB	1.09	0.37	1.36	1.43	0.28	11.3	0.076	0.039
10	1004				C	GB	1.28	0.41	1.59	1.66	0.22	8.1	0.085	0.047
11	1008			Space (1.0)	A	GB	1.59	0.38	1.66	1.83	0.17	5.4	0.080	0.045
12	1009		30	Perimeter (0.17)	A	GB	1.24	0.41	1.59	1.66	0.22	8.2	0.078	0.050
13	1010			Space (1.0)	A	GB	2.24	0.42	2.13	2.42	0.09	2.5	0.083	0.053
14	1011	8	20	Perimeter (0.17)	A	GB	0.63	0.40	1.19	1.11	0.44	25.5	0.054	0.021
15	1012		20	Space (1.0)	A	GB	0.76	0.37	1.52	1.42	0.29	11.5	0.068	0.027
16	1022				C	GB	0.81	0.36	1.61	1.51	0.25	9.2	0.077	0.033
17	2065				B (65%)[b]	GB	0.90	0.39	1.58	1.56	0.24	10.0	0.069	0.021
18	2066				B (80%)[b]	GB	0.90	0.40	1.71	1.70	0.20	8.7	0.074	0.027
19	1023				B (65%)[c]	GB	0.76	0.39	1.33	1.28	0.35	16.8	0.066	0.018
20	1024				B (80%)[c]	GB	0.72	0.40	1.37	1.28	0.35	16.8	0.067	0.020
21	1013	12	20	Perimeter (0.17)	A	GB	0.55	0.37	1.23	1.19	0.39	20.3	0.053	0.016
22	1014		20	Space (1.0)	A	GB	0.57	0.38	1.36	1.31	0.33	15.5	0.055	0.018
23	1015				C	GB	0.62	0.39	1.47	1.43	0.29	12.6	0.060	0.021
24	2067				B (65%)[b]	GB	0.70	0.38	1.50	1.38	0.30	12.1	0.066	0.016
25	2068				B (80%)[b]	GB	0.60	0.37	1.40	1.31	0.33	14.0	0.057	0.018
26	1017				B (65%)[c]	GB	0.61	0.37	1.30	1.21	0.38	18.1	0.065	0.015
27	1018				B (80%)[c]	GB	0.56	0.38	1.29	1.25	0.36	18.0	0.058	0.016
28	1019		30	Space (1.0)	A	GB	0.74	0.41	1.65	1.59	0.24	8.5	0.059	0.021
29	1020	20	20	Perimeter (0.17)	A	GB	0.48	0.36	1.41	1.36	0.31	13.4	0.051	0.013
30	1021		20	Space (1.0)	A	GB	0.63	0.40	1.66	1.60	0.23	9.0	0.058	0.015

Margin - The margin is the ratio of the median collapse capacity to the ground motion level of interest.
a - Fixity assumed only in the design process. OpenSees models use expected grade beam, basement column, and soil stiffnesses.
b - Only first story designed to be weak.
c - First and second stories designed to be weak.
d - Mean when using a lognormal distribution; this value is closer to the median.
A - Expected practitioner design; strength and stiffness stepped over height as would be done in common design practice.
B (%) - Weak story; done by sizing the target weak story(ies) based on code requirements and then strengthening stories above. % is the percentage of strength in the weak story(ies) as compared to the stories above.
C - conservative design; neither size nor reinforcement of beams/columns are decreased over building height
F - Fixed.

Section 6.4.5 previously illustrated the importance of considering structural modeling uncertainties in collapse assessment. To further illustrate this finding, Appendix C presents the collapse performance predictions with and without modeling uncertainties. This shows that including structural modeling uncertainties increases the probability of collapse conditioned on the 2%-in-50-years ground motion from an average of 3% to an average values of 11% (for the 30 buildings considered in this study). The average mean annual frequency of collapse increases from 0.5×10^{-4} collapses/year to 3.1×10^{-4}; in terms of the collapse return period, this is a decrease from 20,000 to 3,200 years.

6.5.2 Effects of Building Height and Period

Of all the design parameters investigated in this study, building height has the most important effect on collapse safety. Table 6.11 presents the collapse results for buildings ranging in height from 1 to 20 stories; Table 6.11a presents the set of space frame buildings and Table 6.11b presents the set of perimeter frame buildings.

Table 6.11 Collapse predictions for buildings of various height. Building sets are expected practitioner designs for strength and stiffness, with 20′ bay spacing: (a) space frame buildings and (b) perimeter frame buildings.

(a)

Height/Design		Period and Pushover Analysis Results			Collapse Predictions, Controlling Horizontal Comp. of Ground Motion				Collapse Drifts	
No. of stories	Design ID Number	First Mode Period (T_1) [sec]	Static Overstr.	RDR_{ult}	Margin Against MCE	Margin Against 2% in 50 Motion	$P[C\|Sa_{2/50}]$ including modeling uncertainty	λ_{col} [10^{-4}], including modeling uncertainty	Median IDR at collapse	Median RDR at collapse
1	2061	0.42	4.0	0.077	1.64	1.76	0.20	7.3	0.071	0.071
2	1001	0.63	3.5	0.085	1.88	2.34	0.10	2.6	0.097	0.075
4	1008	0.94	2.7	0.047	1.66	1.83	0.17	5.4	0.080	0.045
8	1012	1.80	2.3	0.028	1.52	1.42	0.29	11.5	0.068	0.027
12	1014	2.14	2.1	0.022	1.36	1.31	0.33	15.5	0.055	0.018
20	1021	2.36	2.0	0.023	1.66	1.60	0.23	9.0	0.058	0.015

(b)

Height/Design		Period and Pushover Analysis Results			Collapse Predictions, Controlling Horizontal Comp. of Ground Motion				Collapse Drifts	
No. of stories	Design ID Number	First Mode Period (T_1) [sec]	Static Overstr.	RDR_{ult}	Margin Against MCE	Margin Against 2% in 50 Motion	$P[C\|Sa_{2/50}]$ including modeling uncertainty	λ_{col} [10^{-4}], including modeling uncertainty	Median IDR at collapse	Median RDR at collapse
1	2069	0.71	1.6	0.077	1.06	1.26	0.36	17.3	0.078	0.078
2	2064	0.66	1.8	0.067	1.36	1.65	0.23	8.7	0.075	0.061
4	1003	1.12	1.6	0.038	1.36	1.43	0.28	11.3	0.076	0.039
8	1011	1.71	1.6	0.023	1.19	1.11	0.44	25.5	0.054	0.021
12	1013	2.01	1.7	0.026	1.23	1.19	0.39	20.3	0.053	0.016
20	1020	2.63	1.6	0.018	1.41	1.36	0.31	13.4	0.051	0.013

6.5.2.1 Margin against Collapse, Probability of Collapse, and Mean Rate of Collapse

Collapse safety can be expressed in many ways. Figure 6.16 shows how collapse safety is affected by building height, and uses three different indices to express this.

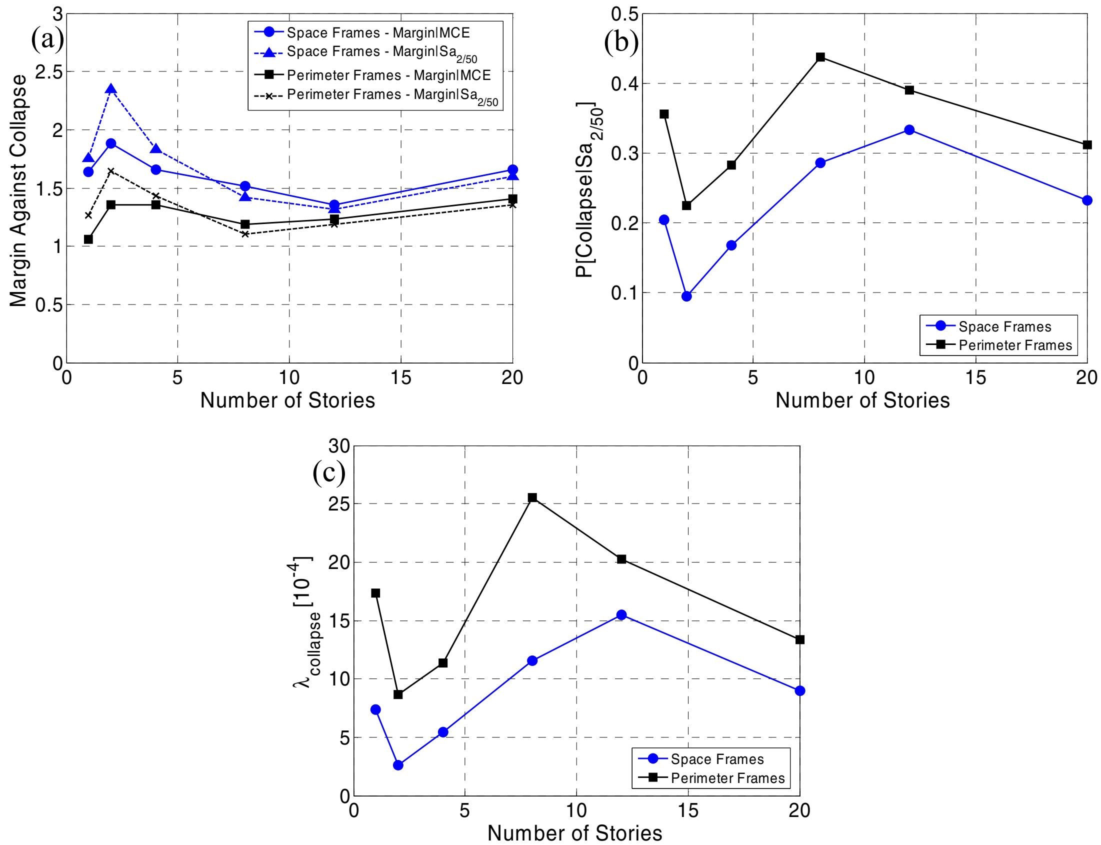

Fig. 6.16 Collapse safety for various buildings heights. Safety expressed in terms of (a) margin against collapse, (b) probability of collapse conditioned on level of ground motion, and (c) mean annual frequency of collapse.

Figure 6.16a shows how the margin against collapse changes with building height, for the set of space frame and set of perimeter frame buildings. The margin against collapse is a rough way to express the collapse safety and is simply a ratio of the median collapse capacity to a ground motion level of interest. This figure shows the margin against the maximum considered earthquake motion (MCE) (ICC 2003), as well as the margin against the 2%-in-50-years motion ($Sa_{2/50}$). The slight difference between these two measures is due to the difference in the hazard as shown previously in Figure 6.2. Due to this minimal difference, the later comparisons consider only $Sa_{2/50}$. Figure 6.16a also shows that the collapse margin is a function of building height and that collapse margin changes from 1.1 to 2.3 for buildings of various heights, where the mid-rise (8–12 story) buildings have the highest collapse risk, and that this trend is the same for both perimeter and space frame buildings. One exception is that the 1-story design is shown to be most critical for perimeter frame buildings when the MCE is used for computing the margin; the higher collapse probabilities of the 1-story buildings may be associated with the lower deformation capacities of these buildings. Note that this observation of 8–12 story buildings being most critical is based to a large extent on the 20-story buildings having a larger collapse margin than the 8–12 story buildings. To have higher confidence in this trend, more tall buildings should be assessed.

Figure 6.16b is similar to Figure 6.16a but shows the trends in probability of collapse given the 2%-in-50-years ground motion. Space frame and perimeter frame buildings have the same trend and again show that the 8–12 story buildings have the highest collapse risk. This figure shows that for the space frame buildings, the collapse probability varies by +/- 23% with building height.

Figure 6.16c shows the trends in mean annual frequency of collapse for the site used in this study. This shows the same trends as the last two figures. This figure shows that for the space frame buildings, the mean annual rate of collapse varies by a factor of six over height.

The following sections look at other interesting aspects of the buildings and how they are affected by height. From these comparisons, we try to explain *why* the collapse risks vary with building height.

6.5.2.2 Fundamental Period

Figure 6.17 shows the relationship between model fundamental period and building height for both space and perimeter frame buildings. For comparison, the figure also shows the mean period estimates by Chopra and Goel (2000), as well as the common rules of thumb that the fundamental period is 0.1N to 0.2N, where N is the number of stories. It is important to clarify that this is the period of the structural model, which only includes structural elements; none of the nonstructural component stiffnesses are reflected in the model. The element stiffnesses are based on our calibration study (Haselton et al. 2007b, Chapter 4), which is calibrated as the secant stiffness at 40% of the yield load.

Figure 6.17 shows that the building periods are greater than those predicted by Chopra and Goel (2000) for all buildings except the 20-story buildings. This figure shows the periods are slightly larger than 0.2N for the 1–8 story buildings, slightly below 0.2N for the 12-story buildings, and in the range of 0.1N–0.15N for the 20-story buildings.

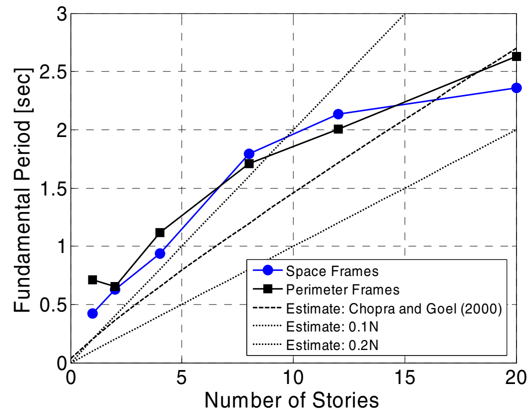

Fig. 6.17 Effects of building height on fundamental periods of space and perimeter frame buildings.

6.5.2.3 Static Overstrength and Effective R Factor

Figure 6.18a shows the relationship between static overstrength and building height for the space and perimeter frame buildings. For space frame buildings, there is a clear trend between static overstrength and building height. Short space frame buildings have high levels of overstrength, which reflects the dominance of gravity loads in the design of this type of building. As the building height increases, the design becomes less dominated by gravity loading, making the overstrength decrease. The overstrength stabilizes at around 2.0 for 8-story buildings and above.

Perimeter frame building design is less dominated by gravity loading, so the static overstrengths are lower and do not depend on building height. Perimeter frame buildings have overstrengths of 1.5–1.8 for building of all heights.

Another way to express the overstrength is with an effective R-factor, as shown in Figure 6.18b. This effective R-factor is defined as the ratio of the design spectral acceleration level (2/3 of the maximum considered earthquake (MCE) ground motion) to the building yield base shear strength (from static pushover analysis). This factor accounts for the overstrength shown in Figure 6.18a, the effects of the period cap used in the ASCE7-02 equations for design base shear demand, and the effects of the minimum design base shear provision.

These trends in static overstrength and effective R-factor are interesting, but comparison to Figure 6.16 shows that these trends do not accurately explain the observed trends in collapse safety with height.

Note that the beneficial contribution of the gravity system to lateral load resistance is neglected in the analysis of perimeter frame systems. The effect of including the gravity system in the analysis model was investigated in a recent study (Haselton et al. 2007e); for a code-conforming 4-story RC SMF building, including the gravity system in the analysis increased the median collapse capacity by approximately 10%.

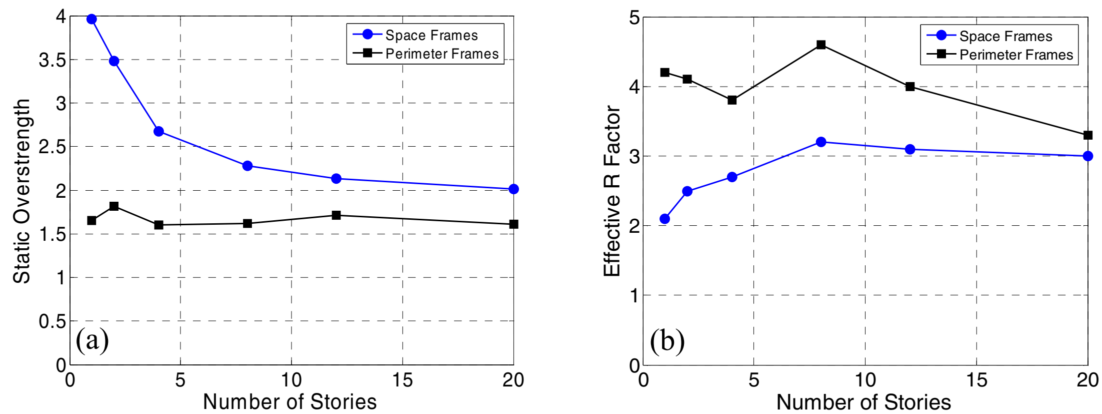

Fig. 6.18 Effects of building height on (a) static overstrength and (b) effective R-factor.

6.5.2.4 Drifts at Collapse

Figure 6.19 shows the drift capacities of the buildings of various heights. This figure reports the median drift ratios near collapse (definition explained in Section 6.4.7), both roof drift and maximum story drift.

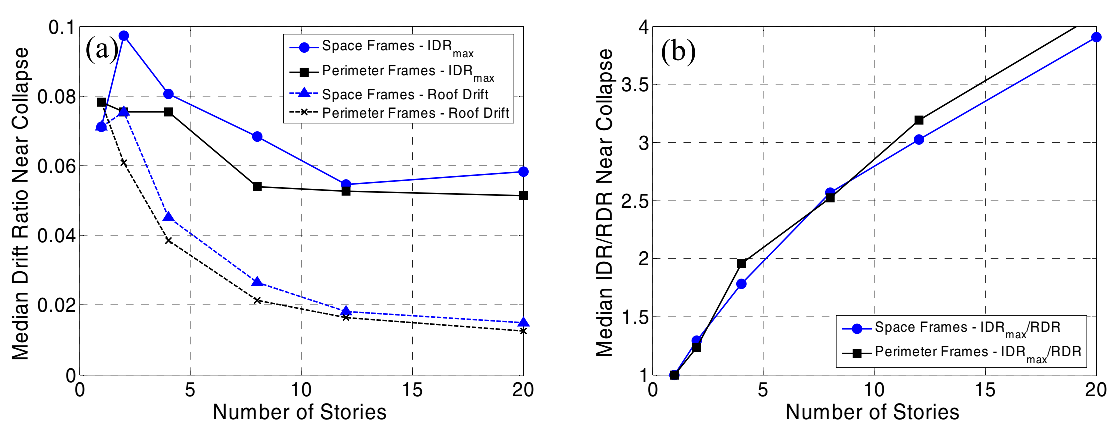

Fig. 6.19 Effects of building height, for both space and perimeter frame buildings, on (a) interstory and roof drifts near collapse and (b) ratio of maximum interstory drift to roof drift.

Figure 6.19a shows that both story and roof drift capacities generally decrease as the building gets taller, but that the collapse drifts nearly stabilize for the 12- and 20-story buildings. This stabilization in drift capacity is consistent with the trends in collapse capacity that were presented earlier. It is noted that these 12- and 20-story buildings are designed for the minimum base shear provision in ASCE7-02 (ASCE 2002), while the shorter buildings are designed for the basic base shear provision; this is investigated in more detail in Section 6.5.3. This may be related to the change in drift capacity behavior for these 12- and 20-story buildings.

This figure also shows that the trend does not hold for 1-story buildings (specifically space frames), which is also consistent with the observations made in Section 6.5.2.1 regarding the lower deformation capacities of the 1-story buildings.

Figure 6.19b shows the ratio of maximum interstory drift at collapse to roof drift at collapse, which indicates how much the damage localizes in a few stories of the building. This shows that the ratio ranges from 1.0 for 1-story buildings (as it must be) to nearly 4.0 for 20-story buildings. This figure also shows that the trend is virtually identical for both space-frame and perimeter-frame buildings.

The story drift capacity decreases with increased height due to (a) column plastic rotation capacities decreasing due to increased axial stresses and (b) increased P-delta effects causing the story to have a negative stiffness at lower drift levels; the latter is the most important effect. The one building that does not follow this trend is the 20-story space frame (ID 1021). Simple design decisions caused this building to be stiffer (P-delta less dominant) and to have less localized damage relative to the 12-story (ID 1014), which caused the 20-story building to actually have slightly higher deformation capacity that the 12-story building; this can be seen in the interstory deformations at collapse (Fig. 6.19 above) and in the pushover results (RDR_{ult} in Table 6.11a).

The roof drift capacity is a more complex issue. The roof drift capacity is based on the drift capacity of each story as well as the number of stories involved in the collapse mechanism. The next section looks at the collapse mechanisms and further explains why the 20-story buildings do not follow the same trends as the 2–12 story buildings.

6.5.2.5 Collapse Mechanisms and Damage Localization

To learn about how the building height affects the number of stories involved in the collapse mechanism, we looked at the collapse mechanisms for each building subjected to each of the 80 ground motions. Table 6.12 gives the percentage of each mechanism for the buildings of various heights, and the average ratio of stories involved in the mechanism. For example, the 12-story perimeter frame building collapsed 73% of the time in a first-second story mechanism, 25% in a first-second-third story mechanism, and 2% of the time in an upper-story (second-third-fourth in this case) mechanism; on average, 18% of the stories of this building are involved in the collapse mechanism. Figure 6.20 shows the predominant collapse mechanism for each of the buildings.

Table 6.12 Relative occurrence of collapse mechanisms for buildings of various heights: (a) space frame buildings and (b) perimeter frame buildings.

(a)

Height/Design		Percentage of Collapse Mechanisms Observed in Nonlinear Dynamic Analyses						
No. of stories	Design ID Number	Story 1	Stories 1-2	Stories 1-3	Stories 1-4	Stories 1-5	Upper Stories	Average Ratio of Stories Involved in Collapse Mechanism
1	2061	100%	--	--	--	--	--	1.00
2	1001	72%	28%	--	--	--	0%	0.64
4	1008	29%	64%	0%	0%	--	7%	0.42
8	1012	0%	75%	25%	0%	0%	0%	0.28
12	1014	8%	85%	3%	4%	0%	0%	0.17
20	1021	0%	9%	14%	0%	60%	17%	0.22

(b)

Height/Design		Percentage of Collapse Mechanisms Observed in Nonlinear Dynamic Analyses						
No. of stories	Design ID Number	Story 1	Stories 1-2	Stories 1-3	Stories 1-4	Stories 1-5	Upper Stories	Average Ratio of Stories Involved in Collapse Mechanism
1	2069	100%	--	--	--	--	--	1.00
2	2064	62%	38%	--	--	--	0%	0.69
4	1003	0%	40%	0%	0%	--	60%*	0.35
8	1011	0%	91%	7%	0%	0%	2%	0.25
12	1013	0%	73%	25%	0%	0%	2%	0.18
20	1020	0%	5%	55%	33%	4%	3%	0.17

* 57% second story mechanism and 3% second-third story mechanism

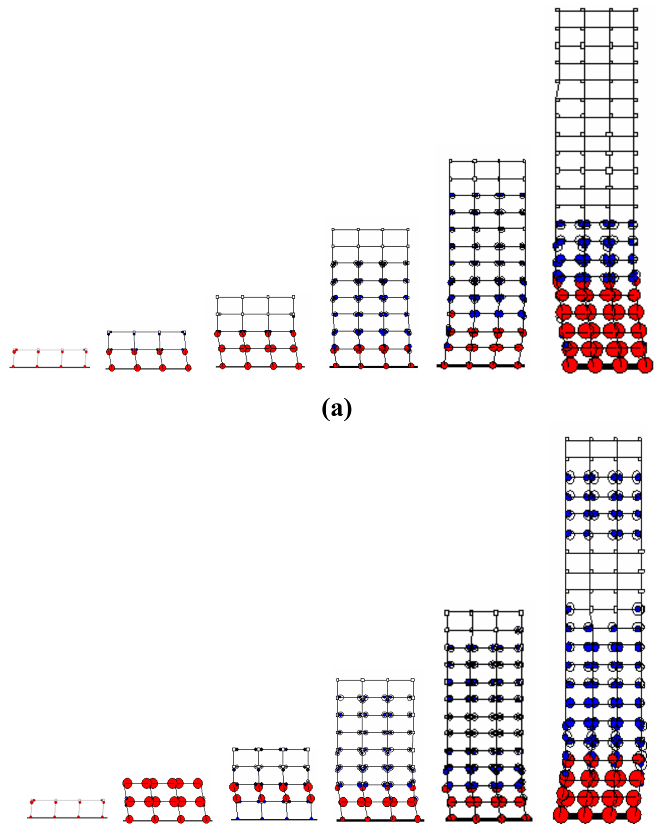

(a)

(b)

Fig. 6.20 Predominant collapse mechanisms for buildings of various heights: (a) space frame buildings and (b) perimeter frame buildings.

As expected, Table 6.12 shows that the ratio of stories involved in the collapse mechanism decreases with height. However, this trend stops or reverses when we get to the 20-story buildings. This behavior mirrors the trends in roof drift capacity shown previously in Figure 6.19, and explains why the collapse risk is reduced for the 20-story building.

When comparing the designs and modeling of the 12- and 20-story buildings, there is no obvious reason why the 20-story buildings should have a larger percentage of the stories involved in the collapse mechanism.

6.5.2.6 Summary

Building height significantly impacts collapse risk. For buildings ranging from 1 to 20 stories, the mean rate of collapse varies by a factor of six, and the collapse probability can range more than +/- 20%.

The differences in collapse safety correlate most closely with the differences in the deformation capacities of each building, with other influences from changes in strength.

The results of this study suggest that the mid-rise 8–12 story buildings have the highest collapse risk, but this observation is based on the 20-story buildings having lower risk than the 8–12 story ones. It is not clear whether this observation is general or based on the specifics of the 20-story building designs used in this study. We feel that more designs/analyses of taller buildings are required before making any strong statements about the mid-rise buildings being the most collapse critical. It is also noted that these 12- and 20-story buildings are designed for the minimum base shear provision in ASCE7-02 (ASCE 2002), while the shorter buildings are designed for the basic base shear provision. This causes a reduced effective R-factor and improvement in the collapse capacities for the 12- and 20-story buildings; this is investigated in more detail in Section 6.5.3.

6.5.3 Impacts of Reduced Minimum Design Base Shear in New ASCE7-05 Design Provisions

When looking at the effects of building height, the last section suggested that mid-rise buildings (8–12 stories) may have a slightly higher collapse risk as compared to 12- and 20-story buildings. The buildings used in the last section were designed by the ASCE7-02 provisions (ASCE 2002), which include a minimum design base shear coefficient (C_s) requirement of 0.044g for the sites used in this study (ASCE 2002, Eq. 9.5.5.2.1-3). This minimum base shear requirement was removed in the updated ASCE 7-05 (ASCE 2005) provisions (for buildings with $S_1 < 0.6g$); this change leads to a significant reduction in the design base shear for tall buildings. For example, the design base shear of a 20-story building designed for $S_1 = 0.595g$ would decrease from $C_s = 0.044g$ to $C_s = 0.022g$.

To examine the impacts of the new ASCE7-05 provisions, we redesigned the 12- and 20-story buildings according to ASCE7-05 at a site with $S_1 = 0.595g$. Because the minimum base shear requirement is not in place, these structures have a significantly lower design base shear than their ASCE 7-02 counterparts. The collapse safety predictions for the redesigned structures are shown in Table 6.13 and Figure 6.21. The effect of the reduced design base shear is significant, reducing the median collapse capacity of the 20-story perimeter frame building by a factor of two, increasing the conditional collapse probability from 13% to 53% and increasing the mean annual frequency of collapse by a factor of 11. In addition, Figure 6.21 shows that the trend of collapse safety with height changes dramatically. Under the revised ASCE 7-05 provisions, taller buildings have a significantly higher risk of collapse than shorter structures.

Table 6.13 Comparison of collapse predictions for buildings designed using ASCE7-02 and ASCE7-05. Note that only difference imposed in ASCE7-05 design is base shear demand.

Height/Design					Period and Collapse Risk Predictions			
Number of stories	Governing Design Provision	Perimeter or Space Frame System	Design Base Shear Coefficient (C_s) [g]	Design ID Number	First Mode Period (T_1) [sec]	Margin Against 2% in 50 year Motion	$P[C\|Sa_{2/50}]$	λ_{col} [10^{-4}]
12	ASCE 7-02	P	0.044	1013	2.01	1.84	0.16	5.2
12	ASCE 7-05	P	0.035	5013	2.40	1.29	0.35	16.9
12	ASCE 7-02	S	0.044	1014	2.14	1.91	0.15	4.7
12	ASCE 7-05	S	0.035	5014	2.18	1.85	0.16	4.9
20	ASCE 7-02	P	0.044	1020	2.63	2.00	0.13	3.7
20	ASCE 7-05	P	0.022	5020	3.77	0.95	0.53	40.7
20	ASCE 7-02	S	0.044	1021	2.36	2.5	0.08	2.0
20	ASCE 7-05	S	0.022	5021	3.45	1.43	0.27	9.2

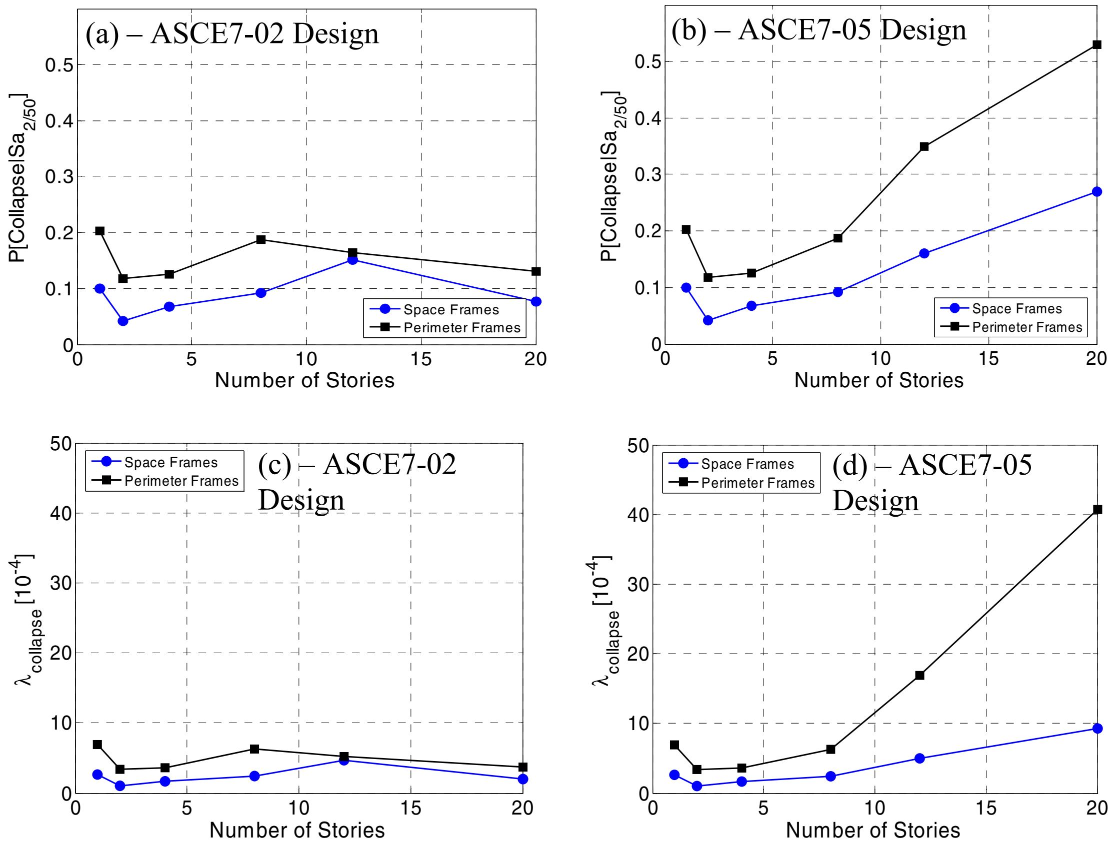

Fig. 6.21 Comparison of effects of height on P[C|$Sa_{2./50}$] when structures designed according to (a) ASCE 7-02 and (b) ASCE 7-05, and $\lambda_{collapse}$ when structures designed according to (c) ASCE 7-02 and (d) ASCE 7-05.

This study suggests that the minimum base shear requirement (ASCE 7-02 Eq. 9.5.5.2.1-3) is an important component of ensuring relatively consistent collapse risk for buildings of varying height. Removing this requirement has made taller buildings significantly more vulnerable to collapse; this should be considered in future revisions of ASCE7.

6.5.4 Effects of Space/Perimeter Framing Layout

This section compares space and perimeter frame buildings and shows that space frames consistently have a lower collapse risk than perimeter frames. When looking at the relative impacts of design changes, the difference in the collapse risk between space/perimeter frame buildings is important, second only to the effects of building height.

Table 6.14 compares the collapse predictions for six pairs of space/perimeter frame buildings. These are the same data as presented in Section 6.5.2, but reordered to contrast the space versus perimeter frame variation.

Table 6.14 Collapse predictions for sets of space versus perimeter frame buildings.

Height/Design				Period and Pushover Analysis Results			Collapse Predictions, Controlling Horizontal Comp. of Ground Motion				Collapse Drifts	
Space/ Perimeter	No. of stories	Bay Spacing [ft]	Design ID Number	First Mode Period (T_1) [sec]	Static Overstr.	RDR_{ult}	Margin Against MCE	Margin Against 2% in 50 Motion	$P[C\|Sa_{2/50}]$ including modeling uncertainty	λ_{col} $[10^{-4}]$, including modeling uncertainty	Median IDR at collapse	Median RDR at collapse
Perimeter	1	20	2069	0.71	1.6	0.077	1.06	1.26	0.36	17.3	0.078	0.078
Space			2061	0.42	4.0	0.077	1.64	1.76	0.20	7.3	0.071	0.071
Perimeter	2	20	2064	0.66	1.8	0.067	1.36	1.65	0.23	8.7	0.075	0.061
Space			1001	0.63	3.5	0.085	1.88	2.34	0.10	2.6	0.097	0.075
Perimeter	4	20	1003	1.12	1.6	0.038	1.36	1.43	0.28	11.3	0.076	0.039
Space			1008	0.94	2.7	0.047	1.66	1.83	0.17	5.4	0.080	0.045
Perimeter	8	20	1011	1.71	1.6	0.023	1.19	1.11	0.44	25.5	0.054	0.021
Space			1012	1.80	2.3	0.028	1.52	1.42	0.29	11.5	0.068	0.027
Perimeter	12	20	1013	2.01	1.7	0.026	1.23	1.19	0.39	20.3	0.053	0.016
Space			1014	2.14	2.1	0.022	1.36	1.31	0.33	15.5	0.055	0.018
Perimeter	20	20	1020	2.63	1.6	0.018	1.41	1.36	0.31	13.4	0.051	0.013
Space			1021	2.36	2.0	0.023	1.66	1.60	0.23	9.0	0.058	0.015

Table 6.14 and the figures in the last section show that:

- Space frames have higher overstrength as compared to perimeter frames. The space frames have a factor of 2.5x the overstrength for low-rise buildings and about 1.2x for the 12- to 20-story buildings. This seems to have a slight effect on the collapse capacity.
- Margin against collapse is 1.1x to 1.3x higher for space frame buildings.
- $P[C|Sa_{2/50}]$ is 6% to 15% lower for space frame buildings.
- Mean annual frequency of collapse is 1.3x to 2.2x lower for space frame buildings.
- Roof drift capacity is 1.1x to 1.2x higher for space frame buildings.

The above table and comparisons show that space frames have a consistently lower collapse risk as compared to perimeter frames. These trends in collapse capacity are closely related to the building deformation capacities (i.e., drifts at collapse). The difference in deformation capacity between space and perimeter frame buildings does not come from changes in element deformation capacities. Beam deformation capacities are similar for both systems, and column deformation capacities are actually much larger for perimeter frame buildings, due to lower axial stresses in the columns.

The difference in deformation capacity seems to come from higher dominance of P-delta effects for perimeter frame buildings. A perimeter frame typically carries 3x to 5x the tributary lateral mass as compared to a space frame. Even though the perimeter frame is designed for this additional mass, the pushover indicates that the P-delta effects are still greater for this type of system. To give an example of this, Figure 6.22 compares the pushover results for 8-story perimeter and space frame buildings. This shows that the deformation capacities (i.e., capping point) predicted by the pushover analysis are similar, but that the perimeter frame has a much steeper negative post-yield slope. This comparison also shows that the space frame has more overstrength (2.3 versus 1.6). The previously presented results suggested that the overstrength changes are not as important as changes in deformation capacity and negative post-yield stiffness.

For this comparison, the combination of the steeper post-yield slope and lower overstrength causes the perimeter frame to have 25% lower collapse roof drifts, which in turn cause the collapse margin to be 30% lower.

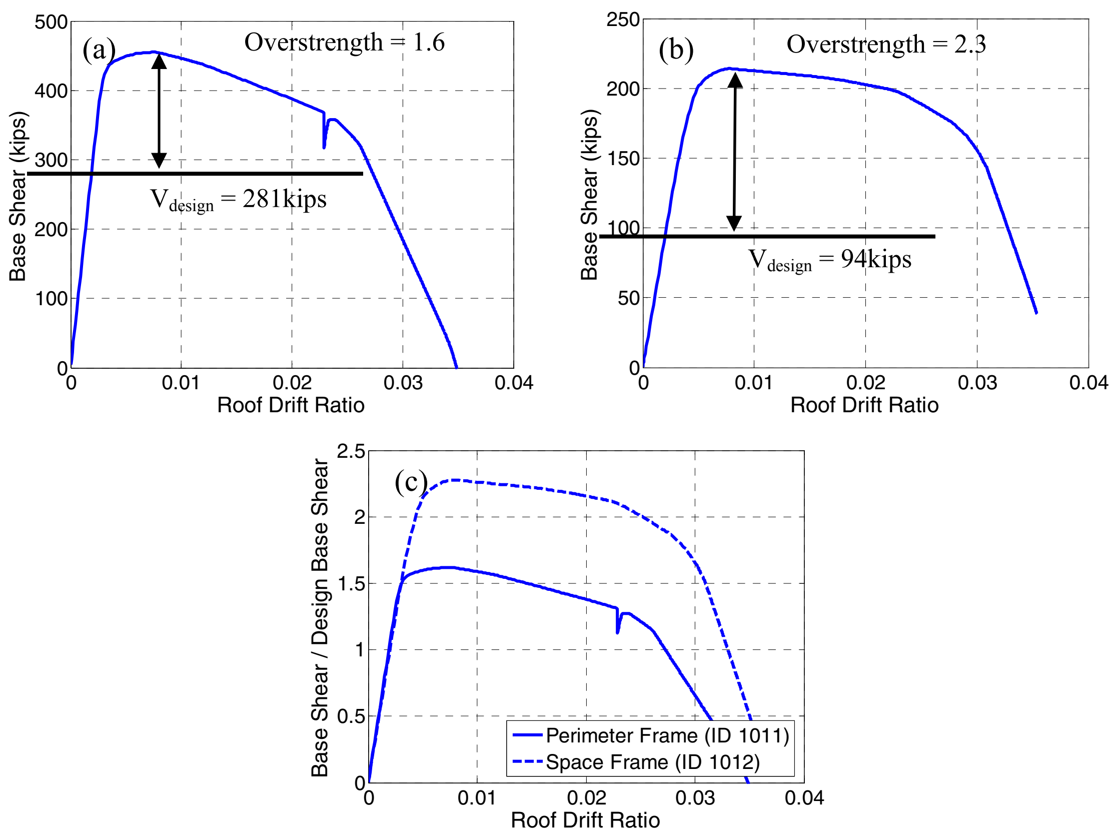

Fig. 6.22 Monotonic static pushover diagram using code-prescribed load pattern (ICC 2003) for (a) 8-story perimeter frame (ID 1011), (b) 8-story space frame (ID 1012), and (c) normalized pushover with both perimeter and space frames.

One simplification of this section is that, for perimeter frame buildings, we did not consider the beneficial effects of the gravity system. If we included the effects of the gravity system, the difference shown in this section would be reduced. This was investigated in a study for a code-conforming 4-story RC SMF building (Haselton et al. 2007e) where the gravity system increased the median collapse capacity by about 10%.

6.5.5 Effects of Strength and Stiffness Distribution

The distribution of strength and stiffness over the height of the building can have obvious effects on the level of damage concentration over height, as well as the static overstrength. The scope of this study does not allow a comprehensive treatment of how differences in strength and stiffness distribution affect performance. Rather, this study looks only at two design cases: (1) the effects of a "conservative" design where the element size and reinforcement are kept constant up the building height and (2) the effects of strength-irregular designs. The first is discussed in this section, and the latter in the next section.

Table 6.15 compares the results for three pairs of building, each with a baseline design and a "conservative" design. These data show that by maintaining constant element sizes and reinforcement, the collapse margin increases by a factor of 1.1–1.2, the collapse probability decreases by 4%–6%, and the mean annual frequency of collapse decreases by a factor of 1.2–1.4.

Intuitively, one may expect that not stepping element sizes and strengths would cause the damage to localize more in lower stories and cause the collapse performance to *decrease*. We now see that this is not the case. Instead, use of uniform element sizes and reinforcement cause the drift capacity, and the resulting collapse capacity, to increase slightly. This change in the collapse performance is not significant when compared to the effects of other design changes.

Table 6.15 Collapse predictions for both baseline designs and designs with constant member sizes and reinforcement.

Height/Design					Period and Pushover Analysis Results			Collapse Predictions, Controlling Horizontal Comp. of Ground Motion				Collapse Drifts	
No. of stories	Strength/ Stiffness Distribution Over Height	Bay Spacing [ft]	Space/ Perimeter	Design ID Number	First Mode Period (T_1) [sec]	Static Overstr.	RDR_{ult}	Margin Against MCE	Margin Against 2% in 50 Motion	$P[C\|Sa_{2/50}]$ including modeling uncertainty	λ_{col} [10^{-4}], including modeling uncertainty	Median IDR at collapse	Median RDR at collapse
4	A	20	Perimeter	1003	1.12	1.6	0.038	1.36	1.43	0.28	11.3	0.076	0.039
	C			1004	1.11	1.7	0.043	1.59	1.66	0.22	8.1	0.085	0.047
8	A	20	Space	1012	1.80	2.3	0.028	1.52	1.42	0.29	11.5	0.068	0.027
	C			1022	1.80	2.6	0.035	1.61	1.51	0.25	9.2	0.077	0.033
12	A	20	Space	1014	2.14	2.1	0.022	1.36	1.31	0.33	15.5	0.055	0.018
	C			1019	2.13	2.1	0.024	1.47	1.43	0.29	12.6	0.059	0.021

A - expected practitioner design; strength and stiffness stepped over height as would be done in common design practice.
C - conservative design; neither size nor reinforcement of beams/columns are decreased over building height

6.5.6 Effects of Strength-Irregular Designs

We looked at the effects of strength irregularities and found that strength-irregular designs that are code-compliant (i.e., meet code required strength demands, even in the weaker stories) are much less detrimental than expected.

To begin investigating the effects of strength irregularities, we designed sets of 8-story and 12-story buildings with weaker first or first/second stories. To achieve the proper story strength ratio, while still maintaining code-compliance, we designed the first two stories based on code strength requirements and then strengthened the upper stories appropriately to make the strength ratios between the weak/strengthened stories be 80% or 65%. In this process, we defined story strength as being proportional to beam strength, since the columns strengths are designed in proportion to beam strengths.

Table 6.16 presents the collapse results for the baseline designs and the 80% and 65% strength-irregular designs for the 8-story and 12-story buildings. This shows that the collapse risk only increases slightly for the weak-story designs. The collapse margin decreases by about a factor of 1.1, the collapse probability increases by 5%, and the mean annual frequency of collapse increases by a factor of about 1.3. Note that the increase in the collapse drift for building ID 1017 is due to a simple change in design decisions that causes the column stirrups to be more closely spaced.

Table 6.16 Collapse predictions for baseline and weak-story designs (first two stories weak).

Height/Design			Period and Pushover Analysis Results			Collapse Predictions, Controlling Horizontal Comp. of Ground Motion				Collapse Drifts	
No. of stories	Strength Ratio of Weak Story	Design ID Number	First Mode Period (T_1) [sec]	Static Overstr.	RDR_{ult}	Margin Against MCE	Margin Against 2% in 50 Motion	$P[C\|Sa_{2/50}]$ including modeling uncertainty	λ_{col} [10^{-4}], including modeling uncertainty	Median IDR at collapse	Median RDR at collapse
8	100% (Baseline)	1012	1.80	2.3	0.028	1.52	1.42	0.29	11.5	0.068	0.027
	80%	1024	1.71	2.7	0.021	1.37	1.28	0.35	16.8	0.067	0.020
	65%	1023	1.57	2.9	0.019	1.33	1.28	0.35	16.8	0.066	0.018
12	100% (Baseline)	1014	2.14	2.1	0.022	1.36	1.31	0.33	15.5	0.055	0.018
	80%	1018	2.09	2.5	0.018	1.29	1.25	0.36	18.0	0.058	0.016
	65%	1017	1.92	2.8	0.016	1.30	1.21	0.38	18.1	0.065	0.015

The small impact that the strength-irregular designs have on the collapse performance comes from the fact that we weakened the first two stories (assuming this would cause damage to localize in these stories); however, the collapse mechanisms for the baseline designs were already predominantly first-second story mechanisms. Figures 6.23 and 6.24 show how the weaker stories caused the damage to localize slightly more for both sets of buildings, with the effects being more predominant for the 8-story set.

One other partially compensating effect that we see in Table 6.15 is that strengthening the upper stories of the building causes the static overstrength to increase.

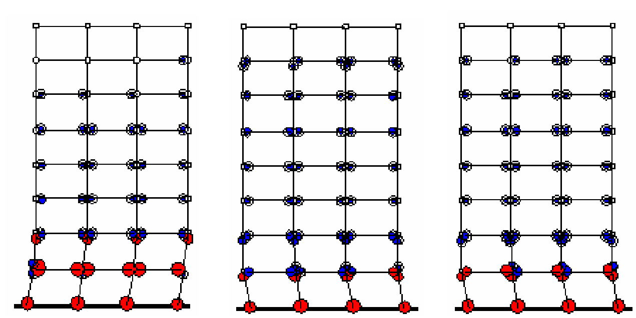

(a) 75% (25% 1–3-story)   (b) 55% (45% 1-story)   (c) 50% (50% 1–2 story)

Fig. 6.23 Predominant collapse mechanisms for 8-story buildings: (a) baseline design (ID 1012), (b) 80% strength irregularity (1–2 stories weak) (ID 1024), and (c) 65% strength irregularity (1–2 stories weak) (ID 1023).

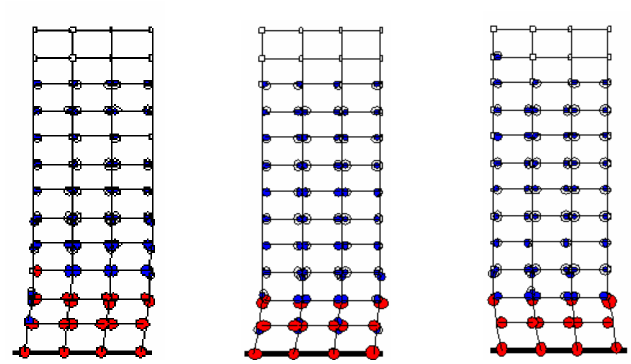

(a) 86%
(9% 1-story)
(5% other)

(b) 72%
(28% 1-story)

(c) 79%
(21% 1-story)

Fig. 6.24 Predominant collapse mechanisms for 12-story buildings: (a) baseline design (ID 1014), (b) 80% strength irregularity (1–2 stories weak) (ID 1018), and (c) 65% strength irregularity (1–2 stories weak) (ID 1017).

In order look more closely at how a strength irregularity can cause damage to localize in a single story and possibly cause the collapse performance to decrease, we designed a second set of buildings with only one weak story. As with the previous cases, the "weak" first story is created by strengthening the upper stories relative to the first story. In these designs, we defined story strength as being the shear that can be carried by the columns in a story, when columns are yielded at both ends.

Table 6.17 presents the collapse predictions for the baseline and strength-irregular designs with only the first story weak. This shows that the collapse performance of these strength-irregular designs is *actually better* than the baseline designs. This improved performance can be partially explained by slight increases in first-story column deformation capacity that resulted randomly from the design process, and an increase in static overstrength (effect should be minimal) that resulted from the upper stories of the building being strengthened. Even considering these two effects, we did not expect the performance to improve over the baseline designs.

Table 6.17 Collapse predictions for baseline and strength-irregular designs (only 1st story weak).

Height/Design			Period and Pushover Analysis Results			Collapse Predictions, Controlling Horizontal Comp. of Ground Motion				Collapse Drifts	
No. of stories	Strength Ratio of Weak Story	Design ID Number	First Mode Period (T_1) [sec]	Static Overstr.	RDR_{ult}	Margin Against MCE	Margin Against 2% in 50 Motion	$P[C\|Sa_{2/50}]$ including modeling uncertainty	λ_{col} [10^{-4}], including modeling uncertainty	Median IDR at collapse	Median RDR at collapse
8	100% (Baseline)	1012	1.80	2.3	0.028	1.52	1.42	0.29	11.5	0.068	0.027
	80%	2066	1.71	2.9	0.031	1.71	1.70	0.20	8.7	0.074	0.027
	65%	2065	1.57	3.3	0.024	1.58	1.56	0.24	10.0	0.069	0.021
12	100% (Baseline)	1014	2.14	2.1	0.022	1.36	1.31	0.33	15.5	0.055	0.018
	80%	2068	2.09	2.5	0.022	1.40	1.31	0.33	14.0	0.057	0.018
	65%	2067	1.92	3.2	0.020	1.50	1.38	0.30	12.1	0.066	0.016

The question of the collapse mechanism is an interesting one in this comparison. Since the strength-irregular designs performed better than the baseline designs, we initially assumed that the strength-irregular was not successful in changing the collapse mechanism. This is surprisingly not the case. The strength-irregular designs have better performance in spite of more frequent first-story collapses.

Figures 6.24 and 6.25 show how the strength-irregular affect the predominant collapse mechanisms for the 8- and 12-story buildings. In the baseline designs, the collapse mechanism typically involves the bottom two stories. For the 65% strength-irregular designs, the collapse mechanism is changed drastically to be 100% first-story mechanisms in both the 8- and 12-story buildings. Of importance is that these are *collapse* mechanisms, which does not necessarily imply that all of the damage is concentrated only in the first story. Before the point of collapse, there is still a great deal of damage and energy dissipation in the upper stories of the building.

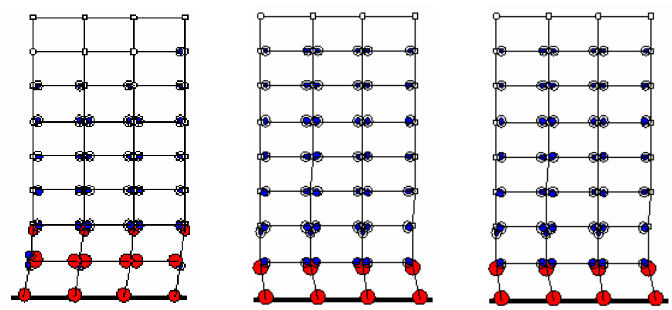

(a) 75%
(25% 1–3 story)

(b) 83%
(17% 1–2 story)

(c) 100%

Fig. 6.25 Predominant collapse mechanisms for 8-story buildings: (a) baseline building (ID 1012), (b) 80% strength irregularity (1st story weak) (ID 1024), and (c) 65% strength irregularity (1st story weak) (ID 1023).

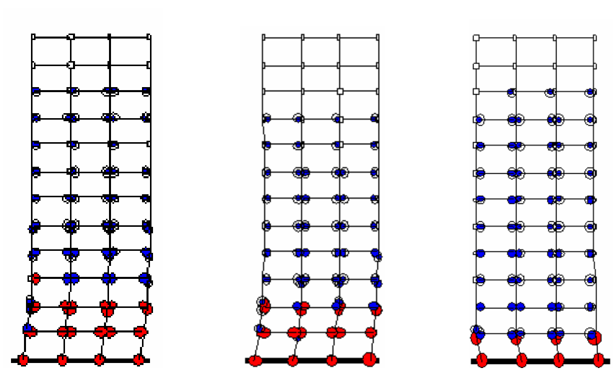

(a) 86%
(9% 1-story)
(5% other)

(b) 51%
(49% 1-story)

(c) 100%

Fig. 6.26 Predominant collapse mechanisms for 12-story buildings: (a) baseline building (ID 1014), (b) 80% strength irregularity (1st story weak) (ID 1018), and (c) 65% strength irregularity (1st story weak) (ID 1017).

6.5.7 Effects of Bay Spacing

The bay spacing makes little difference in the collapse performance. If we compare the collapse results for buildings with 20′ and 30′ bay spacing (Table 6.10 earlier), there seems to be a trend, but when we looked at the details of each building design we found that the differences in performance are more the results of random differences in design decisions rather than of the bay spacing.

The one slight influence of bay spacing occurs when an increase in bay spacing triggers the joint shear requirement to control the design. When this occurs, the column sizes are often increased to accommodate joint shear demands; which in turn reduces axial stress and increases the rotation capacity of the columns. In the end, this only improved the collapse performance a slight amount, so we do not present a separate table of these results.

6.5.8 Effects of Foundation Fixity Assumed in Design

The foundation rotational stiffness assumed in design can affect both the strength and stiffness design of the lower stories. To investigate the effects that this has on strength design, we created three design variants for the 1- and 2-story buildings. These designs vary the foundation fixity assumed in design, using pinned and fixed assumptions, as well as an intermediate assumption that considers the rotational stiffness of the grade beam. Each of these assumptions affects only the structural design. In all cases, the OpenSees analysis model considers the rotational stiffness due to the grade beams and the soil beneath the footings.

Table 6.18 shows an overview of these structural designs for 1- and 2-story buildings, as well as the collapse predictions for these designs. As expected, the static overstrength is largest for the pinned designs, smaller for the grade beam designs, and smallest for the fixed designs; this simply comes from the differences in the column flexural design strengths and capacities. When comparing the pinned and fixed designs, these design differences result in a 20% change in the collapse margin, a +/- 6% change in the collapse probability, and a 2x change in the mean annual frequency of collapse.

Table 6.18 Collapse predictions for sets of buildings designed with various foundation rotational stiffness assumptions.

Height/Design					Period and Pushover Analysis Results			Collapse Predictions, Controlling Horizontal Comp. of Ground Motion				Collapse Drifts	
No. of stories	Strength/ Stiffness Distribution Over Height	Bay Spacing [ft]	Space/ Perimeter	Design ID Number	First Mode Period (T_1) [sec]	Static Overstr.	RDR_{ult}	Margin Against MCE	Margin Against 2% in 50 Motion	$P[C \vert Sa_{2/50}]$ including modeling uncertainty	λ_{col} [10^{-4}], including modeling uncertainty	Median IDR at collapse	Median RDR at collapse
1	GB	20	Space	2061	0.42	4.0	0.077	1.64	1.76	0.20	7.3	0.071	0.071
	P			2062	0.42	4.9	0.079	1.82	1.95	0.16	4.7	0.075	0.075
	F			2063	0.42	4.0	0.077	1.64	1.76	0.20	7.3	0.069	0.069
2	GB	20	Space	1001	0.63	3.5	0.085	1.88	2.34	0.10	2.6	0.097	0.075
	P			1001a	0.56	4.4	0.085	1.95	2.40	0.09	2.2	0.080	0.061
	F			1002	0.63	3.1	0.076	1.59	1.98	0.15	4.8	0.083	0.059

F - Fixed.
GB - "Grade Beam" - this considers the rotational stiffness of the grade beam.
P - Pinned.

6.6 SUMMARY AND CONCLUSIONS

6.6.1 Archetype Framework and Methodology

This paper has summarized a method to assess the performance of a *full class* of buildings. The method involves the clear articulation of possible deterioration and collapse modes, and then the creation of a structural model that captures each mode. This structural model is then used to assess the performance of a large number of designed buildings, where the results of which are used to develop general conclusions about the performance of the building class.

We applied this methodology to reinforced concrete special moment frames (RC SMF) designed by current building code provisions. This provides an illustrative example on how to apply the methodology and also gives insights into the performance implied by modern building codes.

6.6.2 Collapse Performance Predictions for 30 RC SMF Buildings

We assessed the collapse performance of 30 RC SMF building designs ranging from 1 to 20 stories and including various changes in the designs. With the proper ground motion considerations, the collapse margins against the MCE (ratio of median collapse capacity to MCE demand) range from 1.4 to 3.0 for all 30 designs, with an average value of 2.2. The variability in the collapse capacity, coming from variations in ground motions, is surprisingly consistent and ranges from 0.36 to 0.46, with an average of 0.40[6].

For the 2%-in-50-years level of ground motion, the conditional collapse probability ranges from 3% to 20%, with an average value of 11%. The mean annual frequency of collapse ($\lambda_{collapse}$) ranges from 0.7×10^{-4} to 7.0×10^{-4} collapses/year, with an average rate of 3.1×10^{-4}. This collapse rate corresponds to an average collapse return period of 3,200 years, with a range of 1,400 to 14,000 years.

When reviewing the above collapse performance predictions, the natural question becomes: Is this an acceptable level of collapse safety? The engineering profession needs to work with government officials (who represent the public) to answer this question and reach consensus on the appropriate collapse performance targets. In this way, collapse predictions such as those provided in this study have a basis for comparison.

The above results give the collapse predictions for each of the 30 archetype buildings individually. When trying to make statements regarding the collapse safety of an aggregated class of buildings, it may be useful to combine these results in some way. A few possible approaches to defining the collapse capacity distribution for the full class of buildings are as follows:

- Use the average margin and the average $\sigma_{LN(Sa,col)}$, perhaps with an upper bound on the worst-case.
- Use the average margin but use an expanded $\sigma_{LN(Sa,col)}$ to account for the variability in performance between building designs.
- If one desires conservatism, use a conservative estimate of the margin (i.e., mean minus one standard deviation) and use the average $\sigma_{LN(Sa,col)}$.
- If one desires to better reflect the expected building population, use one of the above methods, but apply appropriate weighting factors to the results from the various archetype buildings.

The above collapse performance predictions include an important adjustment that accounts for the spectral shape of the ground motions; this adjustment is critical for a proper collapse performance assessment. If this adjustment were not made, the average collapse margin would decrease from 2.3 to 1.6, the average collapse probability would increase from 0.11 to

[6] This is expressed as a logarithmic standard deviation; this is numerically similar to the ratio of the standard deviation to the mean.

0.26, the mean annual frequency of collapse would increase from 3.1×10^{-4} collapses/year to 11.0×10^{-4} (decrease in collapse return period from 3,200 years to 900 years).

The above collapse predictions also include the effects of structural modeling uncertainties, which is another critical aspect of the collapse assessment. If structural modeling uncertainties were excluded from the collapse assessment, the average collapse probability would decrease from 11% to 3%, and the average mean annual frequency of collapse would decreases from 3.1×10^{-4} collapses/year to 0.5×10^{-4} (increase in collapse return period from 3,200 years to 20,000 years).

6.6.3 Impacts of Design Parameters and Assessment Items on Collapse Performance

We focused on six design parameters and two aspects of the assessment methodology to assess how these may cause the collapse performance to vary. Table 6.19 ranks each of the design parameters according to their impacts on the mean rate of collapse predictions. Two aspects of the assessment methodology are also included in Table 6.19.

This table shows that the aspects of the assessment methodology, the structural modeling uncertainties, and consideration of spectral shape are more important than any of the design parameters considered in this study. Of the design parameters investigated, the building height has the most important effect on collapse performance. The next most important consideration is the difference between space and perimeter frame buildings. The next three design parameters (assumed foundation fixity, conservative design, and weak-story designs) have minimal effect, and bay spacing has no measurable effect on collapse performance.

Table 6.19 Summary of relative importance of structural design parameters and assessment items.

Design or Assessment Parameter	Average values for each of the cases considered: Margin against 2% in 50 motion	$\lambda_{collapse}$ $[10^{-4}]$	$P[C\|Sa_{2/50}]$
Inclusion of structural modeling uncert.[a] (with and without)	1.6, 1.6	11.0, 2.8	26%, 16%
Spectral shape considerations (with adjustment and without)	2.3, 1.6	3.1, 11.0	11%, 16%
Building height[b]	1.6, 2.0	12.4, 5.7	28%, 17%
Space versus perimeter frame	1.7, 1.3	8.6, 16.1	22%, 33%
Foundation fixity in design (pinned versus fixed)	1.9, 1.6	3.5, 6.1	12%, 18%
Strength irregularity (65% versus 100% strength ratios)	1.2, 1.4	17.5, 13.5	37%, 31%
Uniform size and reinf. over height versus baseline design	1.6, 1.4	10.0, 12.8	25%, 30%
Bay spacing (20' versus 30' spacing)	virtually no change		

a - The structural uncertainties do not affect the median collapse capacity because we are using the mean estimate method. If we instead did predictions at a given prediction confidence level, this value would be greater than 1.0.
b - The comparison differs for building height because there are six height levels. The values reported here are the average and the best-case.

The above comparison shows that some aspects of structural design (building height, etc.) are important to collapse performance, but the aspects of the performance assessment method have larger impacts. This finding reinforces that more research is needed to verify/improve the collapse assessment methods used in this study.

This finding also re-emphasizes the importance of having a *systematic codified* assessment method that can be used to demonstrate the performance of a structural system. This is especially critical for building code committees that are reviewing proposals for adding new systems to the building code. Without a codified assessment method, there would be no consistency between various proposals; the predicted performance of each new system would depend almost entirely on how each group carried out their performance assessment. Developing portions of this codified method was one of the primary purposes of this study; the complete method can be found in the ATC-63 project report (currently in progress).

6.6.4 Effects of Building Height and Potential Impacts of New ASCE7-05 Provisions

This study suggests that the minimum base shear requirement (ASCE 7-02 Eq. 9.5.5.2.1-3) was an important component of ensuring relatively consistent collapse risk for buildings of varying height. Removing this requirement has made taller buildings significantly more vulnerable to collapse; this should be considered in future revisions of ASCE7.

For an example 20-story building, this design provision change reduced the design base shear by a factor of two. This caused the median collapse capacity to decrease by a factor of two, the conditional collapse probability to increase from 13% to 53%, and the mean annual frequency of collapse to increase by a factor of 11.

6.7 FUTURE WORK

This study focused on creating an assessment process and then assessing the performance of code conforming RC SMF buildings. We plan to extend this study to look at how each of the building code requirements (e.g., strength demands, strong-column weak-beam provisions, drift limitations, etc.) affect the collapse performance (Haselton et al. 2007d, Chapter 7).

This study suggested that the collapse risk is fairly uniform for 8–20 story buildings designed according to the ASCE7-02 (ASCE 2002) provisions, with the collapse risks being slightly lower for the 20-story buildings. However, the updated ASCE7-05 (ASCE 2005) provisions include a reduced minimum base shear requirement; this causes the design base shear to be lower by a factor of two for 20-story buildings. The findings of this study suggest that this change will cause taller buildings (e.g., 20 stories and higher) to have lower collapse safety as compared to buildings with fewer stories (e.g., 8 stories). This study should be extended to quantitatively show how these updated design requirements affect the collapse safety of tall buildings.

This paper showed that the affects of structural modeling uncertainties is the most influential aspect of the collapse performance assessment. Further study in this area is of critical need.

This paper presented performance predictions for a single site in Los Angeles, California. It would be useful to extend this study to look more closely at how the building site (and corresponding change to the ground motion hazard) affects the estimated mean annual frequency of collapse.

The assessment method developed in this study is general and can be applied to any type of building system. It would be useful to use this method to conduct similar collapse assessment studies focused on other types of structural systems (e.g., steel frames, concrete shear walls, etc.). This would help the profession to better understand the expected collapse performance, and this would also provide code committees useful information for determining design provisions for the various types of structural systems.

APPENDIX 6A: CORRECTION OF COLLAPSE RESULTS FOR SPECTRAL SHAPE EFFECTS

Baker and Cornell (2006b, 2005a) have shown that proper consideration of ground motion spectral shape is critical in performance assessment, especially for collapse when the structural response is highly nonlinear. This is typically accounted for by selecting a ground motion set that has a proper spectral shape with respect to the period of the building of interest (e.g., Goulet et al. 2006a). This was not feasible for this study, since we are considering 30 buildings with various fundamental periods.

To address this issue, Haselton and Baker et al. (2007a, Chapter 3) proposed a simplified method capable of accounting for spectral shape effects when using a general ground motion set. Consideration of spectral shape is not the primary topic of this paper, so we simply use the method proposed in Haselton and Baker et al. (2007a, Chapter 3) and refer the reader to that publication for additional detail. We apply the proposed correction to the mean collapse capacity, but do not correct the dispersion because we are adding modeling uncertainty in the collapse assessment process and an additional correction to the dispersion would have little effect.

In this study, we use the proposed method to adjust the collapse predictions to be approximately consistent with the spectral shape for the 2%-in-50-years ground motion in high seismic regions of California (and the Los Angeles site used previously; Section 6.3.3). This method uses a parameter called "epsilon" as an indicator of spectral shape. To determine the proper target epsilon for a 2%-in-50-years ground motion level, we refer to the United States Geological Survey report on deaggregation of U.S. seismic hazard (Harmsen et al. 2002). The report shows that the epsilon values vary based on geographic location and period, with 1.5 being a reasonable value to use for high seismic regions of California; this value of 1.5 is also fairly consistent with the hazard at the Los Angeles site (Section 6.3.3).

Table 6.20 presents all of the detailed collapse results after adjustment for proper spectral shape. This table is almost identical to the previous table of the collapse results (Table 6.10), but this incorporates the adjustment for proper spectral shape. Comparison of this table and Table 6.10 shows that the spectral shape adjustment causes significant increases in collapse capacities, and decreases in collapse probabilities and rates. The ratio of adjusted/unadjusted median collapse capacity is 1.3–1.6, the collapse probability reduces by 4 to 25%, and the mean annual frequency of collapse decreases by a factor of 2.2 to 5.3.

Table 6.20 shows that for the adjusted collapse results, the collapse margins range from 1.4 to 3.4, with an average value of 2.3. The table continues by presenting the collapse probability conditioned on the 2%-in-50-years motion. Including structural modeling uncertainties, the collapse probability ranges from 3 to 20%, with an average value of 11%. The table ends with reporting the mean annual frequencies of collapse. Including structural modeling uncertainties, these range from 0.7×10^{-4} to 7.0×10^{-4} collapses/year, with a mean value of 3.1×10^{-4} collapses/year; this related to a collapse return period of 1,400 to 14,000 years, with a mean value of 3,200 years.

Comparison of Tables 6.20 and 6.10 shows that the spectral shape adjustment has important impacts on the collapse assessment. This adjustment increases the average collapse margin from 1.6 to 2.3, decreases the average collapse probability from 0.26 to 0.11, and decreases the mean annual frequency of collapse from 11.0×10^{-4} collapses/year to 3.1×10^{-4} (increases the collapse return period from 900 years to 3,200 years).

Table 6.20 Collapse predictions for each of 30 archetype designs after adjustment for proper spectral shape (target of ε = 1.5).

Design Information							Collapse Predictions with Adjustment for Spectral Shape (1.5ε), Controlling Horizontal Component of Ground Motion						
Design Number	Design ID Number	No. of stories	Bay Width [ft]	Tributary Areas: Gravity/ Lateral	Strength/ Stiffness Distribution Over Height	Foundation Fixity Assumed in Design[a]	Adjusted Mean[d] $Sa_{g.m.,col}$ (T_1) [g]	Margin Against MCE	Margin Against 2% in 50 Year Motion	$P[C \mid Sa_{2/50}]$ including modeling uncertainty	λ_{col} [10^{-4}], including modeling uncertainty	$P[C \mid Sa_{2/50}]$ without modeling uncertainty	λ_{col} [10^{-4}], without modeling uncertainty
1	2061	1	20	Space (1.0)	A	GB	3.35	2.24	2.40	0.10	2.6	0.03	0.4
2	2062					P	3.66	2.44	2.62	0.07	1.7	0.01	0.2
3	2063					F	3.36	2.24	2.40	0.10	2.6	0.03	0.4
4	2069			Perimeter (0.11)	A	GB	1.80	1.42	1.69	0.20	7.0	0.09	1.4
5	1001	2	20	Space (1.0)	A	GB	3.55	2.46	3.07	0.04	1.0	0.00	0.1
6	1001a					P	3.65	2.43	3.00	0.04	1.0	0.00	0.1
7	1002					F	2.94	2.04	2.55	0.08	2.0	0.02	0.3
8	2064			Perimeter (0.11)	A	GB	2.48	1.81	2.19	0.12	3.4	0.03	0.6
9	1003	4	20	Perimeter (0.11)	A	GB	1.56	1.94	2.04	0.13	3.6	0.03	0.6
10	1004				C	GB	1.84	2.27	2.37	0.09	2.5	0.02	0.4
11	1008			Space (1.0)	A	GB	2.22	2.31	2.56	0.07	1.7	0.01	0.2
12	1009		30	Perimeter (0.17)	A	GB	1.87	2.41	2.51	0.08	2.1	0.01	0.3
13	1010			Space (1.0)	A	GB	3.17	3.01	3.42	0.03	0.7	0.00	0.1
14	1011	8	20	Perimeter (0.17)	A	GB	1.00	1.90	1.77	0.19	6.3	0.08	1.3
15	1012		20	Space (1.0)	A	GB	1.23	2.44	2.29	0.09	2.4	0.01	0.3
16	1022				C	GB	1.20	2.40	2.25	0.09	2.5	0.01	0.3
17	2065				B (65%)[b]	GB	1.42	2.47	2.44	0.08	2.3	0.01	0.3
18	2066				B (80%)[b]	GB	1.47	2.80	2.78	0.05	1.7	0.00	0.2
19	1023				B (65%)[c]	GB	1.17	2.05	1.97	0.14	4.3	0.04	0.8
20	1024				B (80%)[c]	GB	1.10	2.09	1.95	0.15	4.6	0.05	0.9
21	1013	12	20	Perimeter (0.17)	A	GB	0.85	1.91	1.84	0.16	5.2	0.05	0.9
22	1014		20	Space (1.0)	A	GB	0.83	1.98	1.91	0.15	4.7	0.05	0.8
23	1015				C	GB	0.96	2.26	2.20	0.11	3.1	0.02	0.5
24	2067				B (65%)[b]	GB	1.06	2.26	2.07	0.12	3.2	0.03	0.5
25	2068				B (80%)[b]	GB	0.95	2.20	2.07	0.12	3.1	0.02	0.5
26	1017				B (65%)[c]	GB	0.95	2.02	1.87	0.16	4.5	0.04	0.8
27	1018				B (80%)[c]	GB	0.84	1.95	1.89	0.15	4.9	0.05	0.9
28	1019		30	Space (1.0)	A	GB	1.18	2.63	2.54	0.07	2.1	0.01	0.3
29	1020	20	20	Perimeter (0.17)	A	GB	0.71	2.08	2.00	0.13	3.7	0.03	0.6
30	1021		20	Space (1.0)	A	GB	0.99	2.59	2.50	0.08	2.0	0.01	0.3

Margin - The margin is the ratio of the median collapse capacity to the ground motion level of interest.
a - Fixity assumed only in the design process. OpenSees models use expected grade beam, basement column, and soil stiffnesses.
b - Only first story designed to be weak.
c - First and second stories designed to be weak.
d - Mean when using a lognormal distribution; this value is closer to the median.
A - Expected practitioner design; strength and stiffness stepped over height as would be done in common design practice.
B (%) - Weak story; done by sizing the target weak story(ies) based on code requirements and then strengthening stories above. % is the percentage of strength in the weak story(ies) as compared to the stories above.
C - conservative design; neither size nor reinforcement of beams/columns are decreased over building height
F - Fixed.

APPENDIX 6B: COMPARISONS TO COLLAPSE PREDICTIONS USING ATC-63 GROUND MOTION SCALING METHOD

This study has been a collaborative effort between the Applied Technology Council Project 63 (ATC-63) and the Pacific Earthquake Engineering Research Center (PEER). Both organizations have subtle differences in their approach to collapse performance assessment, so this Appendix compares the methods and shows that the ground motion scaling method has virtually no impact on the final predictions of collapse performance.

The three differences between the ATC-63 and PEER approaches are: (a) the PEER approach uses 80 ground motions, while the ATC-63 approach uses a subset of 44, (b) they use different methods of ground motion scaling, and (c) the ATC-63 approach uses both horizontal components of ground motion, while the PEER approach uses the most detrimental component of ground motion to approximately consider the three-dimensional collapse capacity (Section 6.4.5). Based on our previous experience using the full and reduced ground motion sets, the difference in the ground motion set should not lead to any significant changes in the collapse capacity prediction, so we make no corrections in this comparison to account for the difference in which set is used. This Appendix compares collapse predictions using both ground motion components (consistent with the ATC-63 approach) in order to show the effects of the scaling method alone. For those interested in the effects of using the most detrimental component of ground motion, please refer to earlier comparisons in Section 6.4.9.

Table 6.21 compares collapse predictions using both the ATC-63 and PEER ground motion scaling methods. The primary difference in the two methods is that the ATC-63 method attempts to maintain dispersion in the $Sa(T_1)$ of the records, while the PEER method scales every ground motion pair to the target $Sa(T_1)$[7].

This table shows that, in spite of the scaling difference, the resulting collapse predictions are virtually identical, though there are slight differences between shorter and taller buildings. The mean collapse capacity is an average of 2% lower for the ATC-63 method; this has no trend with building height, and this magnitude of difference is negligible. The record-to-record variability is, on average, identical for the two methods. However, there is a weak trend with height, showing that the ATC-63 variability is on average 10% lower for 1–4 story buildings and 8% higher for 8–20 story buildings. This difference in variability carries over to a slight, but negligible, difference in the collapse probability; the ATC-63 method leads to an average of 1% lower probability for 1–4 story buildings and of 2–3% higher probability for 8–20 story buildings.

[7] When scaling the pair of ground motions, the geometric mean spectral acceleration is scaled to the target. The geometric mean is defined as $Sa_{g.m.}(T_1) = (Sa_{comp1}(T_1) * Sa_{comp2}(T_1))^{0.5}$.

Table 6.21 Comparison of collapse predictions using ATC-63 and PEER ground motion scaling methods.

Design Information		ATC-63 Scaling Method, all Ground Motion Components					Geometric Mean (PEER) Scaling Method, all Ground Motion Components				
Design Number	Design ID Number	Mean[a] Sa_{ATC-63}, col (T_1) [g]	Margin Against MCE	σ_{LN} (Sa,col)	P[C|MCE] without modeling uncertainty	P[C|MCE] with modeling uncertainty	Mean[a] Sa_{ATC-63}, col (T_1) [g]	Margin Against MCE	σ_{LN} (Sa,col)	P[C|MCE] without modeling uncertainty	P[C|MCE] with modeling uncertainty
1	2061	2.94	1.96	0.39	0.04	0.14	2.85	1.90	0.48	0.09	0.18
2	2062	3.30	2.20	0.39	0.02	0.11	3.17	2.12	0.46	0.05	0.14
3	2063	2.95	1.97	0.39	0.04	0.14	2.86	1.91	0.48	0.09	0.18
4	2069	1.50	1.18	0.38	0.33	0.40	1.59	1.26	0.42	0.29	0.36
5	1001	2.97	2.06	0.37	0.03	0.12	3.15	2.19	0.42	0.03	0.11
6	1001a	3.42	2.28	0.41	0.02	0.10	3.40	2.27	0.42	0.03	0.11
7	1002	2.55	1.77	0.37	0.06	0.18	2.72	1.89	0.43	0.07	0.17
8	2064	2.06	1.50	0.37	0.13	0.26	2.17	1.58	0.43	0.15	0.24
9	1003	1.30	1.61	0.38	0.11	0.23	1.27	1.58	0.39	0.12	0.24
10	1004	1.52	1.88	0.39	0.05	0.16	1.51	1.87	0.43	0.07	0.17
11	1008	1.70	1.78	0.41	0.08	0.19	1.82	1.90	0.38	0.05	0.15
12	1009	1.54	1.98	0.38	0.04	0.14	1.42	1.83	0.43	0.08	0.18
13	1010	2.63	2.50	0.41	0.01	0.08	2.65	2.51	0.43	0.02	0.08
14	1011	0.66	1.25	0.39	0.29	0.36	0.72	1.38	0.40	0.21	0.31
15	1012	0.82	1.63	0.38	0.10	0.22	0.86	1.71	0.38	0.08	0.20
16	1022	0.87	1.74	0.42	0.10	0.20	0.92	1.85	0.36	0.05	0.16
17	2065	1.03	1.79	0.40	0.07	0.18	1.04	1.83	0.42	0.08	0.18
18	2066	0.93	1.76	0.42	0.09	0.19	1.03	1.96	0.41	0.05	0.15
19	1023	0.86	1.50	0.44	0.18	0.27	0.89	1.55	0.41	0.15	0.25
20	1024	0.74	1.41	0.45	0.22	0.30	0.83	1.59	0.40	0.12	0.24
21	1013	0.65	1.45	0.38	0.16	0.28	0.64	1.43	0.38	0.18	0.29
22	1014	0.67	1.59	0.42	0.13	0.24	0.65	1.55	0.37	0.12	0.24
23	1015	0.70	1.66	0.41	0.11	0.22	0.70	1.66	0.38	0.09	0.21
24	2067	0.79	1.69	0.44	0.12	0.22	0.81	1.74	0.38	0.07	0.19
25	2068	0.66	1.53	0.42	0.15	0.26	0.69	1.60	0.36	0.10	0.22
26	1017	0.69	1.47	0.49	0.21	0.29	0.70	1.51	0.38	0.14	0.26
27	1018	0.62	1.44	0.45	0.21	0.29	0.65	1.51	0.38	0.14	0.26
28	1019	0.83	1.86	0.40	0.06	0.17	0.84	1.88	0.40	0.06	0.16
29	1020	0.57	1.66	0.37	0.09	0.21	0.55	1.62	0.36	0.09	0.22
30	1021	0.75	1.98	0.41	0.05	0.14	0.71	1.87	0.39	0.05	0.16

a - Mean when using a lognormal distribution; this value is closer to the median.

The insensitivity to the scaling method comes from the fact that we are comparing the collapse capacities, which occur after a great deal of structural damage and period elongation. If we scale the records by the ATC-63 and PEER methods, the dispersion in Sa near T_1 will be much lower for the PEER method, since all the records are scaled to a target Sa(T_1). However, near collapse, the effective period of these ductile buildings is closer to $2T_1$ (Haselton and Baker 2006a, Chapter 3). The dispersion in Sa near $2T_1$ is virtually identical for both scaling methods; this is why the collapse results are the same for both scaling methods. In the case of non-ductile buildings, the period would not elongate as significantly prior to collapse; in these cases the dispersion would likely be significantly smaller for the PEER scaling method.

APPENDIX 6C: COMPARISONS TO COLLAPSE PREDICTIONS WITHOUT INCLUDING EFFECTS OF STRUCTURAL MODELING UNCERTAINTIES

Chapter 5 showed that structural modeling uncertainties caused significant impacts on the collapse performance assessment of a single 4-story RC SMF building. To further generalize this finding we can compare the collapse risk predictions, both with and without considering modeling uncertainties, for the 30 RC SMF buildings (these results were already included in Table 6.20; these results include the correction for spectral shape).

When structural modeling uncertainties are included, the average conditional collapse probability increases from 3%–11%. The average mean annual frequency of collapse increases from 0.5×10^{-4} collapses/year to 3.1×10^{-4}; in terms of collapse return period, this is a decrease from 20,000 years to 3,200 years.

7 Effects of Building Code Design Provisions on Collapse Performance of Reinforced Concrete Special Moment-Frame Buildings

7.1 INTRODUCTION AND GOALS OF STUDY

Previous research by the authors (Haselton et al. 2007c, Chapter 6; Goulet et al. 2006a; Haselton et al. 2007e) has focused on assessing the collapse safety of code-conforming reinforced concrete special moment-frame (RC SMF) buildings. This study builds on previous studies to assess the effects that changes to selected structural design provisions have on the collapse performance of RC SMF buildings. Many design provisions could be investigated, but we chose to focus on three of the major provisions that relate to the system-level strength, stiffness and deformation capacity: the design base shear strength, the strong-column weak-beam ratio (i.e., the ratio of the flexural strengths of columns and beams framing into a joint), and the interstory drift limits.

Our focus is similar to a recent study by Zareian and Krawinkler (Zareian 2006), who looked at the impacts of strength, deformation capacity, and lateral stiffness on the collapse capacity of generic frame and RC wall structures. The primary difference with our study is that we employ buildings that are not generic, but are fully designed according to recent building code provisions (i.e., ASCE7-02).

To understand the impact that these design provisions have on collapse safety, we designed three sets of buildings, for a total of 39 RC SMF buildings, ranging in height from 4–12 stories. The first set of buildings was designed with variable design base shear strength, the second with variable strong-column weak-beam ratio, and the third with variable drift limits. For each building, we created a nonlinear structural model and performed collapse simulation. From these collapse predictions, we computed the median collapse capacity, the conditional collapse probability, and the mean rate of collapse. We then compared these results to learn how each design provision affects collapse risk. Details of the design and assessment procedure are not repeated in this paper and can be found in Haselton et al. (2007c, Chapter 6). The next two sections provide a brief overview these procedures.

7.2 STRUCTURAL DESIGN PROCEDURE

The archetype analysis model[1] used for this study consists of a two-dimensional three-bay frame. Each frame is designed according to the governing code provisions of the 2003 IBC (ICC 2003), ASCE7-02 (ASCE 2002), and ACI 318-02 (ACI 2002). These generic structures are not often used in research. The detailed designs reflect many of the subtle effects that the design requirements have on structural behavior and performance. Haselton et al. (2007c, Chapter 6) presents additional detail regarding the structural design procedure and the rationale for using a three-bay frame model.

We found that many of the subtle code design requirements can cause significant changes in the structural behavior and performance. For example, when we decreased the design base shear strength, the strength of the building decreases, as expected. However, the reduction in lateral loads also reduces the beam capacity shear demands and causes the number of beam stirrups to be significantly reduced; this causes a significant reduction in the beam plastic rotation capacity. Therefore, the reduction in design base shear causes not only a reduction in strength, but a significant reduction in beam plastic rotation capacity. Fully designed frames, based on a complete set of seismic design provisions, are useful for accurately judging how design provisions affect structural behavior and performance. This is in contrast to idealized generic structures that are useful to evaluate trends in behavior for isolated design parameters but do not reflect the interactive effects that design provisions have on structural performance.

7.3 STRUCTURAL COLLAPSE ASSESSMENT PROCEDURE

This study is based on a structural collapse assessment procedure that is described in detail in Haselton et al. (2007c, Chapter 6). The structural model parameters are calibrated to 255 experimental tests of RC columns (Haselton et al. 2007b, Chapter 4). The structural model is subjected to the 40 ground motions (with two components to each motion) that we developed in

---

[1] The "archetype analysis model" is the simplest model able to capture the relevant behavior of the type of building of interest, which are RC SMF buildings in this case. Section 6.4.4 explains the rationale for using a three-bay frame model.

Haselton et al. (2007a, Chapter 3; also paper forthcoming by Kircher et al.). Using the structural model and ground motions, we perform incremental dynamic analyses (IDA) (Vamvatsikos 2002) to determine the ground motion intensity level that causes collapse for each record. We use these collapse intensities for each of the 40x2 records to create a cumulative distribution function of the collapse capacity, which reflects the record-to-record variability. We then increase the dispersion of the collapse capacity distribution to account for the effects of structural modeling uncertainties. We use this final collapse capacity distribution to compute the probabilities of collapse and mean annual rates of collapse[2].

The spectral shape of ground motions is not considered in the ground motion selection, but we adjust the collapse results for spectral shape using the method proposed by Haselton and Baker et al. (2007a, Chapter 3). The collapse results shown in the body of this paper *do not* include this correction for spectral shape, and thus should only be considered valid for *relative* comparisons. Appendix B contains the collapse predictions corrected for proper spectral shape; these results are considered to be correct in an absolute sense.

The following sections present the collapse predictions and show how they are affected by structural design requirements. Appendix A contains more detailed information regarding the calculated collapse performance of each building.

7.4 EFFECT OF DESIGN BASE SHEAR STRENGTH

The appropriate magnitude of design base shear has been a subject of debate for many years, and is currently controlled by the R-factor contained in ASCE7-02 (ASCE 2002). In order to quantify the effect that the design base shear has on the structural collapse performance, we designed four sets of buildings with various levels of design base shear. To gage effects of height, two building heights (4-story and 12-story) were evaluated. To account for the effects that gravity loads have on the design, we used both space frame buildings and perimeter frame buildings for each height level. The code requires that these RC SMF buildings be designed using a strength reduction factor (R-factor) of up to 8.0. To vary the design base shears, we allowed the design R-factor to range from 4.0 – 12.0 (while still enforcing all of the other design

[2] The collapse probability and mean rate of collapse are based on a site in Northern Los Angeles, which is typical of far-field high seismic regions of California. The hazard analysis for this site was completed by Goulet and Stewart (Goulet et al. 2006; Haselton et al. 2007e); the site is also described in Section 6.4.3.

provisions required for a RC SMF building). This change in R leads to variations in the design base shear coefficient, C_S, as shown in Table 7.1, which summarizes the design parameters and the results of static pushover analysis for the 16 buildings. The design base shear coefficient that is used for design is based on the R-factor used in the design. In order to clearly see the effects that the design base shear has on the collapse performance, we did not impose the minimum value of C_s = 0.044g required by ASCE7-02 (ASCE 2002).

Table 7.1 Structural designs and results of nonlinear static analysis for buildings with various design base shear strengths.

Height/Design					Period and Pushover Analysis Results					
Design R-Factor	Design Base Shear Coefficient (Cs) [g]	No. of Stories	Space/ Perimeter Frame	Design ID Number	First Mode Period (T_1) [sec]	Maximum Period used in Design (ASCE7-02 9.5.5.3.2) [sec]	Yield Base Shear Coeff. [g]	Static Overstrength (based on ultimate strength)	Effective R Factor*	RDR_{ult}
4	0.202	4	Perimeter	2051	0.54	0.54	0.346	2.0	2.9	0.055
8	0.092			1009	1.16	0.78	0.141	1.6	3.7	0.050
12	0.062			2052	1.15	0.78	0.104	1.8	5.0	0.038
4	0.185	4	Space	2001	0.74	0.74	0.354	2.3	2.3	0.047
5.3	0.139			2020	0.77	0.77	0.304	2.6	2.6	0.050
8	0.092			1010	0.86	0.78	0.268	2.9	2.6	0.056
10	0.074			2022	0.91	0.78	0.244	3.9	2.7	0.050
12	0.062			2003	0.97	0.78	0.222	4.1	2.8	0.045
4	0.079	12	Perimeter	2053	1.50	1.50	0.120	1.6	3.4	0.031
8	0.044			1013	2.01	2.01	0.075	1.7	4.0	0.026
12	0.023			2054	2.84	2.11	0.036	1.7	5.9	0.009
4	0.070	12	Space	2008	1.83	1.83	0.140	2.1	2.4	0.039
5.3	0.053			2021	1.97	1.97	0.111	2.2	2.8	0.028
8	0.044			2009	1.99	1.99	0.093	2.3	3.3	0.033
10	0.028			2028	2.27	2.11	0.072	2.7	3.7	0.018
12	0.023			2010	2.40	2.11	0.071	3.2	3.5	0.020

* This is defined as the ratio of the design base shear strength [(2/3)$Sa_{MCE}(T_1)$] to the yield base shear strength.

As summarized in Table 7.1, the design base shear strength has a significant effect on the first mode period, especially for perimeter frame buildings where the design is dominated by lateral loads. Figure 7.1 shows the effect that design R-factor has on static overstrength. The static overstrength is relatively constant for perimeter frame buildings, but varies significantly with the R-factor for space frame buildings. This variation comes from the dominance of gravity loads in the design of space frame buildings. This shows that for space frame buildings, a change in the R-factor causes a much smaller change than expected to the actual strength of the building. For example, in the 4-story space frame building a factor of 3.0 change in the R-factor causes the yield base shear to change only by a factor of 1.6. Figure 7.1 also shows that overstrengths of the 12-story space-frame building are less sensitive to the R-factor, since the design of taller buildings is controlled more by lateral loads and less by gravity loads.

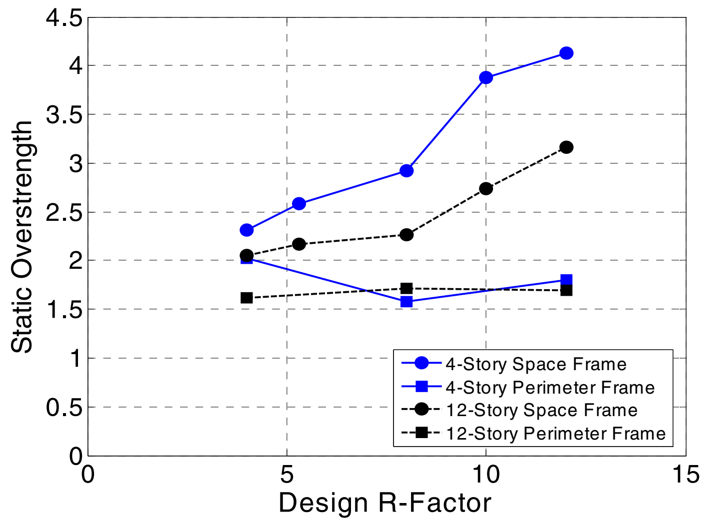

Figure 7.1 Effects that design R-factor has on static overstrength for 4-story and 12-story buildings.

The last column of Table 7.1 shows the RDR_{ult}, which is defined as the pushover roof drift ratio at the point of 20% strength loss. This shows that a decrease in design strength often also causes a decrease in deformation capacity. This is an important finding, and Section 7.4.2.2 provides a detailed discussion of why this occurs.

7.4.1 Nonlinear Dynamic Collapse Capacity Predictions

Table 7.2 presents the collapse predictions for the buildings based on nonlinear dynamic collapse analyses. This table presents the collapse performance in terms of margin against the 2%-in-50-years ground motion level (ratio of median collapse capacity and 2%-in-50-years intensity), conditional collapse probability, and mean annual rate of collapse. This table also presents the collapse drifts, and an inspection of these drifts shows that they follow similar trends as the static pushover deformation capacities (RDR_{ult}).

Table 7.2 Collapse performance predictions for buildings with various design R-factors.

Height/Design				Collapse Predictions			Collapse Drifts	
Design R-Factor	Design Base Shear Coefficient (Cs) [g]	No. of Stories	Space/ Perimeter Frame	Margin Against 2% in 50 Motion	$P[C\|Sa_{2/50}]$ including modeling uncertainty	λ_{col} $[10^{-4}]$, including modeling uncertainty	Median IDR at collapse	Median RDR at collapse
4	0.202	4	Perimeter	2.72	0.07	1.92	0.076	0.049
8	0.092			1.66	0.22	8.17	0.078	0.050
12	0.062			1.31	0.34	16.96	0.068	0.042
4	0.185	4	Space	2.62	0.06	1.64	0.080	0.051
5.3	0.139			2.39	0.09	2.45	0.078	0.050
8	0.092			2.42	0.09	2.51	0.083	0.053
10	0.074			2.15	0.12	3.38	0.076	0.046
12	0.062			2.00	0.14	4.32	0.074	0.043
4	0.079	12	Perimeter	1.92	0.17	5.86	0.069	0.021
8	0.044			1.19	0.39	20.28	0.053	0.016
12	0.023			0.62	0.79	111.93	0.031	0.009
4	0.070	12	Space	1.88	0.16	4.98	0.076	0.025
5.3	0.053			1.53	0.25	8.97	0.065	0.021
8	0.044			1.49	0.26	10.37	0.064	0.024
10	0.028			1.11	0.43	23.12	0.045	0.015
12	0.023			1.16	0.41	20.73	0.054	0.017

Figure 7.2 presents the collapse predictions graphically for the 4-story and 12-story buildings. This shows the margin against collapse[3], the probability of collapse for a 2%-in-50-years ground motion ($P[C|Sa_{2/50}]$), and the mean annual frequency of collapse (λ_{col}). These figures show that the relationship between design R-factor and the collapse margin is approximately linear for the perimeter frame buildings. Even with this linear relationship for perimeter frame buildings, the design R-factor can nonlinearly affect the collapse rate because it is driven by the extreme tail of the collapse capacity distribution. One specifically notable observation is that λ_{col} increases dramatically for the 12-story perimeter frame building designed for R = 12 instead of R = 8. This is caused by both the shape of the hazard curve and the lower collapse capacity of the building. For the R = 12 design, the building collapses under ground motion intensity levels that occurs much more frequently, which results in the large increase in λ_{col}.

[3] The margin is defined as the ratio between the median collapse capacity and the spectral acceleration of the 2%-in-50-years ground motion.

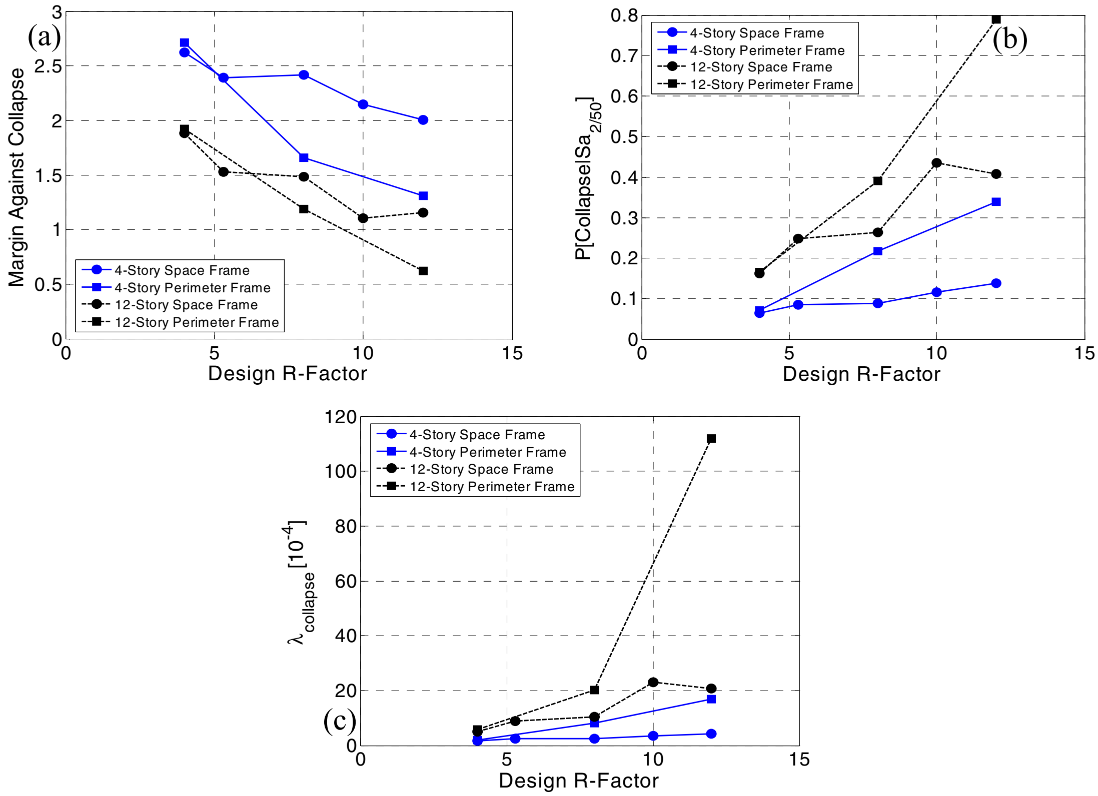

Figure 7.2 Collapse safety for 4-story and 12-story buildings designed for various R-factors. Safety expressed in terms of (a) margin against collapse, (b) probability of collapse conditioned on level of ground motion, and (c) mean annual frequency of collapse.

7.4.2 Discussion of Reasons for Trends in Collapse Safety

7.4.2.1 Issues Related to Building Strength, and Use of Effective R-Factor

The effect that the design R-factor has on the collapse margin is less important for space frame buildings. This is caused by the fact that the design R-factor does not cause a proportional change to the actual strength of the building; this was shown by the overstrength values shown earlier in Figure 7.1. A way to capture the differences between the design strength and actual strength is through use of an *effective* R-factor. This effective R-factor is defined as the ratio of the design spectral acceleration level (2/3 of the maximum considered earthquake (MCE) ground motion) to the building yield base shear strength (from static pushover analysis). This factor accounts for not only the overstrength shown earlier in Figure 7.1b, but also the effects of the period cap used in the ASCE7-02 equations for design base shear demand, and the effects of the minimum design base shear provision.

Figure 7.3 is similar to Figure 7.2, but shows the collapse indices plotted with respect to the *effective* R-factor instead of the *design* R-factor. Comparison of these two figures shows that the *effective* R-factor better explains building collapse performance because it captures the effects listed previously (e.g., static overstrength, etc.).

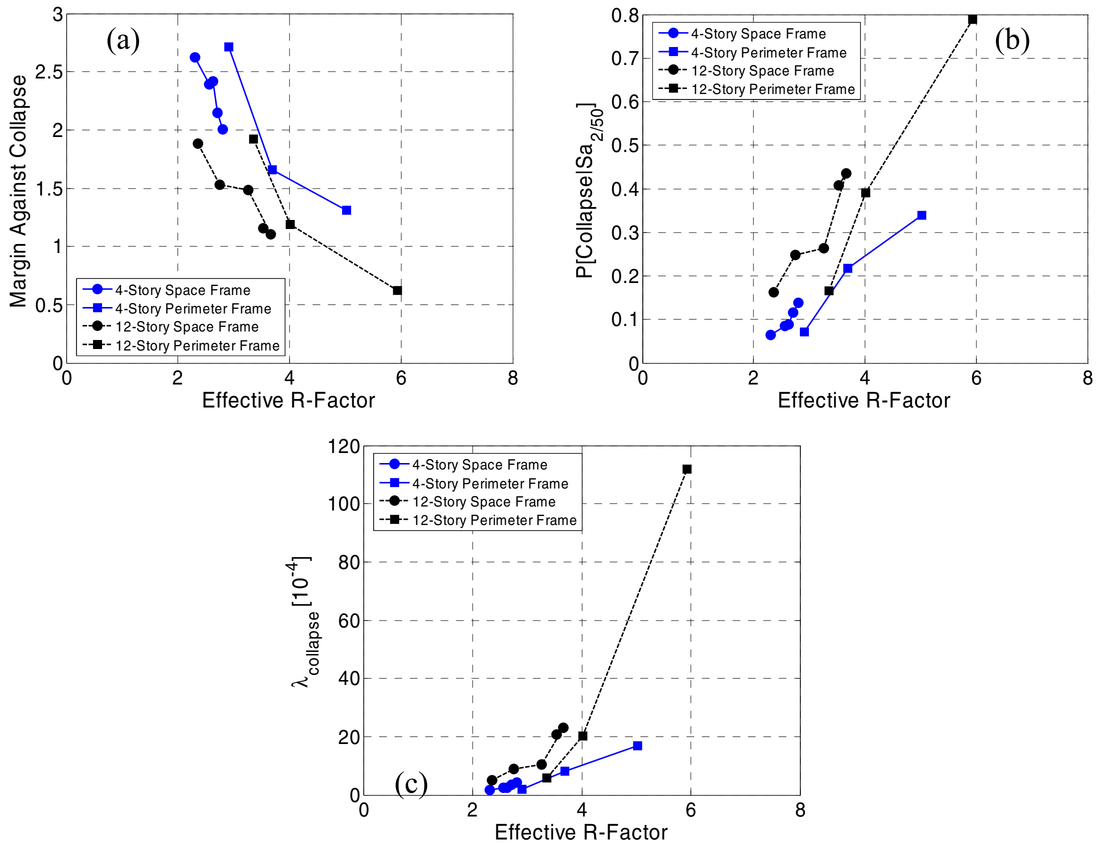

Figure 7.3 Impact of effective R-factor on collapse safety for 4-story and 12-story buildings. Safety expressed in terms of (a) margin against collapse, (b) probability of collapse conditioned on level of ground motion, and (c) mean annual frequency of collapse.

A simpler way to consider just the static overstrength (and not the effects of the code period cap or minimum base shear provisions) is by looking at the yield base shear coefficient, as shown in Figure 7.4. Similarly to the effective R-factor, this figure shows that the yield base shear explains building collapse performance better than the design R-factor, and shows that the trend is similar for space- and perimeter-frame building. Even with the similar trend, the collapse capacity of the 12-story building is still more sensitive to strength. For the 12-story building, a 3x change in base shear strength causes nearly a 3x change in the collapse margin. For the 4-story building, the same 3x change in base shear strength causes only a 2x change in the collapse margin.

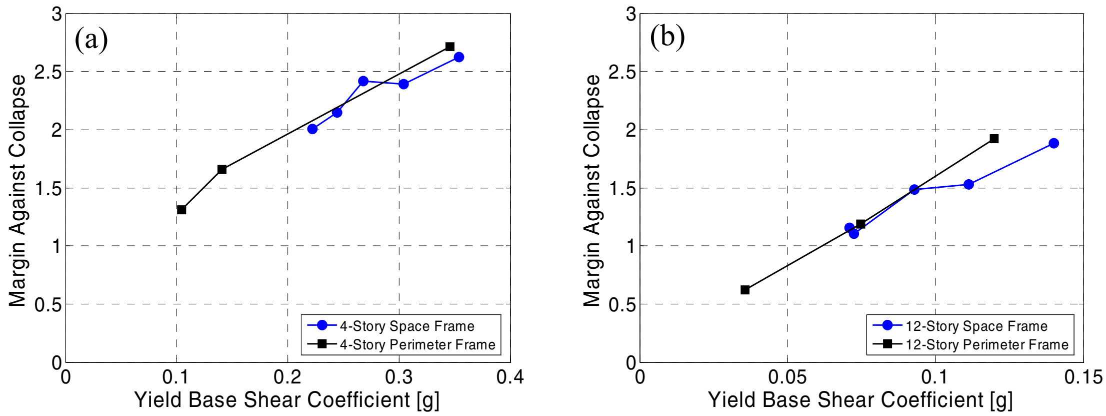

Figure 7.4 Relationship between margin against collapse and yield base shear (from pushover) for (a) 4-story buildings and (b) 12-story buildings.

7.4.2.2 Issues Related to Building Deformation Capacity

In addition to directly affecting the building strength, we found that the design R-factor affects the collapse capacity in two other ways: (a) reduction in design base shear changes the element design and causes the element plastic rotation capacities to be reduced, and (b) for weaker buildings, the damage tends to localize in fewer stories, which we hypothesize comes from increased P-delta effects. This section discusses these two points in detail.

Table 7.3 compares the element properties of one column and one beam from the 12-story space frame buildings designed with high and low strengths (design R values of 4 and 12). The column cross section is smaller for the weaker (R = 12) building, which causes the axial load ratio to increase by 50% and the plastic rotation capacity to decrease by 20%.[4] Additionally, the beam lateral reinforcement ratio (ρ_{sh}) is about 40% lower for the weaker (R = 12) building, which causes the beam plastic rotation capacity to be reduced by about 20%. The beam lateral reinforcement ratio (ρ_{sh}) decreases with decreased design strength because of the shear capacity

[4] According to the predictive equations by Haselton et al. (2007b, Chapter 4), the plastic rotation capacity of RC elements is a function of the axial load ratio, lateral confinement ratio, ratio of stirrup spacing to longitudinal rebar diameter, concrete strength, and longitudinal reinforcement ratio. Increasing the axial load ratio has a negative effect on the rotation capacity; increasing confinement has a positive effect.

design provision; when the beam flexural strength is lower, the beam lateral reinforcement ratio (ρ_{sh}) can also be reduced. These reductions in element deformation capacity, associated with the dual effects of axial load and confinement, are important contributors to the reductions in pushover deformation capacity (Table 7.1) and collapse drift levels (Table 7.2).

Table 7.3 Comparison of element design and deformation capacities in 12-story space frame buildings in (a) 1st-story interior column and (b) 2nd-floor interior beam.

(a)

Structural Design			Properties of First-Story Interior Column			
Design R-Factor	Design Base Shear Coefficient (Cs) [g]	Design ID Number	Column size [inches]	$(P/A_g f'_c)_{exp}$	ρ_{sh}	$\theta_{cap,pl}$ [rad]
4	0.070	2008	24x24	0.20	0.010	0.054
12	0.023	2010	20x20	0.29	0.012	0.045

(b)

Structural Design			Properties of Second-Floor Interior Beam			
Design R-Factor	Design Base Shear Coefficient (Cs) [g]	Design ID Number	Beam size [inches]	ρ_{sh}	$(\theta_{cap,pl})_{pos}$ [rad]	$(\theta_{cap,pl})_{neg}$ [rad]
4	0.070	2008	30x24	0.0056	0.064	0.040
12	0.023	2010	26x20	0.0033	0.072	0.054

The reduction in element-level deformation capacity is not the only reason that reduced design strength leads to reduced structural deformation capacity. Reduced design strength also causes the damage to localize in fewer stories, which causes the system-level deformation capacity to decrease. Figures 7.5 and 7.6 show the collapse mechanisms for the buildings designed for both high and low base shear strengths. While the predominant collapse mechanism for the stronger building is a 3-story mechanism, the mechanism changes to a 2-story mechanism for the weaker building. The reduction in design strength causes the collapse mechanism to involve fewer stories of the building, which then causes a reduction in the building (roof) deformation capacity (as seen in Tables 7.1–7.2).

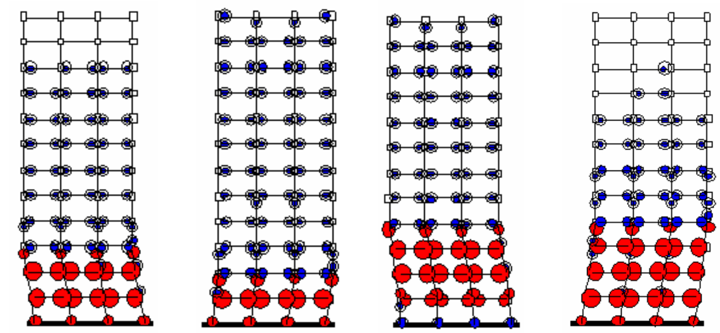

(a) 78% (b) 18% (c) 2% (d) 2%

Figure 7.5 Collapse mechanisms for 12-story perimeter frame building designed for *high* base shear strength (design R of 4) (building ID 2053).

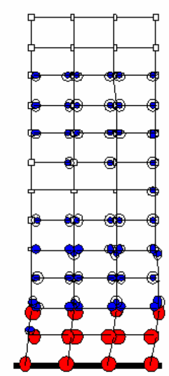

(a) 100%

Figure 7.6 Collapse mechanisms for 12-story perimeter frame building designed for *low* base shear strength (design R of 12) (building ID 2054).

We hypothesize that the above trend stems from the fact that strength reduction causes the P-delta effects to be more dominant in the weaker (R = 12) building. This is because the weaker design has less stiffness, both elastically and inelastically. The increased influences of P-delta cause the post-yield stiffness of the building to be more negative, which prohibits the damage from spreading over more stories of the building.

To illustrate this, Figure 7.7a compares the pushover curves for the two 12-story perimeter frame buildings (designed for both high and low strengths). This figure shows the obvious difference in strength between the two buildings, but also shows that the P-delta effects are remarkably more dominant for the weaker building. The pushover shows a strong post-yield negative stiffness for the weaker building and only a mild post-yield negative stiffness for the stronger building. Figure 7.7b shows that the larger post-yield negative stiffness of the weaker building causes the damage to localize in the first two stories. In contrast, the damage spreads more evenly over many stories of the stronger building.

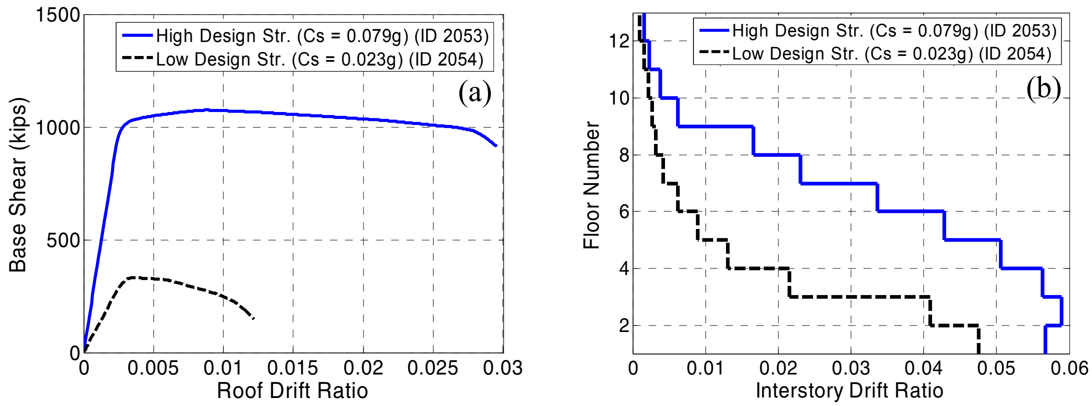

Figure 7.7 Comparison of pushover behavior for 12-story perimeter frame buildings designed for low- and high-design base shear strengths (design R values of 4 and 12, which lead to C_s values of 0.079g and 0.023g): (a) pushover curve and (b) maximum interstory drifts at end of pushover analysis.

The effects discussed in this section (design base shear strength affecting the element deformation capacities and the level of damage localization) are consistent with the results for the set of 4-story perimeter frame buildings. These trends also exist but are less pronounced for the 4-story and 12-story space frame buildings where the P-delta effects are less dominant.

7.5 EFFECT OF STRONG-COLUMN WEAK-BEAM DESIGN RATIO

The aim of the strong-column weak-beam (SCWB) design provision is to avoid localized story mechanisms and thus attain more distributed failure mechanisms. As specified in ACI 318-05 (ACI 2005) and comparable codes, this provision does not fully *prevent* column hinging and incomplete mechanisms but only helps to *delay* column hinging and to spread the damage over more stories of the building.

7.5.1 Structural Designs and Results of Nonlinear Static Analysis

To quantify the effects that the SCWB ratio has on collapse performance, we designed two sets of buildings with various SCWB ratios. As summarized in Table 7.4, one set consists of 4-story space frames and the second consists of 12-story perimeter frames. For each building set, we started with a SCWB ratio of 3.0 and continued reducing the ratio until the majority of columns were controlled by the flexural strength demands. This limit occurred at a SCWB ratio of 0.4 for the 4-story space frame buildings and 0.9 for the 12-story perimeter frame buildings. Note that the SCWB ratio required by the current standard is 1.2 (ACI 318-05, 2005).

Table 7.4 Structural designs and results of nonlinear static analysis for buildings designed with various column/beam flexural strength ratios.

Height/Design				Period and Pushover Analysis Results			
Strong-Column Weak-Beam Ratio	No. of Stories	Space/ Perimeter Frame	Design ID Number	First Mode Period (T_1) [sec]	Yield Base Shear Coeff. (Cs) [g]	Static Overstrength (based on ultimate strength)	RDR_{ult}
0.4	4	Space	2034	0.87	0.194	2.2	0.018
0.6			2025	0.87	0.229	2.6	0.020
0.8			2024	0.85	0.262	3.0	0.032
1.0			2023	0.85	0.269	3.2	0.043
1.2			1010	0.86	0.268	2.9	0.056
1.5			2005	0.86	0.272	3.6	0.060
2.0			2006	0.85	0.268	3.8	0.067
2.5			2007	0.79	0.271	4.1	0.060
3.0			2027	0.74	0.270	4.3	0.057
0.9	12	Perimeter	2060	2.00	0.075	1.7	0.024
1.2			1013	2.01	0.075	1.7	0.026
1.5			2055	2.01	0.074	1.7	0.029
2.0			2056	2.01	0.067	1.6	0.030
2.5			2057	1.90	0.072	1.7	0.038
3.0			2058	1.84	0.074	1.7	0.045

Table 7.4 shows that the first mode periods of the buildings are only mildly affected by the SCWB ratio because changes in column strength did not always require changes in column size. As expected, the static overstrength increases with SCWB ratio for the 4-story buildings, but not in proportion to the column strength. This increase is not observed for the 12-story buildings, presumably because the frame strength is more dependent on the beam flexural strengths. An increase in the SCWB ratio causes increase in the building deformation capacities, as expected, because an increased SCWB ratio causes the damage to spread over more stories of the building.

7.5.2 Nonlinear Dynamic Collapse Capacity Predictions

The dynamic collapse analysis results are summarized in Table 7.5 and Figure 7.8. The collapse drifts follow similar trends as the static pushover deformation capacities (RDR_{ult}) (Table 7.4), which showed than the building deformation capacity increased with increase to the SCWB ratio.

Table 7.5 Collapse performance predictions for buildings designed with various column/beam flexural strength ratios.

Height/Design			Collapse Predictions			Collapse Drifts	
Strong-Column Weak-Beam Ratio	No. of Stories	Space/ Perimeter Frame	Margin Against 2% in 50 Motion	$P[C\|Sa_{2/50}]$ including modeling uncertainty	λ_{col} [10^{-4}], including modeling uncertainty	Median IDR at collapse	Median RDR at collapse
0.4	4	Space	1.07	0.45	28.19	0.051	0.017
0.6			1.24	0.36	18.97	0.055	0.027
0.8			1.68	0.21	7.68	0.065	0.027
1.0			2.14	0.12	3.76	0.075	0.041
1.2			2.42	0.09	2.51	0.083	0.053
1.5			2.57	0.07	1.94	0.079	0.060
2.0			2.64	0.06	1.43	0.092	0.075
2.5			2.67	0.06	1.42	0.093	0.076
3.0			2.75	0.05	1.25	0.122	0.091
0.9	12	Perimeter	1.09	0.45	28.23	0.047	0.014
1.2			1.19	0.39	20.28	0.053	0.016
1.5			1.28	0.35	16.78	0.053	0.018
2.0			1.41	0.29	12.67	0.060	0.022
2.5			1.53	0.25	9.80	0.063	0.027
3.0			1.75	0.18	5.87	0.073	0.035

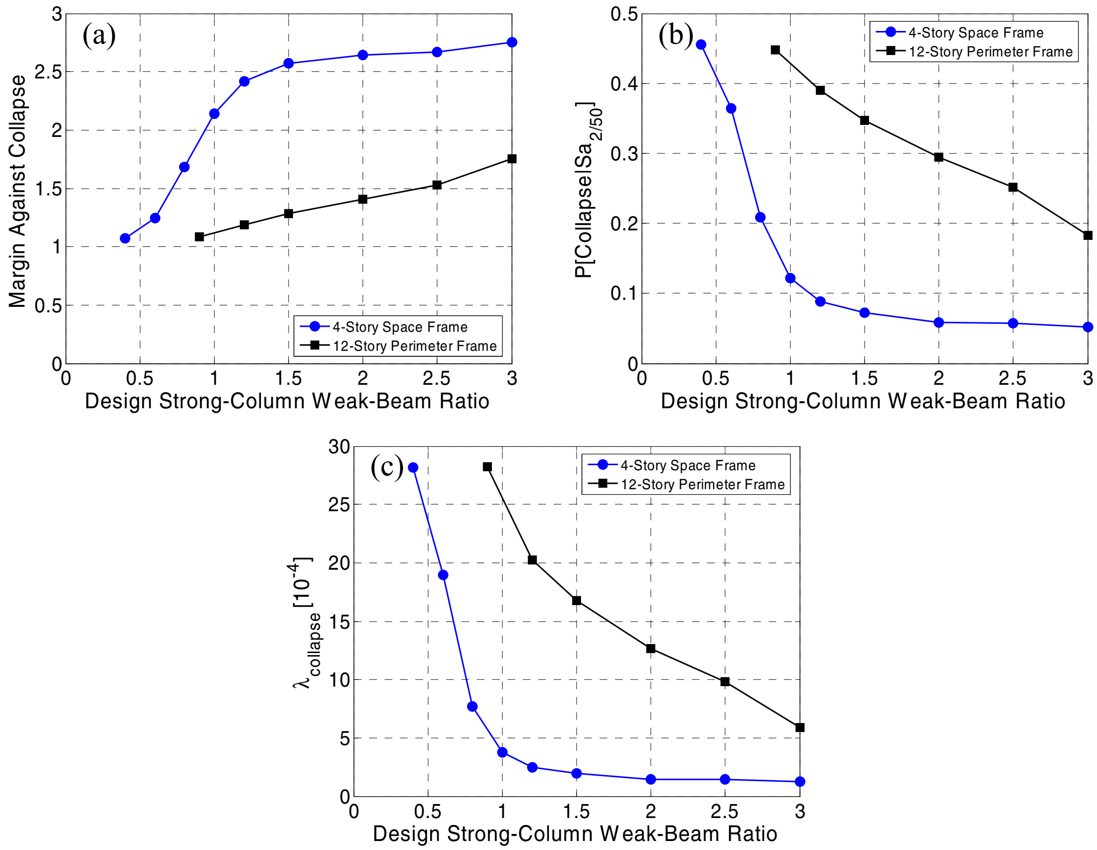

Figure 7.8 Collapse safety for 4-story and 12-story buildings designed for various column/beam flexural strength ratios. Safety expressed in terms of (a) margin against collapse, (b) probability of collapse conditioned on level of ground motion, and (c) mean annual frequency of collapse.

The first apparent difference shown above is that the 4-story space frame has a much higher collapse capacity as compared to the 12-story perimeter frame. This is not important for the relative comparisons of this section, but the differences are so large that a quick explanation is warranted. Haselton et al. (2007c, Chapter 6) found that perimeter frames have a lower collapse capacity due to lower levels of overstrength and more significant P-delta effects. The same study also found that the collapse capacity of 4-story buildings was approximately 15% higher than that of 12-story buildings. These two factors together account for the large difference between frame types in Figure 7.8.

The collapse results show that the SCWB ratio drastically affects the collapse capacity of the 4-story building for SCWB ratios < 1.5, but the effects are much less significant for SCWB ratios > 1.5. In contrast, the collapse capacity of the 12-story building is consistently improved for all increases in the SCWB ratio. This behavior will be explained in the next section.

7.5.3 Discussion of Reasons for Trends in Collapse Safety

We found that the SCWB ratio increases the collapse capacity to the extent that it improves the collapse mechanism and causes the damage to be spread over more stories of the building. Figure 7.9 illustrates this point by showing the predominant collapse mechanisms for each design SCWB value for the 4-story buildings. This shows that the collapse mechanism improves for increasing SCWB value, and a complete mechanism develops for SCWB >= 2.0; any further increase above 2.0 no longer benefits the collapse mechanism. This point where the collapse mechanism becomes complete is close to the point where increases in the SCWB ratio stops improving the collapse capacity (Fig. 7.8). Table 7.6 extends this illustration by showing the percentages of each collapse mechanism observed for each building.

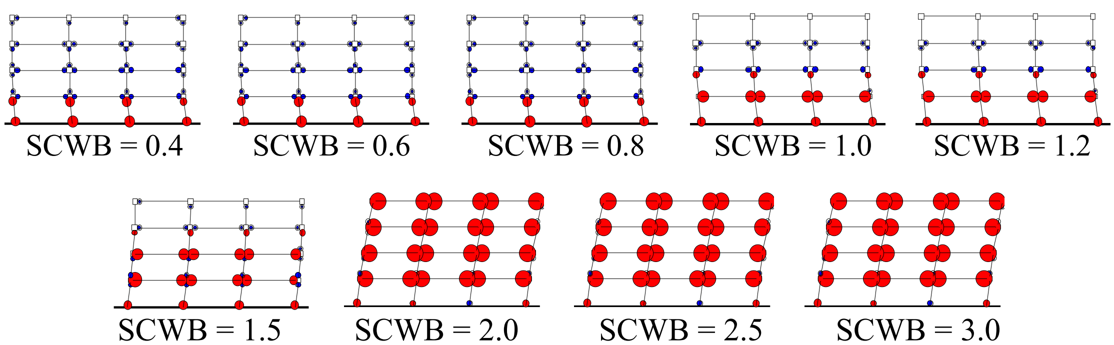

Figure 7.9 Predominant collapse mechanisms for 4-story space frame buildings designed with various strong-column weak-beam ratios.

Table 7.6 Relative occurrence of collapse mechanisms for buildings designed for various strong-column weak-beam ratios for 4-story space frame buildings.

Height/Design		Percentage of Collapse Mech. Observed in Nonlinear Dynamic Analyses			
Strong-Column Weak-Beam Ratio	Design ID Number	First story	Stories 1-2	Stories 1-3	Stories 1-4 (full)
0.4	2034	100%	--	--	--
0.6	2025	100%	--	--	--
0.8	2024	88%	9%	3%	--
1.0	2023	13%	73%	14%	--
1.2	1010	18%	82%	--	--
1.5	2005	--	--	50%	50%
2.0	2006	--	--	--	100%
2.5	2007	--	--	--	100%
3.0	2027	--	--	--	100%

Figure 7.10 shows a similar comparison for the 12-story buildings. In this case, an increase to the SCWB ratio causes an increase in the collapse capacity, and this benefit does not saturate, even up to a SCWB ratio of 3.0. The reason for this is that the collapse mechanism improves for every increase in the SCWB ratio. Table 7.7 shows the percentages of each collapse mechanism observed for the 12-story buildings.

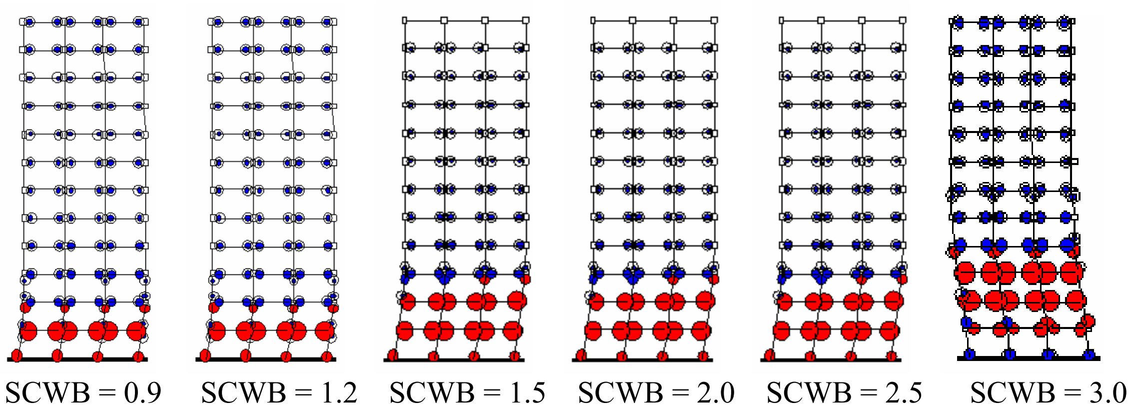

Figure 7.10 Predominant collapse mechanisms for 12-story perimeter frame buildings designed with various strong-column weak-beam ratios.

Table 7.7 Relative occurrence of collapse mechanisms for buildings designed for various strong-column weak-beam ratios for 12-story perimeter frame buildings.

Height/Design		Percentage of Collapse Mechanisms Observed in Nonlinear Dynamic Analyses						
Strong-Column Weak-Beam Ratio	Design ID Number	First story	Stories 1-2	Stories 1-3	Stories 1-4	Stories 1-5	Upper: Stories 2-3	Upper: Stories 2-4
0.9	2060	--	92%	8%	--	--	--	--
1.2	1013	--	73%	25%	--	--	--	2%
1.5	2055	--	38%	62%	--	--	--	--
2.0	2056	3%	10%	70%	--	--	7%	10%
2.5	2057	--	--	88%	--	--	--	12%
3.0*	2058	--	--	29%	14%	14%	--	29%
* This building also has 14% of the collapses in stories 11-12.								

7.6 EFFECT OF DRIFT LIMITS

Interstory drift limits are typically required by the building code to promote structural stability (i.e., to limit the P-delta effects), to limit nonstructural damage, and to help ensure structural integrity of the gravity framing. We found that drift limits have no appreciable effect on safety against global structural collapse, but this finding is based on some important design assumptions that are discussed in this section. This study does not address the question of how more stringent drift limits affect life safety risk due to nonstructural damage and damage to gravity framing components.

7.6.1 Structural Designs and Results of Nonlinear Static Analysis

To quantify the effects that the design interstory drift limit has on collapse safety, we designed a set of 12-story space frame buildings for various interstory drift limits ranging between 0.01 and 0.04 We were unable to design the building for a drift limit greater than 0.04 because a combination of the joint shear provision and maximum beam reinforcement ratio would not allow element sizes to be reduced further.

Table 7.8 lists these designs, their natural vibration periods, and the results of static pushover analyses. As expected, the drift limit has an important effect on the fundamental period of the buildings. The drift limit has only a minor effect on static overstrength and no consistent effects on the building deformation capacity, as judged from the pushover analyses.

Table 7.8 Structural designs and results of nonlinear static analysis for buildings designed with various interstory drift limits.

Height/Design				Period and Pushover Analysis Results			
Design Interstory Drift Limit	No. of Stories	Space/ Perimeter Frame	Design ID Number	First Mode Period (T_1) [sec]	Yield Base Shear Coeff. (Cs) [g]	Static Overstrength (based on ultimate strength)	RDR_{ult}
0.01	12	Space	2015	1.59	0.099	2.5	0.027
0.02			2009	1.99	0.093	2.3	0.033
0.03			2017	2.20	0.091	2.2	0.022
0.04 (unlimited)			2018	2.64	0.087	2.1	0.027

7.6.2 Nonlinear Dynamic Collapse Capacity Predictions

Table 7.9 and Figure 7.11 present the collapse analysis results for the buildings designed with various drift limits. These show that the collapse capacity is virtually unchanged by the design drift limit, and actually increases slightly for the most flexible design. A reason for this behavior may reflect the beneficial effects of the longer periods in the more flexible buildings. Also notice the larger deformation capacities of the more flexible building, which will be discussed in the next section. The findings shown in Table 7.9 and Figure 7.11 are not completely generalizable and are based on the design detailing assumptions discussed later in Section 7.6.3.

Table 7.9 Collapse performance predictions for buildings designed with various interstory drift limits.

Height/Design			Collapse Predictions			Collapse Drifts	
Design Interstory Drift Limit	No. of Stories	Space/ Perimeter Frame	Margin Against 2% in 50 Motion	$P[C\|Sa_{2/50}]$ including modeling uncertainty	λ_{col} $[10^{-4}]$, including modeling uncertainty	Median IDR at collapse	Median RDR at collapse
0.01	12	Space	1.47	0.27	10.82	0.055	0.020
0.02			1.49	0.26	10.37	0.064	0.024
0.03			1.48	0.27	10.93	0.065	0.020
0.04 (unlimited)			1.56	0.23	8.12	0.076	0.025

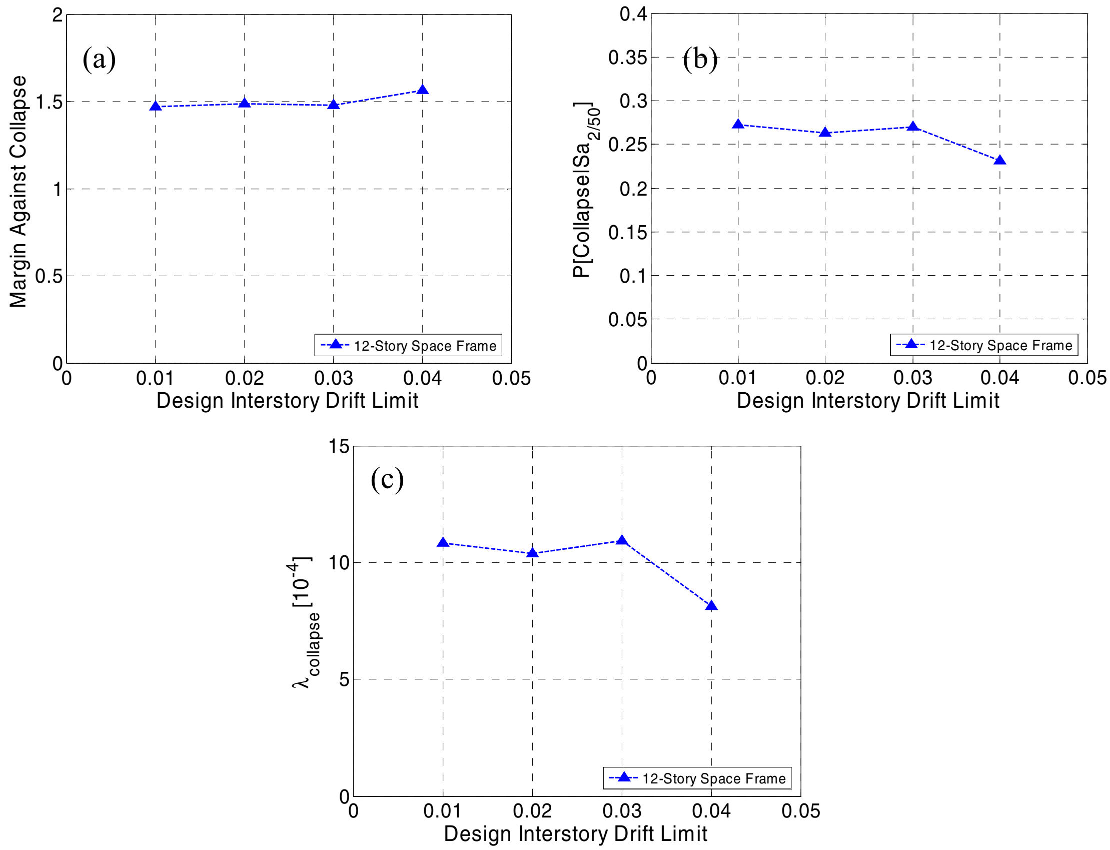

Figure 7.11 Collapse safety of 12-story space frame building designed for various interstory drift limits. Safety expressed in terms of (a) margin against collapse, (b) probability of collapse conditioned on level of ground motion, and (c) mean annual frequency of collapse.

7.6.3 Discussion of Reasons for Trends in Collapse Safety

We expected the more flexible buildings to have higher P-delta effects, and for this to lead to lower collapse capacities. However, we also found that increasing design drift levels also had the compensating effect of increasing element deformation capacities. The longer periods also mean that the buildings are in the region of the response spectra that contain less energy. Due to these compensating effects, we can not separate how much each of the effects would change the collapse capacity.

To illustrate the fact that P-delta effects are more dominant for the more flexible buildings, Figure 7.12 compares the static pushover results for the four buildings designed with interstory drift limits ranging from 0.01 to 0.04. If this P-delta difference were alone dictating the collapse capacity, this would have caused a noticeable reduction in capacity. However, as is clear from the pushovers, the P-delta effects are not the only difference between these buildings; the deformation capacities also change with design drift limit.

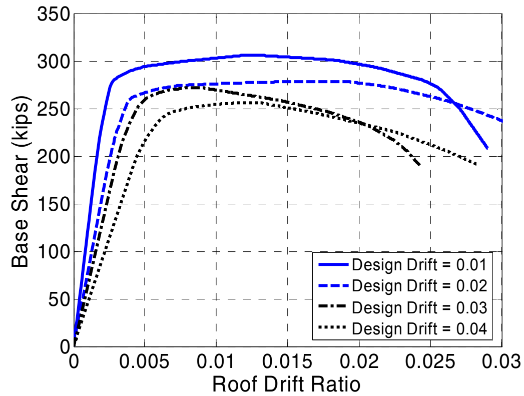

Figure 7.12 Comparison of pushover behavior for 12-story space frame buildings designed for various interstory drift limits.

Table 7.10 compares the designs and deformation capacities for a third-story beam; this beam is representative of the beams in the building. This shows that the beam depth decreases from 34″ to 18″ from the stiffest to most flexible design. Based on the d/4 stirrup spacing requirements in current seismic provisions (ACI 318-05, 2005), this causes the stirrup spacing(s) to decrease accordingly from 7.5″ to 3.5″. When the stirrup spacing decreases, this increases the lateral confinement ratio (ρ_{sh}) from 0.0035 to 0.0066. However, this increase is based on our design decision to maintain between three and four vertical ties at each stirrup location; we could have reduced the number of ties and kept the confinement ratio (ρ_{sh}) relatively constant for the four designs.

The reduction in stirrup spacing and increase in lateral confinement ratio (ρ_{sh}) significantly impacts the plastic rotation capacity ($\theta_{cap,pl}$) of the beam. The plastic rotation capacity ($\theta_{cap,pl}$) increases by a *factor of two* over the various designs. If this effect alone were dictating the collapse capacity, this would cause a noticeable increase in capacity.

The findings presented in this section are predicated on our treatment of confinement ratio (ρ_{sh}) in the design. If, in the design process, we would have kept the confinement ratio (ρ_{sh}) constant, then the effects on the beam plastic rotation capacity would have been less drastic and the increased drift limits may have led to decreased collapse capacity.

Table 7.10 Comparison of element designs and deformation capacities for 12-story space frame building designed with various drift limits.

Structural Design		Properties of Third-Floor Interior Beam				
Design Interstory Drift Limit	Design ID Number	Beam size [inches]	Stirrup spacing [inches]*	ρ_{sh}	$(\theta_{cap,pl})_{pos}$ [rad]	$(\theta_{cap,pl})_{neg}$ [rad]
0.01	2015	34x26	7.5	0.0035	0.053	0.036
0.02	2009	28x24	6.0	0.0045	0.067	0.042
0.03	2017	24x24	5.0	0.0054	0.081	0.052
0.04 (unlimited)	2018	18x27	3.5	0.0066	0.107	0.070
* At each stirrup location, there is a total of four vertical ties (three for ID 2015)						

7.7 SUMMARY AND CONCLUSIONS

This study looked at how three important structural design parameters affect collapse safety. These design parameters are (1) design base shear strength, (2) strong-column weak-beam (SCWB) design ratio, and (3) design interstory drift limit. Based on the findings of this study, Table 7.11 ranks the relative importance of these design provisions and shows that the design base shear strength and SCWB ratio are nearly tied as the most important aspect of design (or those considered here). The design drift limits were found to have minimal effect on collapse safety, but this finding is based on our design assumptions (Section 7.6.3). In a separate study of generic frame structures, Zareian (2006) came to similar conclusions. Ibarra (2003) also looked at the effects that the SCWB ratio has on collapse capacity (for SCWB ratios of 1.0, 1.2, 2.4, and infinite column strength).

This shows that a 3x increase in the SCWB ratio increases the collapse margin by a factor of 1.6-2.1, decreases the mean annual frequency of collapse by a factor of 5–14, and decreases the conditional collapse probability by 27–30%. The table shows comparable results for design base shear strength and design drift limit.

Table 7.11 Summary of relative importance of design parameters considered in study.

	Average values for each of the cases considered		
Design or Assessment Parameter	**Margin against 2% in 50 motion**	**$\lambda_{collapse}$ [10^{-4}]**	**P[C|$Sa_{2/50}$]**
Design base shear strength (R = 4 versus R = 12)*	2.3, 1.3	3.6, 38.5	12%, 42%
Design SCWB ratio (3x change: avg. of 0.4 to 1.2 or 0.9 to 3.0)	1.0, 2.1	28.2, 4.2	45%, 14%
Design interstory drift limit (from 0.01-0.04)	1.5, 1.6	10.8, 8.1	27%, 23%

* This paper shows that the design base shear strength affects both the strength and deformation capacity, so these effects are not soley due to strength.

For comparative purposes, we refer to a similar study by Haselton et al. (2007c, Chapter 6) that examined the importance of other design issues such as building height, space/perimeter frame designs, and weak story designs. The study also looked at two important assessment issues, namely inclusion of structural modeling uncertainty and consideration of spectral shape. Table 7.12 compiles the results of this current study (Table 7.11) and the study by Haselton et al. (2007c, Chapter 6), and then ranks the relative importance of each item.

This table shows that the SCWB ratio and design base shear strength are the two most important design issues considered in these two studies. The issues of third and fourth importance are not design issues, but are assessment concerns, namely inclusion of structural modeling uncertainties and consideration of spectral shape. Other design issues follow and the design drift limit is near the bottom of all the issues considered.

Table 7.12 Comparison of relative importance of design parameters considered in study and design/assessment parameters considered in Chapter 6.

	Average values for each of the cases considered		
Design or Assessment Parameter	**Margin against 2% in 50 motion**	**$\lambda_{collapse}$ [10^{-4}]**	**P[C|$Sa_{2/50}$]**
Design base shear strength (R = 4 versus R = 12)*	2.3, 1.3	3.6, 38.5	12%, 42%
Design SCWB ratio (3x change: avg. of 0.4 to 1.2 or 0.9 to 3.0)	1.0, 2.1	28.2, 4.2	45%, 14%
Inclusion of structural modeling uncert. (with and without)	1.6, 1.6	11.0, 2.8	26%, 16%
Spectral shape considerations (with adjustment and without)	2.3, 1.6	3.1, 11.0	11%, 16%
Building height	1.6, 2.0	12.4, 5.7	28%, 17%
Space versus perimeter frame	1.7, 1.3	8.6, 16.1	22%, 33%
Foundation fixity in design (pinned versus fixed)	1.9, 1.6	3.5, 6.1	12%, 18%
Strength irregularity (65% versus 100% strength ratios)	1.2, 1.4	17.5, 13.5	37%, 31%
Design interstory drift limit (from 0.01-0.04)	1.5, 1.6	10.8, 8.1	27%, 23%
Uniform size and reinf. over height versus baseline design	1.6, 1.4	10.0, 12.8	25%, 30%
Bay spacing (20' versus 30' spacing)	virtually no change		

* This paper shows that the design base shear strength affects both the strength and deformation capacity, so these effects are not soley due to strength.

7.8 FUTURE WORK

Some possible extensions of this work are as follows:

- Element detailing requirements affect element deformation capacities which are critical for collapse safety. This study did not address these design issues and could be extended to look at the effects of design detailing decisions.
- The findings regarding design drift are not fully generalizable, but are limited to our design assumptions. This study could be extended to consider additional designs that may have smaller differences in element deformation capacity. This would likely show that design drifts have a greater effect on the collapse capacity when different design assumptions are used.

APPENDIX 7A: MORE DETAILED COLLAPSE CAPACITY RESULTS FOR ALL DESIGNS

This Appendix presents more detailed collapse predictions for all of the designs presented in this paper. This detail is included for readers that may want to use these results to answer questions that differ from the primary focus of this study.

Table 7.13 presents the design information for all of the buildings used in this study. This table also presents the first mode period of each building and the results of static pushover analysis. The results shown in this table are a compilation of the results presented throughout this paper, and one additional definition of static overstrength is also included (i.e., overstrength defined using the *yield* base shear rather than the *ultimate* base shear).

Table 7.13 Structural design information and results of eigenvalue and static pushover analyses for all buildings considered in study.

Design Information						Period and Pushover Analysis Results					
Building	Design Num.	Design ID	Design R Value	SCWB Ratio	Drift Limit	First Mode Period (T_1) [sec]	Design Base Shear Coefficient (C_s) [g]	Yield Base Shear Coefficient, from Pushover [g]	Static Overstrength (based on yield strength)	Static Overstrength (based on ultimate strength)	Ultimate Roof Drift Ratio (at 20% strength loss) (RDR_{ult})
4-story, 30' space frame	1	2001	4	1.2	0.02	0.74	0.185	0.354	1.9	2.3	0.047
	2	2020	5.3	1.2	0.02	0.77	0.139	0.304	2.2	2.6	0.050
	3	1010	8	1.2	0.02	0.86	0.092	0.268	2.9	2.9	0.056
	4	2022	10	1.2	0.02	0.91	0.074	0.244	3.3	3.9	0.050
	5	2003	12	1.2	0.02	0.97	0.062	0.222	3.6	4.1	0.045
	6	2034	8	0.4	0.02	0.87	0.092	0.194	2.1	2.2	0.018
	7	2025	8	0.6	0.02	0.87	0.092	0.229	2.5	2.6	0.020
	8	2024	8	0.8	0.02	0.85	0.092	0.262	2.8	3.0	0.032
	9	2023	8	1.0	0.02	0.85	0.092	0.269	2.9	3.2	0.043
	10	1010	8	1.2	0.02	0.86	0.092	0.268	2.9	2.9	0.056
	11	2005	8	1.5	0.02	0.86	0.092	0.272	3.0	3.6	0.060
	12	2006	8	2.0	0.02	0.85	0.092	0.268	2.9	3.8	0.067
	13	2007	8	2.5	0.02	0.79	0.092	0.271	2.9	4.1	0.060
	14	2027	8	3.0	0.02	0.74	0.092	0.270	2.9	4.3	0.057
4-st., 30' perim.	15	2051	4	1.2	0.02	0.54	0.202	0.346	1.7	2.0	0.055
	16	1009	8	1.2	0.02	1.16	0.092	0.141	1.5	1.6	0.050
	17	2052	12	1.2	0.02	1.15	0.062	0.104	1.7	1.8	0.038
12-story, 20' space frame	18	2008	4	1.2	0.02	1.83	0.070	0.140	2.0	2.1	0.039
	19	2021	5.3	1.2	0.02	1.97	0.053	0.111	2.1	2.2	0.028
	20	2009	8	1.2	0.02	1.99	0.044	0.093	2.1	2.3	0.033
	21	2028	10	1.2	0.02	2.27	0.028	0.072	2.6	2.7	0.018
	22	2010	12	1.2	0.02	2.40	0.023	0.071	3.1	3.2	0.020
	23	2015	8	1.2	0.01	1.59	0.044	0.099	2.3	2.5	0.027
	24	2009	8	1.2	0.02	1.99	0.044	0.093	2.1	2.3	0.033
	25	2017	8	1.2	0.03	2.20	0.044	0.091	2.1	2.2	0.022
	26	2018	8	1.2	0.04	2.64	0.044	0.087	2.0	2.1	0.027
12-story, 20' perim. frame	27	2053	4	1.2	0.02	1.50	0.079	0.120	1.5	1.6	0.031
	28	1013	8	1.2	0.02	2.01	0.044	0.075	1.7	1.7	0.026
	29	2054	12	1.2	0.02	2.84	0.023	0.036	1.6	1.7	0.009
	30	2060	8	0.9	0.02	2.00	0.044	0.075	1.7	1.7	0.024
	31	1013	8	1.2	0.02	2.01	0.044	0.075	1.7	1.7	0.026
	32	2055	8	1.5	0.02	2.01	0.044	0.074	1.7	1.7	0.029
	33	2056	8	2.0	0.02	2.01	0.044	0.067	1.5	1.6	0.030
	34	2057	8	2.5	0.02	1.90	0.044	0.072	1.6	1.7	0.038
	35	2058	8	3.0	0.02	1.84	0.044	0.074	1.7	1.7	0.045

Table 7.14 presents the collapse performance predictions for all of the buildings used in this study. Many of these results have been presented previously in this report. The additional results shown in this table are listed as follows:

- The record-to-record variability of collapse capacity [$\sigma_{LN(Sa,col)}$].
- The margin against the maximum considered earthquake motion (MCE), which is defined as the ratio between the median collapse capacity and the MCE spectral acceleration.
- The probability of collapse and mean annual frequency of collapse, computed without including structural modeling uncertainties. These are included only to show the effects

of structural modeling uncertainties; we do not consider collapse predictions to be realistic if they do not include the effects of structural modeling uncertainties.

Table 7.14 Detailed collapse performance predictions for all buildings considered in study. Results not corrected for spectral shape effects.

Design Information			Collapse Predictions with no Adjustment for Spectral Shape, Controlling Horizontal Component of Ground Motion							
Building	Design Num.	Design ID	Mean[a] $Sa_{g.m.,col}(T_1)$ [g]	$\sigma_{LN}(Sa,col)$	Margin Against MCE	Margin Against 2% in 50 Year Motion	$P[C\|Sa_{2/50}]$ including modeling uncertainty	λ_{col} [10^{-4}], including modeling uncertainty	$P[C\|Sa_{2/50}]$ without modeling uncertainty[b]	λ_{col} [10^{-4}], without modeling uncertainty[b]
4-story, 30' space frame	1	2001	2.64	0.39	2.16	2.62	0.06	1.64	0.01	0.20
	2	2020	2.33	0.40	2.01	2.39	0.09	2.45	0.01	0.36
	3	1010	2.24	0.42	2.13	2.42	0.09	2.51	0.02	0.39
	4	2022	1.92	0.40	1.95	2.15	0.12	3.38	0.03	0.57
	5	2003	1.69	0.40	1.82	2.00	0.14	4.32	0.04	0.79
	6	2034	0.98	0.38	0.95	1.07	0.45	28.19	0.43	9.02
	7	2025	1.14	0.39	1.10	1.24	0.36	18.97	0.29	5.45
	8	2024	1.57	0.40	1.49	1.68	0.21	7.68	0.10	1.68
	9	2023	2.00	0.42	1.90	2.14	0.12	3.76	0.03	0.67
	10	1010	2.24	0.42	2.13	2.42	0.09	2.51	0.02	0.39
	11	2005	2.38	0.41	2.26	2.57	0.07	1.94	0.01	0.27
	12	2006	2.47	0.37	2.34	2.64	0.06	1.43	0.00	0.16
	13	2007	2.58	0.37	2.27	2.67	0.06	1.42	0.00	0.16
	14	2027	2.77	0.37	2.29	2.75	0.05	1.25	0.00	0.13
4-st., 30' perim.	15	2051	3.35	0.46	2.24	2.72	0.07	1.92	0.02	0.28
	16	1009	1.24	0.41	1.59	1.66	0.22	8.17	0.11	1.88
	17	2052	0.99	0.42	1.27	1.31	0.34	16.96	0.26	4.96
12-story, 20' space frame	18	2008	1.01	0.40	2.04	1.88	0.16	4.98	0.06	0.97
	19	2021	0.74	0.37	1.62	1.53	0.25	8.97	0.13	1.97
	20	2009	0.71	0.38	1.56	1.49	0.26	10.37	0.15	2.41
	21	2028	0.46	0.36	1.16	1.11	0.43	23.12	0.39	6.99
	22	2010	0.46	0.37	1.22	1.16	0.41	20.73	0.35	6.07
	23	2015	0.87	0.39	1.55	1.47	0.27	10.82	0.16	2.66
	24	2009	0.71	0.38	1.56	1.49	0.26	10.37	0.15	2.41
	25	2017	0.63	0.39	1.53	1.48	0.27	10.93	0.16	2.68
	26	2018	0.56	0.35	1.63	1.56	0.23	8.12	0.10	1.64
12-story, 20' perim. frame	27	2053	1.18	0.45	1.97	1.92	0.17	5.86	0.07	1.29
	28	1013	0.55	0.37	1.23	1.19	0.39	20.28	0.32	5.77
	29	2054	0.20	0.33	0.63	0.62	0.79	111.93	0.93	50.82
	30	2060	0.51	0.39	1.12	1.09	0.45	28.23	0.42	9.10
	31	1013	0.55	0.37	1.23	1.19	0.39	20.28	0.32	5.77
	32	2055	0.60	0.38	1.33	1.28	0.35	16.78	0.26	4.55
	33	2056	0.65	0.38	1.46	1.41	0.29	12.67	0.19	3.13
	34	2057	0.77	0.39	1.63	1.53	0.25	9.80	0.14	2.34
	35	2058	0.92	0.37	1.88	1.75	0.18	5.87	0.06	1.15

a - The mean value when using a lognormal distribution; this value is closer to the median.
b - The collapse probability and rate computed without modeling uncertainty is simply for comparison.

Table 7.15 presents the collapse drifts for each of the buildings considered in this paper. These reported drifts are the largest drifts that the building obtained before becoming dynamically unstable and collapsing. The median interstory and roof drift ratios were included in previous tables of this report, but this table also includes the record-to-record variability of the collapse drifts.

Table 7.15 Collapse drift predictions for all buildings considered in study.

Design Information			Collapse Drifts			
Building	Design Num.	Design ID	Median IDR at collapse	σ_{LN}(IDR at collapse)	Median RDR at collapse	σ_{LN}(RDR at collapse)
4-story, 30' space frame	1	2001	0.080	0.29	0.051	0.32
	2	2020	0.078	0.28	0.050	0.30
	3	1010	0.083	0.28	0.053	0.22
	4	2022	0.076	0.28	0.046	0.26
	5	2003	0.074	0.25	0.043	0.22
	6	2034	0.051	0.18	0.017	0.20
	7	2025	0.055	0.28	0.027	0.36
	8	2024	0.065	0.23	0.027	0.24
	9	2023	0.075	0.24	0.041	0.21
	10	1010	0.083	0.28	0.053	0.22
	11	2005	0.079	0.29	0.060	0.29
	12	2006	0.092	0.23	0.075	0.26
	13	2007	0.093	0.28	0.076	0.27
	14	2027	0.122	0.44	0.091	0.43
4-st., 30' perim.	15	2051	0.076	0.37	0.049	0.36
	16	1009	0.078	0.32	0.050	0.26
	17	2052	0.068	0.26	0.042	0.24
12-story, 20' space frame	18	2008	0.076	0.17	0.025	0.18
	19	2021	0.065	0.19	0.021	0.19
	20	2009	0.064	0.26	0.024	0.24
	21	2028	0.045	0.32	0.015	0.27
	22	2010	0.054	0.30	0.017	0.25
	23	2015	0.055	0.33	0.020	0.31
	24	2009	0.064	0.26	0.024	0.24
	25	2017	0.065	0.27	0.020	0.22
	26	2018	0.076	0.18	0.025	0.21
12-story, 20' perim. frame	27	2053	0.069	0.27	0.021	0.18
	28	1013	0.053	0.31	0.016	0.22
	29	2054	0.031	0.37	0.009	0.24
	30	2060	0.047	0.34	0.014	0.21
	31	1013	0.053	0.31	0.016	0.22
	32	2055	0.053	0.28	0.018	0.21
	33	2056	0.060	0.33	0.022	0.25
	34	2057	0.063	0.31	0.027	0.23
	35	2058	0.073	0.32	0.035	0.26

APPENDIX 7B: COLLAPSE CAPACITY RESULTS ADJUSTED FOR PROPER SPECTRAL SHAPE

Baker and Cornell (2006, 2005) have shown that proper consideration of ground motion spectral shape is critical in performance assessment, especially for collapse simulation when the structural response is highly nonlinear.

Proper spectral shape is typically accounted for by selecting a ground motion set that has the proper spectral shape with respect to the fundamental period of the building (e.g., Goulet et al. 2006a). Ground motion selection for proper spectral shape is not feasible for this study, since we are considering a large number of buildings with various fundamental periods. Therefore the ground motions used in this study do not have the proper spectral shape, so the collapse results presented earlier in this paper are conservative. This is acceptable because the primary purpose of this paper is to quantify the *relative* changes in collapse risks due to changes in structural design methods. If the correct collapse risk is desired (correct in an absolute sense), the collapse predictions must be corrected to account for proper spectral shape. The purpose of this Appendix is to present the corrected collapse predictions, which are more correct in an absolute sense.

To address this issue of proper spectral shape, Haselton and Baker et al. (2007a, Chapter 3) proposed a simplified method capable of accounting for spectral shape effects when using a general ground motion set. Consideration of spectral shape is not the primary topic of this paper, so we simply use the method proposed in Haselton and Baker et al. and refer the reader to that publication for additional detail. In this study, we adjust the collapse predictions to be approximately consistent with the spectral shape for the 2%-in-50-years ground motion in high seismic regions of California (which is consistent with the Los Angeles site used in this study; Section 7.3). This method uses a parameter called "epsilon" as an indicator of spectral shape. To determine the proper target epsilon for a 2%-in-50-years ground motion level, we refer to the United States Geological Survey report on deaggregation of the U.S. seismic hazard (Harmsen et al. 2002). This report shows that the epsilon values vary based on geographic location and period, with 1.5 being a reasonable value to use for high seismic regions of California; this value of 1.5 is also fairly consistent with the hazard at the Los Angeles site (Section 7.3).

Table 7.16 presents the collapse predictions after adjustment for proper spectral shape. This table is almost identical to the previous table of collapse results (Table 7.14) but incorporates the adjustment for proper spectral shape. Comparison of this table and Table 7.14 shows that the spectral shape adjustment causes significant increases in the collapse capacities, and decreases in the collapse probabilities and rates. The ratio of the adjusted/unadjusted median collapse capacity is 1.46 on average (range of 1.26–1.66), the collapse probability reduces by an average of 13% (range of 18–51%), and the mean annual frequency of collapse decreases by an average factor of 3.5 (range of 1.9–5.6).

Table 7.16 Collapse performance predictions adjusted to reflect proper spectral shape of ground motions.

Design Information			Collapse Predictions with Adjustment for Spectral Shape (1.5ε), Controlling Horizontal Component of Ground Motion						
Building	Design Num.	Design ID	Adjusted Mean[a] $Sa_{g.m.}$,col (T_1) [g]	Margin Against MCE	Margin Against 2% in 50 Year Motion	P[C|$Sa_{2/50}$] including modeling uncertainty	λ_{col} [10^{-4}], including modeling uncertainty	P[C|$Sa_{2/50}$] without modeling uncertainty[b]	λ_{col} [10^{-4}], without modeling uncertainty[b]
4-story, 30' space frame	1	2001	3.50	2.87	3.48	0.02	0.56	0.00	0.05
	2	2020	3.07	2.64	3.15	0.04	0.89	0.00	0.09
	3	1010	3.17	3.01	3.42	0.03	0.71	0.00	0.07
	4	2022	2.68	2.71	2.99	0.04	1.03	0.00	0.11
	5	2003	2.28	2.45	2.70	0.06	1.52	0.01	0.19
	6	2034	1.23	1.19	1.35	0.32	14.50	0.21	3.79
	7	2025	1.44	1.39	1.58	0.24	9.27	0.12	2.13
	8	2024	2.09	1.97	2.23	0.10	2.99	0.02	0.48
	9	2023	2.80	2.66	3.00	0.05	1.15	0.00	0.14
	10	1010	3.17	3.01	3.42	0.03	0.71	0.00	0.07
	11	2005	3.33	3.16	3.60	0.02	0.55	0.00	0.05
	12	2006	3.36	3.19	3.59	0.02	0.44	0.00	0.03
	13	2007	3.50	3.09	3.63	0.02	0.43	0.00	0.03
	14	2027	3.80	3.14	3.78	0.02	0.36	0.00	0.02
4-st., 30' perim.	15	2051	4.33	2.89	3.51	0.03	0.76	0.00	0.08
	16	1009	1.87	2.41	2.51	0.08	2.06	0.01	0.30
	17	2052	1.48	1.89	1.96	0.15	4.91	0.06	0.98
12-story, 20' space frame	18	2008	1.57	3.19	2.94	0.05	1.04	0.00	0.11
	19	2021	1.13	2.47	2.33	0.09	2.17	0.01	0.28
	20	2009	1.14	2.53	2.41	0.08	2.05	0.01	0.26
	21	2028	0.65	1.63	1.56	0.24	8.23	0.11	1.74
	22	2010	0.65	1.73	1.64	0.21	7.11	0.09	1.43
	23	2015	1.37	2.42	2.30	0.09	2.48	0.02	0.37
	24	2009	1.14	2.53	2.41	0.08	2.05	0.01	0.26
	25	2017	0.95	2.32	2.24	0.10	2.80	0.02	0.42
	26	2018	0.81	2.37	2.27	0.09	2.26	0.01	0.27
12-story, 20' perim. frame	27	2053	1.96	3.26	3.19	0.04	1.04	0.01	0.13
	28	1013	0.85	1.91	1.84	0.16	5.18	0.05	0.91
	29	2054	0.27	0.86	0.83	0.62	52.28	0.71	19.11
	30	2060	0.77	1.70	1.65	0.22	8.10	0.10	1.75
	31	1013	0.85	1.91	1.84	0.16	5.18	0.05	0.91
	32	2055	0.91	2.04	1.96	0.14	4.33	0.04	0.73
	33	2056	1.04	2.31	2.23	0.10	2.78	0.02	0.39
	34	2057	1.22	2.57	2.41	0.08	2.16	0.01	0.30
	35	2058	1.46	2.98	2.78	0.05	1.17	0.00	0.12

a - The mean value when using a lognormal distribution; this value is closer to the median.

b - The collapse probability and rate computed without modeling uncertainty is simply for comparison.

8 Conclusions, Limitations, and Future Research Needs

8.1 SUMMARY AND CONCLUSIONS

8.1.1 Overview

A primary goal of the seismic design requirements of building codes is to protect the safety of building inhabitants during extreme earthquakes. First and foremost, this requires controlling the likelihood of structural collapse such that it remains at an acceptably low level. Although experience with modern code-conforming buildings has generally been good, current codes and standards are empirical in nature, such that the collapse safety of new buildings is not well understood.

The overarching objective of this study was to quantitatively predict the collapse safety of modern reinforced concrete (RC) special moment-frame (SMF) buildings in California[1]. Predicting nonlinear structural response and collapse under earthquake ground motions is complex. To organize this research and combine ground motion hazard with structural response predictions, we used the PEER framework for probabilistic performance assessment. Within this framework, this research addressed many important issues involved in collapse assessment, as summarized in the following list.

- Investigate ground motion issues and the effects that ground motion selection has on collapse assessment, specifically the expected spectral shape of ground motions (Chapter 3).
- Develop a calibrated beam-column element model that is capable of predicting the flexural response that leads to global collapse (Chapter 4).

---

[1] The scope of this study is limited to sites that are not near field..

- Investigate structural modeling uncertainties and their impacts on the uncertainty in collapse capacity (Chapter 5).
- Perform a collapse assessment of a single 4-story RC SMF building to benchmark the collapse safety provided by existing building codes, to exercise the assessment method, and to facilitate further development of the method (Chapter 2).
- Assess the collapse safety of a large number of RC SMF buildings. This helps us better understand the collapse safety of the *full class* of RC SMF buildings rather than assessing the safety of only a *single building design* (Chapter 6).

The above approach was used to meet the primary goal of this research, which was to predict the collapse safety of modern RC SMF buildings in California. Chapter 7 went beyond this primary goal and looked at how changes to the current building code design requirements would affect collapse safety.

8.1.2 Collapse Assessment Framework (Chapter 2)

Chapter 2 presents the global collapse assessment framework that was developed by the PEER Center and further improved in this research. This framework enables us to combine the ground motion hazard with the structural collapse capacity in order to predict the mean annual rate of collapse. In Chapter 2, we illustrated the application of this framework to the assessment of a 4-story RC SMF building.

Our development of this framework focused on exercising/testing the methodology and developing many of the detailed components that are needed for performing a rigorous collapse performance assessment. Some of these components include treatment of ground motions (Goulet and Stewart), identification of deterioration and collapse modes expected for a given structural system, calibration of element models that capture the important deterioration modes, treatment of structural modeling uncertainties, and further development and exercise of an approach for assessing the collapse safety of a class of buildings.

In addition to developing these individual components of the assessment methodology, we looked at how each component impacts the final collapse risk predictions. This showed that both (a) ground motion spectral shape (or ε) and (b) structural modeling uncertainties are critically important for proper collapse assessment and deserve further study.

8.1.3 Accounting for Expected Spectral Shape (Epsilon) in Collapse Performance Assessment (Chapter 3)

Previous research has shown that for rare ground motions in California, the spectral shape is much different than the shape of a code design spectrum or a uniform hazard spectrum (Baker 2005a, Chapter 6; Baker 2006b), and that this shape is related to a parameter called "epsilon" (ε).

Using an example 8-story RC SMF building, we verified Baker's findings that that this spectral shape (ε) effect has significant impacts on collapse capacity. For this building, not accounting for the proper ε or ground motions leads to an underestimation of the median collapse capacity by a factor of 1.6 and overestimation of the mean annual frequency of collapse by more than a factor of 20.

The most direct approach used to account for ε is to select ground motions with proper ε values. This is difficult when assessing the collapse safety of many buildings, because the ε-based ground motion selection depends on the building period and the site, so a unique ground motion set is needed for each building. To make it easier to account for ε in a collapse performance assessment, we developed a simplified method. This method involves (a) using a general far-field ground motion set that is selected without regard to spectral shape, then (b) adjusting both the mean and uncertainty of the collapse capacity distribution to account for the proper ε value for the site and period of interest. This adjustment is a function of building height and deformation capacity. The method is presented in Chapter 3.

We compared the collapse risk predictions using both the simplified regression method and the direct ground motion selection method. Using these two methods, the mean annual rates of collapse were 0.28 $x10^{-4}$ and 0.35 $x10^{-4}$ (collapses/year) and the $P[C|Sa_{2/50}]$ values were 0.5% and 1.2%. These predictions are quite close and provide confidence in use of the simplified method.

8.1.4 Calibration of Beam-Column Element Model for Predicting Flexural Response Leading to Global Collapse of RC Frame Buildings (Chapter 4)

Developing a structural model that includes all of the important modes of in-cycle and cyclic deterioration that lead to global collapse is not trivial. Ibarra et al. (2005) developed a generic material model capable of modeling these important deterioration modes. Proper use of such a model requires estimating each of the many element modeling parameters, including element stiffness, deformation capacity, cyclic deterioration parameters, etc. The existing literature provides only minimal guidance for calculating these element properties.

To aid in creating structural models for collapse assessment, we developed a full set of empirical equations that can be used to predict the parameters of a lumped plasticity model of an RC element. To allow statistically unbiased modeling, we quantified both the mean and uncertainty of each modeling parameter. We developed these equations based on calibration to 255 experimental tests of reinforced-concrete columns failing in flexure or flexure-shear, from the PEER Structural Performance Database (Berry et al. 2004; PEER 2006a). The empirical equations are based on the physical properties of the column (axial load, confinement, etc.) and provide for calculation of the following parameters:

- Initial stiffness
- Strength (method by Panagiotakos and Fardis, 2001)
- Post-yield hardening stiffness
- Plastic rotation capacity to the capping point (the capping point is defined as the onset of strain-softening)
- Post-capping rotation capacity (from capping point to zero strength)
- Energy-dissipation capacity (the cyclic deterioration parameter)

One notable finding from this calibration study is that the plastic rotation capacity of a modern code-conforming RC element is much larger than typically considered. For an element that is tension controlled (i.e., below the balanced point), the mean plastic rotation capacity is typically in the range of 0.05–0.08 radians. The uncertainty (logarithmic standard deviation) is 0.48 or 0.62, for estimation of total or plastic rotation capacities, respectively. Additionally, we found that even when this plastic rotation capacity is reached, and the element begins to strain-soften, the element can typically maintain an additional 0.10 radians of plastic rotation prior to complete strength loss.

8.1.5 Accounting for Structural Design and Modeling Uncertainties in Collapse Performance Assessment (Chapter 5)

Accurately quantifying uncertainty is a critical part of collapse performance assessment, previous research (Ibarra and Krawinkler 2005a; Ibarra 2003, Chapter 6) found that the uncertainties in structural modeling have significant impacts on the uncertainty in collapse capacity. This previous study was based on single-degree-of-freedom systems and judgmental estimates of parameter uncertainties.

We extended Ibarra's work by more rigorously quantifying basic structural modeling parameter uncertainties and then investigating how these uncertainties affect the collapse capacity of a 4-story *multiple*-degree-of-freedom RC SMF building. To quantify this uncertainty in collapse capacity, we (a) quantified the structural modeling uncertainties using previous research and further calibrations to test data, (b) used judgment to establish reasonable correlations between variables, and finally (c) used the first-order second-moment (FOSM) method to propagate the uncertainties. We then incorporated this uncertainty into the assessment process by using a mean estimate approach.

For a 4-story RC SMF building, we found that the collapse capacity uncertainty[2] is $\sigma_{LN(Sa,col)} = 0.35$ when considering only the modeling uncertainty, and $\sigma_{LN(Sa,col)} = 0.45$ when considering uncertainties in both modeling and design. For this modern building, where the extreme tail of the collapse capacity distribution is important in the calculation of collapse risk, this increased uncertainty has important effects. Not accounting for these structural uncertainties causes the mean annual frequency of the collapse estimate to be underpredicted by nearly *a factor of 10*.

For this 4-story RC SMF building, we found that the uncertainty in element plastic rotation capacity has the greatest effect on the uncertainty in the collapse capacity. We also found cyclic strength deterioration is not a critical aspect of collapse simulation. In addition, for this specific building, we found that the post-capping stiffness (or post-capping rotation capacity) was virtually unimportant, which stemmed from the fact that the damage localized in two stories of the building and caused the system to lose strength quickly after element capping. These findings are in agreement with the findings of a single-degree-of-freedom sensitivity study conducted previously by Ibarra (2003).

Finally, we found that the correlation between variables is highly important in the collapse predictions. Correlation assumptions can change the estimated $\sigma_{LN(Sa,col)}$ by a factor of three to five, which results in nearly another *factor of 10 change* in the estimated mean annual frequency of collapse.

[2] These values only reflect uncertainties in structural modeling and/or design, and do not include effects of record-to-record variability.

8.1.6 Collapse Performance Predictions for Reinforced Concrete Special Moment-Frame Buildings (Chapters 6 and 2)

The overarching goal of this study was to predict the collapse risk of RC SMF buildings located at far-field sites of California. To realize this goal, we used the findings from Chapters 3–5 to develop structural models and assess the collapse risk for a large number of RC SMF buildings.

In Chapter 2, we looked at seven alternative designs for a single 4-story RC SMF building. We found that the collapse probabilities range from 2–7% for earthquake ground motions with 2% probability of exceedance in 50 years. Combining the ground motion hazard with the collapse predictions, we found that the mean annual frequencies of collapse are [0.4 to 1.4] x 10^{-4}, which translate to collapse return periods of 7,000–25,000 years.

To generalize these results, we designed and assessed 30 additional RC SMF buildings ranging in height from one to twenty stories (Chapter 6), all based on ASCE7-02 provisions. For these 30 buildings, the collapse probabilities range from 3 to 20% for a 2%-in-50-years ground motion. The mean annual frequencies of collapse are [0.7 to 7.0] x 10^{-4}, which translate to collapse return periods of 1,400–14,000 years. These collapse risk estimates include the effects of structural modeling uncertainties and an adjustment to reflect proper ε values of the ground motions. The assessment of these 30 buildings also suggested that the mid-rise buildings (8–12-story buildings) have slightly higher collapse risk than buildings of other heights.

Given these collapse risk predictions, the obvious question is whether these RC SMF buildings meet the intention of current codes and are "safe enough." The topic of acceptable collapse risk and desired safety goals is worthy of substantial further study. Studies such as this can provide better understanding of the collapse safety of new buildings and can inform a decision making process to determine acceptable collapse risk and desired safety goals.

Chapter 6 also investigated how collapse safety is changed by the removal of the minimum design base shear requirement in the updated ASCE7-05 provisions. The results of this investigation suggest that the minimum base shear requirement (ASCE 7-02 equation 9.5.5.2.1-3) was an important component of ensuring relatively consistent collapse risk for buildings of varying height. Removing this requirement has made taller buildings significantly more vulnerable to collapse; this should be considered in future revisions of ASCE7. For an example 20-story building, removal of the minimum base shear limit reduced the design base shear from $C_s = 0.044g$ to $C_s = 0.022g$, reduced the median collapse capacity of the 20-story perimeter frame building by a factor of two, increased the conditional collapse probability by a factor of four, and increased the mean annual frequency of collapse by a factor of 11.

In addition to looking at how structural design aspects (height, building code used for design, etc.) affect collapse safety, we looked at the impacts of various portions of the collapse assessment methodology. Interestingly, we found that aspects of the structural design (height, framing layout, etc.) are less important than the aspects of the collapse assessment methodology (structural modeling uncertainties, and spectral shape). Even changes in building height from 1 to 20 stories did not affect predicted collapse risk as much as either of these two aspects of the collapse assessment methodology.

The above finding also re-emphasizes the importance of having a *systematic codified* assessment method that can be used to demonstrate the performance of a structural system. This is especially critical for building code committees that are reviewing proposals for adding new systems to the building code. Without a codified assessment method, there would be no consistency between various proposals; the predicted performance of each new system would depend almost entirely on how each group carried out their performance assessment. Developing portions of this codified method was one of the primary purposes of this study; the complete method can be found in the ATC-63 project report (which is currently in progress).

8.1.7 Effects of Building Code Design Provisions on Collapse Performance of Reinforced Concrete Special Moment-Frame Buildings (Chapter 7)

Chapter 7 discusses how three important structural design requirements affect collapse safety. These design parameters are (1) design base shear strength, (2) strong-column weak-beam (SCWB) design ratio, and (3) design interstory drift limit. We found that the SCWB design ratio is most important, with the design base shear strength being a close second. The design drift limits were found to have minimal effect on collapse safety, though this finding is based to some extent on our design assumptions (as described in Chapter 7).

As expected, we found that increasing the SCWB ratio improved collapse performance because it led to a more complete collapse mechanism where damage was spread over a greater number of stories. For 4-story buildings, we found that the benefit of increasing the SCWB ratio saturates at a SCWB ratio of 1.5 when the collapse mechanism becomes complete (i.e., when all of the stories are involved in the mechanism) and further increases in the column strength does not improve the mechanism. For 12-story buildings, we found that even with the SCWB ratio increased up to 3.0, increased column strength continued to improve the collapse capacity, because the collapse mechanism continued to improve. For these 4-story and 12-story buildings, we found that a 3x increase in the SCWB ratio increases the collapse margin by a factor of 1.6–2.1, decreases the mean annual frequency of collapse by a factor of 5–14, and decreases the collapse probability by 27–30%.

Decreasing the design base shear strength will obviously affect the collapse performance because the building is weaker, but we found that the deformation capacity is also reduced when the strength is reduced. This comes from the damage localizing in fewer stories. We found that space frame buildings are less sensitive to the specified design base shear strength, due to the dominance of gravity loads in the design. For the space frame buildings considered in this study, a 3x change in *design* base shear strength resulted in only a 1.5x change in *yield* base shear strength. For comparison, for perimeter frame buildings a change in design base shear strength leads to nearly the same change in yield base shear strength). For all the buildings considered in this study, a 2x increase in design base shear strength increases the collapse margin by a factor of 1.2–2.4, decreases the mean annual frequency of collapse by a factor of 1.5–13, and decreases the collapse probability by 5%–41%.

Decreasing the design interstory drift limit from 0.04 to 0.01 had almost no effect, and actually decreased the collapse capacity slightly. However, this finding is based on our specific set of design assumptions and does not necessarily apply in a general sense.

The results from Chapter 7 can be used by building code committees to better understand how design requirements affect collapse performance. However, Chapter 7 showed that the design requirements have different effects for different types of buildings (e.g., buildings of differing height, space/perimeter frames, etc.). To have a more general understanding of how design requirements affect the collapse performance of RC SMF buildings, this study could be extended to include a larger number of buildings.

8.2 LIMITATIONS AND RECOMMENDATIONS FOR FUTURE RESEARCH

The limitations of this research and potential areas of future research include the following:

- Reinforced concrete element model
  - We calibrated the model based on experimental data which use cyclic loading consistent with common loading protocols; there are few monotonic tests. This made it difficult to accurately calibrate the monotonic backbone and cyclic deterioration rules separately.
  - From the database of tests used in calibration, almost all tests did not continue to deformation levels large enough to show the element deformation capacity and post-capping stiffness. This required us to apply some conservatism in the estimates of these modeling parameters. Future tests should push the specimens to deformations large enough to clearly show these aspects of response. This will provide the data needed to further improve element modeling.
  - We propose that the empirical equations developed in this research be put through a consensus and codification process. Such a codification process would utilize both our proposed equations and equations proposed by other researchers. The goals for such a process would be to develop modeling recommendations that are more complete and better than those proposed by any one study; these recommendations should include prediction of both the mean and uncertainty of the modeling parameters. The ASCE 41 Committee has started this process and is currently utilizing our proposed equations, and those of other researchers, to update the recommendations of FEMA 356 (FEMA 2000a).
- Structural modeling uncertainty
  - The modeling uncertainty work in Chapter 5 was based on analyses of a single 4-story RC SMF building. While we used this estimate of uncertainty for all buildings assessed in this study, further work could be done to generalize the uncertainty calculations.
  - We found that structural modeling uncertainties have significant impacts on the predicted collapse risk. Therefore, significant future research is warranted to more fully understand the impacts that these uncertainties have in collapse assessment.

- This study only addressed uncertainties in structural design and modeling. We did not fully consider many other important uncertainties, such as construction uncertainty, human error, etc. Future research is warranted to better understand the impact of not accounting for such uncertainties in the collapse assessment process.

- Collapse performance predictions for new buildings
  - The collapse assessment method developed by researchers at the PEER Center and further enhanced in this research, is general and can be applied to any building type. It would be useful to conduct similar studies for other modern building types (concrete shear walls, steel moment frames, steel braced frames, etc.). The results of such a study would help the profession to better understand the expected collapse performance for various types of building systems. This could also inform building code revisions with the goal of creating consistent collapse risk between the various types of structural systems. Note that Zareian (2006) has recently completed a study of generic RC walls, which would contribute to this goal.
  - All structural models used in this study were two dimensional.
  - Structural models did not include soil-structure-foundation interaction effects, though these effects are not likely be important for relatively flexible RC frame buildings.
  - This study was limited to far-field regions of California. This study could be extended to look at the collapse performance at near-field sites.
  - All collapse performance assessments were based on a site in northern Los Angeles. It would be useful to extend this study to look at other sites and determine how site location affects the mean annual rate of collapse.
  - This study can be extended by looking more closely at the collapse *displacements* (as opposed to spectral intensity measures) of the 65 buildings assessed in this study. This consideration is important for an engineering audience, who may be more adept at thinking in terms of interstory-drift demands and capacities.
  - New RC SMF buildings are highly ductile and typically do not collapse except under very rare ground motions. Therefore, to assess the collapse of these ductile buildings, we must scale the ground motions, often significantly. For one example building, the median scale factor at collapse was 4.3 (range of 1.3–13.9). Such scaling raises questions about whether the properties of these scaled motions are consistent with the

properties of future extreme motions that may cause the collapse of modern buildings. Further research on extreme ground motions would help answer this question.

- Predictions of structural damage and monetary losses for new buildings
  - In the process of this study, we predicted the nonlinear structural responses of 65 RC SMF building. This study can be extended to utilize these structural response data to predict monetary damage and loss for these buildings.
  - The above structural response data and loss predictions can also be used to develop more detailed fragility models (relating ground motion level to structural damage states) and loss models (relating ground motion to monetary losses). Fragility models could also be developed to predict the probability of a building being red-tagged after an earthquake.
- Acceptable collapse risk
  - It is difficult to judge what level of collapse safety is acceptable. The topics of acceptable collapse risk and desired safety goals are worthy of substantial further study.
- Effects of building code design provisions on collapse performance
  - Chapter 7 did not look at the effects of element detailing requirements. Detailing requirements are important for increasing the element deformation capacities, and this study could be extended to look at how changes to these design requirements would affect collapse safety.
- Packaging collapse assessment tools
  - To make it feasible for others to assess collapse performance, the models and methods must be well packaged and easier to use; this is an important topic of future work.
  - This packaging could include (a) developing a simple tool to predict RC element modeling parameters, (b) developing a packaged collection of OpenSees scripts/procedures for developing structural models and performing analyses, (c) developing a packaged collection of post-processing tools, and (d) preparing a concise summary on how to complete a collapse performance assessment.

References

Abrahamson N.A. and Silva W.J. (1997). Empirical response spectral attenuation relations for shallow crustal earthquake, Seismological Research Letters, **68** (1), 94-126.

Altoontash, A. (2004). *Simulation and Damage Models for Performance Assessment of Reinforced Concrete Beam-Column Joints*, Dissertation, Department of Civil and Environmental Engineering, Stanford University.

American Concrete Institute. (2005). *Building Code Requirements for Structural Concrete (ACI 318-05) and Commentary (ACI 318R-05)*, Farmington Hills, MI.

American Concrete Institute. (2002). *Building Code Requirements for Structural Concrete (ACI 318-02) and Commentary (ACI 318R-02)*, Farmington Hills, MI.

American Society of Civil Engineers. (2005). ASCE7-05: Minimum Design Loads for Buildings and Other Structures, Reston, VA.

American Society of Civil Engineers. (2002). ASCE7-02: Minimum Design Loads for Buildings and Other Structures, Reston, VA.

Aslani, H. (2005a). *Probabilistic Earthquake Loss Estimation and Loss Disaggregation in Buildings*, Ph.D. Dissertation, Department of Civil and Environmental Engineering, Stanford University.

Aslani, H., and Miranda, E. (2005b). Fragility assessment of slab-column connections in existing non-ductile reinforced concrete buildings. Journal of Earthquake Engineering, 9(6), pp. 777-804.

Aslani, H. and Miranda, E. (2004). "Component-Level and System-Level Sensitivity Study for Earthquake Loss Estimation," *13th World Conference on Earthquake Engineering*, Vancouver, B.C., Canada, August 1-6, 2004.

ATC-40, Applied Technology Council (1996). " Seismic Evaluation and Retrofit of Concrete Buildings," Report No. SSC 96-01, *Seismic Safety Commission*, Redwood City, California.

ATC-24, Applied Technology Council (1992). "Guidelines for Cyclic Seismic Testing of Components of Steel Structures", Redwood City, California.

Baker, J.W. and Cornell, C.A., (2006a) " Which Spectral Acceleration Are You Using?" *Earthquake Spectra*. May 2006, Volume 22, Issue 2, pp. 293-312.

Baker J.W. and C.A. Cornell (2006b). "Spectral shape, epsilon and record selection", *Earthquake Engr. & Structural Dynamics*, 34 (10), 1193-1217.

Baker, J. (2005a). *Vector-Valued Ground Motion Intensity Measures for Probabilistic Seismic Demand Analysis*, Ph.D. Dissertation, Department of Civil and Environmental Engineering, Stanford University.

Baker J.W. and C.A. Cornell (2005b). "A vector-valued ground motion intensity measure consisting of spectral acceleration and epsilon", *Earthquake Engr. & Structural Dynamics*, 34 (10), 1193-1217.

Baker, J. (2005c). Personal communication regarding the concept of collapse hazard disaggregation.

Baker, J. and Cornell, C. A. (2003). *Uncertainty Specification and Propagation for Loss Estimation Using FOSM Methods*, PEER Report 2003/07, Pacific Engineering Research Center, University of California, Berkeley, California, 89 pp.

Bazzurro P. and Cornell, C.A. (1999) "Disaggregation of Seismic Hazard," *Bull. Seism. Soc. Am.,* Vol. 89, no. 2, 501-520.

Benjamin, J.R. and Cornell, C.A. (1970). Probability, statistics, and decision for civil engineers, McGraw-Hill, New York, 684 pp.

Bernal, Dionisio (1994). "Viscous Damping in Inelastic Structural Response," *Journal of Structural Engineering*, Vol. 120, No. 4, April 1994, pp. 1240-1254.

Berry, M., Eberhard, M. (2005). "Practical Performance Model for Bar Buckling," *Journal of Structural Engineering*, Vol. 131, No. 7, July 2005, pp. 1060-1070.

Berry, M., Parrish, M., and Eberhard, M. (2004). *PEER Structural Performance Database User's Manual*, Pacific Engineering Research Center, University of California, Berkeley, California, 38 pp. Available at http://nisee.berkeley.edu/spd/ and http://maximus.ce.washington.edu/~peera1/ (March 10, 2005).

Berry, M., Eberhard, M. (2003). *Performance Models for Flexural Damage in Reinforced Concrete Columns*, PEER Report 2003/18, Pacific Engineering Research Center, University of California, Berkeley, California, 158 pp.

Boore D.M., Joyner W.B., and Fumal T.E. (1997). Equations for estimating horizontal response spectra and peak accelerations from western North America earthquakes: A summary of recent work, Seismological Research Letters, **68** (1), 128-153.

Brown, P.C., and Lowes, L.N. (2006). "Fragility Functions for Modern Reinforced Concrete Beam-Column Joints", *Earthquake Spectra,* in review.

Chatterjee, S., Hadi, A.S., and Price, B. (2000). *Regression Analysis by Example*, Third Edition, John Wiley and Sons Inc., New York, ISBN: 0-471-31946-5.

Ching, J., Porter, K. A., and Beck, J. L. (2004). *Uncertainty Propagation and Feature Selection for Loss Estimation in Performance-Based Earthquake Engineering,*" Report No. EERL 2004-02, California Institute of Technology, Pasadena, California.

Chopra, Anil K. (2001). *Dynamic of Structures, Second Edition*, Prentice Hall, New Jersey.

Chopra, A.K. and Goel, R.K. (2000) "Building Period Formulas for Estimating Seismic Displacements" *Earthquake Spectra*. May 2000, Volume 16, Issue 2, pp. 533-536.

Comité Euro-International du Béton (CEB) (1996). "RC Frames Under Earthquake Loading – State of the Art Report," Comité Euro-International du Bénton, Convenor Michael N. Fardis, Published by Thomas Telford, London.

Comité Euro-International du Béton (CEB) (1993). "CEB-FIP Model Code 1990." Thomas Telford, London.

Cordova, P. P., Deierlein, G. G., Mehanny, S, S.F. and Cornell, C. A. (2000). "Development of a Two-Parameter Seismic Intensity Measure and Probabilistic Assessment Procedure," *The Second U.S.-Japan Workshop on Performance-Based Earthquake Engineering Methodology for Reinforced Concrete Building Structures*, Sapporo, Hokkaido, September 2000

Cornell, C.A. (2005). Personal communication regarding a) considerations of uncertainty and use of the mean estimate approach, and b) proper approach when fitting a function to the hazard curve.

Cornell, C. A., Jalayer, F., Hamburger, R. O., and Foutch, D. A. (2002a). "Probabilistic Basis for 2000 SAC Federal Emergency Management Agency Steel Moment Frame Guidelines," *Journal of Structural Engineering*, Vol. 128, No. 4, April 2002, pp. 526-533.

Cornell, C.A. and J.W. Baker (2002b). Personal communication regarding first-order second-moment approximation.

Deierlein, G.G. and C.B. Haselton (2005a). "Benchmarking the Collapse Safety of Code-Compliant Reinforced Concrete Moment Frame Building Systems." *ATC/JSCA US-Japan Workshop on Improvement of Structural Design and Construction Practices, Proceedings of an International Workshop*, Kobe, Japan, October 17 – 19, 2005.

Deierlein, G.G. and C.B. Haselton (2005b), "Developing Consensus Provisions to Evaluate Collapse of Reinforced Concrete Buildings", *US-Japan DaiDaiToku/NEES Workshop on Seismic Response of Reinforced Concrete Structures,* Berkeley, California, July 7-8, 2005, 17 pp.

Deierlein, G. G. (2004). "Overview of a Comprehensive Framework for Earthquake Performance Assessment," *Performance-Based Seismic Design Concepts and Implementation, Proceedings of an International Workshop*, Bled Slovenia, June 28 – July 1, 2004, Peter Fajfar and Helmut Krawinkler, editors. PEER Report 2004/05, PEER, UC Berkeley, pp. 15-26.

Deierlein, G. G., Krawinkler, H., and Cornell, C.A. (2003). "A framework for performance-based earthquake engineering," Proceedings, *2003 Pacific Conference on Earthquake Engineering*. Christchurch, New Zealand, February 2003.

Deierlein G.G., and Kanvinde A.M., 2003. "Seismic Performance of Gypsum Walls – Analytical Investigation." Report W-23, CUREE Woodframe project.

Dhakal, R.P. and Maekawa, K. (2002). "Modeling of Postyielding Buckling of Reinforcement," *Journal of Structural Engineering*, Vol. 128, No. 9, September 2002, pp. 1139-1147.

DRAIN-2DX (1993), "DRAIN-2DX: Basic program description and user guide," Report No. UCB/SEMM-1993/17, by Prakash, V., Powell, G. H., and Campbell, S., University of California, Berkeley, CA, Nov. 1993, 97 pages.

Eberhard, M. (2005). *Structural Performance Database*, Department of Civil and Environmental Engineering, University of Washington, http://maximus.ce.washington.edu/~peera1/ (March 10, 2005).

Eligehousen, R., Popov, E.P., and Bertero, V.V. (1983). "Local Bond Stress-Slip Relationships of Deformed Bars Under Generalized Excitations," EERC Report 83/23, University of California, Berkeley.

Ellingwood, B., Galambos, T.V., MacGregor, J.G., and Cornell, C.A. (1980). *Development of a Probability-Based Load Criterion for American National Standard A58*, National Bureau of Standards, Washington, DC, 222 pp.

Elwood, K.J., Eberhard, M.O. (2006). "Effective Stiffness of Reinforced Concrete Columns," *Research Digest of the Pacific Earthquake Engineering Research Center*, 2006-01, March 2006.

Elwood, K.J., Moehle, J.P. (2005). "Axial Capacity Model for Shear-Damaged Columns," *ACI Structural Journal*, July-August 2005, No. 4, pp. 578-587.

Elwood, K.J. (2002). *Shake Table Tests and Analytical Studies on the Gravity Load Collapse of Reinforced Concrete Frames*, Ph.D. Dissertation, Department of Civil and Environmental Engineering, University of California, Berkeley.

Enomoto, B. and Robertson I. N. (2001). *Hysteretic Modeling of Flat Slab-Column Connections*, Research Report UHM/CE/01-03, Department of Civil and Environmental Engineering, University of Hawaii College of Engineering, May 2001.

Fajfar, P., Vidic, T., Fischinger, M. (1993). "Influence of damping model on the seismic response of nonlinear SDOF systems," *Structural Dynamics – EURODYN'93*, Editors: Moan, et al. Balkema, Rotterdam, ISBN 90 5410 336 1, pp. 133-140.

Fang, J.Q., Jeary, A.P., Wong, C.K. (1999). "Random damping in buildings and its AR model," *Journal of Wind Engineering and Industrial Aerodynamics*, 79 (1999), pp. 159-167.

Fardis, M. N. and Biskinis, D. E. (2003). "Deformation Capacity of RC Members, as Controlled by Flexure or Shear," *Otani Symposium*, 2003, pp. 511-530.

Feenstra, P. H. (1993). *Computational Aspects of Biaxial Stress in Plain and Reinforced Concrete*, Delft University Press, The Netherlands.

Federal Emergency Management Agency (2005). "FEMA 440: Improvement of Nonlinear Static Analysis Procedures", Report No. FEMA 440, Prepared by Applied Technology Council, Prepared for Federal Emergency Management Agency, Washington, DC.

Federal Emergency Management Agency (2001). "FEMA 355A-F: State of the Art Reports", Report No. FEMA 355A-F, Prepared by Applied Technology Council, Prepared for Federal Emergency Management Agency, Washington, DC.

Federal Emergency Management Agency (2000a). "FEMA 356: Prestandard and Commentary for the Seismic Rehabilitation of Buildings", Report No. FEMA 356, Prepared by Applied

Technology Council, Prepared for Federal Emergency Management Agency, Washington, DC.

Federal Emergency Management Agency. (2000b). "FEMA 350: Recommended Seismic Design Criteria for New Steel Moment-Frame Buildings", Report No. FEMA 350, Prepared by Applied Technology Council, Prepared for Federal Emergency Management Agency, Washington, DC.

Federal Emergency Management Agency (1997). "FEMA 273: NEHRP Commentary on the Guidelines for the Seismic Rehabilitation of Buildings", Report No. FEMA 273, Prepared by Applied Technology Council, Prepared for Federal Emergency Management Agency, Washington, DC.

Federal Emergency Management Agency (1992a). "FEMA 222: NEHRP Recommended Provisions for the Development of Regulations for New Buildings and NEHRP Maps, Part 1, 1991 Edition", Federal Emergency Management Agency, Washington, DC.

Federal Emergency Management Agency (1992b). "FEMA 223: NEHRP Recommended Provisions for the Development of Regulations for New Buildings, Part 2, Commentary, 1991", Federal Emergency Management Agency, Washington, DC.

Filippou, F. C. (2005). FEDEAS. http://www.ce.berkeley.edu/~filippou/Research/fedeas.htm (May 24, 2005).

Filippou, F. C., D'Ambrisi, A. and Issa, A. (1999). "Effects of Reinforcement Slip on Hysteretic Behavior of Reinforced Concrete Frame Members," *ACI Structural Journal*, May-June 1999, No. 3, pp. 327-335.

Filippou, F. C. (1999). "Analysis Platform and Member Models for Performance-Based Earthquake Engineering," *U.S.-Japan Workshop on Performance-Based Earthquake Engineering Methodology for Reinforced Concrete Building Structures*, PEER Report 1999/10, Pacific Engineering Research Center, University of California, Berkeley, California, pp. 95-106.

Goulet, C., C.B. Haselton, J. Mitrani-Reiser, J. Beck, G.G. Deierlein, K.A. Porter, and J. Stewart, (2006a). "Evaluation of the Seismic Performance of a Code-Conforming Reinforced-Concrete Frame Building - from seismic hazard to collapse Safety and Economic Losses", *Earthquake Engineering and Structural Dynamics,* (in press).

Goulet, C., C.B. Haselton, J. Mitrani-Reiser, G.G. Deierlein, J.P. Stewart, and E. Taciroglu (2006b), "Evaluation of the Seismic Performance of a Code-Conforming Reinforced-Concrete Frame Building - Part I: Ground Motion Selection and Structural Collapse Simulation", *8th National Conference on Earthquake Engineering (100th Anniversary Earthquake Conference)*, San Francisco, California, April 18-22, 2006, 10 pp.

Hachem, M., S. Mahin, and J, Moehle (2003). *Performance of Circular Reinforced Concrete Bridge Columns Under Bidirectional Earthquake Loading*, PEER Report 2003/06, Pacific Engineering Research Center, University of California, Berkeley, California.

Hamburger, R. O. (2004). "Development of Next-Generation Performance-Based Seismic Design Guidelines," *Performance-Based Seismic Design Concepts and Implementation, Proceedings of an International Workshop*, Bled Slovenia, June 28 – July 1, 2004, Peter Fajfar and Helmut Krawinkler, editors. PEER Report 2004/05, PEER, UC Berkeley, pp. 89-100.

Hamburger, R. O., Foutch, D. A., and Cornell, A. C. (2003). "Translating Research to Practice: FEMA/SAC Performance-based Design Procedures", *Earthquake Spectra,* Vol. 19, No. 2, pp. 255-267.

Harmsen, S.C., Frankel, A.D., and Petersen, M.D. (2002). "Deaggregation of U.S. Seismic Hazard: The 2002 Update", U.S. Geological Survey Open-File Report 03-440, http://pubs.usgs.gov/of/2003/ofr-03-440/ofr-03-440.html (last accessed September 12, 2006).

Harmsen, S.C. (2001). "Mean and Modal ε in the Deaggregation of Probabilistic Ground Motion", *Bulletin of the Seismological Society of America*, **91**, 6, pp. 1537-1552, December 2001.

Hart, Gary C., Vasudevan, Ramaswami (1975). "Earthquake Design of Buildings: Damping," *Journal of the Structural Division*, Vol. 101, No. ST1, January, 1975, pp. 11-20.

Haselton, C.B., J.W. Baker, A.B. Liel, C. Kircher, and G.G. Deierlein (2007a). "Accounting for Expected Spectral Shape (Epsilon) in Collapse Performance Assessment, *Earthquake Spectra* (in preparation). An early version of this paper is included as Chapter 3 of this thesis.

Haselton, C.B., A.B. Liel, S. Taylor Lange and G.G. Deierlein (2007b). "Beam-Column Element Model Calibrated for Predicting Flexural Response Leading to Global Collapse of RC Frame Buildings", *American Concrete Institute Structural Journal*, (in preparation). An early version of this paper is included as Chapter 4 of this thesis.

Haselton, C.B., A.B. Liel, B.S. Dean, and G.G. Deierlein (2007c). "Archetypes: Generalize Collapse Performance Predictions for the Class of Reinforced Concrete Special Moment Frame Buildings," *ASCE Journal of Structural Engineering* (in preparation). An early version of this paper is included as Chapter 6 of this thesis.

Haselton, C.B., A.B. Liel, J. Chou, and G.G. Deierlein (2007d). "Effects of Building Code Design Provisions on Collapse Performance of Reinforced Concrete Special Moment Frame Buildings," *ASCE Journal of Structural Engineering* (in preparation). An early version of this paper is included as Chapter 7 of this thesis.

Haselton, C. B., C. Goulet, J. Mitrani-Reiser, J. Beck, G.G. Deierlein, K.A. Porter, and J. Stewart (2007e). *An Assessment to Benchmark the Seismic Performance of a Code-Conforming Reinforced-Concrete Moment-Frame Building*, PEER Report 2007, Pacific Earthquake Engineering Research Center, University of California, Berkeley, California, (in preparation).

Haselton, C.B., A.B. Liel, S. Taylor Lange and G.G. Deierlein (2007f). *Beam-Column Element Model Calibrated for Predicting Flexural Response Leading to Global Collapse of RC Frame Buildings*, PEER Report 2007, Pacific Engineering Research Center, University of California, Berkeley, California, (in preparation).

Haselton, C.B., A.B. Liel, B.S. Dean, J. Chou, and G.G. Deierlein (2007g), "Seismic Collapse Safety and Behavior of Modern Reinforced Concrete Moment Frame Building"; Proceedings of ASCE-SEI Structures Congress, Long Beach, California, May 2007, 14 pp. (accepted)

Haselton, C.B. and J.W. Baker (2006a), "Ground motion intensity measures for collapse capacity prediction: Choice of optimal spectral period and effect of spectral shape", *8th National Conference on Earthquake Engineering*, San Francisco, California, April 18-22, 2006.

Haselton, C.B. and G.G. Deierlein (2006b). "Toward the Codification of Modeling Provisions for Simulating Structural Collapse," *8th National Conference on Earthquake Engineering (100th Anniversary Earthquake Conference)*, San Francisco, California, April 18-22, 2006, 10 pp.

HAZUS (2003). "Earthquake Model HAZUS-MH MR1 Advanced Engineering Building Module Technical and User's Manual," *Multi-Hazard Loss Estimation Methodology,* Department of Homeland Security, National Institute of Building Sciences, Washington D.C.

Hooper, J. (2006). Personal communication regarding (a) common structural engineering design practice, and (b) specific feedback on the majority of the structural designs used in the reinforce concrete special moment frame archetype study.

Hueste, M.B.D., and J.K. Wight (1999). "Nonlinear Punching Shear Failure Model for Interior Slab-Column Connections," *Journal of Structural Engineering*, Vol. 125, No. 9, September 1999, pp. 997-1007.

Ibarra, L.F., Medina, R.A., and Krawinkler, H. (2005). "Hysteretic models that incorporate strength and stiffness deterioration," *Earthquake Engineering and Structural Dynamics*, Vol. 34, pp. 1489-1511.

Ibarra, L., Krawinkler, H. (2005b). *Effects of Uncertainty in System Deterioration Parameters on the Variance of Collapse Capacity*, 9th International Conference on Structural Safety and Reliability, Rome, Italy, June 19-23, 2005.

Ibarra, L., Krawinkler, H. (2004). *Global Collapse of Deteriorating MDOF Systems*, 13th World Conference on Earthquake Engineering, Vancouver, B.C., Canada, August 1-6, 2004, Paper No. 116.

Ibarra, L. (2003). *Global Collapse of Frame Structures Under Seismic Excitations*, Ph.D. Dissertation, Department of Civil and Environmental Engineering, Stanford University.

Ingham, J.M., Lidell, D., and B.J. Davidson (2001). *Influence of Loading History on the Response of a Reinforced Concrete Beam*, Bulletin of the New Zealand Society for Earthquake Engineering, Vol. 34, No. 2, 2001, pp. 107-124.

International Code Council. (2005). *2005 International Building Code,* Falls Church, VA.

International Code Council. (2003). *2003 International Building Code,* Falls Church, VA.

Jalayer F., 2003. *Direct probabilistic seismic analysis: Implementing non-linear dynamic assessments*, Ph.D. Dissertation, Department of Civil and Environmental Engineering, Stanford University., 244 pp. http://www.stanford.edu/group/rms/ (accessed 3/14/05)

Kaklauskas, G., Ghaboussi, J. (2001). "Stress-Strain Relations for Cracked Tensile Concrete RC Beam Tests," *Journal of Structural Engineering*, Vol. 127, No. 1, January 2001, pp. 64-73.

Kircher and Associates, Consulting Engineers (2005). *Strong-Motion Earthquake Record Set for Soil Sites not Near Source*, personal communication, August 6, 2005.

Kramer, S.L. (1996). *Geotechnical Earthquake Engineering*, Prentice Hall, New Jersey, ISBN: 0-13-374943-6.

Krawinkler, H. (2005). "Van Nuys Hotel Building Testbed Report: Exercising Seismic Performance Assessment," PEER Report 2005/11, PEER, UC Berkeley, 249 pp.

Krawinkler, H., Miranda E., Bozorgnia, Y. and Bertero, V. V. (2004). “Chapter 9: Performance Based Earthquake Engineering,”, *Earthquake Engineering: From Engineering Seismology to Performance-Based Engineering*, CRC Press, Florida.

Krawinkler, H., Zareian, F., Medina, R., and Ibarra, L. (2004). “Contrasting Performance-Based Design with Performance Assessment,” *Performance-Based Seismic Design Concepts and Implementation, Proceedings of an International Workshop*, Bled Slovenia, June 28 – July 1, 2004, Peter Fajfar and Helmut Krawinkler, editors. PEER Report 2004/05, PEER, UC Berkeley, pp. 505-516.

Lee, K., and Foutch, D.A. (2000). “Performance prediction and evaluation of steel special moment frames for seismic loads.” *SAC Background Document SAC/BD-00/25*, SAC Joint Venture, Richmond, California.

Legeron, F., and Paultre, P. (2000). "Behavior of High-Strength Concrete Columns under Cyclic Flexure and Constant Axial Load," *American Concrete Institute Structural Journal*, Vol. 97, No. 4, July-August 2000, pp. 591-601.

Lehman, D.E., and J.P. Moehle (1998). “Seismic Performance of Well-Confined Concrete Bridge Columns,” PEER Report 1998/01, PEER, UC Berkeley, 295 pp.

Liel, A., C.B. Haselton, and G.G. Deierlein (2006a), “The effectiveness of seismic building code provisions on reducing the collapse risk of reinforced concrete moment frame buildings”, 4th International Conference on Earthquake Engineering, Taipei, Taiwan, October 12-13, 2006.

Liel, A., C.B. Haselton, and G.G. Deierlein (2006b), “How have changes in building code provisions for reinforced concrete buildings improved seismic safety?”, *8th National Conference on Earthquake Engineering (100th Anniversary Earthquake Conference)*, San Francisco, California, April 18-22, 2006, 10 pp.

Lowes. L. N., Mitra, N. and Altoontash, A. (2004). *A Beam Column Joint Model for Simulating the Earthquake Response of Reinforced Concrete Frame*, PEER Report 2003/10, Pacific Engineering Research Center, University of California, Berkeley, California, 59 pp.

Lowes, L., Altoontash, A. (2003). “Modeling Reinforced-Concrete Beam-Column Joints Subjected to Cyclic Loading,” *Journal of Structural Engineering*, Vol. 129, No. 12, December 2003, pp. 1686-1697.

Luco, N., Y. Mori, Y. Funahashi, C.A. Cornell, M. Nakashima (2003). *Evaluation of predictors of non-linear seismic demands using “fishbone” models of SMRF buildings*, Earthquake

Engineering & Structural Dynamics, Volume 32, Issue 14, Date: 25 November 2003, Pages: 2267-2288.

Mander, J. B., Priestly, M. J. N., Park, R. (1988a). "Theoretical Stress-Strain Model for Confined Concrete," *Journal of Structural Engineering*, Vol. 114, No. 8, August 1988, pp. 1804-1826.

Mander, J. B., Priestly, M. J. N., Park, R. (1988b). "Observed Stress-Strain Behavior of Confined Concrete," *Journal of Structural Engineering*, Vol. 114, No. 8, August 1988, pp. 1827-1849.

Mathworks (2006) .*MatlabDocumentation.* http://www.mathworks.com/access/helpdesk/help/techdoc/matlab.shtml (last accessed October 23, 2006)

Mazzoni, S., Moehle, J.P. (2001). "Seismic Response of Beam-Column Joints in Double-Deck Reinforced Concrete Bridge Frames," *ACI Structural Journal*, Vol. 98(3), pp. 259-269.

McGuire, R.K. (1995). "Probabilistic seismic hazard analysis and design earthquakes: closing the loop", *Bulletin of the Seismological Society of America*, **85**, pp. 1275-1284.

Medina, R.A. (2002). *Seismic Demands for Nondeteriorating Frame Structures and Their Dependence on Ground Motions*, Ph.D. Dissertation, Department of Civil and Environmental Engineering, Stanford University.

Mehanny, S.S.F. (1999). *Modeling and Assessment of Seismic Performance of Composite Frames with Reinforced Concrete Columns and Steel Beams*, Ph.D. Dissertation, Department of Civil and Environmental Engineering, Stanford University.

Meinheit, D. F. and Jirsa, J. O. (1981). "Shear Strength of R/C Beam-Column Connections," *Journal of the Structural Division*, Vol. 107, No. ST11, November 1981, pp. 2227-2244.

Melchers, Robert E. (1999). *Structural Reliability Analysis and Prediction*, John Wiley and Sons Inc., New York.

Miranda, E. (2005). Personal communication regarding his current research on damping in buildings.

Mitra, N. and Lowes, L. (2006). "Evaluation, Calibration, and Verification of a Reinforced Concrete Beam-Column Joint Model," *ASCE Journal of Structural Engineering*, submitted.

Mitra, N. and Lowes, L. (2004). "Evaluation and Advancement of a Reinforced Concrete Beam-Column Joint Model," *13th World Conference on Earthquake Engineering*, Vancouver, B.C., Canada, August 1-6, 2004.

Mitrani-Reiser, J., C.B. Haselton, C. Goulet, K.A. Porter, J. Beck, and G.G. Deierlein (2006), "Evaluation of the Seismic Performance of a Code-Conforming Reinforced-Concrete Frame Building - Part II: Loss Estimation", *8th National Conference on Earthquake Engineering*

(100th Anniversary Earthquake Conference), San Francisco, California, April 18-22, 2006, 10 pp.

Moehle, J. and T. Kabeyasawa (2005). Proceedings of the First NEES/E-Defense Workshop on Collapse Simulation of Reinforced Concrete Building Structures*, PEER Report 2005/10, September 2005, Pacific Engineering Research Center, University of California, Berkeley, California.*

Moehle, J., Deierlein, G. G.(2005). "A Framework Methodology for Performance-Based Engineering," *Performance-Based Seismic Design Concepts and Implementation, Proceedings of an International Workshop*, Bled, Slovenia, June 28 – July 1, 2004, Peter Fajfar and Helmut Krawinkler, editors. Pacific Earthquake Engineering Research Center, PEER 2004/05, UC Berkeley.

Moehle, J. and Deierlein, G. G. (2004). "A Framework Methodology for Performance-Based Engineering," *13th World Conference on Earthquake Engineering*, Vancouver, B.C., Canada, August 1-6, 2004.

Neuenhofer, A. and Filippou, F. C. (1997). "Evaluation of Nonlinear Frame Finite-Element Models," *Journal of Structural Engineering*, Vol. 123, No. 7, July 1997, pp. 958-966.

Open System for Earthquake Engineering Simulation (Opensees) (2006). Pacific Earthquake Engineering Research Center, University of California, Berkeley, http://opensees.berkeley.edu/ (last accessed December 1, 2006).

Pan, A. and J.P. Moehle (1986). "Lateral Displacement Ductility of Reinforced Concrete Flat Plats," *ACI Structural Journal*, Vol. 86, No. 3, May 1986.

Panagiotakos, T. B. and Fardis, M. N. (2001). "Deformations of Reinforced Concrete at Yielding and Ultimate," *ACI Structural Journal*, Vol. 98, No. 2, March-April 2001, pp. 135-147.

Park, R., and T. Paulay, T. (1975). "*Reinforced Concrete Structures*," A Wiley-Interscience Publication, pp. 740-757.

Park, R. et al. (1972). "Reinforced Concrete Members with Cyclic Loading," *Journal of the Structural Division*, ST7, July 1972.

Paspuleti, C. (2002). *Seismic Analysis of Older Reinforced Concrete Structures*, Master's Thesis, Department of Civil and Environmental Engineering, University of Washington.

Paulay, T. and Priestley, M. J. N. (1992). *Seismic Deign of Reinforced Concrete and Masonry Buildings*, John Wiley and Sons Inc., New York.

Paultre, P., Legeron, F., and Mongeau, D. (2001), "Influence of Concrete Strength and Transverse Reinforcement Yield Strength on Behavior of High-Strength Concrete Columns", American Concrete Institute, *ACI Structural Journal*, Vol. 98, No. 4, July-August 2001,

PEER (2006a). *Pacific Earthquake Engineering Research Center: Structural Performance Database*, University of California, Berkeley, Available at http://nisee.berkeley.edu/spd/ and http://maximus.ce.washington.edu/~peera1/ (last accessed October 22, 2006).

PEER (2006b). *Pacific Earthquake Engineering Research Center: PEER NGA Database*, University of California, Berkeley, http://peer.berkeley.edu/nga/

(last accessed October 22, 2006).

Perus, I., Poljansek, K., and P. Fajfar (2006). "Flexural deformation capacity of recetangular RC columns determined by the CAE method", *Earthquake Engineering and Structural Dynamics*, **35**, 1453-1470.

Porter, K.A., J.L. Beck, and R.V. Shaikhutdinov, (2004). "Simplified Estimation of Economic Seismic Risk for Buildings," Earthquake Spectra, 20 (4), Nov 2004, 1239-1264.

Porter, K. A. (2004). "Simplified PBEE to Estimate Economic Seismic Risk for Buildings," *Performance-Based Seismic Design Concepts and Implementation, Proceedings of an International Workshop*, Bled, Slovenia, June 28 – July 1, 2004, Peter Fajfar and Helmut Krawinkler, editors. Pacific Earthquake Engineering Research Center, PEER 2004/05, UC Berkeley.

Porter, K. A. (2003). "An Overview of PEER's Performance-Based Earthquake Engineering Methodology," *Conference on Applications of Statistics and Probability in Civil Engineering (ICASP9)*, Civil Engineering Risk and Reliability Association (CERRA), San Francisco, CA, July 6-9, 2003.

Porter, K. A., Beck, J. L., Shaikhutdinov, R. V. (2002). *Investigation of Sensitivity of Building Loss Estimates to Major Uncertain Variables for the Van Nuys Testbed*, PEER Report 2002/03, Pacific Engineering Research Center, University of California, Berkeley, California, 41 pp.

Priestly, M.J.N. (1998). "Displacement-Based Approaches to Rational Limit State Design of New Structures," Proceedings, 11th European Conference on Earthquake Engineering, Paris P. Bisch, P. Labbe, and A. Pecker, eds., Balkema, Rotterdam, Sept. 1998, pp. 317-335.

Pujol, S., Ramirez, J.A., Sozen, M.A. (1999). "Drift Capacity of Reinforced Concrete Columns Subjected to Cyclic Shear Reversals," *Seismic Response of Bridges*, SP-187, American Concrete Institute, Farmington Hills, Michigan, pp. 255-274.

Robertson, I. (2002). *Research Progress Presentation at PEER Annual Meeting,* Pacific Earthquake Engineering Research Center Annual Meeting, January 17-18, 2002, Oakland, California.

ROSRINE (2005). Resolution of Site Response Issues from the Northridge Earthquake, 2005. *Website by Earthquake Hazard Mitigation Program & Caltrans*. http://geoinfo.usc.edu/rosrine/.

Saatcioglu, M and Grira, M. (1999). "Confinement of Reinforced Concrete Columns with Welded Reinforcement Grids," *ACI Structural Journal*, American Concrete Institute, Vol. 96, No. 1, January-February 1999, pp. 29-39.

Scott, B. D., Park R., and Priestley, M. J. N. (1982). "Stress-Strain Behavior of Concrete Confined by Overlapping Hoops and Low and High Strain Rates," *ACI Journal*, January-February 1982, No. 1, pp. 13-27.

Seung-Yul, Y., R. O. Hanburger, C. A. Cornell, D. A. Foutch. (2002). "Seismic Performance Evaluation of Steel Moment Frames," *Journal of Structural Engineering*, Vol. 128, No. 4, April 2002, pp. 534-545.

Seneviratna, G.D.P.K. and H. Krawinkler, 1994, "Strength and Displacement Demands for Seismic Design of Structural Walls", *5th National Conference on Earthquake Engineering*, Volume II, pp. 181-190.

Sezen, H. (2003). *Seismic Response and Modeling of Reinforced Concrete Columns*, Ph.D.Dissertation, Department of Civil and Environmental Engineering, University of California, Berkeley.

Shome, N., C.A. Cornell, P. Bazzuro, and J.F. Carballo (1998). "Earthquakes, Records, and Nonlinear Responses," Earthquake Spectra, **14**(3), 469-500.

Soesianawati, M.T., Park, R., and Priestley, M.J.N. (1986). "Limited Ductility Design of Reinforced Concrete Columns," Report 86-10, Department of Civil Engineering, University of Canterbury, Christchurch, New Zealand, March 1986, 208 pages.

Sozen, M.A., Monteiro, P., and Moehle, J.P. (1992). Effects of Cracking and Age on Stiffness of Reinforced Concrete Walls Resisting In-Plane Shear, *Proceedings*, 4th Symposium on

Current Issues Related to Nuclear Power Plant Structures, Equipment and Piping, Orlando, Florida, 1992.

Spacone, E., Filippou, F. C. and Taucer, F. F. (1996a). "Fibre Beam-Column Model for Non-Linear Analysis of R/C Frame: Part I. Formulation," *Earthquake Engineering and Structural Dynamics*, Vol. 25, pp. 711-725.

Spacone, E., Filippou, F. C. and Taucer, F. F. (1996b). "Fibre Beam-Column Model for Non-Linear Analysis of R/C Frame: Part II. Applications," *Earthquake Engineering and Structural Dynamics*, Vol. 25, pp. 727-742.

Stevens, N.J., Uzumeri, S.M., and Collins, M.P. (1991). "Reinforced Concrete Subjected to Reversed Cyclic Shear – Experiments and Constitutive Model," *ACI Structural Journal*, March-April 1991, pp. 135-146.

Stewart, J. (2004). Personal communication regarding footing rotation stiffness for structural modeling.

Takagi, J. (2005). Personal communication.

Tothong, Polsak (2007). *Probabilistic Seismic Demand Analysis using Advanced Ground Motion Intensity Measures, Attenuation Relationships, and Near-Fault Effects*, PhD Dissertation, Department of Civil and Environmental Engineering, Stanford University.

UBC (1997), "Uniform Building Code," *International Conference of Building Officials*, Whittier, California.

Umemura, H. and Aoyama H. (1969). "Evaluation of Inelastic Seismic Deflection of RC Frames Based on Tests of Members," *Proc. 4th WCEE*, Chile.

United States Geological Survey (USGS) (2006). "Interpolated Probabilistic Ground Motion for the Conterminous 48 States by Latitude Longitude, 2002 Data," available at http://eqint.cr.usgs.gov/eq-men/html/lookup-2002-interp-06.html (last accessed October 24, 2006).

Vamvatsikos, D. and C. Allin Cornell (2005). "Developing efficient scalar and vector intensity measures for IDA capacity estimation by incorporating elastic spectral shape information," *Earthquake Engineering and Structural Dynamics*, Vol. 34, Issue 13, pp. 1573-1600.

Vamvatsikos, D. and C. Allin Cornell (2002a). "Incremental Dynamic Analysis," *Earthquake Engineering and Structural Dynamics*, Vol. 31, Issue 3, pp. 491-514.

Vamvatsikos, D. (2002b). *Seismic Performance, Capacity and Reliability of Structures as Seen Through Incremental Dynamic Analysis*, PhD Dissertation, Department of Civil and Environmental Engineering, Stanford University.

Vecchio, F.J. and Collins, M.P. (1986). "The Modified Compression-Field Theory for Reinforced Concrete Elements Subjected to Shear," *ACI Structural Journal*, March-April 1986, pp. 219-231.

Vick, S.G. (2002). *Degrees of Belief: Subjective Probability and Engineering Judgment*, ASCE Press, Reston, Virginia.

Wang, Pao-Tsan, Shah, Surendra, P., Naaman, Antoine E. (1978). "High-Strength Concrete in Ultimate Strength Design," *Journal of the Structural Division*, ST11, November 1978, pp. 1761-1773.

Wen, Y.K., Ellingwood, B.R., Veneziano, D., and J. Bracci (2003). "Uncertainty Modeling in Earthquake Engineering," MAE Center Project FD-2 Report, February 2003.

Xiao, Y. and Martirossyan, A. (1998). "Seismic Performance of High-Strength Concrete Columns," *Journal of Structural Engineering*, March 1998, pp. 241-251.

Yoshikawa, H., Miyagi, T. (2001). "Ductility and Failure Modes of Singly Reinforced Concrete Columns," *Modeling of Inelastic Behavior of RC Structures Under Seismic Loads*, Editors: P. Benson Shing and Tada-Aki Tanabe, American Society of Civil Engineers, 2001, pp. 35-368.

Yun, S., Hamburger, R., Cornell, C.A., and D. Foutch (2002). "Seismic Performance Evaluation for Steel Moment Frame," *Journal of Structural Engineering*, Vol. 128, No. 4, April 2002, pp. 534-545.

Zareian, F. (2006). *Simplified Performance-Based Earthquake Engineering*, Dissertation, Department of Civil and Environmental Engineering, Stanford University.

PEER REPORTS

PEER reports are available from the National Information Service for Earthquake Engineering (NISEE). To order PEER reports, please contact the Pacific Earthquake Engineering Research Center, 1301 South 46th Street, Richmond, California 94804-4698. Tel.: (510) 665-3405; Fax: (510) 665-3420.

PEER 2007/08 *Assessing Seismic Collapse Safety of Modern Reinforced Concrete Moment-Frame Buildings.* Curt B. Haselton and Gregory G. Deierlein. February 2008.

PEER 2007/06 *Development of Improved Procedures for Seismic Design of Buried and Partially Buried Structures.* Linda Al Atik and Nicholas Sitar. June 2007.

PEER 2007/05 *Uncertainty and Correlation in Seismic Risk Assessment of Transportation Systems.* Renee G. Lee and Anne S. Kiremidjian. July 2007.

PEER 2007/02 *Campbell-Bozorgnia NGA Ground Motion Relations for the Geometric Mean Horizontal Component of Peak and Spectral Ground Motion Parameters.* Kenneth W. Campbell and Yousef Bozorgnia. May 2007.

PEER 2007/01 *Boore-Atkinson NGA Ground Motion Relations for the Geometric Mean Horizontal Component of Peak and Spectral Ground Motion Parameters.* David M. Boore and Gail M. Atkinson. May. May 2007.

PEER 2006/12 *Societal Implications of Performance-Based Earthquake Engineering.* Peter J. May. May 2007.

PEER 2006/11 *Probabilistic Seismic Demand Analysis Using Advanced Ground Motion Intensity Measures, Attenuation Relationships, and Near-Fault Effects.* Polsak Tothong and C. Allin Cornell. March 2007.

PEER 2006/10 *Application of the PEER PBEE Methodology to the I-880 Viaduct.* Sashi Kunnath. February 2007.

PEER 2006/09 *Quantifying Economic Losses from Travel Forgone Following a Large Metropolitan Earthquake.* James Moore, Sungbin Cho, Yue Yue Fan, and Stuart Werner. November 2006.

PEER 2006/08 *Vector-Valued Ground Motion Intensity Measures for Probabilistic Seismic Demand Analysis*. Jack W. Baker and C. Allin Cornell. October 2006.

PEER 2006/07 *Analytical Modeling of Reinforced Concrete Walls for Predicting Flexural and Coupled–Shear-Flexural Responses*. Kutay Orakcal, Loenardo M. Massone, and John W. Wallace. October 2006.

PEER 2006/06 *Nonlinear Analysis of a Soil-Drilled Pier System under Static and Dynamic Axial Loading.* Gang Wang and Nicholas Sitar. November 2006.

PEER 2006/05 *Advanced Seismic Assessment Guidelines.* Paolo Bazzurro, C. Allin Cornell, Charles Menun, Maziar Motahari, and Nicolas Luco. September 2006.

PEER 2006/04 *Probabilistic Seismic Evaluation of Reinforced Concrete Structural Components and Systems.* Tae Hyung Lee and Khalid M. Mosalam. August 2006.

PEER 2006/03 *Performance of Lifelines Subjected to Lateral Spreading.* Scott A. Ashford and Teerawut Juirnarongrit. July 2006.

PEER 2006/02 *Pacific Earthquake Engineering Research Center Highway Demonstration Project.* Anne Kiremidjian, James Moore, Yue Yue Fan, Nesrin Basoz, Ozgur Yazali, and Meredith Williams. April 2006.

PEER 2006/01 *Bracing Berkeley. A Guide to Seismic Safety on the UC Berkeley Campus.* Mary C. Comerio, Stephen Tobriner, and Ariane Fehrenkamp. January 2006.

PEER 2005/16 *Seismic Response and Reliability of Electrical Substation Equipment and Systems.* Junho Song, Armen Der Kiureghian, and Jerome L. Sackman. April 2006.

PEER 2005/15 *CPT-Based Probabilistic Assessment of Seismic Soil Liquefaction Initiation.* R. E. S. Moss, R. B. Seed, R. E. Kayen, J. P. Stewart, and A. Der Kiureghian. April 2006.

PEER 2005/14 *Workshop on Modeling of Nonlinear Cyclic Load-Deformation Behavior of Shallow Foundations.* Bruce L. Kutter, Geoffrey Martin, Tara Hutchinson, Chad Harden, Sivapalan Gajan, and Justin Phalen. March 2006.

PEER 2005/13 *Stochastic Characterization and Decision Bases under Time-Dependent Aftershock Risk in Performance-Based Earthquake Engineering.* Gee Liek Yeo and C. Allin Cornell. July 2005.

PEER 2005/12 *PEER Testbed Study on a Laboratory Building: Exercising Seismic Performance Assessment.* Mary C. Comerio, editor. November 2005.

PEER 2005/11 *Van Nuys Hotel Building Testbed Report: Exercising Seismic Performance Assessment.* Helmut Krawinkler, editor. October 2005.